Influence des propriétés du réseau d'écoulement sur les processus de transport dans les aquifères fracturés et karstiques : de l'expérience de laboratoire et de terrain jusqu'à la modélisation numérique

Chaoqi Wang

THÈSE POUR OBTENIR LE GRADE DE DOCTEUR DE L'UNIVERSITÉ DE MONTPELLIER

École doctorale GAIA (N°584)

Filière Sciences de la Terre et de l'Eau

Unité de recherche HydroSciences Montpellier (HSM), UMR 5151 UM-CNRS-IRD

Influence des propriétés du réseau d'écoulement sur les processus de transport dans les aquifères fracturés et karstiques : de l'expérience de laboratoire et de terrain jusqu'à la modélisation numérique.

Présentée par Chaoqi Wang

Le 28 Juin 2022

Devant le jury composé de

David LABAT, Professeur, Université Paul Sabatier Toulouse 3, France	Président du jury
Abderrahim JARDANI, Maître de conférence, HDR, Université de Rouen, France	Membre du jury
Naomi MAZZILLI, Maître de conférences, Université d'Avignon, France	Membre du jury
Catherine BERTRAND, Maître de conférences, Université de Franche-Comté, France	Rapporteur
Hervé JOURDE, Professeur, Université de Montpellier, France	Directeur de thèse
Vincent GUINOT, Professeur, Université de Montpellier, France	Co-Directeur de thèse

UNIVERSITÉ DE MONTPELLIER

Influence of drainage network properties on transport processes in fractured and karst aquifers: from lab and field experiments to numerical modeling.

by

Chaoqi Wang

Thesis manuscript for the obtention of the Doctor of Philosophy (PhD) degree in the specialty **Water and Earth Sciences**

Thesis prepared at Université de Montpellier

2022

Abstract :

Dye tracing experiments are generally set up to identify karst springs catchments or transport properties of heterogeneous or homogeneous aquifers. They are also relevant methods for characterizing flow and transport processes in fractured and karst aquifers, and get insights about their complex structure and heterogeneity. A precise analysis of breakthrough curves (BTCs) obtained from dye tracing experiments in synthetic pipe networks and fracture networks of know geometry and topology should thus allow a better assessment of the relationship between drainage network properties and transport processes.

In this work, solute transport experiments consisting of step tracing are thus conducted, with a focus on dual-conduit structure. Five groups of experiments have been carried out to investigate how the following factors related to the dual-conduit structure may influence the transport processes: length ratio, total length (fixing the length ratio), connection angle, aperture contrast, and flow rate. Numerical models are then applied to fit the experimental BTCs and quantitatively evaluate the solute transport processes. The single-peaked BTCs are simulated considering i) the Advection Dispersion Equation (ADE) model, ii) the Dual Region Mobile Immobile Model (DRMIM), and iii) the Transfer Function Approach (TFA). The dual-peaked BTCs are simulated considering i) the Dual Region Advection Dispersion (DRAD) model, ii) the Weighted Sum Advection–Dispersion Equation (WSADE) model and iii) the DRMIM. Based on these results, a method has been proposed for estimating underground karstic conduit lengths from experimental dual peaked BTCs. For some experiments, it is shown that the TFA allows a better fitting than the ADE model and DRMIM. In order to assess what physical information contain the TFA parameters, we analyse the equivalence between TFA and Advection Dispersion Equation (ADE). We then obtain two equations that, under certain conditions, make TFA and ADE produce identical BTCs and allow expressing the TFA parameters as a function of the variable and parameters considered in the ADE.

Finally, a methodology for characterizing a karst conduit network at the scale of an experimental field site where both pumping test and dye tracing experiment have been performed is proposed. This characterization is based on a hydraulic tomography method which considers a discrete conduit network model to explicitly represent the underground conduit network, integrating hydraulic data and dye tracing data to constrain the diameter distribution of the karst conduit network.

The results of these lab scale and field scale experiments, together with the proposed numerical tools, should help hydrogeologists to better interpret the results of the tracing tests realized in real karst aquifers and improve their understanding of transport processes. These results may also guide hydrogeologists to select the most suitable model for interpreting their dye tracing experiment.

Résumé:

Les essais par traçages sont généralement mis en place pour identifier le bassin d'alimentation de sources karstiques ou les propriétés de transport des aquifères hétérogènes ou homogènes. Elles sont également des méthodes pertinentes pour caractériser les processus d'écoulement et de transport dans les aquifères fracturés et karstiques afin mieux appréhender la complexité de leur structure et leur forte hétérogénéité. Ainsi, les relations entre les propriétés du réseau de drainage et les processus de transport peuvent être appréciée par une étude précise des courbes de restitutions de traçages dans un réseau de conduits ou de fractures de géométrie et de topologie connues.

Dans ce travail, nous étudions le processus de transport de soluté dans des réseaux synthétiques de conduits ou et de fractures de géométrie et de topologie connues. Pour ce faire, nous réalisons des expériences de transport de soluté consistant en l'injection d'un créneau de concentration, en étudiant tout particulièrement l'influence d'une structure à double conduit. Des modèles numériques sont ensuite appliqués pour ajuster les courbes de restitutions expérimentales et évaluer quantitativement les processus de transport de soluté. Les courbes de restitutions à un seul pic sont simulées en utilisant i) le modèle basé sur l'équation d'advection dispersion (ADE), ii) le modèle DRMIM (Dual Region Mobile Immobile Model), et iii) l'approche de la fonction de transfert (TFA). Les courbes de restitutions à deux pics sont simulés en considérant i) le modèle de dispersion par advection à deux régions (DRAD), ii) le modèle d'équation d'advection-dispersion à somme pondérée (WSADE) et iii) le DRMIM. Sur la base de ces résultats, une méthode a été proposée pour estimer la longueur des conduits karstiques souterrains à partir courbes de restitutions expérimentales à deux pics. Pour certaines expériences, il est montré que le TFA permet un meilleur ajustement que le modèle ADE et le DRMIM. Afin d'évaluer quelles informations physiques contiennent les paramètres de la TFA, nous analysons l'équivalence entre la TFA et l'équation de dispersion par advection (ADE). Nous obtenons alors deux équations qui, sous certaines conditions, permettent de génèrer des courbes de restitutions identiques et d'exprimer les paramètres de la TFA en fonction de la variable et des paramètres considérés dans l'ADE.

Enfin, une méthodologie de caractérisation d'un réseau de conduits karstiques à l'échelle d'un site de terrain expérimental où ont été réalisés à la fois des essais par pompage et des expériences de traçages est proposée. Cette caractérisation est basée sur une méthode de tomographie hydraulique qui considère un modèle de réseau de conduits pour représenter explicitement le réseau de conduits souterrains, et intègre des données hydrauliques et des données de traçage de colorant pour contraindre la distribution de diamètre du réseau de conduits karstiques.

Les résultats de ces expériences à l'échelle du laboratoire et du terrain, ainsi que les outils numériques proposés, devraient aider les hydrogéologues à mieux interpréter les résultats des tests de traçage réalisés dans des aquifères karstiques réels et à améliorer leur compréhension des processus de transport. Ces résultats peuvent également guider les hydrogéologues à choisir le modèle le plus approprié pour interpréter

leur expérience de traçage de colorant.

ACKNOWLEDGEMENTS

Firstly, I would like to thank my three supervisors: Hervé Jourde, Vincent Guinot, and Samer Majdalani. During my study in the lab, they always give me valuable instructions and unconditional support. My professors held numerous meetings to hear my research progress and instruct me to carry out further research. The frequency was about once every two weeks in the first year and the meeting was still frequent after the first year. For example, Prof. Jourde directed my research to be closely related to hydrology application; Prof. Guinot gave me lessons in mathematics and algorithm programming; Prof. Majdalani has installed the experimental devices and materials in the lab, so I can effectively complete the lab experiments. Sincerely I honor such devotion and dutifulness. With their help, I managed to overcome all of the difficulties in my research and complete this Ph. D study. Besides, my professors well organized all of the administrative events required in my Ph. D, including organizing the Comite de Suivi Individuel (CSI) and the defense of Ph. D thesis. I would also like to thank Xiaoguang Wang, who also participated to the Ph. D progress meetings for the valuable instructions and encouragement.

I thank “China scholarship council” for providing the funding for this Ph. D.

I thank the other participants of my thesis committee for their support. Christian Leduc, Jean-Luc Seidel and Stéphane Binet. Every year, they listened to my annual research progress carefully, then provided helpful opinions on my future research plan. Their devotions are important for the completion of my research work.

I thank doctor Mohammed Aliouache, who is my office colleague and a good friend. Because I cannot well understand French, I always need him to help me with the preparation of the administrative documents. His support has made my work much easier. He was always patient and welcoming to me. And we spent many weekends together. We shared our opinions on many different topics, and we shared our featured food from our own countries. I thank him for offering such friendship to me.

I thank my parents. I have been away from home for about four years. Despite we could not meet face to face, they express their caring and support to me via video calls every week. They always feel proud of my tiny progress or achievements. And they would always understand my obstacles and then convince me that the future must be bright.

TABLE OF CONTENT

LIST OF FIGURES

CHAPTER 1

Résumé : Ce premier chapitre introduit les concepts de base liés à cette étude. Nous introduisons d'abord les aquifères fracturés et karstiques qui se caractérisent par une forte hétérogénéité. Ensuite, nous introduisons les essais par traçage et leur intérêt pour étudier ces aquifères. Les processus de transport anormaux dans les aquifères karstiques peuvent en effet être difficiles à interpréter en raison de la forte hétérogénéité de ces milieux. Enfin, nous introduisons les principaux objectifs et la structure principale de la thèse.

1. Introduction.

1.1 Fractured and karst aquifers

Fractured and karstified aquifers supply a large proportion of the water resources around the world. To be more specific, Karst springs supplies 25% of the world population with drinking water (Ford & Williams, 2007). This makes the study of karst aquifers an important research topic.

Fractured and karst aquifers have three main types of structure: the carbonate matrix, fractures and karst conduits. The matrix has very low permeability: from 10^{-22} to 10^{-14} m^2 (Brace, 1980; Nooruddin et al., 2014). The matrix permeability measured in situ can be higher, because of the existence of micro-fractures. For these aquifers, the matrix can be considered as impermeable.

The existence of fractures and conduits take up a small proportion of the total aquifer volume (Pyrak-Nolte et al., 1987), while are considered to be responsible for more or less 90% of the total flow (Borghi et al., 2016). Open fractures permeability that are orders of magnitude higher than that of the rock matrix (Geiger & Matthäi, 2014).

Karst is a special type of landscape that develops predominantly by the dissolution of rock (Ford & Williams, 2007). It is strongly developed in dense carbonate rock, for example limestone. The diameter of karst conduit ranges from a few centimeters to several meters (Upchurch et al., 2019). In turn, the permeability of a conduit can be larger than a fracture by several magnitudes.

These reservoirs are known to be highly heterogeneous (White, 2002). The dominant flow can be confined in a few preferential flow paths. Such high heterogeneity makes it very difficult to investigate the fractured and karst aquifers (Bakalowicz, 2005).

1.2 Solute transport processes

1.2.1 Tracing test

Tracing tests are deemed as the most powerful method to delineate the catchment areas of karst springs (Goldscheider, 2005). A Tracing test involves injecting a slug (pulse) of tracer at one upstream position, and monitoring the arrival of the tracer at a downstream position. Tracing test allows identifying a potential hydrogeological connection between the injection site and the monitoring point. Afterwards, the monitored time-concentration (breakthrough) curves are usually fitted with a numerical model to derive the transport model parameters. Goldscheider et al. (2008) presented a brief summary of the most important tracers in hydrogeology. Fuorescent dyes and salts are often used as tracers.

1.2.2 Advection-Dispersion model

The basic equation for the transport of a conservative tracer is based on three physical processes: advection, diffusion, and dispersion. Advection is the transport of a substance or quantity by bulk motion of a fluid. The advected substance can be fluid, energy, solutes or insoluble sediments.

Diffusion is the net movement of microscopic particles or energy from a region of higher concentration to a region of lower concentration. Diffusion is driven by the gradient of concentration.

Mechanical dispersion (hydrodynamic dispersion) results from groundwater moving at different linear velocity. Because the solute-containing water does not travel at the same velocity everywhere, mixing occurs along flow paths. This mixing is called mechanical dispersion.

Bear (1972) proposed the most classical Advection Dispersion Equation to model the solute transport process in a homogeneous and isotropic porous medium:

$$\frac{\partial C(x,t)}{\partial t} + u\frac{\partial C(x,t)}{\partial x} - D\frac{\partial^2 C(x,t)}{\partial x^2} = 0, \quad \text{(Eq. 1-1)}$$

where, C is the concentration in dimensions of [M/L^3]; D is dispersion coefficient [L^2/T]; t is time [T]; u is advection velocity [L/T]; x is the position [L]. The dispersion coefficient in the ADE equation accounts for the combined effects of mechanical dispersion and molecular diffusion, both of which cause spreading of the contaminant plume from highly concentrated areas toward less concentrated areas.

$$D = D_m + u\alpha, \quad \text{(Eq. 1-2)}$$

where, D_m is the molecular diffusion coefficient [L^2/T]; and α is dispersivity [L].

1.2.3 Anomalous transport

In the field of solute transport, we use the terms ‘‘anomalous’’ and ‘‘non-Fickian’’ interchangeably to denote any transport behavior which differs from that described by the classical ADE (Brian & Berkowitz, 2006). The anomalous transport is characterized the BTCs that exhibit asymmetry with long tails or multiple peaks (Goldscheider, 2008; Hauns et al., 2001; Massei et al., 2006; Moreno & Tsang, 1991; Perrin & Luetscher, 2008).

The anomalous transport process is especially complicated for the tracing tests in fractured and karst aquifers, because of the strong heterogeneity of these aquifers. A series of different factors have been found to influence the anomalous transport process. Researchers have applied different methods to investigate the transport process among these aquifers. However, a series of problems still remain to be studied.

1.3 The current state of art of the tracing test in karst aquifers

Tracing test is an important tool to investigate the hydrological characteristics of karst aquifers. The primary function of tracing test is to identify flow direction and a potential hydrogeological connection between the injection site and the monitoring points (spring or the pumping well on the well site). The information of connections allows hydrologists to better delineate the catchment area. Except for this primary application, tracing test has more sophisticated applications.

1.3.1 Derivation of hydrological and transport parameters

A common objective of realizing tracing tests is to characterize the hydrodynamic and transport

parameters of the hydraulic system. Concentration-time curve or breakthrough curve (BTC) is the primary result of a tracing test, it is also the basis for quantitative analysis of a tracing test. Assuming an instantaneous point injection, the typical shape of the BTC is presented in Figure 1.1. It commonly consists of three parts: rising limb, peak concentration range, and recession (falling) limb.

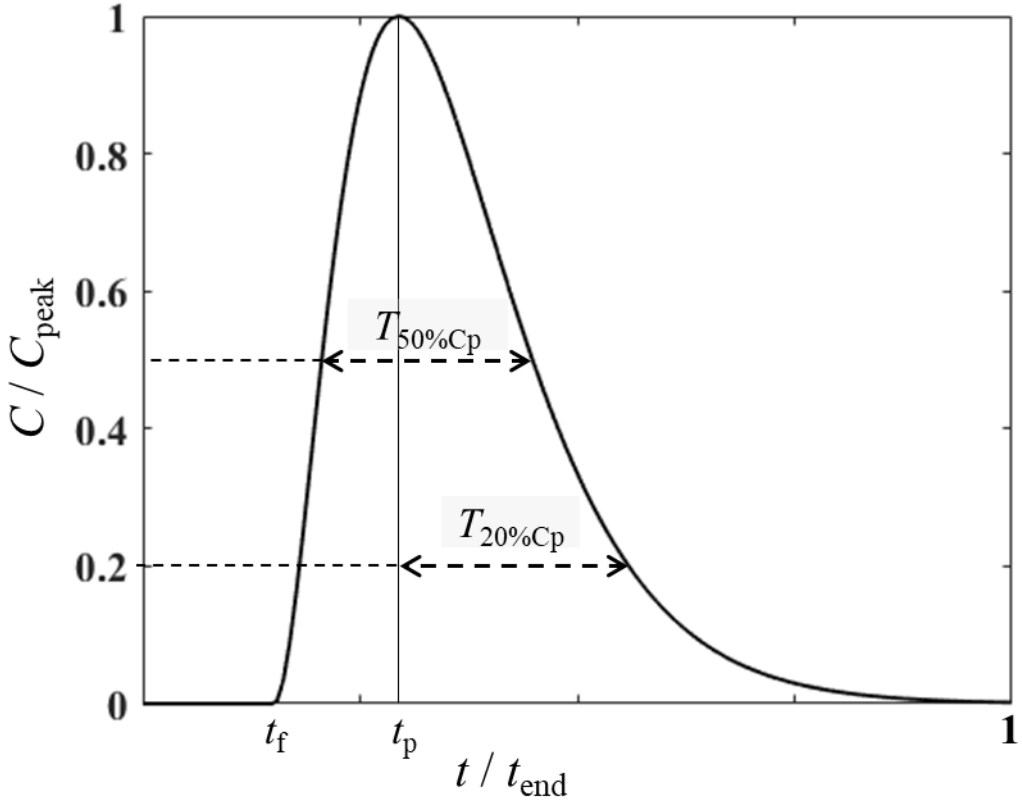

Figure 1.1. Typical normalized-breakthrough curve and its measurable solute-transport parameters (Modified after Mohammadi et al., 2019).

There are two common ways of deriving the hydrodynamic and transport parameters. The first way is to directly calculate some transport parameters from the BTCs. Figure 1.1 exhibits some of the transport parameters that can be obtained from this way, including peak concentration (C_p), peak time (T_p), tracer arrival time (t_f), slope of rising limb (SRL). $T_{50\%Cp}$ is an expression of elapsed time interval from 50% of C_p of the rising limb to 50% of C_p of the recession limb. Simply, the average groundwater velocity can be estimated by the following equation:

$$v_p = \frac{LS}{T_p}, \qquad \text{(Eq. 1-3)}$$

where: L [L] is the linear distance between the injection point and monitoring point, S is tortuosity factor.

The second way is to apply the numerical transport models to fit the sampled BTCs and calibrate the model parameters. The common transport models include Advection Dispersion Equation (ADE), Mobile Immobile Model (MIM), Transient Storage Model (TSM), Continous time Randow Walk theory??? (CTRW), etc (Gao et al., 2009). The common transport model parameters include flow velocities,

longitudinal dispersivities, retardation and degradation, as well as the conduit-matrix interactions (Geyer et al., 2007; Massei et al., 2006). These parameters can be used to effectively evaluate a transport process. In this Ph. D, most of the experimental BTCs are analyzed in the second way to derive effective transport parameters of different transport models.

1.3.2 Estimation of underground karst structures and properties

Tracing data and flow measurements may help hydrologists to gain insight into the realistic network configuration and structure for a given karst system. First, some particular shapes of the BTCs can indicate some specific structures qualitatively. For example, the late tailing effect on the BTC may indicate the existence of a large pool connected to the underground conduit, which has caused transient storage of the tracer; the multi-peaked BTCs may indicate that there are multiple conduit flow paths, that diverge at an upstream position and converge at a downstream position. The above estimations are qualitative.

Further, BTCs can be quantitatively evaluated to estimate some geometric properties about the karst configurations. For example, Zhao et al. (2021) found it feasible to estimate the volume of the stagnant karst pool from the transport BTCs. Whether qualitative or quantitative, such predictions would be of great interest for geologists as practitioners, and in their work as consultants or authorized experts (Benischke, 2021).

1.3.3 Hydraulic tomography with tracing data

Hydraulic tomography (HT) is a sequential cross-hole hydraulic test followed by inversion of all the data to map the spatial distribution of aquifer hydraulic properties, e.g. transmissivity (K) and storativity (S).

The HT can be realized with the hydraulic test data like head and/or flow rate data. In addition, tracing test data also have been applied for inversion studies. Borghi et al. (2016) have applied inversion methods to tracing data and managed to estimate a karst network geometry. Somogyvári et al. (2017) applied the method to estimate a fracture network geometry. The results of HT have been extensively improved through the integration with data from tracer tests (Illman et al., 2010; Zha et al., 2014; Zhu et al., 2009).

1.3.4 Evaluation of the groundwater vulnerability

The concept of groundwater vulnerability represents the tendency and possibility of pollutants to reach a specific location in the uppermost aquifer (Bosch 1995). Various groundwater vulnerability assessment models have been developed to quantitatively evaluate groundwater vulnerability to contamination and it is expressed in the form of vulnerability map. Tracing test has been found to be effective to validate the vulnerability map of a karst aquifer (Goldscheider et al., 2001). If the recovered BTC exhibits a low tracer residence time, high maximum concentration and a high recovery rate, it suggests a high vulnerability.

1.4 Objectives

This thesis aims to obtain an enhanced understanding of the solute transport process in karst aquifers and to explore the application of tracing tests to estimate some structural and hydraulic properties of a karst aquifer. The main objective will be realized by achieving the following specific objectives.

1.4.1 Objectives of the lab experiments (Chapters 2-3)

For tracing tests in karst aquifers, the dual-peaked BTCs are frequently obtained (Dewaide *et al.*, 2018; Field and Leij, 2012; Maloszewski *et al.*, 1992; Göppert and Goldscheider, 2008; Perrin and Luetscher, 2008). The lab experiments confirmed that the dual-conduit structure caused dual-peaked BTCs (Field and Leij, 2012). This experiment result is helpful for the hydrologists, if they carried out a tracing test in karst aquifers and obtained the dual-peaked BTCs, they can deduce that there should exist the dual-conduit structure in the underground.

This interpretation is qualitative and limited. We cannot obtain any further geometric information about the dual-conduit configuration. First, we cannot have information about the relative comparison of the lengths of the two conduits; second, we cannot have information about the relative comparison of the diameters of the two conduits.

Under the condition that we obtain a dual-peaked (or multiple-peaked) BTCs, it would be useful if we could obtain more geometric information about the conduit network configuration by analyzing the dual-peaked BTC, without realizing more tests. It is an interesting study to carry out. Such analysis and such information would be possible if we understand the relationship between the conduit network geometry and the exact shape of the BTCs. Up to our best knowledge, until the moment when we carried out the study, no research has been dedicated to studying this relationship.

In order to investigate this unknown relationship between the BTCs shape and the geometric property of the conduit network, we carry out solute transport experiments in dual-conduit structures with various geometries (1. Different length setup; 2. Different aperture setup). After this relationship is figured out, we can propose methods to analyze the dual-peaked BTCs. So that we can further estimate the properties of the dual-conduit structure.

1.4.2 Objectives of studying the TFA concept (Chapters 4)

Although it has been a long time for hydrologists to apply different transport models to characterize the tracing BTCs, and although many classical transport models exist, researchers are still studying the transport models. New studies on transport models are still being published until recently. This indicates that there still exist undiscovered properties to be studied and revealed for the transport models. Thus, it is possible for us to study on some transport models and discover some new properties, which may be interesting and useful to the hydrologists specialized in karst media.

In the first aspect, researchers are still developing new transport models. The major reason (or

motivation) to develop new models is that hydrologists have obtained the tracing BTCs that cannot be well reproduced by the existing models; then the researchers need a more sophisticated model to well reproduce these BTCs. For example, the BTCs with tailing effect cannot be well reproduced by the most classical ADE, so researchers developed the Mobile-Immobile (MIM) Model (van Genuchten and Wierenga, 1976) and the Continuous Time Random Walk (CTRW) theory (Berkowitz et al., 2006). For another example, (Yin et al., 2022) proposed a dual heterogeneous domain model (DHDM) to better quantify the BTCs that exhibit multiple peaks and transient tailing behaviors.

In the second aspect, researchers explore the characteristics and properties of the existing models. First, by applying different transport models to the same BTCs, researchers can evaluate the fitting performance of the models. Second, researchers identified some new characteristics or properties of the models. For example, Sivelle et al. (2019) proposed the Transfer Function Approach method to model the tracing BTCs from the karst aquifer, one parameter of this model can be used to represent the intrinsic heterogeneity of the target aquifer. Third, some researchers have studied the correlation between transport model parameters and karst properties; then the transport parameters can be correlated to some properties of the karst configuration. Zhao et al. (2021) found that the model parameters can be used to estimate geometry information about the underground conduit-pool configuration. In addition, researchers have proposed some different methods to evaluate the parameter identifiability of the models (Wagener et al., 2002; Kelleher et al., 2013). Those methods have been applied to evaluate the identifiability of different transport models. The researchers remind the community to look at the multi-solution effect in estimating the transport parameters, “Only identifiable and unique parameters should be used to formulate reliable conclusions with the parameter estimatations.” (Harvey et al., 1996; Harvey and Wagner, 2000).

In this Ph. D study, we have the chance and convenience to study the transport models. We reviewed the existing transport models and choose the suitable ones for our lab-scale tracing experiments. The experimental BTCs should be fitted by different transport models to derive effective transport parameters. The modeling process is a good chance for us to study these transport models. We can compare their fitting performance to different BTCs; we can also study the characteristics of the transport models.

In our search for transport models, a transfer function approach (TFA) is found to be interesting. According to the procedures suggested by Sivelle et al. (2019), we can apply the TFA to the tracing tests that have been carried out under different flow conditions and among the same trajectory in the same karst aquifer. The calibrated parameter can represent the intrinsic heterogeneity of the karst aquifer, which can bring hydrologists unique insight into the unknown underground aquifer. This intrinsic property makes the TFA advantageous. However, this TFA has one limitation. We applied mathematical methods to overcome this limitation. So, the TFA has been made a good candidate model for the community.

1.4.3 Objectives of the HT characterization of Terreieu (Chapters 5)

After Chapters 2-4, we are determined to carry out the HT characterization of the Terrieu site (chapter

5). Because we have not looked enough at the real tracing test data in the large scale of real karst aquifers. Although the experiments should help us to better understand the solute transport process in nature, the lab-scale experiments have much smaller than in nature. Except that the scale is larger, field tracing tests can be different from laboratory experiments in the following aspects: field experiments are carried out under mainly unknown conditions (karst configurations, initial conditions and boundary conditions) and lab experiments have been carried out under known conditions; field tracing tests exhibit tracer recovery rates lower than 100% and the lab-scale experiments exhibit recovery rate of 100%. Considering the significant contrast between lab and natural karst aquifers, we decided not limit our studies to the lab-scale. We should look at the real field-scale data and explore new methods to better explain the field data. And we should consider the effect of different hydraulic conditions, and consider the unknown complexity of real karst aquifers.

So we explored the technique of hydraulic tomography. As introduced before, HT is one important application for tracing test data. Previously, the HT technique was used to characterize the Terrieu site with data from hydraulic pumping tests, rather than tracing data. Despite that a series of tracing tests have been carried out on this well site to study the inter-borehole connectivity. It should be an innovative advance if we can apply that tracing data in the inversion for characterizing the site.

We further developed the HT technique to better asses the drainage network properties of karst aquifers at field site scale. This new HT technique proposes a joint inversion of pumping test data and tracing test data. Then, the underground karst features are explicitly expressed by the discrete conduit network model. With those two innovations, the new HT method is possible to realize better characterization of a karst aquifer.

1.4.4 Why we studied three different topics?

In this thesis , we studied three different topics: laboratory experiments, transport models and hydraulic tomography. The used methods are also different for these studies. The methods used may vary, but the principle is the same: to help the hydrologists better look at the tracing test data and to derive more insight into the karst aquifer. The specific reasons are as follow:

First, we improved the comprehensiveness of the thesis work. There are four aspects of the applications of the tracing tests, which have been summarized in the current state of art. This Ph. D covered three of the four (except the validation of the vulnerability map). The main results of Chapters 2-3 can be used to estimate underground karst structures; the modeling work of Chapters 2-4 can be used to help hydrologists to select an optimal transport model to quantify their tracing BTCs; the new HT technique can be used to characterize the property of the karst network. This thesis contributes to the various methods for helping hydrologists to better interpret their tracing data.

Second, we improved the practicality of the thesis work by taking into consideration both lab-scale and field-scale data. Chapters 2-3 focused on lab-scale tracing tests. In Chapters 4-5, field tracing data are

taken for analysis. The main advantage of lab experiments is that the experimental conditions (including underground geometrical configurations) can be known and controlled; while in the field site, the karst configurations are usually unknown and some hydraulic conditions are not controllable. The HT technique studied in Chapter 5 is used to explore the unknown conditions of a true karst aquifer. By taking into the difference between the experiments of different scales, this thesis can be more practical and useful to the karst community. We aimed at contributing a full-scale and comprehensive exploration of the applications of tracing tests. By applying three different methods, we can improve the practical and scientific value of the thesis.

Third, studying different but relevant aspects can be good for the future development of the Ph. D student. The Ph. D period is very valuable for the young researcher to learn more skills. In this Ph. D study, I have become familiar with the procedures of lab experiments, numerical simulations with commercial software, some mathematical techniques (Laplace transform, Fourier transform, consistency analysis) and hydraulic tomography technique. These techniques will be valuable tools for my future research career. They will qualify me to keep on researching and discovering interesting results.

1.5 Main contributions

The thesis will contribute to the value of the tracing test as an investigation tool for karst aquifers. The main results of the thesis will help the hydrologists to further interpret their tracing BTCs and gain more insight into the unknown underground aquifer. To be more specific, this thesis contributes to three of the four aspects of the current state of art (Section 1.3).

1.5.1 Deriving hydrological and transport parameters

This Ph. D work should provide insight and guide on choosing an optimal transport model under different conditions. The classical ADE model often fails to characterize the BTCs with anomalous features. For single-peaked BTCs without strong tailing, TFA model is a suitable transport model; and for single-peaked BTCs with strong tailing, MIM of the similar TSM model is suitable. For dual-peaked BTCs, the parallel flowing transport models are selected. Dual region adevection dispersion equation (DRADE), weighted sum adevection dispersion equation (WSADE) models may be able to well reproduce the dual-peaked BTCs. If these two models fail, a weighted sum mobile-immobile (WSMIM) model, with more parameters and thus more flexibility, should be able to well reproduce the dual-peaked BTCs.

This Ph. D work reminds the community to be cautious with the multi-solution phenomenon of the models. Sometimes hydrologists may adopt transport models that have more parameters to improve the fitting performance. However, the model output can be insensitive to some parameters of the model; and some parameters may interact with each other to influence the modeling output. These effects would cause the relevant transport parameters to be less identifiable, and may further cause the multi-solution effect. For example, in Chapter 3, the WSMIM model has more parameters than the WSADE and exhibited better

fitting performance, however, WSMIM exhibited strong multi-solution effects and some poorly identifiable parameters. Thus, it is optimal for hydrologists to check the parameter identifiability, and to be cautious when they need to draw any conclusion with the less identifiable parameters.

1.5.2 Estimating underground karst structures and properties

This Ph. D work will help the hydrologists to analyze the tracing data and deduce more information about the realistic network configuration and structure, either qualitative or quantitative.

a) From fully-separated dual-peaked BTCs, a method is proposed to quantitatively calculate underground conduit lengths of the dual-conduit structures.

b) From dual-peaked BTCs that are not fully separated, a flow chart is proposed to qualitatively evaluate the aperture comparison of the dual-conduit structures.

c) According to the numerical simulations in Chapter 4, if the transport BTCs have generated very large dispersion values, this may indicate the existence of a complex network of karst conduit or fracture.

d) According to the modeling results in Chapter 4, if the calibrated parameter N of the TFA model is very small, it suggests stronger intrinsic heterogeneity of the karst network.

1.5.3 Hydraulic tomography with tracing data

In Chapter 5, we applied the HT technique with both hydraulic and tracing data, to characterize the geometric structure and the properties of the karst network. This study contributes to the current state of art in the following aspects:

a) This study reveals how the tracing and hydraulic data provide different restraints on the tomography results.

b) This study provides one innovative and feasible procedure to characterize the underground karst network. The karst conduits have been explicitly expressed and the spatial variation of the conduit properties has been characterized.

c) With the new procedure and real field data, we carried out new characterization of the karstic field site of Terrieu.

1.6 Thesis structure

Chapter 2 presents laboratory solute transport experiments on different dual-conduit structures. Three groups of structures were constructed by varying: (1) length ratio between the two conduits while fixing the length of the main conduit; (2) the total length of the conduits, while fixing the length ratio. (3) the connection angle between the conduits. The BTCs generated by the tracing experiments were fitted by a Dual-Region Advection Dispersion (DRAD) model to derive effective transport parameters.

Chapter 3 presents laboratory solute transport experiments on 11 lab-scale dual-conduit structures. These 11 structures have been manufactured by varying the apertures of the two conduits and we conduct solute transport experiments consisting of step tracing. We investigate how the transport process can be

influenced by the following two factors: flow rate and aperture width of both conduits. We apply two numerical models to fit the experimental BTCs: Weighted Sum Advection–Dispersion Equation (WSADE) and Dual Region Mobile Immobile Model (DRMIM). The DRMIM exhibits better performance than the WSADE.

Chapter 4 investigates a transfer function approach (TFA) for interpreting tracer BTCs in karst systems. The TFA is have been noted to be an effective method for interpreting the solute transport processes in karst aquifers. However, the parameters of TFA cannot directly reflect the properties of the transport process. To overcome this limitation, we investigated how the TFA parameters can be related to the classical transport parameters (velocity and dispersion). Afterwards, we compare the ability of three numerical models: ADE, TFA, MIM by applying them to fit different transport BTCs.

Chapter 5 proposes a methodology for characterizing a karst conduit network at the scale of an experimental field site. It is based on a hydraulic tomography method which considers a discrete conduit network model to explicitly represent the underground conduit network, integrating hydraulic data and dye tracing data to constrain the diameter distribution of the karst conduit network. The characterization of the karst conduit network is realized by a joint inversion of interference pumping test data and dye tracing test data.

References

Bakalowicz, M. (2005). Karst groundwater: a challenge for new resources. *Hydrogeology Journal*, *13*(1), 148–160.

Bear, J. (1972). *Dynamics of fluids in porous media*. Courier Corporation.

Benischke, Ralf. "Advances in the methodology and application of tracing in karst aquifers." Hydrogeology journal 29.1 (2021): 67-88.

Borghi, A., Renard, P., & Cornaton, F. (2016). Can one identify karst conduit networks geometry and properties from hydraulic and tracer test data? *Advances in Water Resources*, *90*, 99–115.

Brace, W. F. (1980). Permeability of crystalline and argillaceous rocks. *International Journal of Rock Mechanics and Mining Sciences & Geomechanics Abstracts*, *17*(5), 241–251.

Brian, & Berkowitz. (2006). Modeling non-Fickian transport in geological formations as a continuous time random walk. *Reviews of Geophysics*.

Ford, D., & Williams, P. D. (2007). *Karst hydrogeology and geomorphology*. John Wiley & Sons.

Gao, G., Zhan, H., Feng, S., Huang, G., & Mao, X. (2009). Comparison of alternative models for simulating anomalous solute transport in a large heterogeneous soil column. Journal of hydrology, 377(3-4), 391-404.

Geyer, T., Birk, S., Licha, T., Liedl, R., Sauter, M., 2007. Multitracer test approach to characterize reactive transport in karst aquifers. Groundwater 45 (1), 36–45.

Geiger, S., & Matthäi, S. (2014). What can we learn from high-resolution numerical simulations of single-and multi-phase fluid flow in fractured outcrop analogues? *Geological Society, London, Special Publications*, *374*(1), 125–144.

Goldscheider, N. (2005). Karst groundwater vulnerability mapping: application of a new method in the Swabian Alb, Germany. *Hydrogeology Journal*, *13*(4), 555–564.

Goldscheider, N. (2008). A new quantitative interpretation of the long-tail and plateau-like breakthrough curves from tracer tests in the artesian karst aquifer of Stuttgart, Germany. *Hydrogeology Journal*, *16*, 1311–1317. https://doi.org/10.1007/s10040-008-0307-0

Hauns, M., Jeannin, P.-Y., & Atteia, O. (2001). Dispersion, retardation and scale effect in tracer breakthrough curves in karst conduits. *Journal of Hydrology*, *241*(3–4), 177–193.

Massei, N., Wang, H. Q., Field, M. S., Dupont, J. P., Bakalowicz, M., & Rodet, J. (2006). Interpreting tracer breakthrough tailing in a conduit-dominated karstic aquifer. *Hydrogeology Journal*, *14*(6), 849–858.

Moreno, L., & Tsang, C. F. (1991). Multiple-Peak Response to Tracer Injection Tests in Single Fractures: A Numerical Study. *Water Resources Research*, *27*(8), 2143–2150.

Nooruddin, H. A., Hossain, M. E., Al-Yousef, H., & Okasha, T. (2014). Comparison of permeability models using mercury injection capillary pressure data on carbonate rock samples. *Journal of Petroleum Science and Engineering*, *121*, 9–22.

Perrin, J., & Luetscher, M. (2008). Inference of the structure of karst conduits using quantitative tracer tests and geological information: example of the Swiss Jura. *Hydrogeology Journal*, *16*(5), 951–967.

Pyrak-Nolte, L. J., Myer, L. R., Cook, N. G. W., & Witherspoon, P. A. (1987). Hydraulic and mechanical properties of natural fractures in low permeability rock. *6th ISRM Congress*.

Upchurch, S., Scott, T. M., Alfieri, M. C., Fratesi, B., & Dobecki, T. L. (2019). Controls on Karst Landforms in Florida. In *The Karst Systems of Florida* (pp. 207–265). Springer.

White, W. B. (2002). White WB.. Karst hydrology: recent developments and open questions. Eng Geol 65: 85-105. *Engineering Geology*, *65*(2–3), 85–105.

CHAPTER 2

Résumé :

Ce chapitre présente une étude expérimentale du processus de transport de soluté dans une structure karstique particulière : les structures à double conduit. Nous avons fabriqué trois groupes de structures à double conduit en faisant varier : (1) le rapport de longueur entre les deux conduits pour une longueur fixe du conduit le plus court, (2) la longueur totale des conduits pour un rapport de longueur fixe, et (3) l'angle de connexion entre les conduits.

Les résultats ont confirmé que la structure à double conduit déclenche les BTC à double pic et que la séparation des pics augmente lorsque le rapport de longueur augmente ou lorsque la longueur du conduit (pour un rapport de longueur fixe) augmente. Les angles de connexion entre les deux conduits θ_1 et θ_2 influencent également les BTC : en augmentant θ_1 et en diminuant θ_2, le premier pic devient plus petit et le second plus grand. Le modèle DRAD a permis de reproduire les BTC à deux pics alors que son application au cas des BTC à un seul pic peut être problématique en raison de la forte interaction entre les paramètres du modèle. Sur la base de ces résultats, une méthode a été proposée pour estimer la longueur des conduits karstiques souterrains à partir de CTB expérimentales à double pic.

Chapter 2 Influence of dual conduit structure on solute transport in karst tracer tests: an experimental laboratory study

Journal of Hydrology 590 (2020) 125255

Contents lists available at ScienceDirect

Journal of Hydrology

journal homepage: www.elsevier.com/locate/jhydrol

Research papers

Influence of dual conduit structure on solute transport in karst tracer tests: An experimental laboratory study

Chaoqi Wang, Xiaoguang Wang*, Samer Majdalani, Vincent Guinot, Hervé Jourde

Hydrosciences Montpellier, UMR 5569, France

https://doi.org/10.1016/j.jhydrol.2020.125255

Influence of dual conduit structure on solute transport in karst tracer tests: an experimental laboratory study

Chaoqi Wang[1], Xiaoguang Wang[2], Samer Majdalani[1], Vincent Guinot[13], Herve Jourde[1]

1. Laboratories Hydrosciences Montpellier, UMR 5151 CNRS-UM-IRD, Montpellier, France, 34000
2. Chengdu University of Technology, Sichuan, China, 610059
3. Inria Lemon, Univ. Montpellier, Montpellier, France, 34000

Highlights:

The effect of dual conduit structure on solute transport is investigated using lab experiments

Increasing length ratio or total conduit length cause larger separation of dual peaks of BTCs

The connection angle affects tracer partition to the two conduits

A method for estimating the length of subsurface karst conduits based on BTCs is proposed

Abstract

We conducted lab-scale experiments to investigate the mechanism of dual-peaked breakthrough curves (BTCs) in karst tracer tests. Three groups of dual conduit structures were constructed by varying: (1) the length ratio between the two conduits for a fixed length of the shorter conduit, (2) the total length of the conduits for a fixed length ratio, (3) the connection angle between the conduits. The BTCs generated by the tracing experiments were fitted by a Dual-Region Advection Dispersion (DRAD) model to derive effective transport parameters.

Our results confirm that the dual conduit structure triggers the double-peaked BTCs. Increasing the conduit length for a fixed length ratio or increasing the length ratio increases peak separation. The connection angles between the two conduits θ_1 and θ_2 also influence the BTCs: increasing θ_1 and decreasing θ_2 causes the first peak to get smaller and the second peak to get larger. The DRAD model can reproduce the dual-peaked BTCs while its application to the case of single-peaked BTCs may be problematic due to strong interaction between model parameters. A method is proposed for estimating underground karstic conduit lengths from experimental dual-peaked BTCs in field tracer tests.

2.1 Introduction

The methodology of tracer test initially developed for the investigation of karst aquifers is still widely used in karst hydrogeology. Tracer tests can provide information about groundwater trajectories and yield breakthrough curves (BTCs) that can be used for obtaining transport model parameters (Goldsheider and Drew, 2007).

Due to the strong heterogeneity of karst aquifers, the BTCs may exhibit asymmetry with long tails or multiple peaks (Moreno and Tsang, 1991; Hauns, Jeannin and Atteia, 2001; Massei *et al.*, 2006; Goldscheider *et al.*, 2008; Perrin and Luetscher, 2008). The Advection–Dispersion-Equation (ADE) performs poorly in characterizing these BTCs. To handle the tailing effect, some researchers considered including further processes in the transport model and generate more adjustable tails (Morales *et al.*, 2010): the Mobile-Immobile Model (MIM) developed by (van Genuchten and Wierenga, 1976) partitions the aquifer into mobile and immobile regions; Skopp et al. (1981) proposed a dual-permeability model with two mobile regions using the ADE model. This model is referred to as Multiple Region Advection-Dispersion (MRAD) by Majdalani et al. (2018). Berkowitz et al. (2006) proposed the Continuous Time Random Walk (CTRW) theory by conceptualizing solute transport as a series of particle jumps or transitions with spatially changing velocities, CTRW was recently also applied to karst aquifers (Göppert and Goldscheider, 2008). Dual-peaked BTCs were successfully modeled by the application of the Dual Advection Dispersion Equation (DADE) and the Weighted Sum Advection-Dispersion Equation (WSADE) model (Field and Leij, 2012).

Dual-peaked BTCs in karst tracer tests may be caused by the presence of underground lakes (Dewaide

et al., 2018), underground pool (Field and Leij, 2012). Another possible explanation is the presence of multiple flow paths (Maloszewski *et al.*, 1992; Göppert and Goldscheider, 2008; Perrin and Luetscher, 2008). This hypothesis has been investigated using laboratory scale experiments in the past (Moreno and Tsang, 1991; Field and Leij, 2012). Among the different experiments used for a better understanding of karst aquifer solute transport, some scale models account for both the conduit and the matrix (Florea and Wicks, 2001; Li, Loper and Kung, 2008; Mohammadi, Gharaat and Field, 2019), while others focus on transport in conduits only (Field and Leij, 2012; Zhao *et al.*, 2017, 2019). Field and Leij (2012) noted that the presence of pools or auxiliary conduits causes dual-peaked BTCs. Mohammadi et al. (2019) studied how the hydraulic head gradient influences BTCs by a bench-scale karst model. Zhao et al. (2017, 2019) found that the existence of pools on the conduit would increase the tailing of BTCs. However, these studies did not show whether karst conduit properties can be inferred from BTC shapes.

To better assess the relationship between conduit structure and BTCs, we studied how the dual conduit geometry influences the BTCs shape by laboratory tracer experiments. Three groups of solute transport experiments were carried out. The obtained BTCs were fitted using a one-dimensional transport model to achieve a quantitative comparison.

2.2 Materials and methods

2.2.1 Experimental setup

A series of lab-scale, idealized dual conduit structure models were built using silicone pipes with an internal diameter of 0.4 cm. The dual conduit structure consists of three parts: the inlet, dual conduit and outlet. At the inlet and outlet parts, the flow is restricted in the single conduit; at the dual conduit part, the flow is divided into two conduits of different lengths (Figure 2.1). The shorter and the longer conduit lengths are denoted as l_1 and l_2, respectively. The deviation angles between the shorter and longer conduits at both the inlet and outlet connecting part are denoted respectively as θ_1 and θ_2. During the experiments, the dual conduit structure is placed on a horizontal platform to eliminate gravity effects.

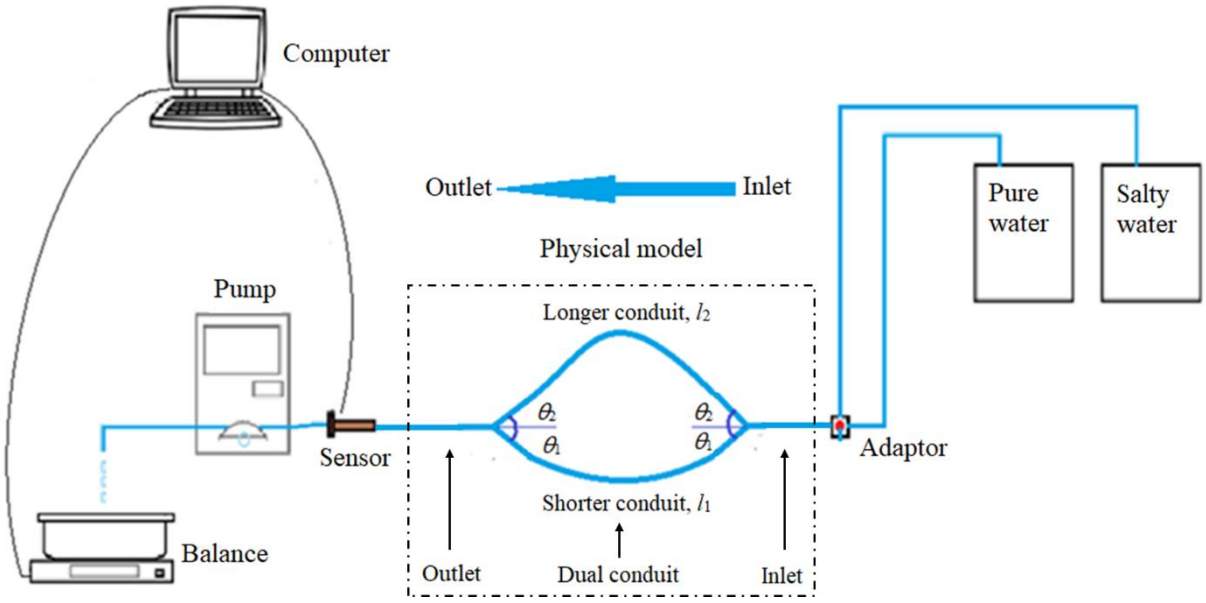

Figure 2.1. Schematic diagram showing the experimental setup used in the study.

The inflowing flow is supplied using a peristaltic pump (Lead Fluid brand) at a constant rate. The discharge Q is set at 0.6846 cm^3/s, and hence the calculated velocity through the outlet conduit is 5.4480 cm/s. The inlet is connected in parallel to a pure water supply and a salty water supply. A three-way adapter is used to switch between salty water and pure water. The salty water (deionized water + NaCl at $C_0 = 0.06$ mol/L) is used as the tracer. A pulse tracer release is realized by switching the adaptor to the salty water supply for 5 seconds (3.42 mL). As the experimental physical models don't exchange mass with outside, the recovery rate should be 100% for all of the experiments.

We use a scale (Mettler Toledo^{TM}) to estimate the discharge. A conductimeter (WTW TetraCon 325^{TM}, accuracy is 1×10^{-6} mol/L), is used to measure the outlet tracer concentration. The scale and conductimeter are connected to a data logger (Campbell CR1000^{TM}) for automatic data recording at a time step of 1 second. In each experiment, the tracer injection is initiated after the flow within the system is stabilized. Each experiment is repeated for three times. A mean BTC is derived from the replicates to reduce the measurement error.

Three groups of experiments are performed (Table 2.1). The notation for the experiment name takes the format of l_1 - l_2 - θ_1 - θ_2 (Figure 2.1). Experiment Group 1 is designed to study the effect of length ratio of the two conduits on the transport process. l_1 is set at 10 cm, while l_2 is set to 20 cm, 40 cm, 60 cm, and 120 cm, respectively. The angles θ_1 and θ_2 are both fixed at 30 degrees. Experiment Group 2 is designed to study the effect of total conduit length variation on the transport process, keeping the length ratio of two conduits as 1:6. l_1 is set to be 10 cm, 20 cm and 60 cm and l_2 is set to be 60 cm, 120 cm, and 360 cm, respectively. The angles θ_1 and θ_2 of the connectors are also fixed at 30 degrees. Experiment Group 3 is designed to study the effect of conduit connection angle on the transport process. l_1 is set at 10 cm and l_2 is

60 cm, and three different connection types are made by arranging the θ_1 and θ_2 combinations. In total, eight tracer tests have been performed (the 10-60-30-30 experiment is used in all of the three groups).

Table 2.1 Geometrical parameters of dual conduit structures for the three groups of experiments.

Group	Experiment label	Conduit length (cm)		Connection angles (deg)	
		l_1	l_2	θ_1	θ_2
1	10-20-30-30	10	20	30	30
	10-40-30-30	10	40	30	30
	10-60-30-30	10	60	30	30
	10-120-30-30	10	120	30	30
2	10-60-30-30	10	60	30	30
	20-120-30-30	20	120	30	30
	60-360-30-30	60	360	30	30
3	10-60-30-120	10	60	30	120
	10-60-30-30	10	60	30	30
	10-60-120-30	10	60	120	30

2.2.2 One-dimensional modeling

2.2.2.1 Dual Region Advection Dispersion (DRAD) model

To quantitatively investigate the dual-peaked BTCs obtained in section 2.1, we apply a Dual Region Advection Dispersion (DRAD) model. This model has been called Two-Region MRAD model by Majdalani et al. (2018) and DADE model by Field and Leij (2012). DRAD model assumes two regions flowing in parallel and exchanging mass due to concentration difference; in both regions, the ADE mode is assumed valid (Figure 2.2). We do not consider solute degradation or adsorption/desorption in our model. The DRAD model is chosen because it is the possible simplest model to reproduce the dual-peaked BTCs.

The governing equations are given as follows:

$$\frac{\partial C_i}{\partial t} + u_i \frac{\partial C_i}{\partial x} - D_i \frac{\partial^2 C_i}{\partial x^2} = \frac{k_{ij}}{w_i}(C_j - C_i), \ (i = 1, 2; j = 2, 1), \quad \text{(Eq. 2-1)}$$

$$k_{12} = k_{21}, \quad \text{(Eq. 2-2)}$$

$$w_1 + w_2 = 1. \quad \text{(Eq. 2-3)}$$

The total concentration at the outlet is computed as:

$$C(x,t) = w_1 C_1(x,t) + w_2 C_2(x,t), \quad \text{(Eq. 2-4)}$$

where t is time (T), x is distance (L), C_i is the concentration (ML^{-3}) of region i, u_i, D_i and w_i are respectively the flow velocity (LT^{-1}), dispersion coefficient (L^2T^{-1}) and volumetric fraction in region i, k_{ij} is the

coefficient for solute exchange between the region *i* and *j* (T^{-1}). Since we consider only two-region systems, $k_{12} = k_{21}$, and $w_1 + w_2 = 1$. As a result, six parameters are used in the calibration: w_1, k_{12}, u_1, u_2, D_1 and D_2. In our discussions, the quicker region is referred to as region 1 while the slower region is region 2 (i.e., $u_1 > u_2$).

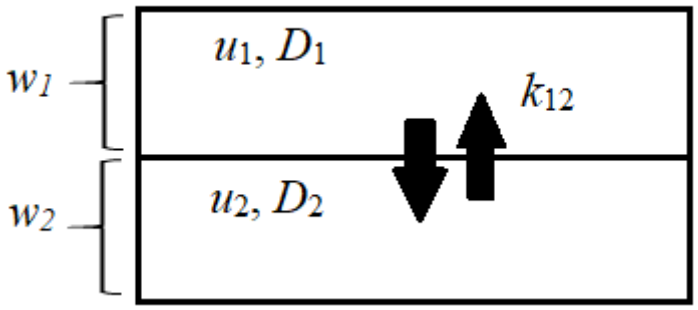

Figure 2.2. Schematic diagram of the DRAD model.

2.2.2.2 DRAD model parameter estimation

The six principle DRAD model parameters were estimated using the MCMC method (Haario *et al.*, 2006). The MCMC method is a Bayesian approach that evaluates the posterior distributions of parameters for an assumed error structure (Vrugt *et al.*, 2006). Using the Bayes rule, the probability density function of the model parameter set $\boldsymbol{\theta}$=$\{w_1, k_{12}, u_1, u_2, D_1, D_2\}$ is given as:

$$p(\boldsymbol{\theta}|\mathbf{Y}) \propto L(\boldsymbol{\theta}|\mathbf{Y}) \cdot p(\boldsymbol{\theta}), \quad \text{(Eq. 2-5)}$$

where $p(\boldsymbol{\theta})$ and $p(\boldsymbol{\theta}|\mathbf{Y})$ are the prior and posterior parameter distribution, respectively, $Y = \{y(t_1), \dots, y(t_n)\}$ is the observations, $L(\boldsymbol{\theta}|\mathbf{Y})$ is the likelihood function. The prior distribution $p(\boldsymbol{\theta})$ was assumed to be uniformly distributed. The model residual for outlet concentrations are assumed to be independent and follow a Gaussian distribution with zero mean and a constant variance σ^2. Thus, the posterior distribution is given by:

$$p(\boldsymbol{\theta}|\mathbf{Y}, \sigma^2) \propto \frac{1}{(2\pi\sigma^2)^{N/2}} \exp\left(-\frac{\sum_i^n (C_i - Y_i)^2}{2\sigma^2}\right), \quad \text{(Eq. 2-6)}$$

where *N* is the number of observations, C_i and Y_i are the simulated and observed concentrations time *i*. The convergence performance of MCMC chains is evaluated with a Root-Mean-Square-Error (RMSE) objective function, which is defined as:

$$RMSE = \sqrt{\frac{\sum_{i=1}^n (C_i - Y_i)^2}{N}}. \quad \text{(Eq. 2-7)}$$

We used the Metropolis-Hastings (MH) algorithm to successively draw samples from the posterior distribution by forming a Markov chain of model parameter set $\boldsymbol{\theta}$. The MH construct a Markov chain by four main steps: (1) choose an initial parameter set $\boldsymbol{\theta}^0$ and a proposal density distribution $q(\boldsymbol{\theta}_k|\boldsymbol{\theta}_{k-1})$; (2) at each iteration k + 1, generate a new sample $\boldsymbol{\theta}^*$ from $q(\boldsymbol{\theta}^*|\boldsymbol{\theta}^k)$ and calculate the probability of

acceptance, $\pi = \min\left(\frac{p(\boldsymbol{\theta}^*)L(\boldsymbol{\theta}^*|\mathbf{Y})q(\boldsymbol{\theta}^k|\boldsymbol{\theta}^*)}{p(\boldsymbol{\theta}_k)L(\boldsymbol{\theta}_k|\mathbf{Y})q(\boldsymbol{\theta}^*|\boldsymbol{\theta}^k)}, 1\right)$, draw a random number u from a uniform distribution between 0 and 1; (3) if $\pi > u$, set $\boldsymbol{\theta}^{k+1} = \boldsymbol{\theta}^*$; otherwise $\boldsymbol{\theta}^{k+1} = \boldsymbol{\theta}^k$; (4) repeat step 2 and 3 until a given maximum number of iteration is reached.

To achieve a fast convergence of the chain, we first perform a manual fitting of the DRAD response to the experimental BTCs to find the initial parameter set. In this work, we assume the posterior probability density is of a Gaussian type. For each chain, 16000 iterations were executed, and the last 1000 sampled parameter sets that allow the model to adequately fit the observed data were chosen to evaluate the posterior parameter distribution and the pairwise parameter correlations. Except for 10-20-30-30, all of the fitted parameters are set to be the mean value of these 1000 sets. For 10-20-30-30, the fitted parameters were chosen with the criterion: $w_1 > 0.5$.

The parameter correlations are characterized by scatterplots of parameter pairs and the correlation coefficient r, which is a statistical measure of the linear relationship between two variables. Given paired data $\{(x_1, y_1), (x_2, y_2), \ldots, (x_n, y_n)\}$, r is defined as:

$$r = \frac{\sum_{i=1}^{n}\left(x_i - \bar{x}\right)\left(y_i - \bar{y}\right)}{\sqrt{\sum_{i=1}^{n}\left(x_i - \bar{x}\right)^2}\sqrt{\sum_{i=1}^{n}\left(y_i - \bar{y}\right)^2}}, \qquad \text{(Eq. 2-8)}$$

where n is the sample size; $\bar{x}$ and $\bar{y}$ are the mean value for x and y, respectively. The parameter variability (or uncertainty) is represented by the parameter histogram and relative standard deviation (RSD) value. RSD is calculated by:

$$\mathrm{RSD} = \frac{\sqrt{\frac{\sum_{i=1}^{n}\left(x_i - \bar{x}\right)^2}{n-1}}}{\left|\bar{x}\right|}. \qquad \text{(Eq. 2-9)}$$

2.3 Results

2.3.1 Length ratio study (experiment Group 1)

The BTCs from Experiment Group 1 (Figure 2.3) trigger the following observations. When the length ratio is small (e.g., 2), the BTC only exhibits a single peak; for length ratio of 4, 6 and 12, the BTCs exhibit two peaks. As the length ratio increases, the first peak arrives slightly earlier while the arrival of the second peak is delayed. The value of the first peak (C_{peak1}) decreases first from the 10-20-30-30 to the 10-40-30-30 case, and then increases as the length ratio is further increased. The concentration value of the second peak (C_{peak2}) decreases as the length ratio increases.

Using the DRAD model and the MCMC calibration algorithm, we try to correctly fit the experimental BTCs. Visually the simulated BTCs can capture the main shape of the experimental BTCs. The overall fitting performance is quite good for the 10-40-30-30 system with a maximum error value of 0.0233 (Table 2.2). However, the recession limb of the second peak of some experimental BTCs (Figure 2.3b, c) exhibit a slight skewness, which the DRAD model is unable to capture exactly (Figure 2.3b, c, d). For the first experiment (Figure 2.3. 3a), the DRAD model allows a good fit of the BTC curve. For the dual-peaked BTCs (Figure 2.3b, c), the fit of the second peak is not as good as the fit of the first peak but the overall BTC behavior is correctly reproduced by the DRAD model. The parameters of the fitting result for Group 1 are listed in Table 2.2 and plotted in Figure 2.4. We do not plot the variation of the exchange rate k_{12} because of the very small values that indicate a negligible exchange rate and therefore a negligible effect on the BTC.

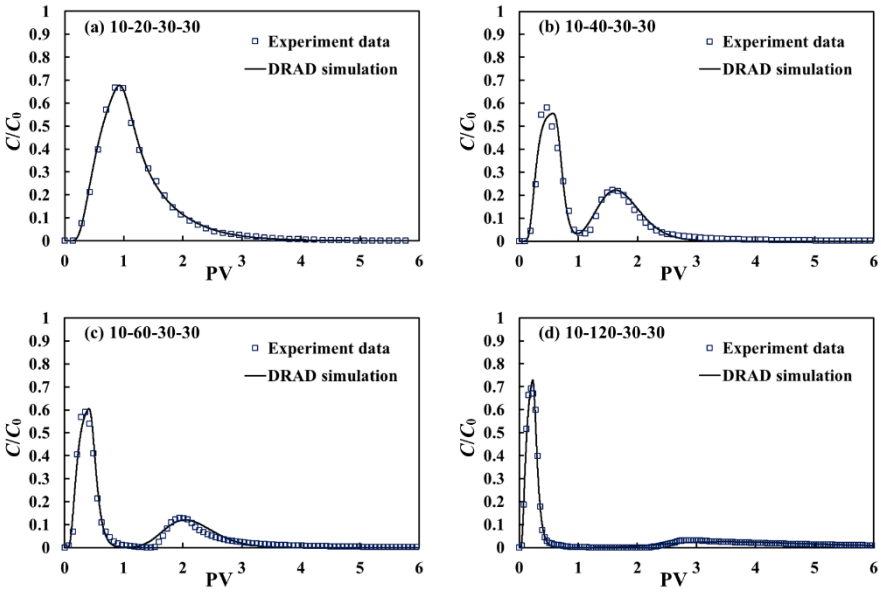

Figure 2.3. DRAD calibration results of Group 1 experiments.

Table 2.2 DRAD model calibration results for Group 1 experiments.

	10-20-30-30	**10-40-30-30**	**10-60-30-30**	**10-120-30-30**
t_{peak1} (s)	6.45	4.85	4.55	4.40
t_{peak2} (s)	6.45	17.20	27.85	73.00
u_1 (m/s)	4.46×10^{-2}	5.04×10^{-2}	5.13×10^{-2}	5.09×10^{-2}
u_2 (m/s)	1.89×10^{-2}	9.40×10^{-3}	5.27×10^{-3}	1.46×10^{-3}
u_1 (m/PV)	3.17×10^{-1}	5.43×10^{-1}	7.41×10^{-1}	1.29×10^{0}
u_2 (m/PV)	1.34×10^{-1}	1.01×10^{-1}	7.61×10^{-2}	3.71×10^{-2}
D_1 (m^2/s)	5.71×10^{-4}	3.99×10^{-4}	7.42×10^{-4}	1.05×10^{-3}
D_2 (m^2/s)	3.86×10^{-4}	4.03×10^{-5}	1.82×10^{-5}	1.47×10^{-5}
k_{12} (1/s)	7.14×10^{-37}	3.25×10^{-25}	3.08×10^{-28}	1.99×10^{-26}
w_1 (–)	0.526	0.562	0.632	0.653
RMSE (–)	0.00967	0.0233	0.0165	0.0120

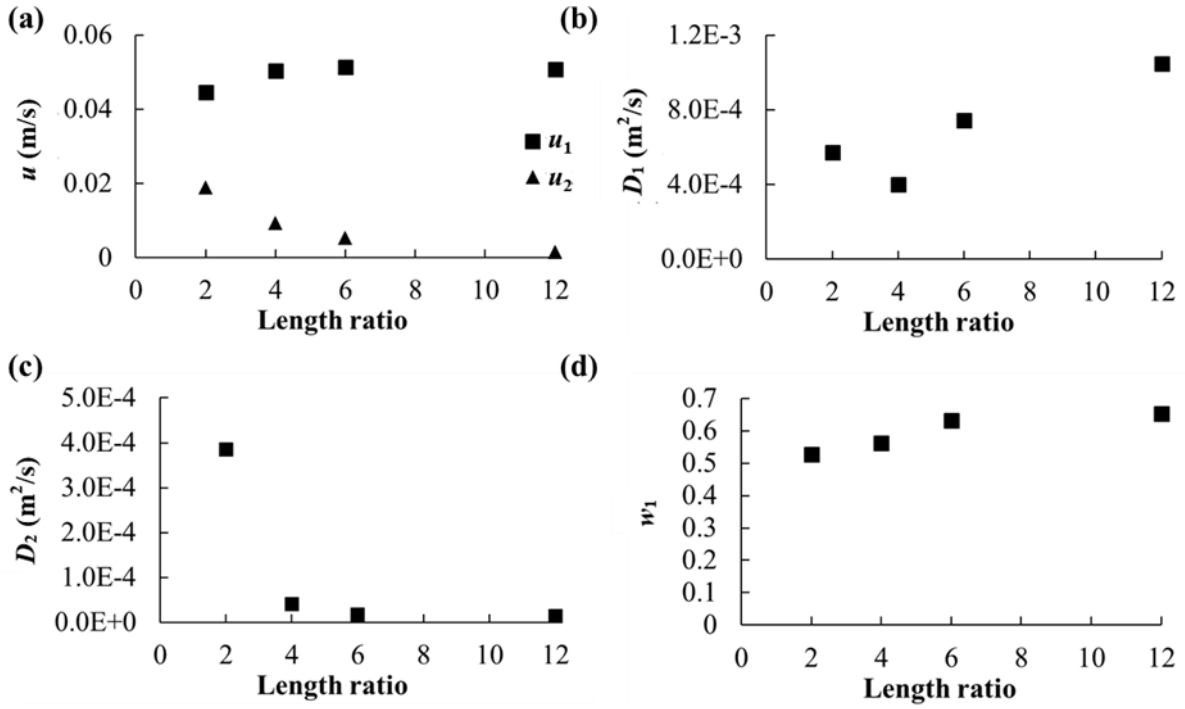

Figure 2.4. Variation of fitted parameter values with experimental model length for Group 1 experiments. (a) Velocities in the two regions, u_1 and u_2, (b) Dispersion coefficient of region 1, D_1, (c) Dispersion coefficient of region 2, D_2, (d) Water content ratio of region 1, w_1.

From Figure 2.4a, we find that, as the length ratio increases from 2 to 12, the velocity of region 1 (u_1) increases from 4.46×10^{-2} to 5.09×10^{-2} (1:1.14). The major increase in u_1 value occurs when transiting between 10-20-30-30 and 10-40-30-30 cases, while the u_1 is only slightly increased from 10-40-30-30 to 10-120-30-30 cases. The velocity of region 2 (u_2) shows a significant decreasing trend, decreases from

1.89×10^{-2} to 1.46×10^{-3} (12.9:1) from 10-20-30-30 to 10-120-30-30 and u_2 decreases from 9.40×10^{-3} to 1.46×10^{-3} (6.45:1) from 10-40-30-30 to 10-120-30-30. This is consistent with the fact that from 10-40-30-30 to 10-120-30-30 the second peak gets increasingly delayed (Figure 2.3). As we can see from Figure 2.4b, the D_1 value does not show any continuous increasing trend: as the ratio increases from 2 to 12, D_1 increases from 5.71×10^{-4} to 1.05×10^{-3} (1:1.84), and as the ratio increases from 4 to 12, D_1 increases from 3.99×10^{-4} to 1.05×10^{-3} (1:2.63). Such a behavior of D_1 variation may be caused by the strong correlation between some parameters for the case of 10-20-30-30 (see parameter identifiability results in Section 3.4 and discussion in Section 4.4). As the ratio increases from 2 to 12, D_2 decreases from 3.86×10^{-4} to 1.47×10^{-5} (2.73:1). As the ratio increases from 2 to 12, w_1 increases from 0.526 to 0.653 (1:1.24), w_2 decreases from 0.474 to 0.347 (1.36:1). This is in agreement with the trend observed from Figure 2.3 (except for 10-20-30-30, because 10-20-30-30 experiment only has one peak): as the length ratio increases, the area below the second peak (A_2), and thus the mass transported through the longer conduit, decreases.

2.3.2 Total length study (experiment Group 2)

In this series of experiments, the length ratio is fixed to 6.0 and the total length (l_1+l_2) varies. The experimental BTCs and the numerical fitting of Group 2 are shown in Figure 2.5. For Group 2, all of the tested dual conduit structures exhibit double-peaked BTCs. As the length increases, the two peaks become increasingly separated. As the length increases, both C_{peak1} and C_{peak2} show a decreasing trend, with C_{peak2} decreasing faster than C_{peak1}. For experiment 60-360-30-30, the longer conduit has strong flow resistance, so the tracer that enters this conduit is much less, so the second peak has a low peak concentration (0.0148) and this second peak is not so obvious on the plot.

A visual inspection indicates that the DRAD does not equally capture the two peaks of the experimental BTCs. Similar to the analysis of Group 1 results, the second peak of the BTCs are not perfectly fitted by the DRAD model because of the presence of strong skewness. The parameters of the fitting result are listed in Table 2.3. The fitted parameters for Group 2, except the exchange rate k_{12} which remains negligible, are plotted in Figure 2.6.

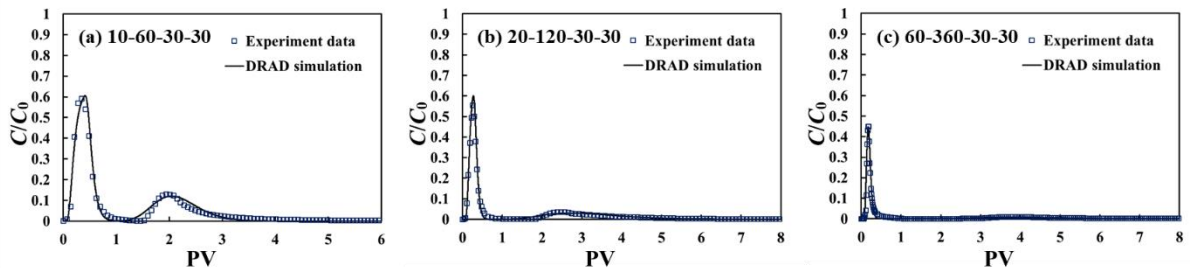

Figure 2.5. DRAD calibration results for Group 2 experiments.

Table 2.3 DRAD model calibration results for Group 2 experiments

	10-60-30-30	**20-120-30-30**	**60-360-30-30**
t_{peak1} (s)	4.55	7.20	16.30
t_{peak2} (s)	27.85	5.90	291.60
u_1 (m/s)	5.13×10^{-2}	5.18×10^{-2}	5.25×10^{-2}
u_2 (m/s)	5.27×10^{-3}	2.99×10^{-3}	2.03×10^{-3}
u_1 (m/PV)	7.41×10^{-1}	1.41×10^{0}	4.13×10^{0}
u_2 (m/PV)	7.61×10^{-2}	8.16×10^{-2}	1.60×10^{-1}
D_1 (m^2/s)	7.42×10^{-4}	1.11×10^{-3}	1.63×10^{-3}
D_2 (m^2/s)	1.82×10^{-5}	4.43×10^{-5}	4.77×10^{-5}
k_{12} (1/s)	3.08×10^{-28}	4.01×10^{-52}	1.56×10^{-38}
w_1 (–)	0.633	0.635	0.721
RMSE (–)	0.0165	0.00620	0.00895

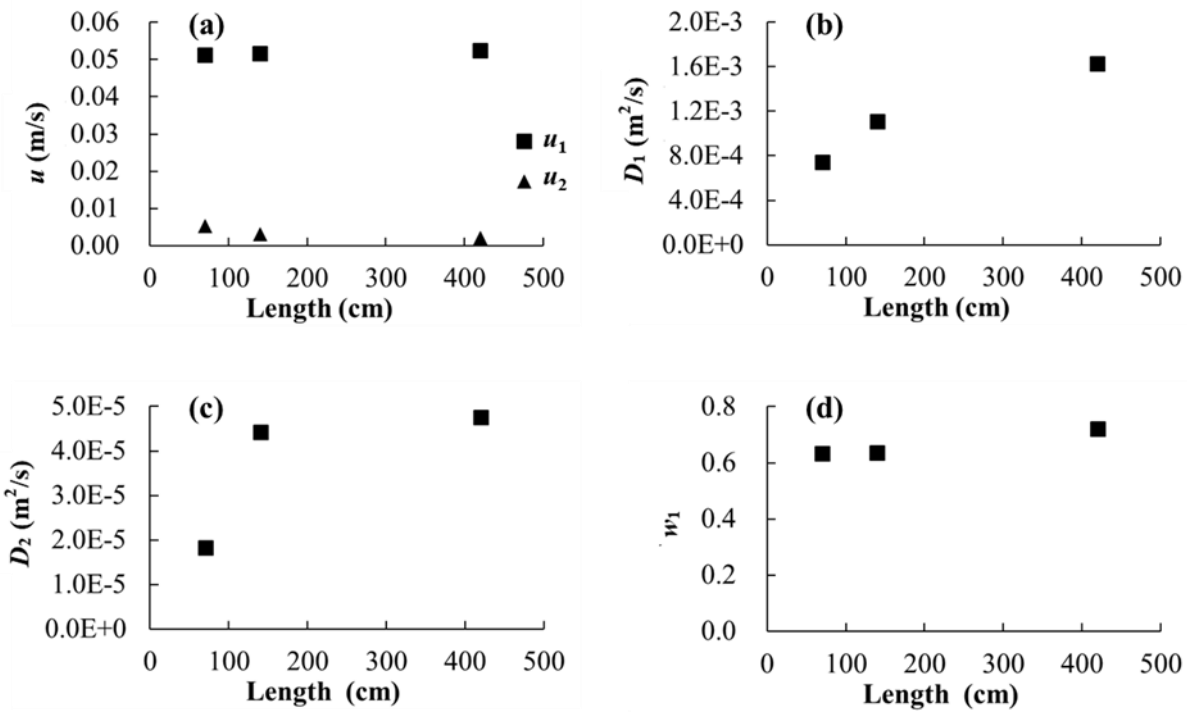

Figure 2.6. Variation of fitted parameter values with experimental model length for Group 2 experiments. (a) Velocities in the two regions, u_1 and u_2, (b) Dispersion coefficient of region 1, D_1, (c) Dispersion coefficient of region 2, D_2, (d) Water content ratio of region 1, w_1.

As shown in Figure 2.6. As the length increases from 10cm-60cm to 60cm-360cm (1:6), the region 1

velocity increases from 5.13×10^{-2} to 5.25×10^{-2} (1:1.02), and the region 2 velocity decreases from 5.27×10^{-3} to 2.03×10^{-3} (2.60:1) (Figure 2.6a). The dispersion coefficient of both regions increases: D_1 increases from 7.42×10^{-4} to 1.63×10^{-3} (1:2.19), D_2 increases from 1.82×10^{-5} to 4.77×10^{-5} (1:2.62), (Figure 2.6 b, c). w_1 remains almost the same, from 0.633 to 0.721 (1:1.14), (Figure 2.6d).

2.3.3 Connection angle (experiment Group 3)

For Group 3 experiments (Figure 2.7), the connector angle between two conduits has an important influence on the flow and transport process. As the (θ_1-θ_2) value increases, the two peaks become closer to each other; and C_{peak1} decreases, C_{peak2} increases.

Same with previous groups, the fit is better for the first peak of the experiment BTCs than for the second peak, with a maximum error value to be 0.0168 (Table 2.4). The fitted parameters for Group 3 are plotted in Figure 2.8.

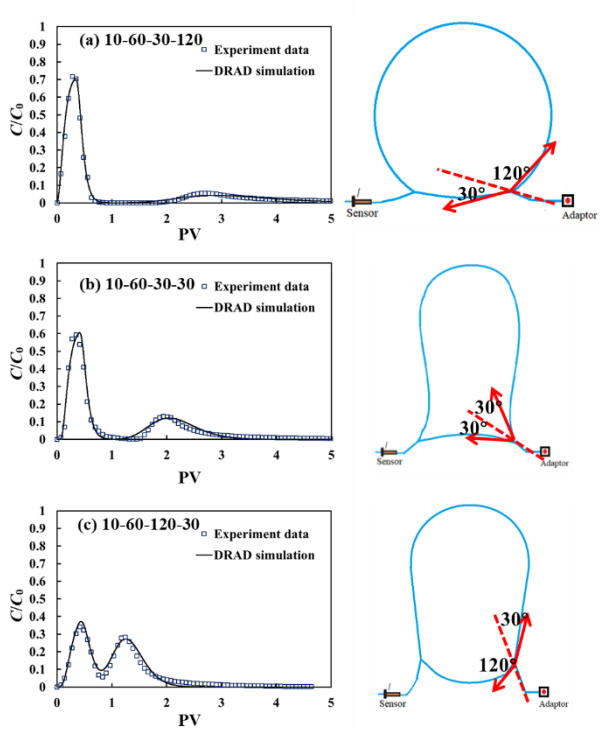

Figure 2.7. DRAD calibration results of Group 3 experiments.

Table 2.4 DRAD model calibration results for Group 3 experiments

	10-60-30-120	**10-60-30-30**	**10-60-120-30**
(θ_1-θ_2) (deg)	-90	0	90
t_{peak1} (s)	4.40	4.55	6.15

t_{peak2} (s)	39.65	27.85	17.60
u_1 (m/s)	5.39×10^{-2}	5.13×10^{-2}	2.99×10^{-2}
u_2 (m/s)	3.31×10^{-3}	5.27×10^{-3}	8.56×10^{-3}
u_1 (m/PV)	7.78×10^{-1}	7.41×10^{-1}	4.32×10^{-1}
u_2 (m/PV)	4.78×10^{-2}	7.61×10^{-2}	1.24×10^{-1}
D_1 (m^2/s)	7.81×10^{-4}	7.42×10^{-4}	3.55×10^{-4}
D_2 (m^2/s)	2.22×10^{-5}	1.82×10^{-5}	3.17×10^{-5}
k_{12} (1/s)	6.33×10^{-34}	2.19×10^{-33}	9.28×10^{-26}
w_1 (-)	0.732	0.633	0.451
RMSE (-)	0.0131	0.0165	0.0168

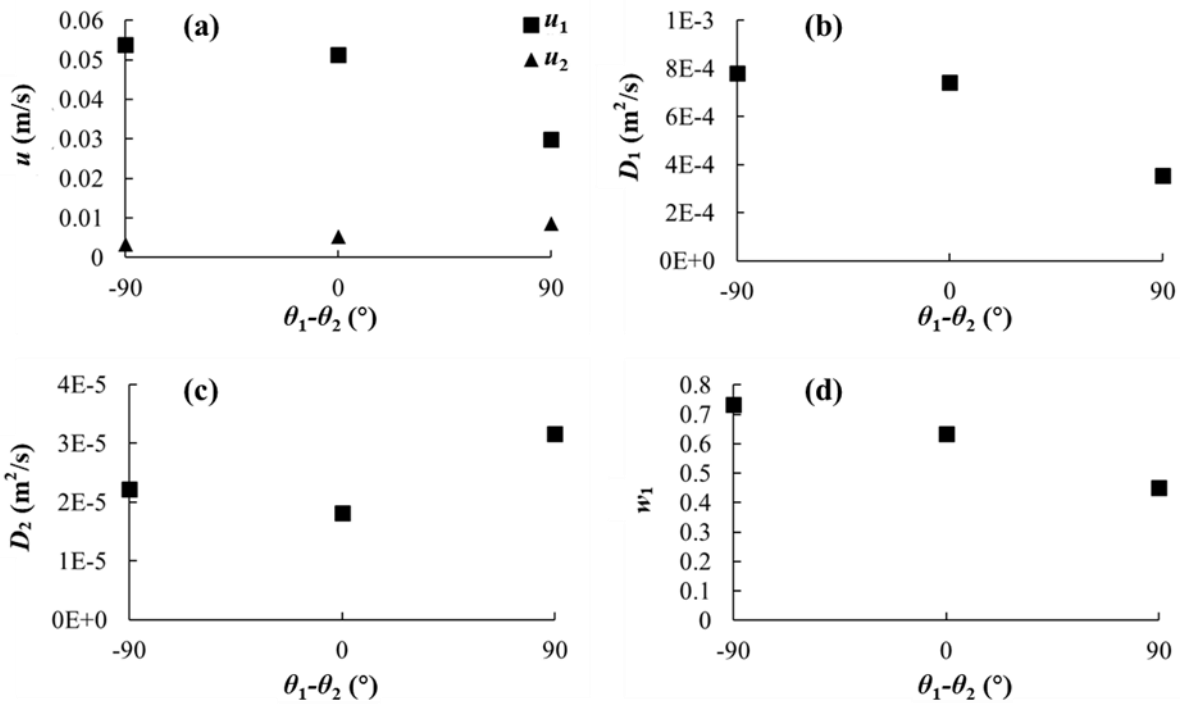

Figure 2.8. Variation of fitted parameters with angle difference, θ_1 - θ_2, for Group 3 experiments. (a) Velocities in the two regions, u_1 and u_2, (b) Dispersion coefficient of region 1, D_1, (c) Dispersion coefficient of region 2, D_2, (d) Water content ratio of region 1, w_1.

Figure 2.8a shows that as (θ_1 - θ_2) increases from -90° to 90°, u_1 decreases from 5.39×10^{-2} m/s to 2.99×10^{-2} m/s (i.e., by 1.8 times) and u_2 increases from 3.31×10^{-3} m/s to 8.56×10^{-3} m/s (~ 2.6 times). This conforms to the fact that as (θ_1-θ_2) increases, the first peak is delayed and the second peak appears sooner (Figure 2.7). The D_1 decreases from 7.81×10^{-4} m^2/s to 3.55×10^{-5} m^2/s (~ 2.2 times) (Figure 2.8b); the D_2 increases from 2.22×10^{-5} m^2/s to 3.17×10^{-5} m^2/s (~ 1.4 times) (Figure 2.8c). w_1 decreases from 0.732 to

0.451 (~ 1.6 times) while w_2 increases from 0.268 to 0.549 (~ 2 times) (Figure 2.8d). The changes in w_1 and w_2 values are consistent with a smaller first peak and a larger second peak (Figure 2.7).

2.3.4 Parameter identifiability

As presented in section 3.1, the variation of estimated parameter set for the 10-20-30-30 experiment does not show a trend consistent with that of other experiments. We thus perform a study to check the identifiability of model parameters for various Group 1 experiments based on the statistics extracted from respective MCMC chains. Figure 2.9 and Figure 2.10 present the MCMC statistics for the 10-20-30-30 and 10-60-30-30 experiments, respectively. The on-diagonal plots of these figures are the estimated posterior parameter distributions for each parameter, while the off-diagonal plots correspond to scatterplots between parameter pairs. A widespread point cloud on the scatterplots indicates that the parameters are independent. A narrow stripe on the scatterplots means a strong correlation between two parameters. The correlation intensity is quantified by the correlation coefficient r (as defined by Eq. 6), which is indicated in the scatterplots. The 95 percentiles of the breakthrough curves are shown in the inset above the diagonal.

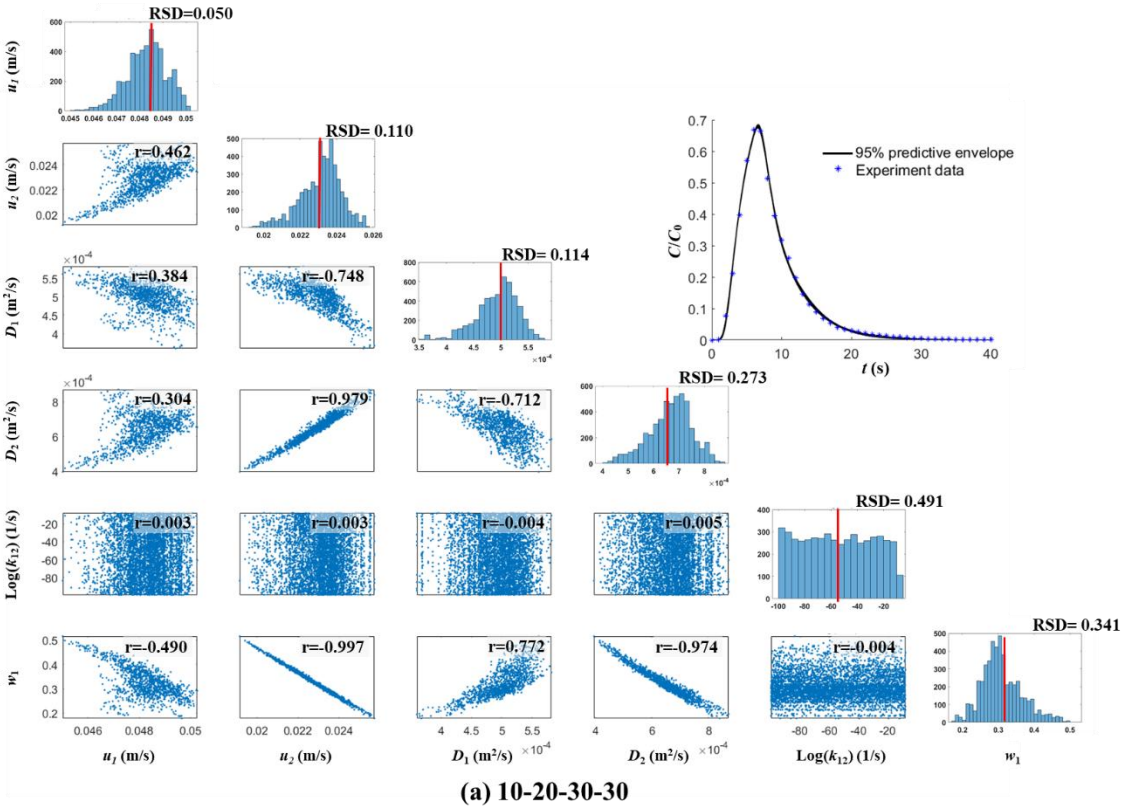

(a) 10-20-30-30

Figure 2.9. MCMC solutions to experiment of 10-20-30-30.

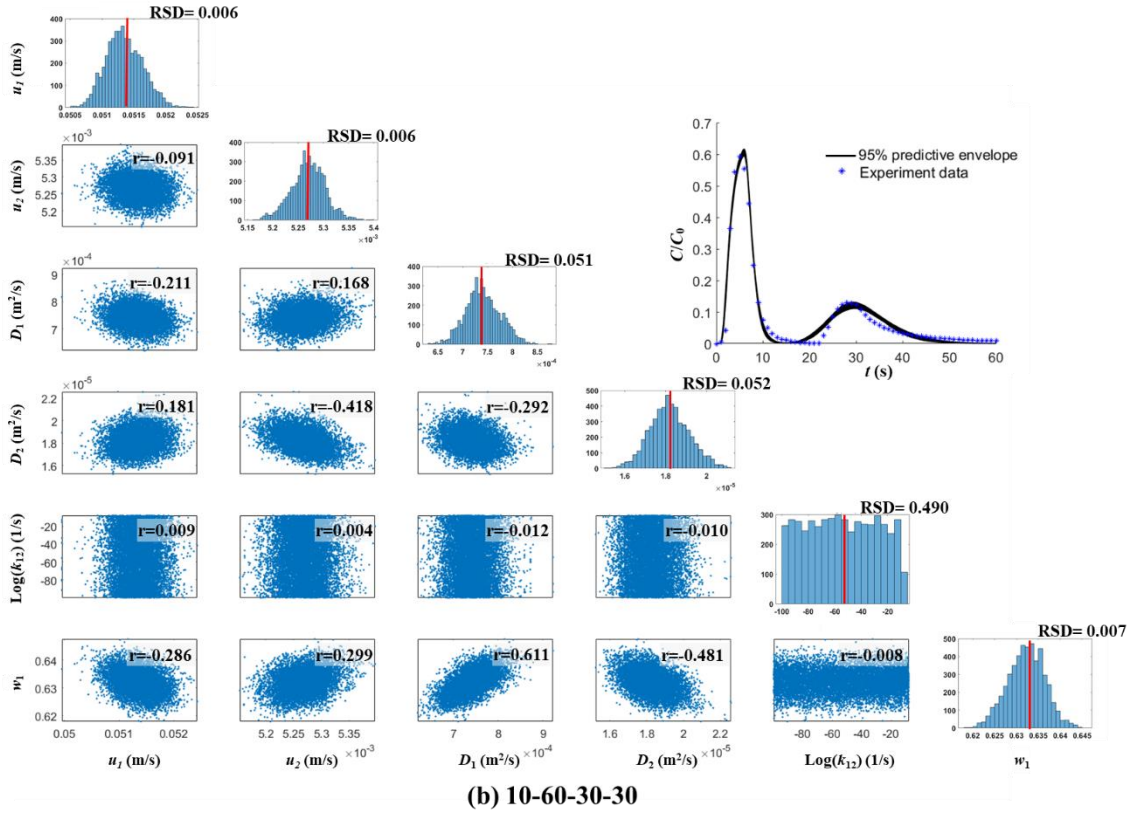

(b) 10-60-30-30

Figure 2.10. MCMC solutions to experiment of 10-60-30-30.

Table 2.5. A priori distribution of DRAD parameters used in the MCMC calibration

	Initial input		Range		Distribution
	10-20-30-30	10-60-30-30	Min	Max	
u_1 (m/s)	3.04×10^{-2}	5.50×10^{-2}	$u_1\times0.005$	$u_1\times200$	Uniform
u_2 (m/s)	1.60×10^{-2}	5.30×10^{-3}	$u_2\times0.005$	$u_2\times200$	Uniform
D_1 (m^2/s)	8.71×10^{-4}	9.30×10^{-4}	0	$500\times D_1$	Uniform
D_2 (m^2/s)	6.00×10^{-6}	1.82×10^{-5}	0	$500\times D_2$	Uniform
k_{12} (1/s)	4.50×10^{-8}	4.50×10^{-8}	1.00×10^{-100}	1.00×10^{-5}	Uniform
w_1 (–)	0.5	0.6325	0.01	0.99	Uniform

It can be seen that except for k_{12}, all other parameters are appropriately identified as their posterior distribution is essentially of a Gaussian type (Figure 2.9). In a simple sensitivity test, we observe that varying k_{12} within a wide range between 10^{-90} and 10^{-8} and fixing all other parameters, there is no change in the outlet breakthrough curve. Changes in breakthrough curves only occur when k_{12} takes a large value, which is on the magnitude of 10^{-3}. This means that the model is insensitive to k_{12} as long as its value is small.

For the other parameters, the 10-20-30-30 experiment exhibited a strong interaction between parameters (Figure 2.9). According to the parameter correlation plots, we find some parameter pairs, for example, u_2-D_2, u_2-w_1 and D_2-w_1, even exhibited a linear trend on the cross plot. The strong correlations are also shown by the high values of correlation coefficients $|r|$ (nearly equal to 1; Figure 2.9). The other

parameter pairs like u_2-D_1, D_1-D_2 and D_1-w_1 exhibited a slightly lower correlation strength, with $|r|$ values of 0.748, 0.712 and 0.772.

In contrast, the 10-60-30-30 experiment exhibited a stronger parameter identifiability and much weaker parameter interaction (Figure 2.10). No obvious correlation between the parameters was found. The maximum $|r|$ value of 0.611 was found for the parameter pair D_1-w_1. The variation range of posterior distributions of the parameters was also smaller. The dispersion coefficients, D_1 and D_2, have the largest RSD values of 0.051 and 0.052, respectively. The RSD values of other parameters such as u_1, u_2, w_1 are quite small, i.e., 0.006, 0.006, 0.007, respectively. These observations indicate the DRAD model parameters were properly identified for the 10-60-30-30 experiment. Similar behavior has also been found for other experiments (not shown here) with larger conduit length ratios.

2.4 Discussion

2.4.1 Representativeness of the experiments for karst tracer tests

We examine to which degree our experiments are representative of natural karst systems and the possibility to extrapolate our laboratory finding to the characterization of karst aquifers based on field tracer tests**.** We calculate three dimensionless quantities (i.e., the conduit length to diameter ratio, Péclet number and Reynolds number) to evaluate the geometric, kinematic and dynamic similarities between our experiments and previous field studies (Table 2.6, see also Appendix A for a summary of parameter values reported in literature). Péclet number is a measure of the relative importance of advection versus diffusion, it is calculated as:

$$\text{Pé} = \frac{Lu}{D}, \qquad \text{(Eq. 2-10)}$$

where: L is the characteristic length (L), u is the local flow velocity (LT^{-1}), D is the diffusion coefficient (L^2T^{-1}). The Reynolds number is the ratio of inertial forces to viscous forces within a fluid, it is calculated as:

$$\text{Re} = \frac{\rho u d}{\mu}, \qquad \text{(Eq. 2-11)}$$

where: ρ is the density of the fluid (ML^{-3}), u is the local flow velocity (LT^{-1}), d is the diameter of the tube (L), μ is the dynamic viscosity of the fluid ($M\ L^{-1}T^{-1}$).

The range of values of the geometric and kinematic similarity criteria (i.e., the conduit length-diameter ratio and Péclet number) of our experiments fall within the range of values obtained under field conditions. Regarding the dynamic similarity criterion, the Reynolds number of our experiments is quite small compared to the that obtained from field tracer tests. In our experiments, the fluid flow in conduits was under laminar flow condition (i.e., Reynolds number < 2000), while it is well known that the turbulent flow often occurs in natural karst aquifers. Although the difference in flow regime may induce a discrepancy in pressure or flow rate in the conduits, the general trend that the flow rate is positively correlated to hydraulic head gradient is still respected. Thus, the observed effect of conduit geometry on transport responses may still provide important insights for the interpretation of field tracer tests in natural karst systems.

Table 2.6 Comparison of dimensionless quantities between published field data and our experiments

Similarity criterion	Dimensionless number		Range of Values in nature (karst tracer tests)	Range of Values for the experiment
Geometry	Conduit length to diameter ratio	$\frac{l}{d}$	25-25000	37.5-162.5
Kinematic	Péclet number	$\frac{Lu}{D}$	12-331	7.77-21.27

Dynamic	Reynolds number	$\frac{\rho u d}{\mu}$	6500-87000	144

Our experimental work confirms that the dual conduit structure generally results in the dual-peaked BTCs, as shown in previous studies (Smart, 1988; Perrin and Luetscher, 2008; Field and Leij, 2012). We further found that the number of the BTC peaks is not necessarily the same as the number of conduits when the length of the two conduits is similar. For example, the BTC of experiment 10-20-30-30 showed only one peak. The single peak is composed of two overlapping concentration fronts, whose arrival times to the outlet are similar.

2.4.2 Inferring conduit lengths from the dual-peaked BTCs

We propose to use tracer BTCs to infer the length of conduits that form a looped network as shown in Figure 2.1 and Figure 2.12. For dual-peaked BTCs, we denote the area below the first peak as A_1 and that of the second peak as A_2. For cases where the two peaks are adequately separated, A_1/A_2 may be used to approximate the ratio of the tracer amount of the two conduits. When the Péclet number is sufficiently high (as in our experiments, *Pe* varies between 7.77 and 21.27), advection dominates the flow process. Under such a condition, the flow rate ratio between the conduits may be approximated by the ratio of tracer amount passing through the two conduits, i.e., $Q_1/Q_2 \approx A_1/A_2$, (See Appendix B for details of the derivation). Also, the arrival time of the two packs of tracer at the outlet may be estimated by the concentration peak times t_{peak1} and t_{peak2}. If all conduits are assumed to have a constant diameter, which may be estimated by field investigations, by applying mass conservation at the diverging and converging points of the dual-conduit network, the length of the shorter and longer conduits can be estimated by:

$$l_{1e} = \frac{Q_1\left[(Q_1+Q_2)t_{\text{peak1}} - LS_f\pi R^2\right]}{Q_2\pi R^2}, \quad \text{(Eq. 2-12)}$$

$$l_{2e} = \frac{Q_2 t_{\text{peak2}} + Q_1 t_{\text{peak1}} - LS_f\pi R^2}{\pi R^2}, \quad \text{(Eq. 2-13)}$$

where l_{1e} and l_{2e}, are respectively the estimated lengths of the shorter and longer conduits; L is total length of the dual-conduit structure, i.e., the distance from the injection point to the sampling point via the shorter conduit; S_f is the **sinuosity factor;** R is the conduit radius; Q_1 and Q_2 are respectively the flow rates of shorter and longer conduits.

We demonstrate the usage of the proposed method for estimating lengths of subsurface conduits by applying it to our experimental data of Groups 1 and 2. In order to obtain more accurate peak time, the BTCs has been interpolated by 0.5 s. The ratios between the estimated length and the actual length for the two conduits, $\boldsymbol{l_{1e}/\ l_1}$ **and** $\boldsymbol{l_{2e}/\ l_2}$ are shown in Figure 2.11. It can be seen that the length ratios for various experiments scatter around 1.0, which indicates an effective estimation. The average value of this ratio is

1.058, the estimated value tend to be slightly larger than the true value. The shorter conduit length seems better identified than that of the longer conduit. This may be caused by the stronger skewness of the second peak (i.e., stronger dispersion in the longer conduit). The most biased case is the 10-60-30-120 experiment, where the ratio for the shorter conduit, $l_{1e}/\ l_1$ = 1.20. However, the ratio is still very close to 1.0. This indicates that the proposed method is valid at least for the tested conduit network configurations and flow conditions. It has to be mentioned that the method is based on the assumption the conduit diameter is constant for the entire system and is known. The geometrical complexities of natural karst system may invalidate the assumption and imply to consider an equivalent conduit diameter. We will extend the method to more general cases of variable conduit diameter when experimental data for such experiments become available.

The method is applicable when BTCs show fully separated dual peaks. However, there are some cases of special dual-peaked BTCs worth our further notice. First, like the 10-40-30-30 and 10-60-120-30 experiment of this paper, the two peaks are not fully separated, we can use the minimum concentration point between the two peaks to approximately separate the two peaks and calculate the area under the two peaks, the result still seems reasonable. Second, for experiment 60-360-30-30, the second peak concentration of the 60-360-30-30 experiment is so low that it becomes inconspicuous. This make us realize that we may lost some information when dealing with real tracer tests because the low concentration signal is very possible to be hidden behind the background noise signals.

Second, for experiment 60-360-30-30, the second peak concentration of the 60-360-30-30 experiment is so low that it becomes inconspicuous. For real karst tracer test, the low concentration signal is very possible to be hidden behind the background noise signals. This suggests us not to ignore the low concentration signals when performing tracer tests in real karst aquifers. Because this low concentration peak may indicate the existence of very long secondary conduits, through which a few quantity of tracer is transported.

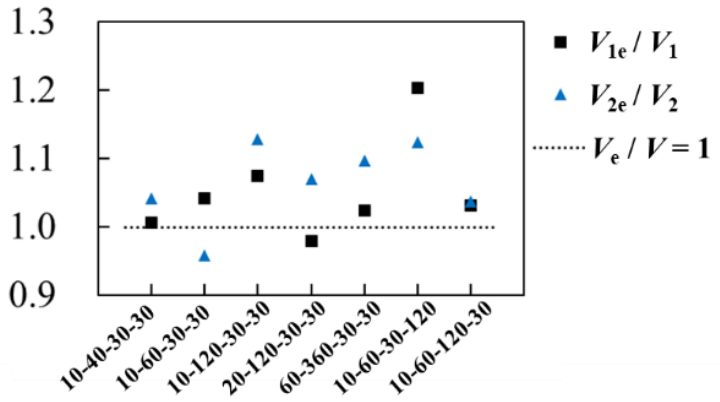

Figure 2.11. Calculated values of estimated to true conduit length ratio for various experiments.

2.4.3 Parameter identifiability of DRAD model

The distributions for the sets of parameters of 10-20-30-30 exhibited a strong interaction (u_2-D_1, D_1-D_2, D_1-w_1). In the 10-20-30-30 experiment, the concentration fronts from the two flowing regions do not separate, i.e., the concentration is similar at a certain time. On the other hand, solute migration in the two regions of DRAD are modeled using two similar transport equations. Since the two transport equations have to handle similar concentration, it is likely that the contribution of the two transport equations to the model responses is indistinguishable. However, it should be noted that the issue of difficult to separate model parameters observed in our study is different from the equifinality issue as discussed in (Younes *et al.*, 2016). In the study, the authors used a similar dual flowing continuum model to examine transport problem in porous media that includes biofilm phases. The equifinality of their model due to the non-separated concentration fronts in model responses is essentially resulted from a high exchange rate between the dual flowing phases. In contrast, in our experiments there is no mass exchange between the two conduits. The non-separation of concentration peaks is resulted from the similar arrival times of two packs of solute travel through the two conduits.

According to the RSD and r values, the fitting MCMC chain of 10-60-30-30 showed weaker interaction. The DRAD showed different parameter identifiability for 10-20-30-30 and 10-60-30-30 data. One model may perform good parameter identifiability when characterizing one BTC and exhibits weak identifiability for another. This has been noted by previous studies (Wagner and Harvey, 1997; Kelleher *et al.*, 2013; Rana *et al.*, 2019). It seems necessary to study the model parameter identifiability with more cases.

For the single-peaked BTC, the DRAD model may reproduce the curve sufficiently well but the some of the estimated parameters show strong correlations. Such a deficiency indicates that the DRAD may not be a suitable model in the particular case of single-peaked BTC. For the dual-peaked BTCs, DRAD can adequately characterize the dual-peaked BTCs on the whole with good parameter identifiability, but does not satisfyingly characterize the skewness of the BTC peaks. Here, the objective of quantitative examination of geometrical effects of conduits on BTCs is achieved. We, thus, do not seek for another model to perfectly characterize the BTCs. However, this will be attempted in our future work.

For the model, there exists a negligible exchange rate. The issue of correlated parameters arises because the conceptual structure of DRAD is different from the actual transport process in the dual conduit structure. For the DRAD model, exchange happens all along the model, while for the experiment model exchange only happens at the divergence and convergence between the tubes. This is why there should be an exchange in the DRAD model, although this exchange is not perfectly accounted by the DRAD.

2.5 Conclusions

In this paper, we studied the solute transport process in dual conduit structures by lab-scale experiments. The main contributions of this study are summarized as follows.

First, we studied how the dual-conduit structure may influence the BTCs shape, specifically: 1) As the length ratio increases, on the c-t plot, the two peaks get more separated, the concentration value of the first peak (C_{peak1}) increases and the second peak (C_{peak2}) decreases; 2) As the total length increases, the two peaks become increasingly separated and the concentration value of both peaks decreases, while C_{peak2} decreases much more than C_{peak1}; 3) As the (θ_1-θ_2) value of the dual-conduit connection increases, the size of the first peak (A_1), and thus the mass transported through the shorter conduit, gets smaller and the size of the second peak (A_2), and thus the mass transported through the longer conduit, gets bigger.

Second, we proposed one method to estimate the underground conduit length from recorded dual-peaked BTCs, assuming the average diameter of conduits is known. The method showed a good performance in estimating the conduit length from our experimental BTCs and whether the method is applicable to the real karst tracer tests should be confirmed by field experiments**.**

Third, we studied the ability of the DRAD model to reproduce BTCs with a single peak and double peaks. For the single-peaked BTCs, the DRAD is deemed useless because of the low parameter identifiability, although the data fitting appears acceptable. For the dual-peaked BTCs, DRAD achieved a good fitting with stronger parameter identifiability except that the exchange coefficient is insensitive during fitting. However, it would be better if we could further develop the model to produce the dual-peaked BTCs with skewness. While the DRAD model may be considered useful for predictive purposes for a given site on which it has been properly calibrated, the analysis of the fitting results show that its parameters do not necessarily bear a physical meaning. A path for research thus focuses on the development of models, the parameters of which reflect the geometric and hydraulic reality of the experiments.

However, this study has three limitations. First, the flow regime of our experiments is laminar flow while in nature it is turbulent. Second, we did not study the structures with conduit diameter variation. Third, we did not study the influence of velocity variation. These will be explored in future work.

References

Berkowitz, B. *et al.* (2006) "Modeling Non-fickian transport in geological formations as a continuous time random walk," *Reviews of Geophysics*, 44(2). doi:10.1029/2005RG000178.

Dewaide, L. *et al.* (2018) "Double-peaked breakthrough curves as a consequence of solute transport through underground lakes: a case study of the Furfooz karst system, Belgium," *Belgium. Hydrogeology Journal*, 26(2), pp. 641–650. doi:10.1007/s10040-017-1671-4ï.

Duran, L. *et al.* (2016) "Assessing the Nonlinearity of Karst Response Function under Variable Boundary Conditions," *Groundwater*, 54(1), pp. 46–54. doi:https://doi.org/10.1111/gwat.12337.

Doummar, J., Margane, A., Geyer, T. and Sauter, M., 2012. Artificial Tracer Test 5A – June 2011. - Special Report No. 6 of Technical Cooperation Project "Protection of Jeita Spring", Department of Applied Geology, University of Göttingen, Germany & Federal Institute for Geosciences and Natural Resources (BGR), Germany.

Field, M.S. (1999) *The QTRACER program for tracer-breakthrough curve analysis for karst and fractured-rock aquifers*. National Center for Environmental Assessment–Washington Office, Office of~….

Field, M.S. (2002) *The QTRACER2 program for tracer-breakthrough curve analysis for tracer tests in karstic aquifers and other hydrologic systems*. National Center for Environmental Assessment–Washington Office, Office of~….

Field, M.S. and Leij, F.J. (2012) "Solute transport in solution conduits exhibiting multi-peaked breakthrough curves," *Journal of Hydrology*, 440–441, pp. 26–35. doi:10.1016/J.JHYDROL.2012.03.018.

Florea, L.J. and Wicks, C.M. (2001) "Solute transport through laboratory-scale karstic aquifers," *Journal of Cave and Karst Studies*, 63(2), pp. 59–66.

van Genuchten, M.T. and Wierenga, P.J. (1976) "Mass transfer studies in sorbing porous media I. Analytical solutions," *Soil science society of america journal*, 40(4), pp. 473–480.

Goldscheider, N. *et al.* (2008) "Tracer tests in karst hydrogeology and speleology," *International Journal of speleology*, 37(1), pp. 27–40.

Goldsheider, N. and Drew, D. (2007) "Methods in Karst hydrogeology. International contribution to hydrogeology, IAH." Taylor & Francis/Balkema, London.

Göppert, N. and Goldscheider, N. (2008) "Solute and Colloid Transport in Karst Conduits under Low- and High-Flow Conditions," *Groundwater*, 46(1), pp. 61–68. doi:https://doi.org/10.1111/j.1745-6584.2007.00373.x.

Haario, H. *et al.* (2006) "DRAM: efficient adaptive MCMC," *Statistics and computing*, 16(4), pp. 339–354.

Hauns, M., Jeannin, P.-Y. and Atteia, O. (2001) "Dispersion, retardation and scale effect in tracer

breakthrough curves in karst conduits," *Journal of hydrology*, 241(3–4), pp. 177–193.

Kelleher, C. *et al.* (2013) "Identifiability of transient storage model parameters along a mountain stream," *Water Resources Research*, 49(9), pp. 5290–5306.

Li, G., Loper, D.E. and Kung, R. (2008) "Contaminant sequestration in karstic aquifers: Experiments and quantification," *Water Resources Research*, 44(2).

Majdalani, S. *et al.* (2018) "Modelling solute dispersion in periodic heterogeneous porous media: model benchmarking against intermediate scale experiments," *Journal of Hydrology*, 561, pp. 427–443.

Maloszewski, P. *et al.* (1992) "Mathematical modelling of tracer experiments in the karst of Lurbach system," *Steierische Beiträge zur Hydrogeologie*, 43, pp. 116–136.

Massei, N. *et al.* (2006) "Interpreting tracer breakthrough tailing in a conduit-dominated karstic aquifer," *Hydrogeology Journal*, 14(6), pp. 849–858.

Mohammadi, Z., Gharaat, M.J. and Field, M. (2019) "The Effect of Hydraulic Gradient and Pattern of Conduit Systems on Tracing Tests: Bench-Scale Modeling," *Groundwater*, 57(1), pp. 110–125.

Morales, T. *et al.* (2010) "Solute transport modelling in karst conduits with slow zones during different hydrologic conditions," *Journal of Hydrology*, 390(3–4), pp. 182–189.

Moreno, L. and Tsang, C.F. (1991) "Multiple-peak response to tracer injection tests in single fractures: A numerical study," *Water Resources Research*, 27(8), pp. 2143–2150.

Perrin, J. and Luetscher, M. (2008) "Inference of the structure of karst conduits using quantitative tracer tests and geological information: example of the Swiss Jura," *Hydrogeology Journal*, 16(5), pp. 951–967.

Rana, S.M.M. *et al.* (2019) "Parameter uncertainty with flow variation of the one-dimensional solute transport model for small streams using Markov chain Monte Carlo," *Journal of Hydrology*, 575, pp. 1145–1154.

Skopp, J., Gardner, W.R. and Tyler, E.J. (1981) "Solute movement in structured soils: Two-region model with small interaction," *Soil Science Society of America Journal*, 45(5), pp. 837–842.

Smart, C.C. (1988) "Artificial tracer techniques for the determination of the structure of conduit aquifers," *Groundwater*, 26(4), pp. 445–453.

Upchurch, S. *et al.* (2019) *The Karst Systems of Florida: Understanding Karst in a Geologically Young Terrain*. Springer.

Vrugt, J.A. *et al.* (2006) "Multi-objective calibration of forecast ensembles using Bayesian model averaging," *Geophysical Research Letters*, 33(19).

Wagner, B.J. and Harvey, J.W. (1997) "Experimental design for estimating parameters of rate-limited mass transfer: Analysis of stream tracer studies," *Water Resources Research*, 33(7), pp. 1731–1741.

Younes, A. *et al.* (2016) "Global sensitivity analysis and Bayesian parameter inference for solute transport in porous media colonized by biofilms," *Journal of Contaminant Hydrology*, 191, pp. 1–18.

Zhao, X. *et al.* (2017) "Laboratory investigation and simulation of breakthrough curves in karst conduits with pools," *Hydrogeology Journal*, 25(8), pp. 2235–2250.

Zhao, X. *et al.* (2019) "Effects of flow rate variation on solute transport in a karst conduit with a pool," *Environmental Earth Sciences*, 78(7), pp. 1–18.

Appendix

Appendix A.

The diameter of karst conduit ranges from a few centimeters to several meters (Upchurch *et al.*, 2019). The karst aquifer length is between 0.5 km to 10 km (Göppert and Goldscheider, 2008; Morales *et al.*, 2010; Duran *et al.*, 2016). Various flow velocities have been reported: 31.9 ~ 117.6 m/h (Morales *et al.*, 2010), 24.8 ~ 136.9 m/h (Göppert and Goldscheider, 2008) and 63 ~ 121.4 m/h (Duran *et al.*, 2016). If we assume the water viscosity μ = 1 mPa·s and the lower and upper values for conduit diameter are 0.2 m and 2 m, the Reynolds numbers are approximately 6500 ~ 44000 (Morales *et al.*, 2010), 7600 ~ 34000 (Göppert and Goldscheider, 2008), 6700 ~ 87000 (Duran *et al.*, 2016), respectively. This indicates that the natural karst flow is frequently under turbulent flow regime. In our experiments, the inlet flow velocity v = 0.054 m/s and conduit diameter d = 0.004 m. Thus, the characteristic Reynolds number Re = 144, i.e. the experiments are under the laminar flow condition. For real karst systems in previous studies, the calculated Peclet number range is: 167 ~ 256 (Massei *et al.*, 2006), 77 ~ 140 (Field, 1999), 12 ~ 113 (Field, 2002), 279 ~ 331 (Doummar et al., 2012). The Peclet number of our experiments lies between 7.77 and 21.27.

Appendix B.

The schematic diagram for natural karst systems with a dual conduit structure is shown in Figure 2.12. l' and l'' are the lengths of the two convergence conduit parts, Q_0 is the flow rate of these two parts, l_1 and l_2 are the lengths of the shorter and the longer conduit, Q_1 and Q_2 are the flow rates of the shorter and the longer conduit. From the mass conservation law, we have:

$$Q_0 = Q_1 + Q_2 \qquad \text{(Eq. 2-14)}$$

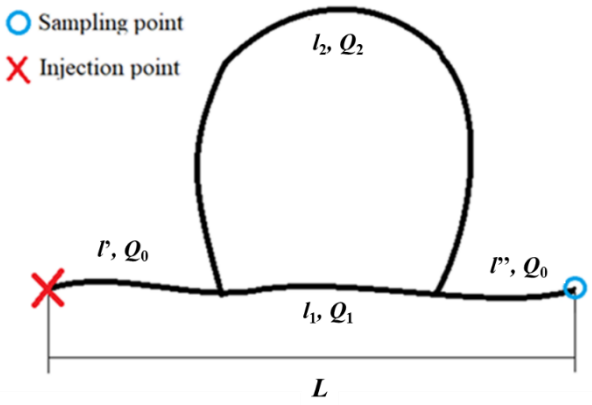

Figure 2.12. Schematic diagram of a dual-conduit structure.

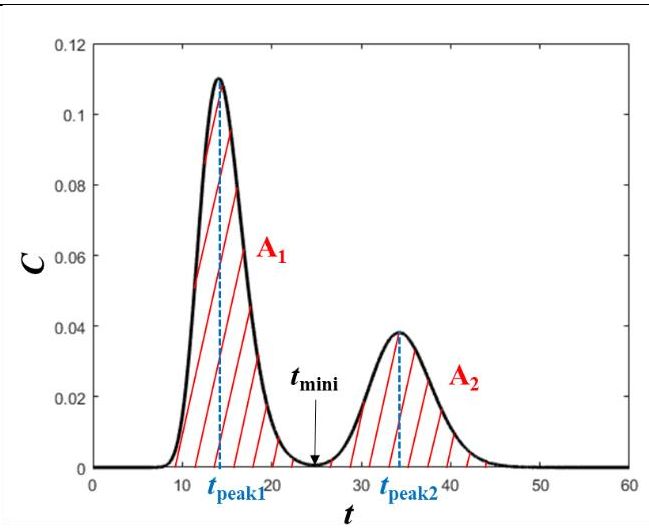

Figure 2.13. Schematic diagram explaining the method for conduit length estimation using BTCs.

Figure 2.13 presents a typical double-peaked BTC resulted from a dual-conduit structure shown in Figure 2.12. When the two peaks are fully separated, the tracer mass that migrated through the two conduits can be calculated by:

$$m_1 = \int_{t=0}^{t_{mini}} Q_0 C(t)dt = Q_0 \int_{t=0}^{t_{mini}} C(t)dt = Q_0 A_1 , \quad \text{(Eq. 2-15)}$$

$$m_2 = \int_{t_{mini}}^{t_{max}} Q_0 C(t)dt = Q_0 \int_{t_{mini}}^{t_{max}} C(t)dt = Q_0 A_2 , \quad \text{(Eq. 2-16)}$$

where t_{mini} is the time when the concentration reaches the minimum value between the two peaks, t_{max} is the final time of the tracer test, Q_0 is the flow rate at the outlet point, C(t) is the transient concentration at the outlet point; A_1 is the area below the first peak of the BTC, A_2 is the area below the second peak.

From Equations B2 and B3, we have:

$$\frac{m_1}{m_2} = \frac{A_1}{A_2} . \quad \text{(Eq. 2-17)}$$

Assuming that the advection dominates the transport process, the tracer mass that enters the two conduits can also be approximated at the upstream connector where the flow and mass are diverged (Figure 2.14) by:

$$m_1 \approx \int_{t=0}^{t_{max}} Q_1 C(t)dt = Q_1 \int_{t=0}^{t_{max}} C(t)dt , \quad \text{(Eq. 2-18)}$$

$$m_2 \approx \int_{t=0}^{t_{max}} Q_2 C(t)dt = Q_2 \int_{t=0}^{t_{max}} C(t)dt . \quad \text{(Eq. 2-19)}$$

Thus, it can be shown that

$$\frac{m_1}{m_2} = \frac{A_1}{A_2} \approx \frac{Q_1}{Q_2} , \quad \text{(Eq. 2-20)}$$

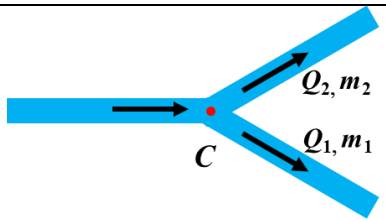

Figure 2.14. Schematic diagram showing the division of flow and mass into the two conduits at the connector.

From Equations B1 and B7, the flow rates in the two conduits, Q_1 and Q_2, can be estimated. The total length of the system L is evaluated from:

$$L \times S_f = l' + l_1 + l'' = \frac{V' + V_1 + V''}{\pi R^2} = \frac{V_0 + V_1}{\pi R^2}, \quad \text{(Eq. 2-21)}$$

where L is the distance between the inlet and the outlet points; S_f is the sinuosity factor to estimate underground conduit length; V', V'', V_1 are respectively the volumes of the inlet, outlet, and shorter conduits; V_0 is the sum of V' and V''.

The concentration peak times t_{peak1} and t_{peak2} may represent the mean tracer travel time, thus,

$$\frac{V_0}{Q_1 + Q_2} + \frac{V_1}{Q_1} = t_{peak1} \quad \text{(Eq. 2-22)}$$

$$\frac{V_0}{Q_1 + Q_2} + \frac{V_2}{Q_2} = t_{peak2} \quad \text{(Eq. 2-23)}$$

where V_2 is **t**he volume of the longer conduit. In Equations B8 to B10, the value of L, S_f, Q_1, Q_2, t_{peak1} and t_{peak2} may be estimated from field surveys. Thus, the three unknown variables V_1, V_2 and V_0 can be obtained by solving Equations B8 to B10 together:

$$V_1 = \frac{Q_1\left[(Q_1 + Q_2)t_{peak1} - LS_f \pi R^2\right]}{Q_2} \quad \text{(Eq. 2-24)}$$

$$V_2 = Q_2 t_{peak2} + Q_1 t_{peak1} - LS_f \pi R^2 \quad \text{(Eq. 2-25)}$$

$$V_0 = \frac{(Q_1 + Q_2)\left(LS_f \pi R^2 - Q_1 t_{peak1}\right)}{Q_2} \quad \text{(Eq. 2-26)}$$

If the average diameters of the conduits can also be inferred from cave explorations, the lengths of the conduit can thus be obtained by:

$$l_{1e} = \frac{Q_1\left[(Q_1 + Q_2)t_{peak1} - LS_f \pi R^2\right]}{Q_2 \pi R^2} \quad \text{(Eq. 2-27)}$$

$$l_{2e} = \frac{Q_2 t_{peak2} + Q_1 t_{peak1} - LS_f \pi R^2}{\pi R^2} \quad \text{(Eq. 2-28)}$$

$$l_{0e} = l_e' + l_e'' = \frac{(Q_1 + Q_2)\left(LS_f \pi R^2 - Q_1 t_{peak1}\right)}{Q_2 \pi R^2} \quad \text{(Eq. 2-29)}$$

Appling this method, we calculate the conduit lengths of our first two groups of experiments according to the BTCs we obtained. Because the 10-20-30-30 experiment BTC has only one peak, the method is not applicable. The calculation process and results are shown in Table 2.7.

Table 2.7. True and estimated values of conduit properties for various dual-conduit systems

Experiment name	10-20-30-30	10-40-30-30	10-60-30-30	10-120-30-30	20-120-30-30	60-360-30-30
True V_1/ (cm^3)	1.27	1.27	1.27	1.27	2.53	7.55
True V_2/ (cm^3)	2.53	5.04	7.55	15.09	15.09	45.25
True l_1/ (cm)	10	10	10	10	20	60
True l_2/ (cm)	20	40	60	120	120	360
Estimated V_1/ (cm^3)	N.A.	1.28	1.32	1.36	2.47	7.73
Estimated V_2/ (cm^3)	N.A.	5.25	7.24	17.04	16.16	49.63
Estimated l_1/ (cm)	N.A.	10.16	10.52	10.86	19.68	61.55
Estimated l_2/ (cm)	N.A.	41.80	57.64	135.63	128.62	394.93

CHAPTER 3

Résumé : Ce chapitre poursuit l'investigation expérimentale du chapitre précédent. Nous étudions plus avant le processus de transport de soluté dans les structures à double conduit. 11 structures à double conduit à l'échelle du laboratoire ont été construites en faisant varier les ouvertures des deux conduits. Différent du chapitre précédent, ce chapitre étudie l'influence de deux autres facteurs : le débit et la largeur d'ouverture des deux conduits. Lorsque le conduit le plus court a une plus grande ouverture que le conduit le plus long, la structure à double conduit présente des courbes de percée à deux pics ou des courbes de percée à un seul pic avec une bosse sur le membre descendant. Lorsque le conduit le plus court a une ouverture plus petite que le conduit le plus long, les structures à double conduit conduisent à des courbes de percée à pic unique ou à des courbes de percée à double pic dont le pic initial est plus bas que le pic final. Lorsque le débit augmente, les structures à double conduit sont plus susceptibles de présenter des courbes de restitution à double pic. Nous avons appliqué deux modèles numériques pour ajuster les courbes de restitution expérimentales : le modèle WSADE et le DRMIM, ce dernier modèle ayant présenté les meilleures performances.

Chapter 3 Solute transport in dual conduit structure: effects of aperture and flow rate

Journal of Hydrology 613 (2022) 128315

Contents lists available at ScienceDirect

Journal of Hydrology

journal homepage: www.elsevier.com/locate/jhydrol

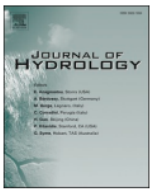

Research papers

Solute transport in dual conduit structure: Effects of aperture and flow rate

Chaoqi Wang [a], Samer Majdalani [a], Vincent Guinot [a,b], Hervé Jourde [a,*]

[a] HSM, Univ. Montpellier, IRD, CNRS, Montpellier, France
[b] Inria Lemon, Univ. Montpellier, Montpellier, France

https://doi.org/10.1016/j.jhydrol.2022.128315

Chapter 3 Solute transport in dual conduit structure: effects of aperture and flow rate.

Chaoqi Wang[1], Samer Majdalani[1], Vincent Guinot[1,2], Hervé Jourde[1]

1. HSM, Univ. Montpellier, IRD, CNRS, Montpellier, France

2. Inria Lemon, Univ. Montpellier, Montpellier, France

Highlights:

1. This study provides experiment material to enhance understanding of transport processes in dual-conduit structures.
2. For dual-conduit structures, the influence of aperture combination and flow rate are investigated.
3. Experimental BTCs were well simulated by the DRMIM transport model.

Abstract

A typical karst aquifer configuration is the multiple conduit structure. However, it remains to be investigated how the aperture distributions and the flow rate should influence the transport process in the multiple conduit structures.

To better understand the transport process in the multiple conduit structures, 11 lab-scale dual-conduit structures are manufactured by varying the apertures of the two conduits (h_1 and h_2 denote the aperture width of the shorter conduit and the longer conduit respectively). Solute transport experiments of three different flow rates are conducted on these structures. As the flow rate increases, the dual-conduit structures are more likely to present dual-peaked BTCs. The 11 structures make one exhaustive representation of the possible aperture combination of the dual-conduit structures and the transport experiments have been conducted by three flow rates (varying by 2 degrees of magnitude), so the experimental results constitute a detailed material that should improve the understanding of transport processes in such structures.

Two numerical models, Weighted Sum Advection–Dispersion Equation (WSADE) and Dual Region Mobile Immobile Model (DRMIM), are applied to fit the experimental BTCs in order to obtain some insight into the actual solute-transport processes by exploring the calibrated model parameters. Considering the possible effect of solute detention, we initially applied the DRMIM model. This DRMIM better replicated the experimental BTCs than the WSADE. This study suggests the karst community shall take the DRMIM as one candidate transport model for characterizing the dual-peaked BTCs obtained in karst aquifers.

3.1 Introduction

Artificial tracing is a useful tool for investigating karst aquifers (Goldscheider et al., 2008a). Injecting a known quantity of tracer at an upstream position, and monitoring the variations in the tracer concentration at a downstream location yields a BreakThrough Curve (BTC). BTCs can bring information on underground karst geometry (Wang et al., 2020; Zhao et al., 2021) and effective transport parameters (Goldscheider and Drew, 2007).

Laboratory experiments have been widely applied to investigate the flow and transport processes through complex karst aquifers. The major advantage of lab-scale experiments over field experiments is their flexibility, in that they allow for a flexible selection of sampling points, easy implementation of different hydraulic conditions, as well as detailed knowledge of the geometry of the studied media (Mohammadi et al., 2021).

According to Mohammadi et al. (2021), the common laboratory karst models can be categorized into three groups: rock block, pipe/fracture network, and pipe-matrix coupling model. For the rock block model, artificial fractures or conduits can be created on a rock block to make a physical model. The rock block model has supported various research works, including hydraulic tomography (Brauchler et al., 2003, 2013; Sharmeen et al., 2012), investigation of the flow process (Anaya et al., 2014; Cherubini et al., 2012; Develi

& Babadagli, 2015; DiFrenna et al., 2008; Leven et al., 2004), investigation of solute (Cherubini et al., 2012) and heat transport process (Cherubini et al., 2017; Pastore et al., 2015). Concerning the pipe/fracture network model, researchers have manufactured single-fracture models (Qian et al., 2007, 2011; Tzelepis et al., 2015), fracture networks (Hull et al., 1987; Karay & Hajnal, 2015) and conduit networks (Anger & Alexander, 2013; Field & Leij, 2012; Wu et al., 2019; Zhao et al., 2019, 2021). The experiments on these lab-scale models have revealed some fundamental mechanisms controlling the flow and transport process in karst media. For example, Qian et al. (2011) found that the solute transport process in a single fracture exhibit BTCs with heavy tailing; Field and Leij (2012) found that three karst geometries may exhibit multi-peaked BTCs: an auxiliary conduit is connected to the main conduit, waterfall, and pools. While the effect of matrix is not considered in the pipe/ fracture network models. Several studies have focused on the effect of the transport exchange between conduits and matrix. To this end, they have used pipe-matrix coupling models (Castro, 2017; Faulkner et al., 2009; Florea & Wicks, 2001; Gallegos et al., 2013; Li et al., 2008; Mohammadi et al., 2019; Xiao et al., 2018). For example, Li et al. (2008) have studied contaminant retention processes in the matrix of pipe-matrix coupling models; Mohammadi et al. (2019) built bench-scale karst models and investigated the influence of hydraulic gradient and cave pattern on tracing test BTCs.

The classical Advection-Dispersion-Equation (ADE) (Bear, 1988; Majdalani et al., 2015) model often fails to reproduce the BTCs of the tracing tests (Goldscheider et al., 2008b; Hauns et al., 2001; Massei et al., 2006; Moreno & Tsang, 1991; Perrin & Luetscher, 2008). The ADE is valid for the BTCs obtained in homogeneous porous media under some conditions (Berkowitz et al., 2006). However, all aquifers are heterogeneous to different degrees (Bakalowicz, 2005; Ghodrati & Jury, 1992; Levy & Berkowitz, 2003) and among them, fractured and karst aquifers are particularly heterogeneous (Bakalowicz, 2005). Heterogeneous media entail ‘anomalous’’ or ‘‘non-Fickian’’ transport behaviors, which may exhibit BTCs with early arrivals and late time tails or multi-peaked BTCs. These particularities cannot be well represented by the ADE model.

A variety of models accounting for anomalous transport have been developed. Mobile-Immobile Model (MIM) (van Genuchten & Wierenga, 1976) and Transient Storage Model (TSM) (Runkel, 1998) have a similar structure: one mobile region (the main channel) governed by ADE and one immobile (stagnant) region; the two regions exchange mass due to concentration difference. The TSM has been applied to reproduce BTCs from solute transport experiments in lab-scale karst models (Dewaide et al., 2016; Zhao et al., 2019, 2021). The multi-region ADE model (Majdalani et al., 2015, 2018) consists of two or more ADE regions flowing in parallel and these regions exchange mass due to concentration differences. These multi-region ADE models were successfully used to model lab-scale solute transport experiments (Field & Leij, 2012; Majdalani et al., 2015, 2018; Wang et al., 2020). The so-called Weighted-Sum ADE (WSADE) model (Field & Leij, 2012) also considers several parallel ADE regions while the mass exchange

between the regions is not considered. Dual-peaked BTCs can be reproduced by the two-region ADE model (Wang et al., 2020) or the WSADE model (Field & Leij, 2012).

The tracing BTCs can be influenced by different properties of karst aquifers. Via numerical simulation of solute transport process in a conceptual karst model of dual flow system (i.e. conduit and matrix), Peely et al. (2021) have studied the effect of six properties on the BTCs, including (i) tracing distance and karst tortuosity, (ii) hydraulic gradient, (iii) matrix hydraulic conductivity, (iv) exchange flow, (v) conduit diameter and (vi) conduit roughness height. For example, increasing tracing distance causes the peak concentration (C_p) to decrease and the peak time (T_p) to become longer; increasing tortuosity also causes C_p to decrease and T_p to lengthen. For another example, increasing the exchange coefficient (the degree of hydraulic connection between the conduit and the host matrix) causes C_p to increase and T_p to shorten. The diameter variation of a single conduit may cause BTCs with strong tailing (Hauns et al., 2001; Zhao et al., 2019, 2021). The different karst network patterns should influence the BTCs' shape (Mohammadi et al., 2019), and multi-peaked BTCs are frequently observed in karst aquifers. In a previous study (Wang et al., 2020), we carried out solute transport experiments on different dual-conduit karst configurations and investigated how the dual-peaked BTCs can be influenced by some properties of the dual-conduit structure. Specifically, increasing the length ratio causes the two peaks to be more separated; increasing the total length causes the two peaks to be more separated and the concentration value of both peaks to be lower; the connection angles between the divergence conduits and the convergence conduit also influence the BTCs**.**

However, the study presented by Wang et al. (2020) has two main limitations. First, we assumed an ideal situation for all the structures: the two conduits have the same diameter. Since the objective of (Wang et al., 2020) is to study the effect of length and connection angle of the conduits, this ideal situation does not harm the previous experimental conclusions. According to the field observations, the different conduits usually bear different diameters. It is unclear how the different conduit diameter combinations may influence the transport process. Thus, it is important to study the structures that have different conduit diameter combinations in order to better understand the transport process in such dual-conduit structures. Second, the previous transport experiments have been conducted under a constant flow rate, while in natural karst aquifers flow rate is not constant. It is also unclear how the flow rate may influence the transport process.

The objective of this paper is to answer two research questions that arose from the one-dimensional experiments reported in Wang et al. (2020), namely the influence of conduits aperture and flow rate on the transport process in dual-conduit structures. 11 bench-scale physical configurations with different aperture combinations are built. Solute transport experiments are conducted under three different flow rates. Then, two transport models are applied in this study: the Weighted Sum Advection–Dispersion Equation (WSADE) model and the Dual-Region Mobile-Immobile model (DRMIM). We use both models to fit the

observed BTCs and check how the different transport processes may influence the calibrated model parameters. Along with Wang et al. (2020), the purpose of the present paper is to enrich and complement the available experimental and modeling material on the transport process in dual-conduit structures.

3.2 Experimental setup

3.2.1 Dual-conduit structures

The dual-conduit experimental models are made of transparent PVC boards assembled in three layers. The top and bottom layers (Figure 3.1a-c) are the same: a single PVC board (150 × 25 × 2 cm). The middle layer (Figure 3.1a-c) includes five boards of various sizes with a thickness of 0.5 cm. The three layers are assembled (Figure 3.1d) with transparent silicone. The void in the middle layer serves as the space for fluid flow in this physical model.

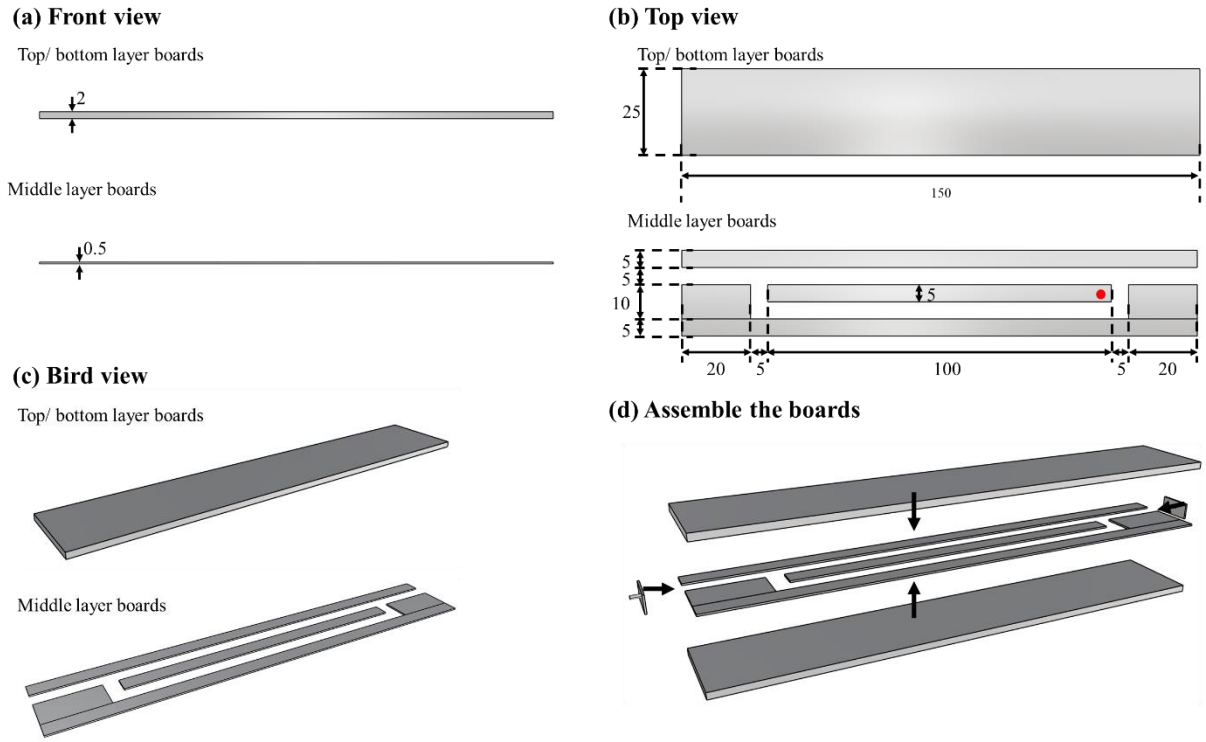

Figure 3.1 Geometry of dual-conduit structure (All lengths in cm).

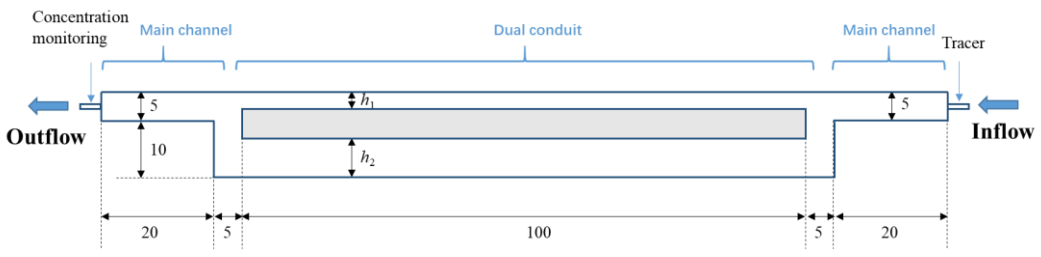

Figure 3.2 Void in the physical model (All lengths in cm).

We make 11 different physical configurations by varying the position of the central board in the middle layer (marked by the red point in Figure 3.2b). We denote the apertures of the two conduits as h_1 and h_2 (Figure 3.2). Apertures h_1 and h_2 are varied by ± 1 cm such that $h_1 + h_2 = 10$ cm for all configurations (Table

3.1). We label the configurations as "h_1-h_2". For the central board in the middle layer, the spacing from the longitudinal axis is denoted as M ($M = h_2 - 5$ cm $= 5$ cm $- h_1$). According to the geometry of the physical models, we calculate the volume of the void inside the physical models, V_m. Since the equation of (h_1+ h_1=10 cm) remains valid, the 11 models have a same volume, $V_m = 675$ cm^3.

Table 3.1 Aperture setting of physical models.

Configurations	Label	h_1 (cm)	h_2 (cm)	M (cm)
1	5-5	5	5	0
2	4-6	4	6	1
3	3-7	3	7	2
4	2-8	2	8	3
5	1-9	1	9	4
6	0-10	0	10	5
7	6-4	6	4	-1
8	7-3	7	3	-2
9	8-2	8	2	-3
10	9-1	9	1	-4
11	10-0	10	0	-5

3.2.2 Step tracing experiments

The experimental setup of solute tracing experiments is shown in Figure 3.3. The physical model is placed on a horizontal platform to eliminate the density effect. The physical model is first filled with deionized water. The inlet is connected to a solution tank (deionized water + NaCl, concentration $C_0 = 0.06$ mol/l). A peristaltic pump (Lead Fluid^{TM}) supplies the flow rate, Q (L^3/s). At the outlet, a sensor (WTW TetraCon 325^{TM} conductimeter, accuracy is 1×10^{-6} mol/L) is used to measure the tracer concentration and infer the BTC. The balance (Mettler Toledo^{TM}) measurements permit the calculation of the flow rate. Sensor and balance are connected to a data logger (Campbell CR1000^{TM}) for automatic data sampling.

A step tracing test is conducted under a given flow rate until the concentration at the outlet reaches C_0. To reduce measurement error, each experiment is replicated three times. The final data is obtained as the average of the three experimental BTCs, denoted as $C(t)$. The derivative of $C(t)$ to t, denoted as $C_{der}(t)$, is used in model benchmarking because they allow for better model discrimination than the original step signal (Majdalani et al., 2018).

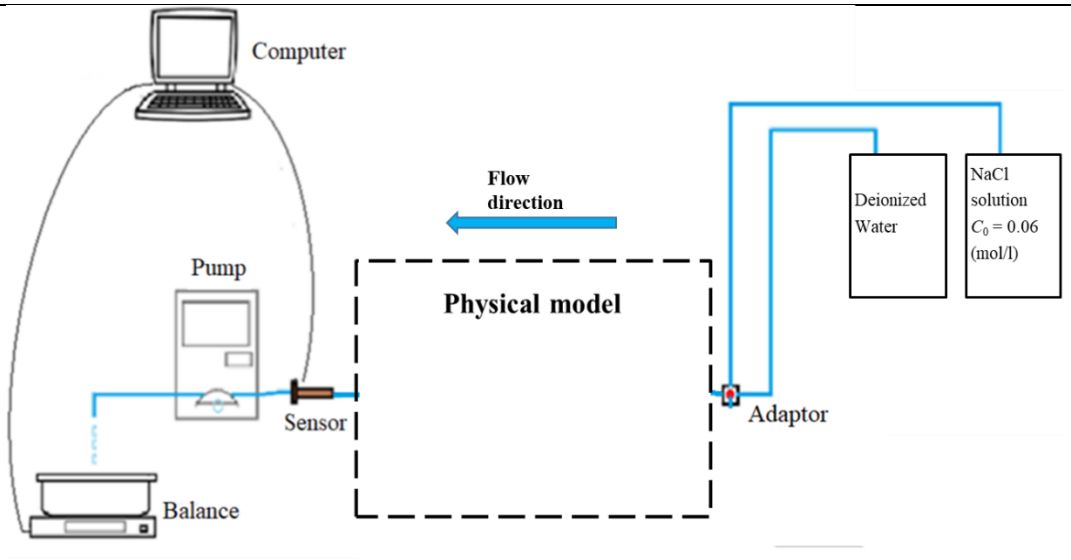

Figure 3.3. Tracing experiments setup.

Three different flow rates, spanning two orders of magnitudes, are used. We check the flow regime of the experiments by calculating the Reynolds number:

$$\mathrm{Re} = \frac{\rho u D_\mathrm{H}}{\mu} = 4\frac{\rho u A}{\mu P} = 4\frac{\rho Q}{\mu P}, \qquad \text{(Eq. 3-1)}$$

where A (L^2) is the cross-section area, D_H (L) is the hydraulic diameter of the pipe, P (L) is the wetted perimeter, Q (L^3T^{-1}) is the flow rate, u (LT^{-1}) is the average flow velocity, μ ($ML^{-1}T^{-1}$) is the fluid dynamic viscosity and ρ (ML^{-3}) is the fluid density. For the three flow rates, the Re values in the main channel part (Figure 3.2) are given in Table 3.2.

Table 3.2. Experimental flow rates and Reynolds number.

Pumping speed (rpm)	Q (L/s)	Velocity in the main channel (cm/s)	Re (main channel) (-)	Data sampling interval (s)
200	6.62×10^{-3}	2.6	241	1
20	6.84×10^{-4}	0.27	24	1
2	6.69×10^{-5}	0.027	2	5

According to the Reynolds numbers in Table 3.2, the flow regime is laminar (Re < 2000) in the present experiments. We are clear that the turbulent flow regime is more generally observed in natural karst conduits. Some researchers noted that Re varies between 6500 and 80000 in karst (Morales et al., 2010; Duran et al., 2016). In practice, it would be difficult to achieve a turbulent flow regime owing to the experimental dimensions and the availability of deionized water. The lab-scale tracing experiments under the laminar flow regime can also provide insights into the solute transport process in natural karst systems (Wang et al., 2020).

3.3 Numerical modeling

3.3.1 Transport models

a) Weighted Sum Advection–Dispersion Equation (WSADE) model with two regions

We consider applying the two-region WSADE model because the physical structures have two flow conduits. The definition sketch of the two-region WSADE is shown in Figure 3.4, two regions are assumed to flow in parallel without any exchange; in both regions, the ADE model is assumed valid:

$$\frac{\partial C_i}{\partial t} + u_i \frac{\partial C_i}{\partial x} - D_i \frac{\partial^2 C_i}{\partial x^2} = 0, (i = 1, 2) \quad \text{(Eq. 3-2a)}$$

$$w_1 + w_2 = 1. \quad \text{(Eq. 3-2b)}$$

The total concentration at the outlet is the superposition of the two ADE-based regions:

$$C = \frac{w_1 u_1 C_1 + w_2 u_2 C_2}{w_1 u_1 + w_2 u_2}, \quad \text{(Eq. 3-3)}$$

where C_i is the outlet concentration (ML^{-3}) of Region i; D_i is the dispersion coefficient (L^2T^{-1}); L is model length (according to the physical model geometry, L=1.5m); t is time (T); u_i is the flow velocity (LT^{-1}); x is the space coordinate (L); w_i is the volume fraction of Region i (–). Owing to Eq. 3-2b, only one of the two fractions (w_1, w_2) has one degree of freedom. Five parameters (u_1, u_2, D_1, D_2, and w_1) are calibrated to fit the experimental BTCs. To reduce the size of the parameter space, Regions 1 and 2 are distinguished by imposing $u_1 > u_2$ by definition.

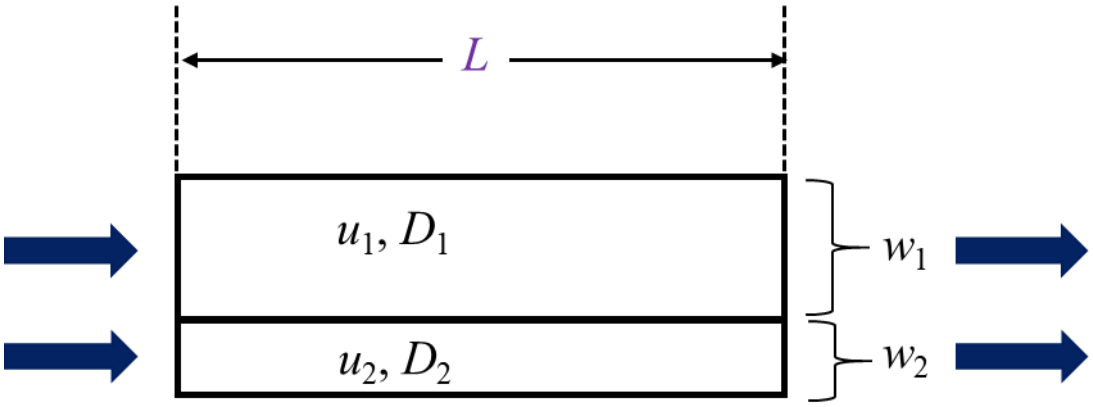

Figure 3.4. Definition sketch of WSADE model.

b) Dual Region Mobile ImMobile (DRMIM) model

The Dual Region Mobile ImMobile (DRMIM) model is based on the Mobile ImMobile (MIM) model (van Genuchten and Wierenga, 1976). The MIM consists of a mobile region governed by the conventional ADE and an immobile region; the two regions are coupled by an exchange term. For the DRMIM model, the total concentration at the outlet is the superposition of two regions of MIM (Figure 3.5). The governing equations of DRMIM are given as:

$$w_{\mathrm{m},i} \frac{\partial C_{\mathrm{m},i}}{\partial t} + w_{\mathrm{im},i} \frac{\partial C_{\mathrm{im},i}}{\partial t} = w_{\mathrm{m},i} D_i \frac{\partial^2 C_{\mathrm{m},i}}{\partial x^2} - w_{\mathrm{m},i} u_{\mathrm{m},i} \frac{\partial C_{\mathrm{m},i}}{\partial x}, (i = 1, 2) \quad \text{(Eq. 3-4a)}$$

$$w_{\mathrm{im},i} \frac{\partial C_{\mathrm{im},i}}{\partial t} = k_i (C_{\mathrm{m},i} - C_{\mathrm{im},i}) \ , (i = 1, 2) \quad \text{(Eq. 3-4b)}$$

$$w_{\mathrm{im},i} + w_{\mathrm{m},i} = w_{\mathrm{MIM},i}, (i = 1, 2) \quad \text{(Eq. 3-4c)}$$

$$w_{\mathrm{MIM1}} + w_{\mathrm{MIM2}} = 1. \quad \text{(Eq. 3-4d)}$$

The total concentration at the outlet is the superposition of the two mobile regions:

$$C = \frac{w_{m1}u_{m1}C_{m1}+w_{m2}u_{m2}C_{m2}}{w_{m1}u_1+w_{m2}u_2}, \quad \text{(Eq. 3-5)}$$

where C_{m1} and C_{m2} are the concentration (ML^{-3}) of the two mobile regions; C_{im1} and C_{im2} are the concentration (ML^{-3}) of the two immobile regions; D_{m1} and D_{m2} (L^2T^{-1}) are the dispersion coefficients in the two MIM regions; k_1 and k_2 (T^{-1}) are the mass transfer coefficients; u_{m1} and u_{m2} (LT^{-1}) are the flow velocities; w_{m1} (-) and w_{m2} (-) are the volume fractions of the mobile regions; w_{im1} (-) and w_{im2} (-) are the volume fractions of the immobile regions; w_{MIM1} and w_{MIM2} are the volumetric fractions of the two MIM regions. Owing to Eq. 3-4c and d, the four fractions ($w_{m1}, w_{m2}, w_{im1}, w_{im2}$) have three degrees of freedom. In practice, nine independent parameters are calibrated to fit the experimental BTCs: u_{m1}, D_{m1}, k_1, w_{m1}, u_{m2}, D_{m2}, k_2, w_{m2}, w_{MIM1}. We restrict that the flow velocity in Region 1 is larger than Region 2 (i.e., $u_{m1} > u_{m2}$). The DRMIM model has more parameters thus more flexibility than the WSADE model, then the DRMIM should be able to better reproduce some BTCs than the WSADE.

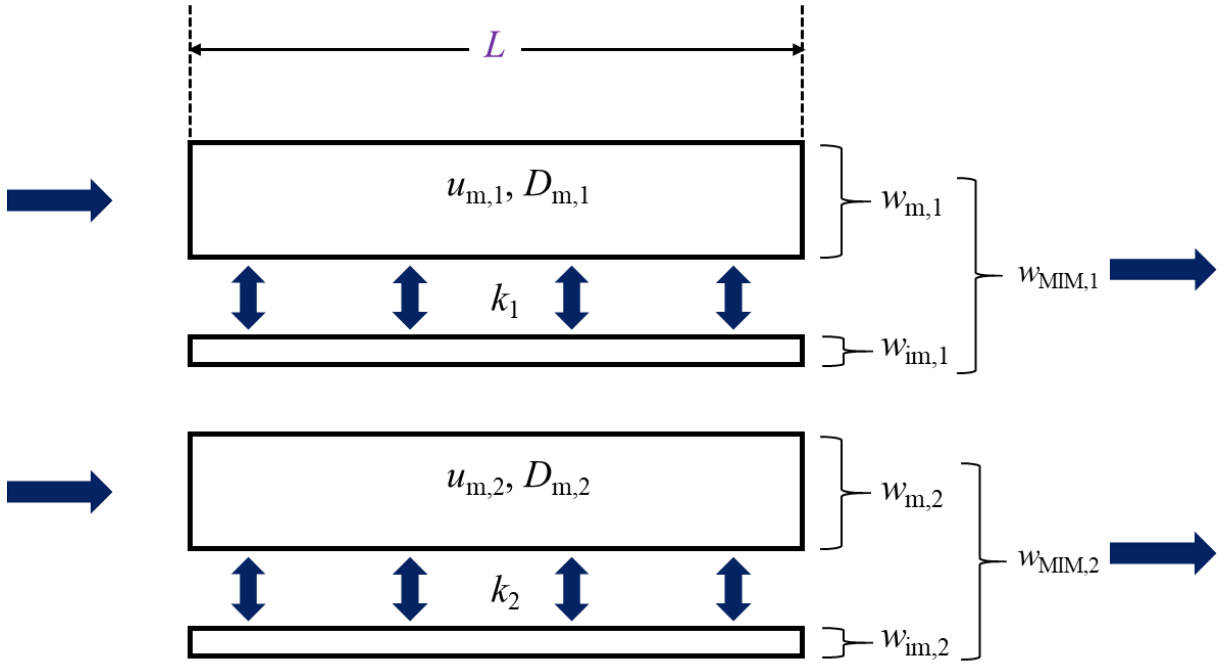

Figure 3.5. Definition sketch of DRMIM model.

3.3.2 Parameter calibration technique.

The model parameters are calibrated with the Markov Chain Monte Carlo (MCMC) method (Haario et al., 2006). The MCMC method is a Bayesian approach that evaluates the posterior distributions of parameters (Vrugt et al., 2006). To achieve a fast convergence of the chain, we first perform a manual fitting of the model response to the experimental BTCs to find the initial parameter set. Then the Metropolis-Hastings algorithm (Robert, 2015) successively draws samples from the posterior distribution by forming a Markov chain of the model parameter set. In this work, we assume the posterior probability density is of a Gaussian type. For each chain, 10000 iterations are executed. The mean value of the last 50 sampled parameter sets is determined as the calibrated parameter value. The Root-Mean-Square-Error (RMSE) objective function is applied to evaluate the deviation and the convergence of the MCMC chains:

$$\mathrm{RMSE} = \sqrt{\frac{\sum_{i=1}^{n}(X_i - Y_i)^2}{n}}. \quad \text{(Eq. 3-6)}$$

where X is the experimental data, n is the data quantity, Y is the simulated data.

3.4 Results

3.4.1 Experiment results

To better exhibit the experiment results, we transform the experiment BTCs in two ways. The first transformation is as follows:

$$\mathrm{PV} = \frac{tQ}{V_\mathrm{m}}, \quad \text{(Eq. 3-7a)}$$

$$C_\mathrm{N}(t) = \frac{C_\mathrm{der}(t)}{\int_0^{+\infty} C_\mathrm{der}(t)\ \mathrm{PV}(t)\ \mathrm{d}t} \quad \text{(Eq. 3-7b)}$$

where C_N is the normalized concentration (–); PV represents injected pore volume fraction (–); V_m is the volume of the physical model (L^3). After the normalization, the area underneath the curve of C_N-PV is 1 (unitless). This transformation makes it convenient for us to compare the experiment BTCs of different flow rates.

The second way is to transform the BTCs into residence time distribution (RTD) curves:

$$\mathrm{RTD}(t) = \frac{C_\mathrm{der}(t)q(t)}{\int_0^{+\infty} C_\mathrm{der}(t)q(t)\mathrm{d}t}. \quad \text{(Eq. 3-8)}$$

The area under the curve of RTD-t is 1 (unitless), thus this transformation makes it convenient for us to reproduce the experiment BTCs with the numerical models. In this study, if we need to exhibit the experiment results of different flow rates, the curves will be transformed into C_N-PV; if we need to exhibit the experiment results of the same flow rate or we need to model the experiments, the curves will be transformed into RTD-t.

3.4.1.1 Effect of flow rate

Figure 3.6 shows the experimental C_N-PV curves for the three flow rates.

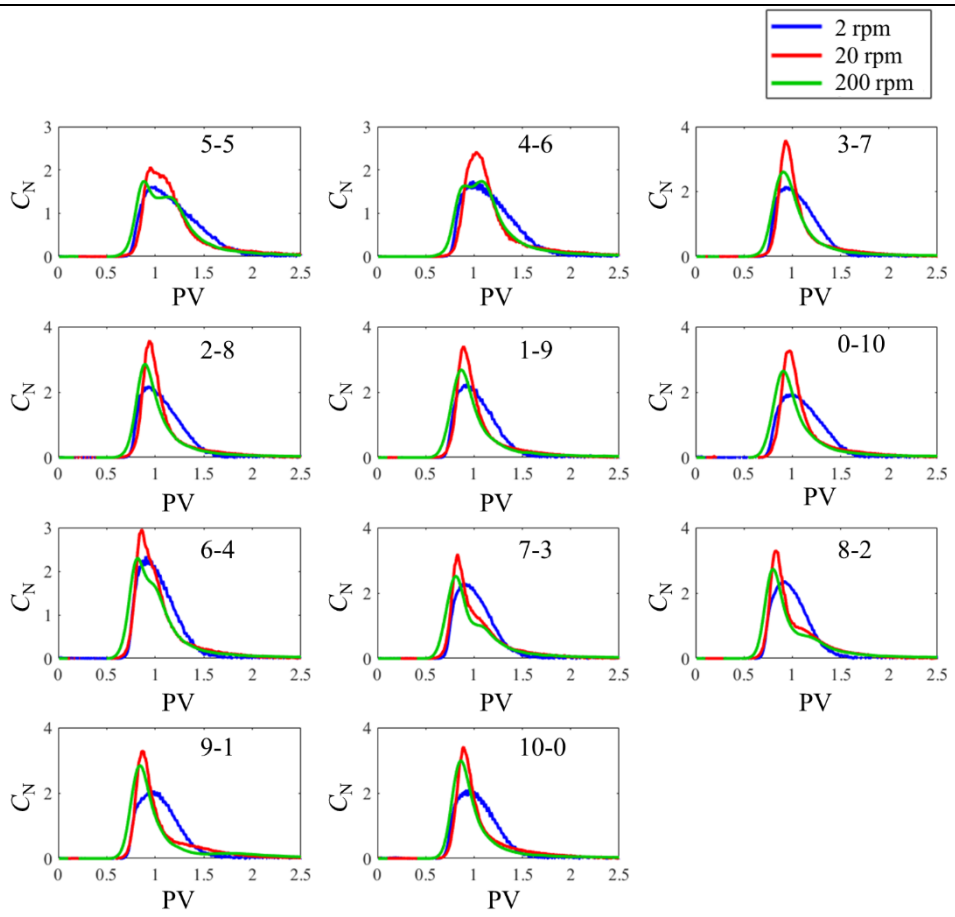

Figure 3.6. Experimental C_N-PV curves (Three flow rates).

For the lowest flow rate of 2 rpm, the curves have the lowest peak value when compared to the other two flow rates. The falling limbs of the 2-rpm curves are less curved than the 20-rpm and 200-rpm curves. The 20-rpm curves have the largest peak value and sharpest peak. All of the 20 rpm curves are still single-peaked, while there is a bump on the falling limb of the 8-2 curve, which indicates the existence of two separate tracer plumes.

The 200-rpm curves have a medium peak value. Under this flow rate, there are three types of curves: 1) some curves show obvious dual peaks (5-5, 4-6, 9-1); 2) other curves have one peak while there is an obvious bump on the falling limb (6-4, 7-3, 8-2), these BTCs are similar to the dual-peaked BTCs, but he two peaks are so close that they superpose; 3) some configurations exhibit curves with only one peak (3-7, 2-8, 1-9, 0-10, 10-0). The falling limbs of the 200 rpm curves are curved in the same way as the 20-rpm curves. When compared to 2-rpm and 20-rpm, more curves under 200-rpm exhibit dual-peaked curves.

3.4.1.2 Effect of aperture

These 200-rpm curves should better illustrate the effect of the aperture variation because the contrast among the curves of different configurations is more significant than the other two flow rates (2 and 20 rpm). We divide the 11 BTCs into two groups for plotting: for Group 1, $h_1 \leq h_2$ ($M \geqslant 0$ cm, Figure 3.7a); for Group 2, $h_1 \geq h_2$ ($M \leqslant 0$ cm, Figure 3.7b).

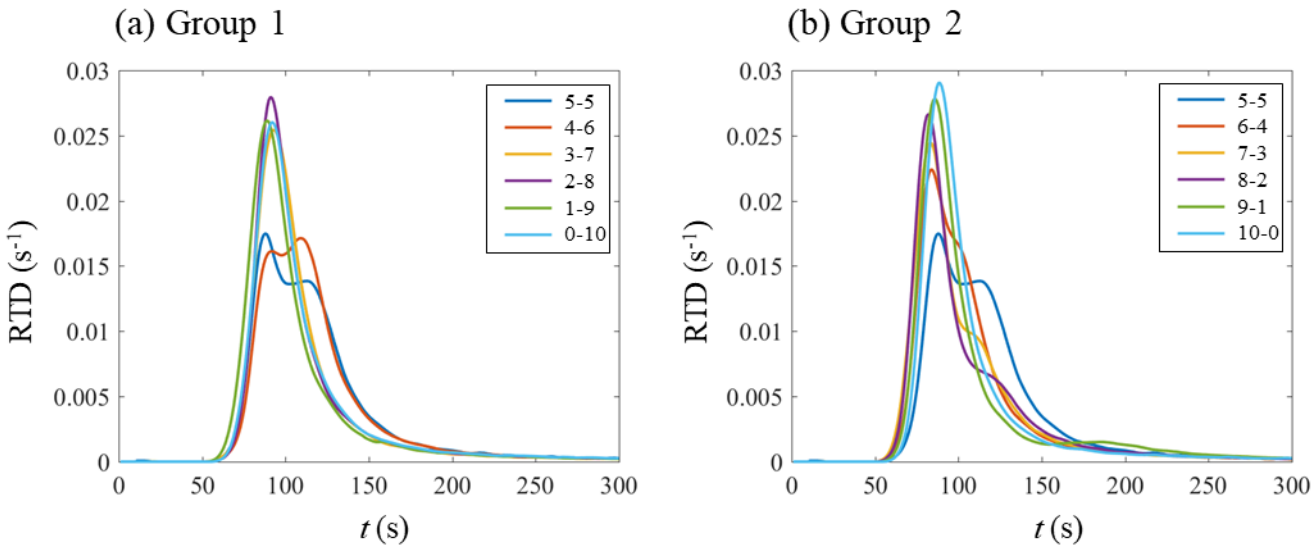

Figure 3.7. Experiment BTCs of highest flow rate (200 rpm).

In Figure 3.7a, Configurations 5-5 and 4-6 yield BTCs with two peaks. For 5-5, the early peak is larger than the later peak. The dual-peaked BTC of 4-6 is special: the early peak is smaller than the later peak. This is rather unusual in that dual-peaked BTCs are known to mostly exhibit a larger early peak than the late peak (Florea and Wicks, 2001; Field and Leij, 2012; Mohammadi et al., 2019; Wang et al., 2020). The remaining configurations (3-7, 2-8, 1-9, 0-10) exhibit single-peaked BTCs with tailing. Those BTCs are similar to one another.

For the transport process in the dual-conduit structures, the tracer diverges into two tracer plumes in the dual-conduit structures. If the contrast between the arrival time of the two tracer plumes is large, dual-peaked BTCs are obtained, as in Configurations 5-5 and 4-6. If the two arrival times are close to each other, the two peaks merge into a single one, as in Configurations 3-7, 2-8, 1-9, and 0-10.

In Figure 3.7b, the BTCs of Configurations 6-4, 7-3, 8-2 exhibit a single peak, but a bump is visible within the falling limb. These BTCs seem to be in the middle state between the dual-peaked and single-peaked BTCs. As the configuration changes from 5-5 to 8-2, the BTCs peak (the early plume) occurs increasingly earlier; as the configuration changes from 8-2 to 10-0, the BTCs peak occurs increasingly later. As the configuration changes from 6-4 to 10-0, the late plume (bump or the second peak) occurs increasingly delayed. If we roughly estimate the quantity of two tracer plumes by the concentration value of the peaks or the bumps, from 6-4 to 10-0, the quantity of the early tracer plume increases and the late tracer plume decreases.

Comparing Group 1 to Group 2, we find that Configurations 4-6 and 6-4 exhibit very different BTCs: for 4-6, the early peak is smaller than the late peak; for 6-4, there is a bump on the falling limb. Similarly, Configuration 3-7 exhibits different results from 7-3, etc. The difference between the two groups suggests that both conduit lengths and apertures influence the transport process.

In this study, the double peaks overlap to a large extent (5-5, 4-6). In contrast with dual-peaked BTCs

reported by (Field and Leij, 2012; Wang et al., 2020), the present experiments exhibit only a slight separation between the two peaks. This is because the length ratio of the two conduits is small (170/150 ≈ 1.13) for our dual-conduit structures. As discussed in (Wang et al., 2020), the lower length ratio makes the two peaks get closer to each other. Thus in all of the experiment configurations, the arrival time of the two tracer plumes are very close.

3.4.1.3 Effective transport volume

We calculate the effective transport volume (V_e) for all of the experiments (11 configurations × 3 flow rates):

$$V_e = \frac{\left(T - \int_0^T C(t)\,dt\right)}{C_0} Q, \qquad \text{(Eq. 3-9)}$$

where T denotes the total experiment duration of the step tracing experiments (T). The results are shown in Table 3.3. And the values of V_e are compared to the value of the physical model (V_m = 675 cm^3).

Table 3.3. Effective transport volume (V_e) of the experiments, unit: cm^3.

M (cm)	Configurations	Flow rate (rpm)		
		2	20	200
0	5-5	813.83	815.16	807.67
1	4-6	797.56	806.63	788.83
2	3-7	722.64	730.76	713.64
3	2-8	728.21	731.64	725.51
4	1-9	699.37	705.59	700.21
5	0-10	742.87	754.83	742.29
-1	6-4	696.24	702.95	697.94
-2	7-3	687.07	692.15	682.86
-3	8-2	672.01	692.63	689.27
-4	9-1	712.06	728.90	718.96
-5	10-0	699.27	719.07	693.27

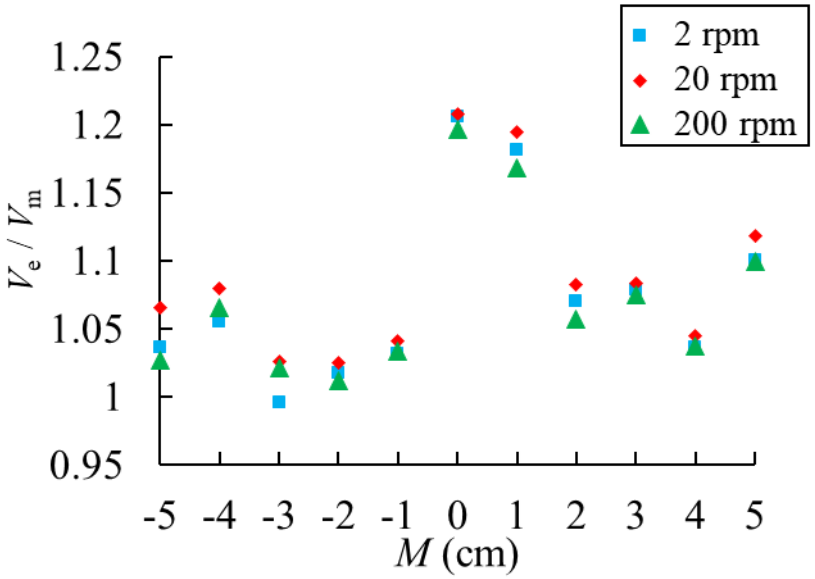

Figure 3.8. Comparison between effective transport volume (V_e) and physical model (V_m).

The values of (V_e / V_m) are shown in Figure 3.8. Most (V_e/V_m) values are larger than 1 (except for 8-2, 2 rpm), which indicates the existence of dead (i.e. stagnant) zones, which causes the solute detention effect.

One part of the solute travels via the main flow path of the structure in a relatively shorter period; the other part of the solute gets trapped in dead zones temporarily and gets released back to the main flow path in a relatively long period. Solute detention in dead zones usually induces BTCs with tailing (Hauns et al., 2001; Zhao et al., 2021).

The tracing experiments of different flow rates can generate similar values of V_e. By contrast, the aperture configuration generates a more significant influence on the values of V_e. Configurations 5-5 and 4-6 (M = 0 and 1 cm) exhibit the largest V_e values: the (V_e/V_m) values for these experiments are above 1.15, suggesting more significant effects of solute detention on the transport process.

3.4.2 Modeling results

In this section, we present the modeling results of the 200-rpm curves, and investigate how the aperture setup may influence the model parameters. The modeling results of the 2-rpm curves and the 20-rpm curves can be found in Appendix A.

3.4.2.1 WSADE

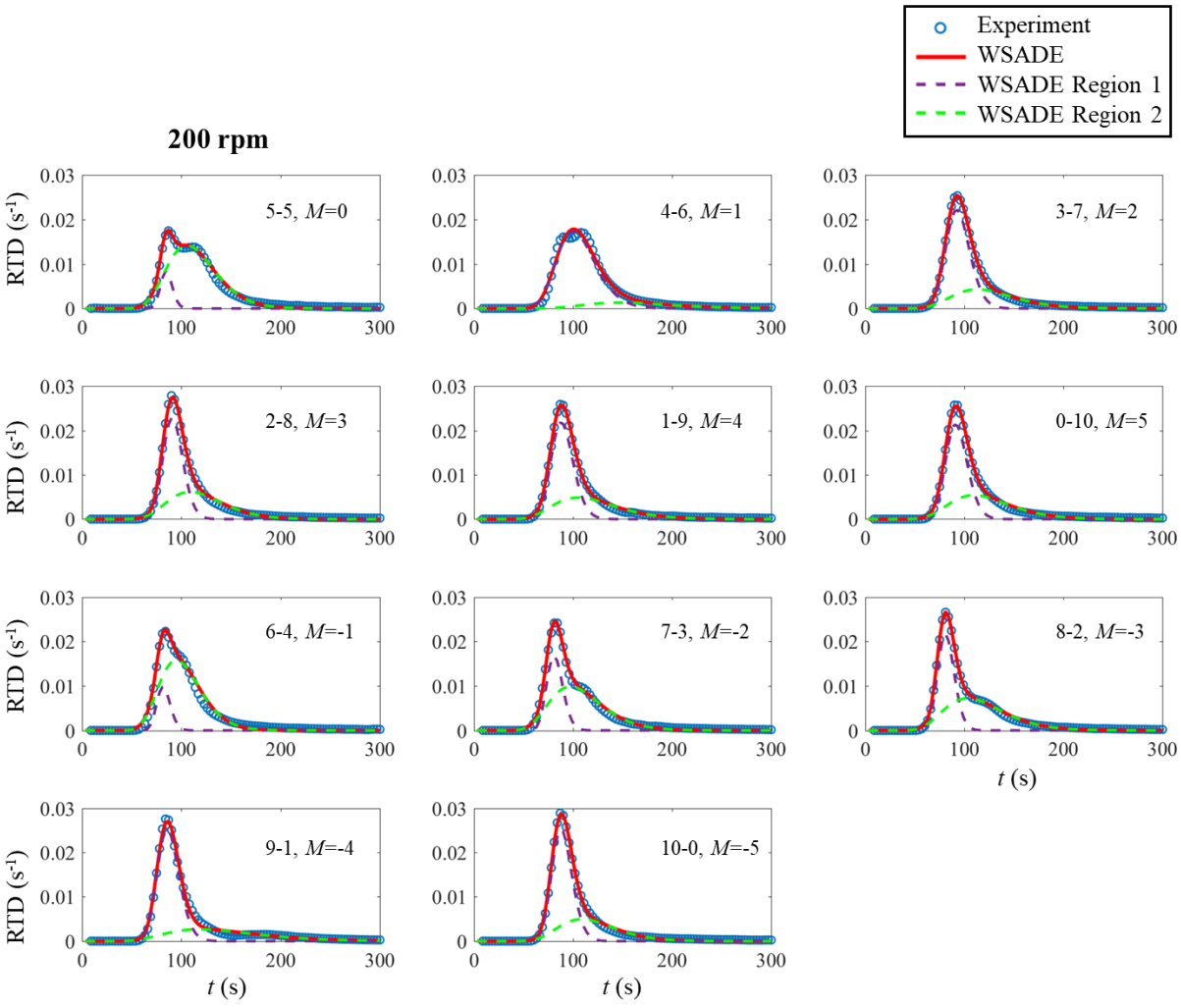

Figure 3.9. WSADE model fitting 200 rpm experimental BTCs.

The WSADE model can reproduce most of the BTCs (Figure 3.9). The RMSE values range between

2.59×10^{-4} and 6.36×10^{-4} m^2/s (Table 3.4). For Configuration 5-5, the dual-peaked BTC is well reproduced (RMSE = 4.87×10^{-4}): Region 1 accounts for the first peak of the BTC, Region 2 accounts for the second one. For Configuration 4-6, WSADE exhibits a degraded fitting performance (RMSE = 5.69×10^{-4}), the WSADE model fails to reproduce the double peak behavior. For Configurations 3-7, 2-8, 1-9, 0-10, and 10-0, the WSADE well reproduces the single-peaked BTCs (RMSE ranges between 2.59×10^{-4} and 3.96×10^{-4}). For Configurations 6-4, 7-3, and 8-2, the fitting performances are also good (RMSE ranges between 2.81×10^{-4} and 6.36×10^{-4}): Region 1 accounts for the first peak, and Region 2 accounts for the bump on the falling limb. For Configuration 9-1, the fitting performance is degraded, because the second peak is not well reproduced (RMSE = 4.70×10^{-4}).

Table 3.4. Calibrated parameters of WSADE to 200 rpm experiments

Pump Speed (rpm)	h_1-h_2 (cm)	M (cm)	u_1 (m/s)	u_2 (m/s)	D_1 (m^2/s)	D_2 (m^2/s)	w_1 (-)	RMSE
200	5-5	0	1.77×10^{-2}	1.38×10^{-2}	6.34×10^{-5}	5.47×10^{-4}	0.099	4.87×10^{-4}
	4-6	1	1.47×10^{-2}	9.71×10^{-3}	4.13×10^{-4}	6.16×10^{-4}	0.793	5.69×10^{-4}
	3-7	2	1.61×10^{-2}	1.28×10^{-2}	2.00×10^{-4}	7.04×10^{-4}	0.609	2.59×10^{-4}
	2-8	3	1.64×10^{-2}	1.34×10^{-2}	1.45×10^{-4}	6.34×10^{-4}	0.515	3.96×10^{-4}
	1-9	4	1.69×10^{-2}	1.36×10^{-2}	2.00×10^{-4}	8.94×10^{-4}	0.556	2.97×10^{-4}
	0-10	5	1.64×10^{-2}	1.32×10^{-2}	1.71×10^{-4}	7.47×10^{-4}	0.527	3.37×10^{-4}
	6-4	-1	1.83×10^{-2}	1.54×10^{-2}	9.48×10^{-5}	5.48×10^{-4}	0.144	6.36×10^{-4}
	7-3	-2	1.85×10^{-2}	1.49×10^{-2}	1.38×10^{-4}	7.92×10^{-4}	0.294	4.18×10^{-4}
	8-2	-3	1.85×10^{-2}	1.39×10^{-2}	1.46×10^{-4}	8.32×10^{-4}	0.385	2.81×10^{-4}
	9-1	-4	1.74×10^{-2}	1.17×10^{-2}	2.04×10^{-4}	1.22×10^{-3}	0.597	4.70×10^{-4}
	10-0	-5	1.70×10^{-2}	1.34×10^{-2}	1.69×10^{-4}	6.56×10^{-4}	0.590	3.72×10^{-4}

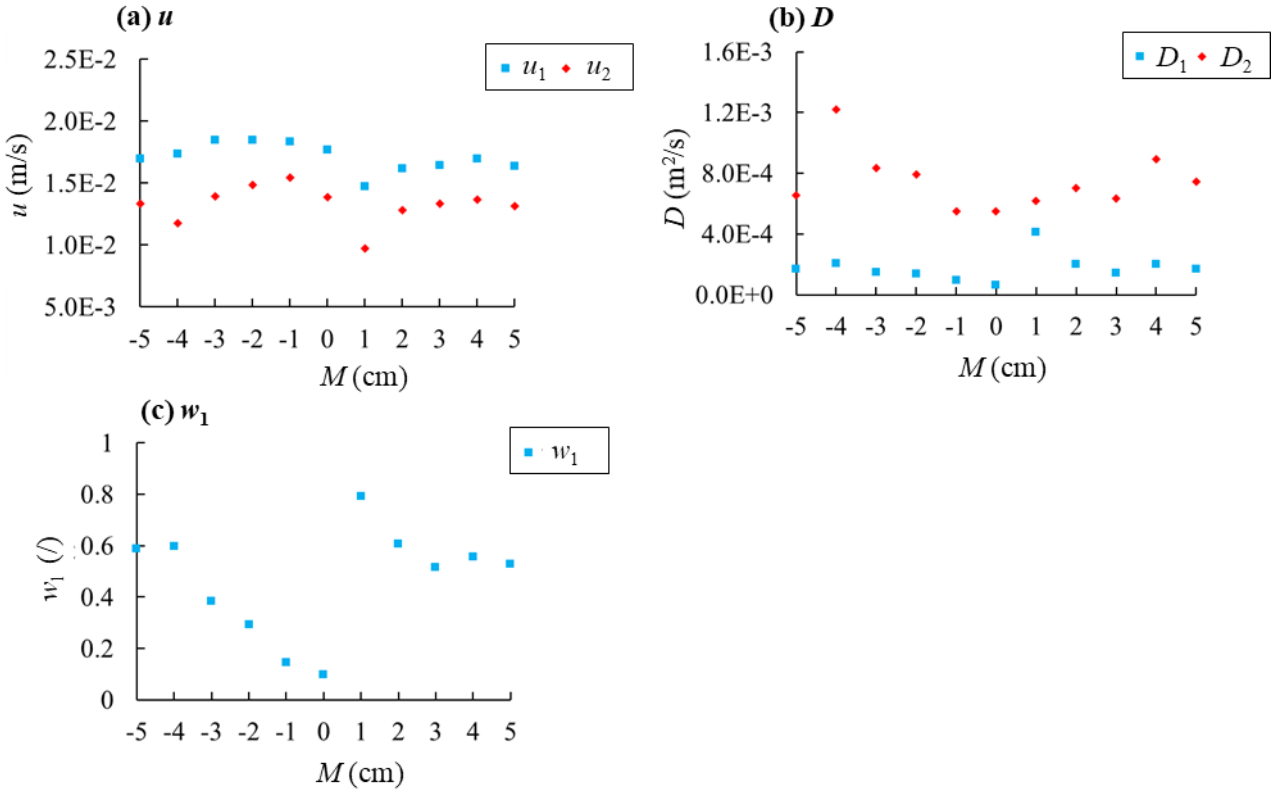

Figure 3.10. Calibrated parameters of WSADE for 200 rpm experiments.

We examine the calibrated WSADE parameters for the configurations with $M \geqslant 1$ cm, the velocity u_1 is larger than u_2, the dispersion D_1 is smaller than D_2, and the volume fraction w_1 is larger than 0.5. Configuration 4-6 (M = 1 cm) presents the smallest u_1 and the smallest u_2 among all configurations. The small values of u_1 and u_2 indicate that t_{peak1} and t_{peak2} (the peak time of WSADE Region 1 and Region 2, respectively) are larger than for the other configurations. Configuration 4-6 presents the largest D_1 (4.13×10^{-4} m^2/s) and the largest w_1 (0.793). This is because the WSADE Region 1 covers most of the BTC while Region 2 covers only a small part of the tail for 4-6 (Figure 3.9). From Configurations 3-7 to 0-10 (M = 2 to 5 cm), u_1 ranges between 1.61×10^{-2} and 1.69×10^{-2} m/s, u_2 ranges between 1.28×10^{-2} and 1.36×10^{-2} m/s; D_1 ranges between 1.45×10^{-4} and 2.00×10^{-4}, D_2 ranges between 6.34×10^{-4} to 8.94×10^{-4} m^2/s. w_1 shows decreasing trend on the whole: it decreases from 0.609 to 0.527.

Then, we introduce the calibrated WSADE parameters for the configurations with $M \leqslant 0$ cm. From Configuration 5-5 to 8-2 (M=0, -1, -2, -3), u_1 increases from 1.77×10^{-2} to 1.85×10^{-2}; from 8-2 to 10-0 (M=-3, -4, -5) u_1 decreases to 1.70×10^{-2}. From 5-5 to 6-4, u_2 increases from 1.38×10^{-2} to 1.54×10^{-2}; then from 6-4 to 9-1, u_2 decreases from 1.54×10^{-2} to 1.17×10^{-2}. The values u_1 and u_2 reflect how the two peaks vary in the horizontal direction in Figure 3.7b. From 5-5 to 9-1 (M=0 ~ -4), D_1 increases from 6.34×10^{-5} to 2.04×10^{-4} and D_2 increases from 5.47×10^{-4} to 1.22×10^{-3}; w_1 increases from 0.099 to 0.597. The increase of w_1 means the decrease of w_2. The variations in w_1 and w_2 reveal that the quantity of the early tracer plume increases and the late tracer plume decreases.

For all of the configurations, D_2 is always larger than D_1. Larger D_2 values are needed so that WSADE Region 2 can generate a wider peak to reproduce the later tail of the experimental BTCs.

3.4.2.2 DRMIM

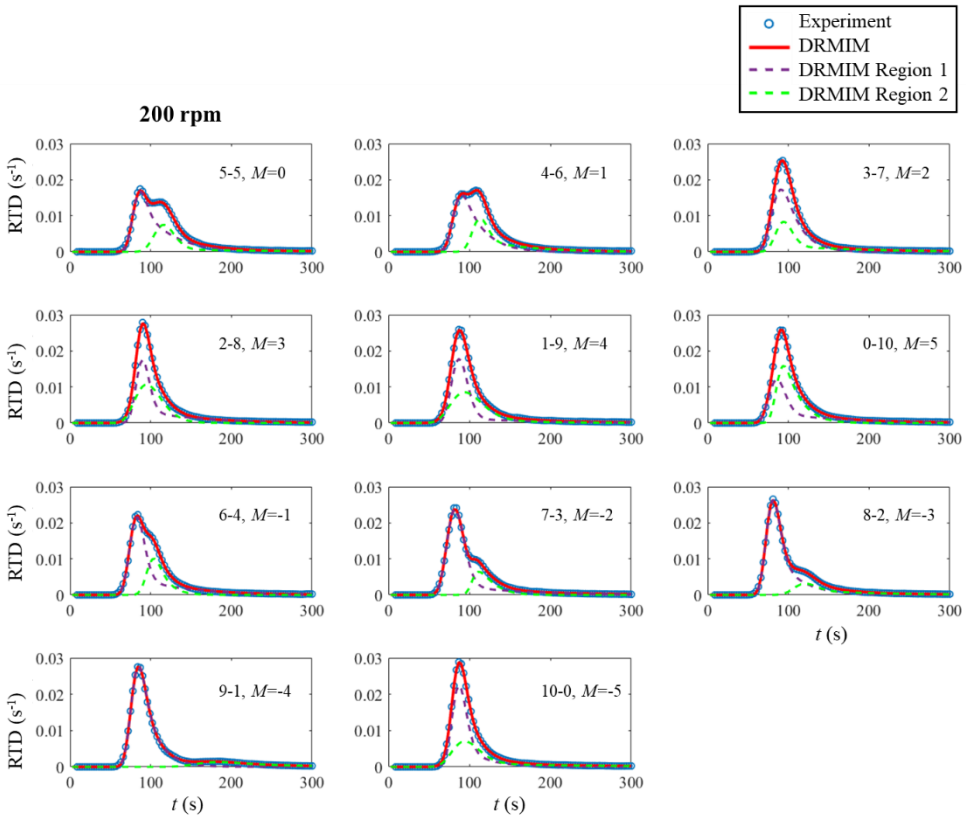

Figure 3.11. DRMIM model fitting 200 rpm experimental BTCs.

The DRMIM can well reproduce all of the BTCs (Figure 3.11), it can capture all of the features of the BTCs: the peaks, the bumps, and the tails. Visually, the DRMIM exhibits better characterization for the dual-peaked curves (5-5, 4-6, 9-1) and the bump-tail curves (6-4, 7-3, 8-2) than the WSADE (Figure 3.9). Quantitatively, the RMSE values of the DRMIM are much lower than the WSADE (Figure 3.12). As shown in Section 3.4.1.3, stagnant regions exist for the experimental transport processes. Thus, the DRMIM catches better the transport process in the dual-conduit structures.

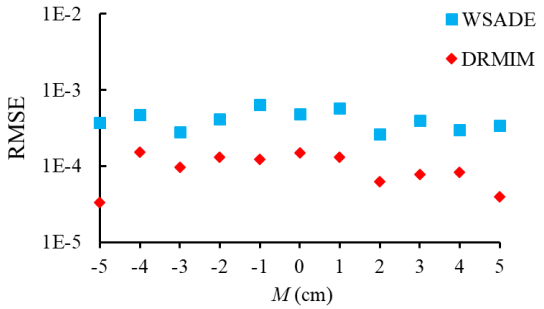

Figure 3.12. Comparison of the fitting performance of the two models.

The calibrated DRMIM parameters are presented in Table 3.5 and shown in Figure 3.13. As shown in Figure 3.13a, u_{m1} value has exhibited a relatively smaller variance than u_{m2}. For the single-peaked BTCs (M=2, 3, 4, 5, -5 cm), the contrasts between u_{m1} and u_{m2} are relatively smaller; for the dual-peaked BTCs

(M=0, 1, -4 cm) or the bump-tailed BTCs (M=-1, -2, -3 cm), the contrasts between u_{m1} and u_{m2} are relatively larger. As the Configuration changes from 5-5 to 8-2 (M decreases from 0 to -3), the early peak arrives increasingly earlier, thus u_{m1} increases from 1.74×10^{-2} to 1.83×10^{-2} m/s; from 8-2 to 10-0 (M decreases from -3 to -5), the early peak arrives increasingly delayed, thus u_{m1} decreases from 1.83×10^{-2} to 1.70×10^{-2} m/s. As the Configuration changes from 6-4 to 9-1 (M decreases from -1 to -4), the late peak arrives increasingly delayed, thus u_{m2} decreases from 1.46×10^{-2} to 8.27×10^{-3} m/s.

While no clear trend is observed for parameters D_{m1}, D_{m2}, k_1, k_2, w_{im1}, w_{im2} (Figure 3.13b-e). These variations may be caused by parameter equifinality, which means that more than one parameter set will reproduce the observations equally well concerning a particular performance measure (Cobelli and DiStefano, 1980). Equifinality can be caused by parameters that are insensitive (Johnston and Pilgrim, 1976) and/or interactive (Ibbitt and O'Donnell, 1971). In Appendix B, we show that the problem of parameter equifinality does exist in the parameter calibration process. As M increases from -4 to 5, w_{m1} decreases from 0.675 to 0.370. w_{m2} increases from 0.206 to 0.423.

Table 3.5. Calibrated parameters of DRMIM to 200 rpm experiments

	h_1-h_2	M (cm)	u_{m1} (m/s)	D_{m1} (m^2/s)	k_1 (1/s)	w_{m1} (-)	u_{m2} (m/s)	D_{m2} (m^2/s)	k_2 (1/s)	w_{m2} (-)	w_{MIM1} (-)	RMSE
200 rpm	5-5	0	1.74×10^{-2}	1.24×10^{-4}	9.88×10^{-3}	0.491	1.27×10^{-2}	1.11×10^{-4}	2.26×10^{-3}	0.285	0.619	1.49×10^{-4}
	4-6	1	1.69×10^{-2}	1.37×10^{-4}	1.09×10^{-2}	0.477	1.32×10^{-2}	7.06×10^{-5}	4.91×10^{-3}	0.357	0.561	1.31×10^{-4}
	3-7	2	1.67×10^{-2}	1.74×10^{-4}	9.35×10^{-3}	0.530	1.57×10^{-2}	1.39×10^{-4}	4.25×10^{-3}	0.284	0.597	6.21×10^{-5}
	2-8	3	1.65×10^{-2}	1.02×10^{-4}	4.46×10^{-3}	0.449	1.62×10^{-2}	2.67×10^{-4}	1.36×10^{-2}	0.377	0.589	7.70×10^{-5}
	1-9	4	1.69×10^{-2}	1.60×10^{-4}	2.28×10^{-3}	0.434	1.50×10^{-2}	4.72×10^{-4}	1.54×10^{-3}	0.424	0.542	8.17×10^{-5}
	0-10	5	1.72×10^{-2}	1.80×10^{-4}	4.61×10^{-3}	0.370	1.64×10^{-2}	8.22×10^{-5}	1.22×10^{-2}	0.423	0.519	3.95×10^{-5}
	6-4	-1	1.78×10^{-2}	1.59×10^{-4}	4.39×10^{-3}	0.557	1.46×10^{-2}	6.79×10^{-5}	7.92×10^{-3}	0.268	0.712	1.24×10^{-4}
	7-3	-2	1.78×10^{-2}	2.18×10^{-4}	2.78×10^{-3}	0.610	1.40×10^{-2}	3.22×10^{-5}	1.55×10^{-2}	0.199	0.775	1.30×10^{-4}
	8-2	-3	1.83×10^{-2}	1.59×10^{-4}	5.66×10^{-3}	0.624	1.22×10^{-2}	1.25×10^{-4}	4.64×10^{-3}	0.212	0.714	9.55×10^{-5}
	9-1	-4	1.77×10^{-2}	1.47×10^{-4}	7.36×10^{-3}	0.675	8.27×10^{-3}	1.19×10^{-4}	4.84×10^{-3}	0.206	0.750	1.52×10^{-4}
	10-0	-5	1.70×10^{-2}	1.30×10^{-4}	3.46×10^{-3}	0.480	1.51×10^{-2}	3.63×10^{-4}	2.70×10^{-3}	0.337	0.522	3.31×10^{-5}

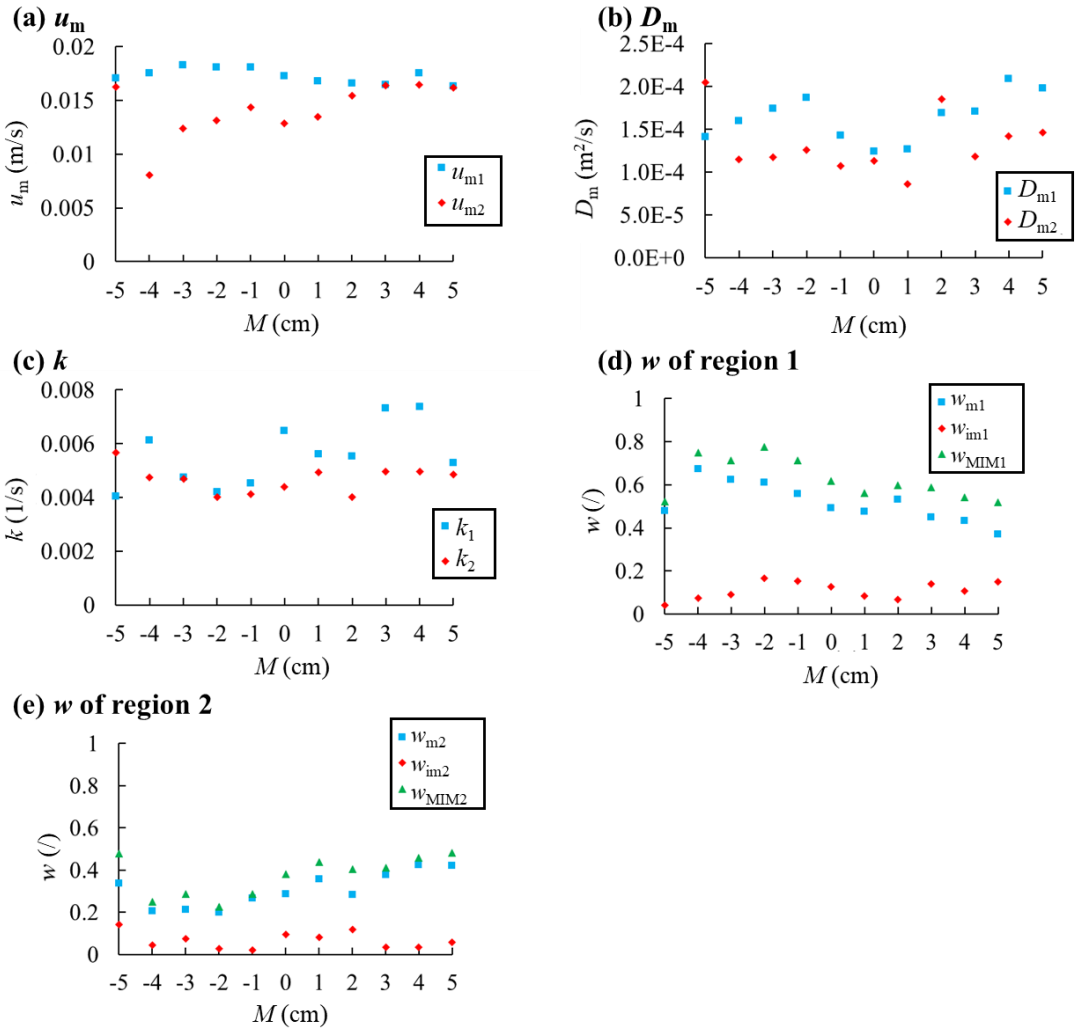

Figure 3.13. Calibrated parameters of DRMIM to 200 rpm experiments.

3.5 Discussion

3.5.1 Flow rate effect

According to our experiment results (Figure 3.6), the flow rate influences the BTCs significantly. The dual-peak effect is more obvious under a higher flow rate. This result is in accordance with the previous experimental study of Mohammadi et al. (2019): under high hydraulic gradient (thus large flow rate), the tracing tests in the conduit network of branchwork structure generated multi-peaked BTCs; under low hydraulic gradients (thus small flow rates), the network exhibited single-peaked BTCs.

For the same system, multi-peaked BTCs may bring us more information about the system investigated by the tracing test. Firstly, dual-peaked BTC suggests the existence of the tracer bifurcation along the flow path. Secondly, we can further identify the average transport velocity. Thirdly, we can estimate the underground conduit length of different channels as proposed by Wang et al. (2020).

3.5.2 Aperture effect

The dual-conduit geometry influences the two tracer plumes in two aspects: (i) the tracer plume travel

time and (ii) the plume concentration value.

i) The tracer plume travel time. For each conduit, larger aperture means smaller flow resistivity. This smaller flow resistivity causes larger flow velocity, thus smaller travel time for the tracer. On the contrary, smaller aperture means larger tracer travel time.

ii) The plume concentration value. For each conduit, larger aperture causes not only a larger flow velocity but also a larger cross-sectional area. Thus larger aperture causes larger flow rate to travel through this conduit. Conversely, a smaller aperture means a smaller flow rate. The flow rate distribution further influences the transport process, because the concentration will change drastically at the convergence position (green point in Figure 3.15) due to the mixing effect:

$$C_{0\_C} = \frac{Q_1 C_{1\_C} + Q_2 C_{2\_C}}{Q_1 + Q_2}. \quad \text{(Eq. 3-10)}$$

This means the concentration in the shorter conduit, C_{1_C}, will be diluted by $\frac{Q_1}{Q_1+Q_2}$; the concentration in the longer conduit, C_{2_C}, will be diluted by $\frac{Q_2}{Q_1+Q_2}$. Thus, as Q_1 increases, the tracer of the shorter conduit will cause larger concentration on the BTCs; under a constant inflow, as Q_1 increases, Q_2 decreases, the tracer of the longer conduit will cause smaller concentration on the BTCs.

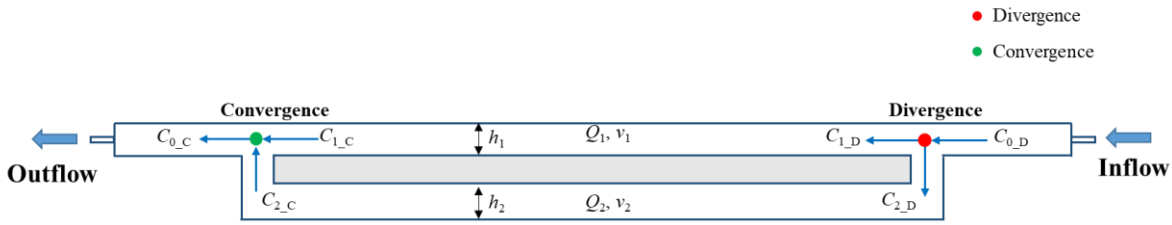

Figure 15. The divergence and the convergence process.

According to the above analysis, we can explain how the aperture configurations influence the experimental BTCs (Figure 3.7). From Configurations 5-5 to 1-9, h_1 decreases and h_2 increases, this means v_1 decreases and v_2 increases. Thus, the early peak gets increasingly delayed and the second peak arrives increasingly early. Until Configurations 3-7, 2-8, and 1-9, the two peaks have very similar arrival times and the two tracer plumes exhibit only one peak. From 5-5 to 4-6, h_1 decreases and h_2 increases, which means that Q_1 decreases and Q_2 increases, thus the tracer in the shorter conduit causes smaller concentration on the final BTC and the tracer in the longer conduit causes larger concentration. This is why the concentration of the first peak (C_{peak1}) is smaller than the second peak (C_{peak2}) for 4-6.

From 5-5 to 9-1, h_1 increases and h_2 decreases, this means v_1 increases and v_2 decreases. Thus, the early peak gets increasingly early and the second peak arrives increasingly delayed (Figure 3.7). From 5-5 to 9-1, the aperture variations cause Q_1 to increase and Q_2 to decrease, this means C_{peak1} increases and C_{peak2} decreases.

3.5.3 Limitation of the considered numerical models

In our application of the WSADE model to fitting the experimental BTCs. We find some WSADE model parameters do not bear the physical meaning we have assumed. For example, when we apply the WSADE to fit the BTC of 5-5, 200 rpm (Figure 3.9, Table 3.4), we find that the calibrated values of w_1 and w_2 cannot correctly represent the true tracer quantity repartition in the two conduits. Because the conceptual structure of the WSADE is similar to the experimental model, in that the WSADE has two regions and the experimental model has two conduits. We have expected that the WSADE Region 1 parameters (u_1, D_1, and w_1) should represent the properties of the transport process of the shorter conduit, which makes the early peak of the BTC; and the WSADE Region 2 parameters (u_2, D_2, and w_2) should represent the properties of the transport process of the longer conduit, which makes the late peak. According to the experimental BTC, the early peak is higher than the late peak, which suggests that the mass of the early tracer plume should be more than the late tracer plume. The calibrated value $w_1 = 0.099$ and $w_2 = 1- w_1 = 0.901$. w_1 is nine times smaller than w_2, while the quantity of the early tracer plume cannot be nine times smaller than the late tracer plume. Thus the values of w_1 and w_2 are unrealistic and cannot correctly represent the true quantity repartition between the two tracer plumes.

In this fitting, the values of D_1 and D_2 are also not realistic: the calibrated value of D_2 is around 8.6 times larger than D_1 ($D_1 = 6.34\times10^{-5}$ m^2/s, $D_2=5.47\times10^{-4}$ m^2/s). The contrast between the two values is too large: the length ratio of the two conduits is around 1.13 and the cross-section areas of the two conduits are the same for Configuration 5-5. The properties of the two conduits cannot differ by 8.6 times. Thus, parameters D_1 and D_2 cannot correctly represent the dispersion effect of the two conduits. For the WSADE model fitting the experiment of 5-5, 200 rpm, some parameters (w_1, w_2, D_1, and D_2) of WSADE do not represent the physical meanings we have expected.

According to the characteristic of the experimental BTCs and the WSADE model, we explain the cause of the above problem. First, according to Figure 3.6, the BTCs under 20-rpm and 200-rpm exhibit a significant tailing effect for the falling limb. The tailing effect has caused the falling limb to last for a relatively long time scale. The tailing effect has been caused by the solute detention effect introduced in Section 4.1.3. Second, the two-region WSADE consists of two parallel-flowing regions governed by the ADE model (Figure 3.4). It is well acknowledged that the simple ADE model cannot well reproduce the BTCs with the tailing effect. To properly reproduce the falling limb, the WSADE Region 2 is more widespread and has a larger size. So, the calibrated values of D_2 and w_2 are unrealistically large.

Compared to the two-region WSADE, the DRMIM catches better the transport process in the dual-conduit structures (Figure 3.12). The DRMIM has better fitting performance because the conceptual structure of the DRMIM is more similar to the experimental solute transport process in the dual-conduit structures. The DRMIM consists of two parallel-flowing MIM models, and each MIM model considers a stagnant region existing along the flow region. For the experimental solute transport process, stagnant

regions also exist for the experimental transport processes (as shown in Section 3.4.1.3). Thus, the DRMIM presents more satisfying fitting performance.

3.6 Conclusions

We studied the solute transport process in dual conduit structures by lab-scale experiments. By definition, h_1 is the aperture of the shorter conduit and h_2 is the aperture of the longer conduit. If $h_1 < h_2$ and the contrast between the two apertures is low, the dual-conduit structures generate dual-peaked BTCs that exhibit a lower early peak than the late peak; if $h_1 < h_2$ and the contrast between h_1 and h_2 is large, we obtain single-peaked BTCs; if $h_1 \geqslant h_2$, dual-peaked BTCs or bump-tailed BTCs are observed. As the flow rate increases, it is more likely to observe the separation of the two tracer plumes.

The experimental BTCs are fitted by two numerical models. The WSADE model properly reproduces the bump-tailed BTCs and some of the dual-peaked BTCs, but it failed to correctly reproduce the dual-peaked BTC obtained from configuration 4-6 under 200 rpm. The DRMIM exhibited better performances than the WSADE model and captured all of the symptoms of the BTCs: the second peak, the bump, and the tailing.

References

Bear, J., 1972. Dynamics of Fluids in Porous Media. American Elsevier Publishing, New York.

Berkowitz, B. et al. (2006) “Modeling Non-fickian transport in geological formations as a continuous time random walk,” Reviews of Geophysics, 44(2). doi:10.1029/2005RG000178.

Bakalowicz, M., 2005. Karst groundwater: a challenge for new resources. Hydrogeology journal, 13(1), pp.148-160.

Cobelli, C. and Distefano 3rd, J.J., 1980. Parameter and structural identifiability concepts and ambiguities: a critical review and analysis. American Journal of Physiology-Regulatory, Integrative and Comparative Physiology, 239(1), pp.R7-R24.

Dewaide, L., Bonniver, I., Rochez, G. and Hallet, V., 2016. Solute transport in heterogeneous karst systems: dimensioning and estimation of the transport parameters via multi-sampling tracer-tests modelling using the OTIS (One-dimensional Transport with Inflow and Storage) program. Journal of Hydrology, 534, pp.567-578.

Dewaide, L. et al. (2018) “Double-peaked breakthrough curves as a consequence of solute transport through underground lakes: a case study of the Furfooz karst system, Belgium,” Belgium. Hydrogeology Journal, 26(2), pp. 641–650. doi:10.1007/s10040-017-1671-4ï.

Duran, L., Fournier, M., Massei, N. and Dupont, J.P., 2016. Assessing the nonlinearity of karst response function under variable boundary conditions. Groundwater, 54(1), pp.46-54.

Field, M.S. and Leij, F.J., 2012. Solute transport in solution conduits exhibiting multi-peaked breakthrough curves. Journal of Hydrology, 440, pp.26-35.

Florea, L.J. and Wicks, C.M., 2001. Solute transport through laboratory-scale karstic aquifers. Geography/Geology Faculty Publications, p.11.

Goldscheider, N., Meiman, J., Pronk, M. and Smart, C., 2008. Tracer tests in karst hydrogeology and speleology. International Journal of Speleology, 37(1), pp.27-40.

Ghodrati, M. and Jury, W.A., 1992. A field study of the effects of soil structure and irrigation method on preferential flow of pesticides in unsaturated soil. Journal of contaminant Hydrology, 11(1-2), pp.101-125.

Haario, H., Laine, M., Mira, A. and Saksman, E., 2006. DRAM: efficient adaptive MCMC. Statistics and Computing, 16(4), pp.339-354.

Hauns, M., Jeannin, P.Y. and Atteia, O., 2001. Dispersion, retardation and scale effect in tracer breakthrough curves in karst conduits. Journal of hydrology, 241(3-4), pp.177-193.

Ibbitt, R., and T. O'Donnell (1971), Designing conceptual catchment models for automatic fitting methods, Int. Assoc. Hydrol. Sci. Publ., 101(2), 461–475.

Johnston, P.R. and Pilgrim, D.H., 1976. Parameter optimization for watershed models. Water Resources Research, 12(3), pp.477-486.

Levy, M. and Berkowitz, B., 2003. Measurement and analysis of non-Fickian dispersion in heterogeneous porous media. Journal of contaminant hydrology, 64(3-4), pp.203-226.

Moreno, L. and Tsang, C.F., 1991. Multiple-peak response to tracer injection tests in single fractures: A numerical study. Water Resources Research, 27(8), pp.2143-2150.

Majdalani, S., Chazarin, J.P., Delenne, C. and Guinot, V., 2015. Solute transport in periodical heterogeneous porous media: Importance of observation scale and experimental sampling. Journal of Hydrology, 520, pp.52-60.

Majdalani, S., Guinot, V., Delenne, C. and Gebran, H., 2018. Modeling solute dispersion in periodic heterogeneous porous media: Model benchmarking against experiment experiments. Journal of Hydrology, 561, pp.427-443.

Massei, N., Wang, H.Q., Field, M.S., Dupont, J.P., Bakalowicz, M. and Rodet, J., 2006. Interpreting tracer breakthrough tailing in a conduit-dominated karstic aquifer. Hydrogeology Journal, 14(6), pp.849-858.

Mohammadi, Z., Gharaat, M.J. and Field, M., 2019. The Effect of Hydraulic Gradient and Pattern of Conduit Systems on Tracing Tests: Bench-Scale Modeling. Groundwater, 57(1), pp.110-125.

Morales, T., Uriarte, J.A., Olazar, M., Antigüedad, I. and Angulo, B., 2010. Solute transport Modeling in karst conduits with slow zones during different hydrologic conditions. Journal of Hydrology, 390(3-4), pp.182-189.

Perrin, J. and Luetscher, M. (2008) "Inference of the structure of karst conduits using quantitative tracer tests and geological information: example of the Swiss Jura," Hydrogeology Journal, 16(5), pp. 951–

967.

Runkel, R.L., 1998. One-dimensional transport with inflow and storage (OTIS): A solute transport model for streams and rivers (Vol. 98, No. 4018). US Department of the Interior, US Geological Survey.

Robert, C.P. (2015). The Metropolis–Hastings Algorithm. In Wiley StatsRef: Statistics Reference Online (eds N. Balakrishnan, T. Colton, B. Everitt, W. Piegorsch, F. Ruggeri and J.L. Teugels). https://doi.org/10.1002/9781118445112.stat07834

Rana, S.M., Boccelli, D.L., Scott, D.T. and Hester, E.T., 2019. Parameter uncertainty with flow variation of the one-dimensional solute transport model for small streams using Markov chain Monte Carlo. Journal of Hydrology, 575, pp.1145-1154.

Van Genuchten, M.T. and Wierenga, P.J., 1976. Mass transfer studies in sorbing porous media I. Analytical solutions. Soil science society of america journal, 40(4), pp.473-480.

Vrugt, J.A. et al. (2006) "Multi-objective calibration of forecast ensembles using Bayesian model averaging," Geophysical Research Letters, 33(19).

Wang, C., Wang, X., Majdalani, S., Guinot, V. and Jourde, H., 2020. Influence of dual conduit structure on solute transport in karst tracer tests: An experimental laboratory study. Journal of Hydrology, 590, p.125255.

Younes, A., Delay, F., Fajraoui, N., Fahs, M. and Mara, T.A., 2016. Global sensitivity analysis and Bayesian parameter inference for solute transport in porous media colonized by biofilms. Journal of contaminant hydrology, 191, pp.1-18.

Zhao, X., Chang, Y., Wu, J. and Peng, F., 2017. Laboratory investigation and simulation of breakthrough curves in karst conduits with pools. Hydrogeology Journal, 25(8), pp.2235-2250.

Zhao, X., Chang, Y., Wu, J. and Xue, X., 2019. Effects of flow rate variation on solute transport in a karst conduit with a pool. Environmental Earth Sciences, 78(7), pp.237.

Zhao, X., Chang, Y., Wu, J., Li, Q. and Cao, Z., 2021. Investigating the relationships between parameters in the transient storage model and the pool volume in karst conduits through tracer experiments. Journal of Hydrology, 593, p.125825.

Appendix

Appendix A. The modeling result of 2 rpm and 20 rpm pump velocity experiments

1. WSADE

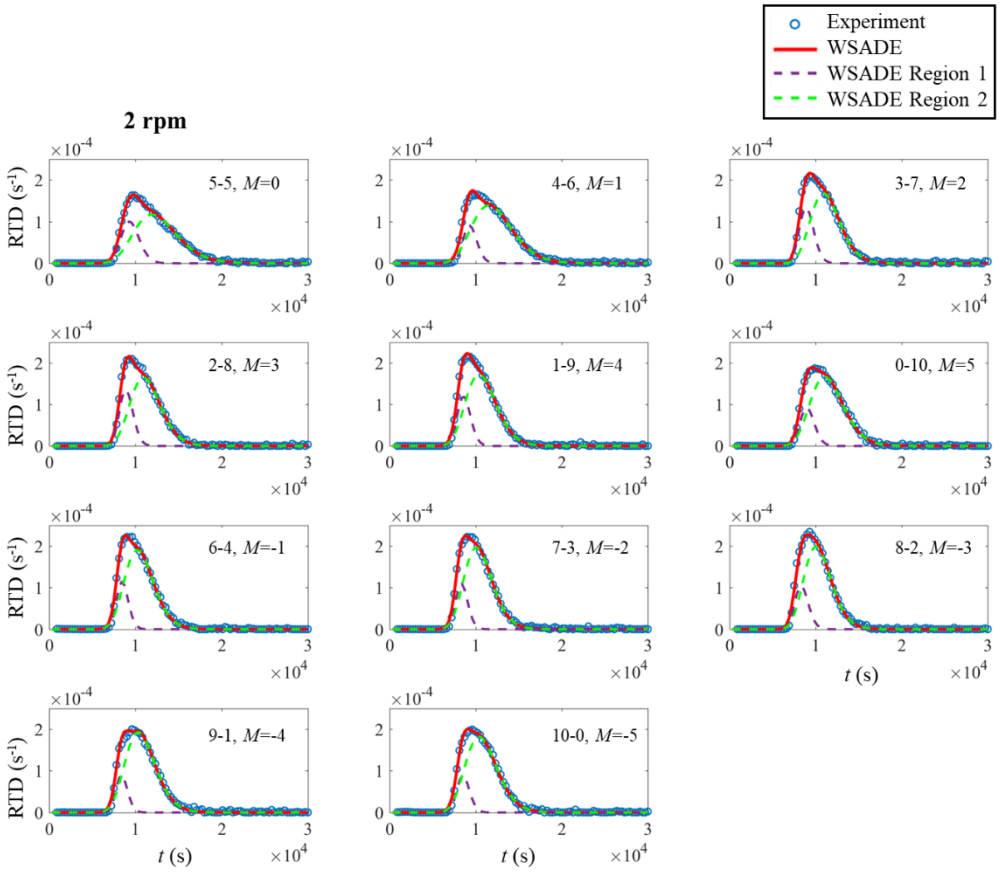

Figure 3.14. WSADE model fitting the 2 rpm experimental BTCs.

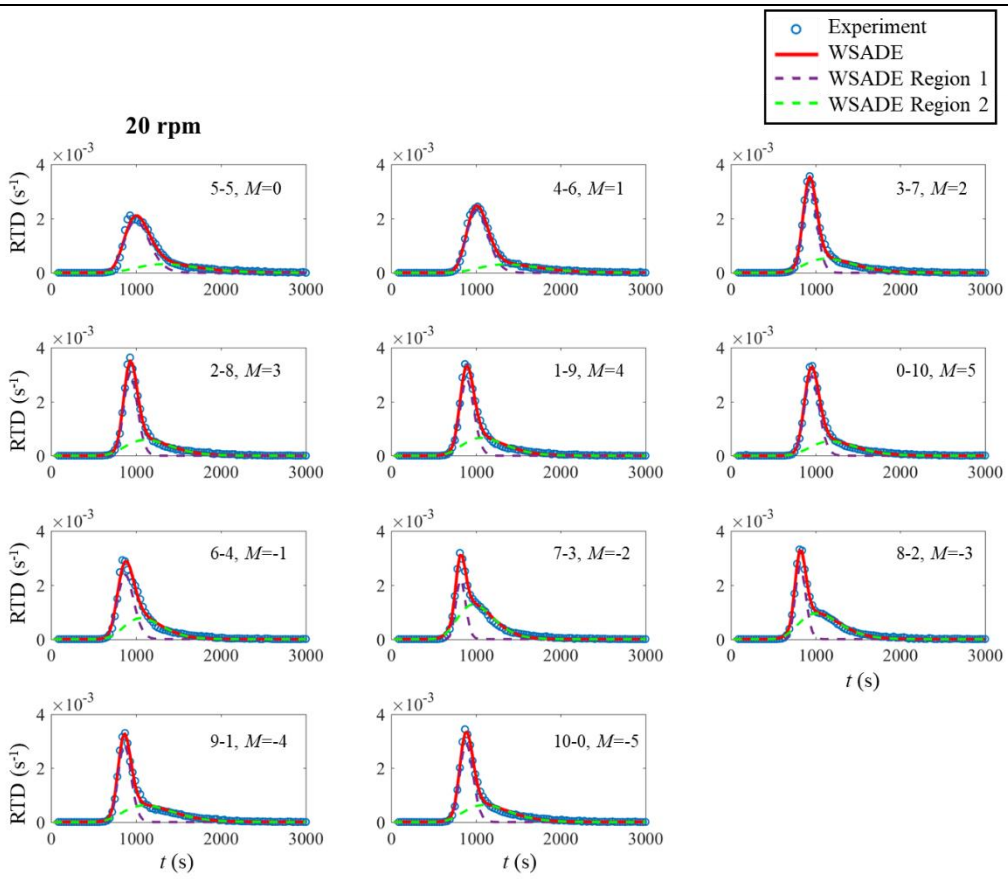

Figure 3.15. WSADE model fitting the 20 rpm experimental BTCs.

Table 3.6. Calibrated parameters of WSADE to all of the experiments

Pump Speed (rpm)	M (cm)	u_1 (m/s)	u_2 (m/s)	D_1 (m^2/s)	D_2 (m^2/s)	w_1 (-)	RMSE
2	0	1.60×10^{-4}	1.23×10^{-4}	1.49×10^{-6}	3.99×10^{-6}	0.214	3.62×10^{-6}
	1	1.61×10^{-4}	1.28×10^{-4}	8.85×10^{-7}	3.86×10^{-6}	0.149	4.20×10^{-6}
	2	1.68×10^{-4}	1.36×10^{-4}	1.10×10^{-6}	2.46×10^{-6}	0.239	4.17×10^{-6}
	3	1.68×10^{-4}	1.35×10^{-4}	9.75×10^{-7}	2.61×10^{-6}	0.227	3.93×10^{-6}
	4	1.74×10^{-4}	1.42×10^{-4}	1.05×10^{-6}	3.05×10^{-6}	0.198	3.80×10^{-6}
	5	1.67×10^{-4}	1.34×10^{-4}	1.06×10^{-6}	3.00×10^{-6}	0.160	3.51×10^{-6}
	-1	1.77×10^{-4}	1.45×10^{-4}	8.49×10^{-7}	2.91×10^{-6}	0.165	4.09×10^{-6}
	-2	1.80×10^{-4}	1.47×10^{-4}	9.35×10^{-7}	2.88×10^{-6}	0.162	3.83×10^{-6}
	-3	1.80×10^{-4}	1.47×10^{-4}	1.20×10^{-6}	2.74×10^{-6}	0.175	4.14×10^{-6}
	-4	1.79×10^{-4}	1.43×10^{-4}	8.37×10^{-7}	3.04×10^{-6}	0.123	4.32×10^{-6}
	-5	1.76×10^{-4}	1.42×10^{-4}	9.57×10^{-7}	3.25×10^{-6}	0.135	3.58×10^{-6}
20	0	1.49×10^{-3}	1.09×10^{-3}	2.35×10^{-5}	5.95×10^{-5}	0.640	7.25×10^{-5}
	1	1.48×10^{-3}	1.07×10^{-3}	1.67×10^{-5}	5.35×10^{-5}	0.654	3.46×10^{-5}
	2	1.61×10^{-3}	1.29×10^{-3}	8.55×10^{-6}	6.00×10^{-5}	0.570	4.74×10^{-5}
	3	1.60×10^{-3}	1.31×10^{-3}	8.46×10^{-6}	5.36×10^{-5}	0.558	5.15×10^{-5}
	4	1.68×10^{-3}	1.37×10^{-3}	1.02×10^{-5}	5.73×10^{-5}	0.525	5.56×10^{-5}
	5	1.57×10^{-3}	1.24×10^{-3}	9.52×10^{-6}	4.73×10^{-5}	0.581	4.53×10^{-5}
	-1	1.71×10^{-3}	1.38×10^{-3}	1.46×10^{-5}	4.49×10^{-5}	0.507	8.51×10^{-5}
	-2	1.83×10^{-3}	1.51×10^{-3}	6.67×10^{-6}	5.28×10^{-5}	0.277	5.57×10^{-5}
	-3	1.83×10^{-3}	1.44×10^{-3}	7.84×10^{-6}	5.97×10^{-5}	0.362	3.66×10^{-5}

	-4	1.73×10^{-3}	1.31×10^{-3}	9.76×10^{-6}	6.68×10^{-5}	0.473	5.30×10^{-5}
	-5	1.69×10^{-3}	1.33×10^{-3}	9.59×10^{-6}	5.90×10^{-5}	0.508	4.69×10^{-5}

2. DRMIM

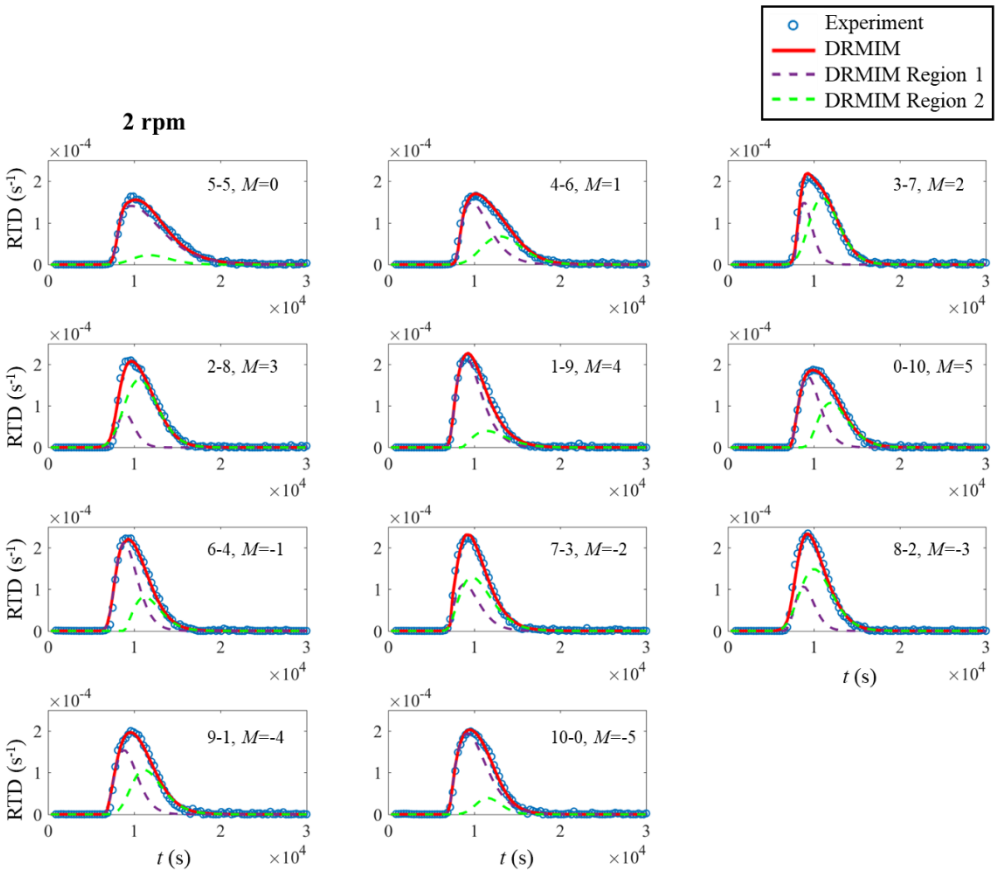

Figure 3.16. DRMIM model fitting the 2 rpm experimental BTCs.

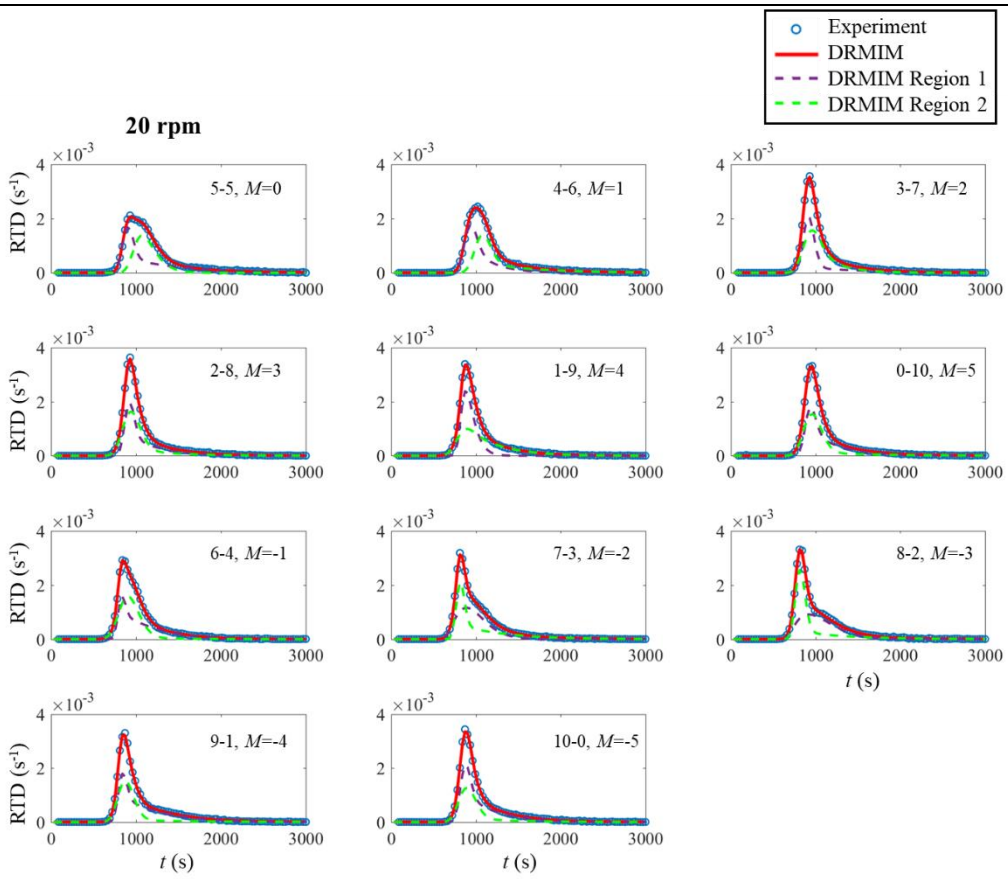

Figure 3.17. DRMIM model fitting the 20 rpm experimental BTCs.

Table 3.7. Calibrated parameters of DRMIM to all of the experiments

Pump Speed (rpm)	M (cm)	u_{m1} (m/s)	D_{m1} (m^2/s)	k_1 (1/s)	w_{m1} (-)	u_{m2} (m/s)	D_{m2} (m^2/s)	k_2 (1/s)	w_{m2} (-)	w_{MIM1} (-)	RMSE
2 rpm	0	1.77×10^{-4}	5.30×10^{-7}	2.36×10^{-4}	0.624	1.39×10^{-4}	2.78×10^{-6}	4.34×10^{-4}	0.110	0.876	3.72×10^{-6}
	1	1.76×10^{-4}	2.56×10^{-7}	3.06×10^{-4}	0.434	1.34×10^{-4}	2.16×10^{-6}	4.83×10^{-4}	0.370	0.551	4.80×10^{-6}
	2	1.84×10^{-4}	2.21×10^{-7}	4.00×10^{-4}	0.225	1.63×10^{-4}	1.45×10^{-6}	5.18×10^{-4}	0.598	0.255	6.13×10^{-6}
	3	2.13×10^{-4}	5.11×10^{-11}	1.03×10^{-3}	0.134	1.68×10^{-4}	3.10×10^{-6}	8.72×10^{-4}	0.665	0.176	5.93×10^{-6}
	4	1.95×10^{-4}	3.23×10^{-7}	3.87×10^{-4}	0.597	1.66×10^{-4}	7.62×10^{-8}	4.30×10^{-4}	0.169	0.767	5.00×10^{-6}
	5	2.00×10^{-4}	4.06×10^{-8}	6.39×10^{-4}	0.358	1.58×10^{-4}	1.85×10^{-7}	5.17×10^{-4}	0.398	0.468	2.76×10^{-6}
	-1	1.95×10^{-4}	7.05×10^{-7}	4.34×10^{-4}	0.511	1.65×10^{-4}	2.25×10^{-9}	5.01×10^{-4}	0.282	0.628	5.54×10^{-6}
	-2	2.00×10^{-4}	3.19×10^{-10}	4.25×10^{-4}	0.283	1.94×10^{-4}	5.97×10^{-7}	4.40×10^{-4}	0.457	0.368	4.60×10^{-6}
	-3	2.26×10^{-4}	3.32×10^{-9}	1.08×10^{-3}	0.192	1.88×10^{-4}	2.59×10^{-6}	6.95×10^{-4}	0.555	0.265	5.98×10^{-6}
	-4	2.18×10^{-4}	1.64×10^{-8}	7.09×10^{-4}	0.326	1.45×10^{-4}	1.52×10^{-6}	1.98×10^{-4}	0.481	0.446	5.47×10^{-6}
	-5	1.97×10^{-4}	2.72×10^{-7}	3.79×10^{-4}	0.621	1.29×10^{-4}	1.51×10^{-6}	1.52×10^{-3}	0.157	0.840	3.79×10^{-6}
20 rpm	0	1.65×10^{-3}	6.33×10^{-6}	7.01×10^{-4}	0.420	1.48×10^{-3}	6.13×10^{-6}	1.91×10^{-3}	0.375	0.578	2.82×10^{-5}
	1	1.60×10^{-3}	7.67×10^{-6}	6.08×10^{-4}	0.389	1.38×10^{-3}	7.96×10^{-6}	4.04×10^{-4}	0.457	0.438	2.18×10^{-5}
	2	1.63×10^{-3}	5.83×10^{-6}	3.16×10^{-4}	0.372	1.55×10^{-3}	1.38×10^{-5}	4.92×10^{-4}	0.488	0.458	1.87×10^{-5}
	3	1.62×10^{-3}	4.55×10^{-6}	6.77×10^{-4}	0.420	1.57×10^{-3}	1.43×10^{-5}	2.26×10^{-4}	0.452	0.500	2.19×10^{-5}
	4	1.77×10^{-3}	3.77×10^{-6}	1.95×10^{-3}	0.393	1.70×10^{-3}	1.90×10^{-5}	1.05×10^{-3}	0.447	0.428	1.54×10^{-5}
	5	1.60×10^{-3}	5.18×10^{-6}	7.72×10^{-4}	0.441	1.54×10^{-3}	1.38×10^{-5}	1.79×10^{-4}	0.413	0.529	1.54×10^{-5}
	-1	1.80×10^{-3}	3.73×10^{-6}	1.28×10^{-3}	0.408	1.62×10^{-3}	2.07×10^{-5}	6.37×10^{-5}	0.442	0.543	1.98×10^{-5}
	-2	2.10×10^{-3}	8.44×10^{-6}	4.56×10^{-3}	0.351	1.84×10^{-3}	4.81×10^{-6}	7.14×10^{-4}	0.388	0.481	2.14×10^{-5}
	-3	1.92×10^{-3}	1.31×10^{-5}	2.85×10^{-3}	0.377	1.83×10^{-3}	6.72×10^{-6}	3.70×10^{-4}	0.402	0.513	2.14×10^{-5}
	-4	1.78×10^{-3}	4.84×10^{-6}	1.06×10^{-3}	0.458	1.69×10^{-3}	1.41×10^{-5}	1.64×10^{-4}	0.332	0.620	2.40×10^{-5}
	-5	1.71×10^{-3}	6.22×10^{-6}	8.02×10^{-4}	0.516	1.65×10^{-3}	1.58×10^{-5}	2.03×10^{-4}	0.323	0.639	1.70×10^{-5}

Appendix B. Parameter identifiability.

We check the parameter identifiability of the DRMIM model by plotting the parameter histogram and correlation plots from the parameter sets on the MCMC chain. Correlation plots reveal the interaction between the parameters (Rana et al., 2019; Wang et al., 2019). Histograms allow direct estimation of uncertainty (relative standard deviation, RSD) and identifiability (whether the distribution is Gaussian). The Gaussian distribution of the posterior parameter sets is deemed essential to parameter identifiability (Younes et al., 2016) because the Gaussian distribution allows us to uniquely identify the parameter estimates from the experimental data.

The correlation between two data is evaluated by the correlation coefficient, r. Given paired data $\{(x_1, y_1), (x_2, y_2), \ldots, (x_n, y_n)\}$, r is defined as:

$$r = \frac{\sum_{i=1}^{n}(x_i-\overline{x})(y_i-\overline{y})}{\sqrt{\sum_{i=1}^{n}(x_i-\overline{x})^2}\sqrt{\sum_{i=1}^{n}(y_i-\overline{y})^2}}, \quad \text{(Eq. 3-11)}$$

where n is the sample size; $\bar{x}$ and $\bar{y}$ are the mean value for x and y, respectively.

The parameter variability (or uncertainty) is represented by the relative standard deviation (RSD) value:

$$\mathrm{RSD} = \frac{\sqrt{\frac{\sum_{i=1}^{n}(x_i-\overline{x})^2}{n-1}}}{|\overline{x}|}, \quad \text{(Eq. 3-12)}$$

To better address parameter equifinality, it is optimal to investigate as many as possible the parameter sets which can reproduce the experimental data by certain criteria. However, the common practice of launching MCMC calibration for once may not be enough. Because, in our experience of applying the MCMC for optimization, the different initial parameter sets may attribute to different results: the starting point influences the path and the endpoint of the automatical searching algorithm. Different from the common practice, we carry out 20 times of MCMC calibrations for this identifiability study, to fully address the possible parameter space. Each MCMC calibration starts with different randomly generated initial parameter sets and contains 18000 iterations. The last 400 iterations of the 20 MCMC chains, thus 8000 parameter sets in total, are used in this identifiability study.

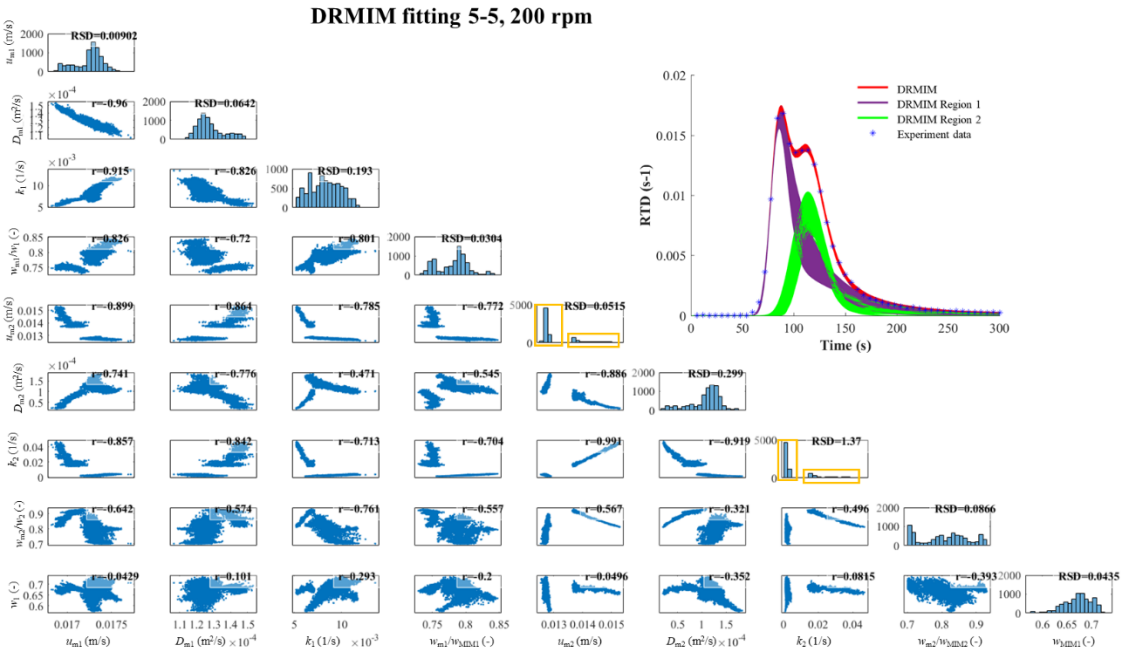

Figure 3.18. Parameter histograms and correlation plots of the MCMC chain of DRMIM fitting experiment of 5-5, 200 rpm.

The results shown in Figure 3.18 suggest that different parameter sets can make the DRMIM model well reproduce the experimental BTC. The parameter histograms exhibit scattered distributions. The multi-solution phenomenon is especially severe for u_{m2} and k_2: there exist two separated groups of values (marked by the yellow bracket). With these different parameter sets, the DRMIM Region 1 generates various BTCs (the purple curves in Figure 3.18); Region 2 also generates various BTCs (the green curves in Figure 3.18). When the simulated BTCs of the two Regions are summed up, the simulated BTCs of the DRMIM model show little variance (the red curves in Figure 3.18) and all of the simulated BTCs are approximate to the experimental BTC.

Due to this equifinality problem, the calibrated DRMIM parameters may fall into a wide possible range. This has caused some calibrated DRMIM parameters to exhibit discontinuous variations with the M value (Figure 3.13b-e).

CHAPTER 4

Résumé:

Ce chapitre étudie la propriété de l'approche par fonction de transfert (TFA) pour l'interprétation des courbes de restitutions de traçages dans les réseaux de conduits ou de fractures. Les courbes de restitution des expériences de transport, présentées dans les chapitres précédents sont reproduites au moyen de cette approche. Celle-ci permet un meilleur ajustement des courbes de restitution que le modèle ADE et le DRMIM dans certaines conditions. Cependant, la principale limite de la TFA est que les paramètres n'ont pas de signification physique évidente. Afin d'évaluer quelles informations physiques contiennent les paramètres de la TFA, nous analysons l'équivalence entre la TFA et l'équation d'advection dispersion (ADE). Nous obtenons ainsi deux équations qui, sous certaines conditions, permettent de générer des courbes de restitutions identiques et d'exprimer les paramètres de la TFA en fonction de la variable et des paramètres considérés dans l'ADE, dont la signification physique est plus facile à appréhender.

Chapter 4 Interpretation of the intrinsic heterogeneity of karst conduit network by evaluating the tracing BTCs using the transfer function approach

Chaoqi Wang[1], Samer Majdalani[1], Xiaoguang Wang[2], Vianney Sivelle[1], Vincent Guinot[1,3], Herve Jourde[1]

1. Hydrosciences Montpellier, UMR 5569, France
2. Chengdu University of Technology, Chengdu, China
3. Inria Lemon, Univ. Montpellier, Montpellier, France

Submitted to Journal of Hydrology. Under revision.

Highlights:

1. The transfer function approach is applied for interpreting artificial tracer tests in karst systems.
2. Two equations are obtained to make the TFA and the ADE produce identical BTCs under certain conditions.
3. We provide suggestions on selecting the optimal model from the ADE, TFA, and MIM models for different BTCs.

Abstract

The transfer function approach (TFA) effectively interprets tracer BreakThrough Curves (BTCs) in karst systems. However, the parameters of TFA cannot directly reflect the properties of the transport process. To overcome this limitation, we study the equivalence between TFA and Advection Dispersion Equation (ADE). We derive two equations that make TFA and ADE produce identical BTCs under certain conditions. If we apply the TFA to model transport BTCs, we can transform the TFA parameters (*A, N,* and τ) to equivalent ADE parameters (u and D) with the two derived equations. The transformed parameters are more suitable for characterizing the transport process.

We take two groups transport BTCs in karst media and fit them with three numerical models: ADE, TFA, MIM. The ADE fails to reproduce most of the BTCs. The TFA has better fitting performance than the ADE but it cannot reproduce the BTCs with tailing effect. The MIM performs the best fitting performance. The three models have different applicable situations. We provide suggestions on choosing the optimal transport model for different BTCs.

4.1 Introduction

Artificial tracing is a useful tool for investigating karst aquifer properties (Goldscheider et al., 2008). The common implementation has three steps: (i) inject a quantity of tracer solution at an upstream position; (ii) monitor tracer concentration variation (BreakThrough Curve, BTC) at a downstream position; (iii) adjust the parameters of numerical models to reproduce the BTC. The calibrated model parameters can reflect the properties of the solute transport process and the target aquifer.

Researchers developed different numerical models to analyze BTCs. The classical Advection-Dispersion-Equation (ADE) (Bear, 1972; Majdalani et al., 2015) model often fail to reproduce the BTCs (Moreno and Tsang, 1991; Hauns et al., 2001; Massei et al., 2006; Perrin and Luetscher, 2008, Goldscheider et al., 2008). The ADE assumes homogeneous media, while all aquifers are heterogenous to varying degrees (Ghodrati and Jury, 1992; Bakalowicz, 2005; Levy and Berkowitz, 2003). Fractured and karst aquifers are particularly heterogeneous (Bakalowicz, 2005). Because in karst systems, heterogeneity is exacerbated by the high contrasts in conduit diameters (Moreno and Tsang, 1991; Florea and Wicks, 2001) and multiple conduit system patterns (Florea and Wicks, 2001; Mohammadi et al., 2019). Heterogeneous media causes ‘anomalous’’ or ‘‘non-Fickian’’ transport. Anomalous transport process may exhibit BTCs with skewness, late time tails (Levy and Berkowitz, 2003) and multiple peaks (Florea and Wicks, 2001; Field and Leij, 2012; Wang et al., 2020). These particularities cannot be well captured by the ADE model.

Some researchers modify the ADE model by including additional processes (Morales et al., 2010) to handle anomalous transport processes. Along this line, there are the Mobile-Immobile Model (MIM) developed by van Genuchten and Wierenga (1976) and the Transient Storage Model (TSM) proposed by

Runkel (1998). In these models, the main pathway for flow and transport is regarded as a mobile region, while the dead-end conduits and matrix are represented by an immobile region. The transport in the mobile region is governed by ADE and the immobile region is coupled to the mobile region through an exchange term. Although conceptually simple, those models are effective tools for analyzing real-world transport data (Runkel, 1998; Edwardson et al., 2003; Gooseff et al., 2003; Martinez and Wise, 2003; Keefe et al., 2004). The Multi-Rate Mass Transfer (MRMT) method further extends the MIM by considering one mobile region and multiple immobile regions (Roth and Jury, 1993; Silva et al., 2009). The other ADE-based transport models represent the transport process using two or more ADE regions in parallel and the regions may exchange solutes due to concentration differences. For example, the two-region ADE model is valid for various field and experimental conditions (Skopp et al., 1981; Field and Leij, 2012; Majdalani et al. 2015, 2018; Tinet et al., 2019; Wang et al, 2020).

The analytical properties of a cascade of linear reservoirs have been known for decades (Nash, 1957). Only recently, the scientific community has set out to apply this concept to the transport processes in karst media (Becker and Bellin, 2013; Labat and Mangin, 2015). For such practices, karst media is conceptualized as a cascade of idealized reactors (or tanks, reservoirs). For example, Becker and Bellin (2013) considered several mixed reactors placed in series, each connected to a side reactor; Labat and Mangin (2015) considered two flow components with different flow velocities; Sivelle and Labat (2019) considered a plug flow reactor connected with a series of mixed-flow reactors. The model of (Sivelle and Labat, 2019) incorporates a delay function, a process that was not considered in Nash's (1957) original publication. Since the governing equations of such systems are solved in terms of transfer functions, this family of models is known as the Transfer Function Approach (TFA).

Although ADE and TFA have been used to characterize tracer transport experiments, until now, no formal analysis has been conducted to study the differences or similarities between the responses of the TFA and ADE models. In some circumstances, the TFA parameters may be unsuitable for characterizing a transport process because they don't bear a direct physical meaning about the transport process. This work is devoted to finding a relationship between the TFA of Sivelle and Labat (2019) and the ADE parameters. The study is accomplished by a series of analytical techniques: Laplace transform, Taylor Series Expansion, and consistency analysis.

The study has three steps: (i) investigate the condition that allows the TFA and the ADE to generate identical BTCs; derive two equations to correlate the parameters of the two models; (ii) fit two groups of transport BTCs with three models (ADE, TFA, MIM) and compare the fitting performances of the three models; (iii) transform the calibrated TFA parameters into equivalence ADE parameters. This study provides implications to the application of the TFA to tracer tests carried out in karst media.

4.2 Modeling

4.2.1 Transfer Function Approach (TFA): derivation and properties

4.2.1.1 Model presentation

The TFA is based on the following conceptual model (Figure 4.1). *N* identical tanks are placed in a cascade. Perfect mixing is assumed in each of these tanks (as indicated by the agitation blades). A steady-state discharge, q [L^3/T], flows through all the tanks. The concentration in all of the tanks is initially zero. The inflowing concentration signal $C_{\text{in}}(t)$ is first delayed by a time τ, and then routed through the cascade of tanks. The solute is transferred instantaneously from the outlet of a given tank to the inlet of the next one. It travels through the *N* tanks and reaches the outlet of the whole system. The concentration signal flowing out of the *N*th tank, denoted by $C_{\text{TFA}}(t)$, is the modelled BreakThrough Curve (BTC) of the karst system.

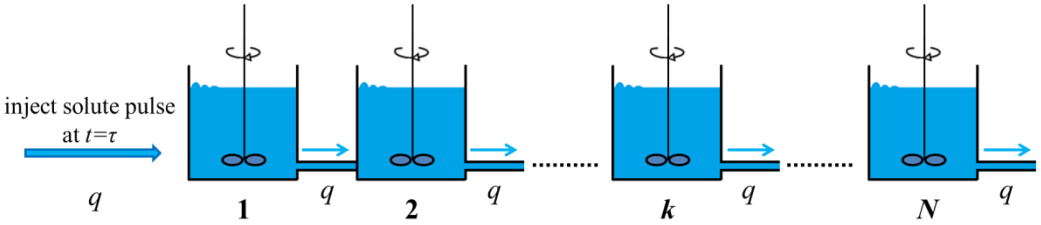

Figure 4.1 TFA model definition sketch.

Denoting the concentration within the *k*th tank as $C_k(t)$, the mass balance for the *k*th tank with the abovementioned perfect mixing assumption is:

$$V\frac{\mathrm{d}C_k(t)}{\mathrm{d}t} = Q\left(C_{k-1}(t) - C_k(t)\right) \qquad \text{(Eq. 4-1)}$$

where q (L^3/T) and V (L^3) are respectively the flow rate and the volume of a tank. Introducing the residence time $A = V/q$ (T), Eq. 4-1 becomes

$$\frac{\mathrm{d}C_k}{\mathrm{d}t} = \frac{C_{k-1} - C_k}{A} \qquad \text{(Eq. 4-2)}$$

4.2.1.2 Governing equation, unit response, and breakthrough solution

The unit response of the model in the time domain is straightforward from (Nash, 1957) by incorporating the delay function τ (T):

$$C_{\text{in}}(t) = \delta(t) \Longrightarrow C_{\text{TFA}}(t) = \begin{cases} 0 & \text{for} \quad t < \tau \\ \frac{A^N}{\Gamma(N)}(t-\tau)^{N-1}e^{-A(t-\tau)} & \text{for} \quad t \geq \tau \end{cases} \qquad \text{(Eq. 4-3)}$$

where $\delta(t)$ is Dirac's function and the Gamma function is the generalization of the factorial, allowing for non-integer *N*.

4.2.1.3 Solution in the Laplace space

To obtain the unit response of the model, an alternative method is to use Laplace transforms. Denoting by $\widehat{D}$ the Laplace transform of the delay process, one has

$$\widehat{D}(s) = \exp(-\tau s), \quad \text{(Eq. 4-4)}$$

where s is the Laplace variable. The Laplace Transform of Eq. 4-2 yields:

$$s\hat{C}_k = \frac{1}{A}\left(\hat{C}_{k-1} - \hat{C}_k\right) \Leftrightarrow \hat{C}_k = \hat{R}\hat{C}_{k-1}, \hat{R} = \frac{1}{1+As}, \quad \text{(Eq. 4-5)}$$

where $\hat{C}_k$ is the Laplace transform of $C_k(t)$, $\hat{R}$ is the unit response of a single reservoir.
The Laplace transform of the response of the whole system is:

$$\hat{C}_{\mathrm{TFA}} = \hat{C}_{\mathrm{in}}(s)\widehat{D}(s)\hat{R}^N = \exp(-\tau s)\left(\frac{1}{1+As}\right)^N \hat{C}_{\mathrm{in}}(s). \quad \text{(Eq. 4-6)}$$

where, $\hat{C}_{\mathrm{in}}(s)$ is the Laplace transform of the signal induced by solute injection, $C^{\mathrm{in}}(t)$. In what follows, the inflowing concentration signal is a pulse (Dirac) function at $t = 0$, consequently $\hat{C}_{\mathrm{in}}(s) = 1 \forall s$ and the output of the system in the Laplace domain is:

$$\hat{C}_{\mathrm{TFA}}(s) = \exp(-\tau s)\left(\frac{1}{1+As}\right)^N. \quad \text{(Eq. 4-7)}$$

The BTC in the time domain is obtained by applying the inverse Laplace transform to the $\hat{C}_{\mathrm{TFA}}(s)$. The solution of $C_{\mathrm{TFA}}(t)$ is determined by three independent parameters: A, N, and τ. As in (Nash, 1957), non-integer (positive) values are allowed for N to increase the flexibility of the model. Those who are not familiar with the TFA model please check Appendix C for the sensitivity tests of the TFA parameters.

4.2.2 Equivalence between TFA and ADE

Via numerical techniques, we investigate the required condition for the TFA and ADE to generate identical BTCs.

4.2.2.1 Equivalence with the ADE model with uniform parameters

We study this equivalence by applying the Laplace transform and Taylor Series Expansion (TSE) to the two models. The governing equation of the classical ADE model is:

$$\frac{\partial C_{\mathrm{ADE}}(x,t)}{\partial t} + u\frac{\partial C_{\mathrm{ADE}}(x,t)}{\partial x} - D\frac{\partial^2 C_{\mathrm{ADE}}(x,t)}{\partial x^2} = 0. \quad \text{(Eq. 4-8)}$$

Its solution in the Laplace domain is given as (see Appendix B for the derivation process):

$$\hat{C}_{\mathrm{ADE}}(x,s) = \exp\left(\frac{x}{2}\left(\frac{u}{D} - \sqrt{\left(\frac{u}{D}\right)^2 + \frac{4s}{D}}\right)\right). \quad \text{(Eq. 4-9)}$$

The responses of the TFA and ADE models are now compared in the limit of vanishing s. Assuming the length of the ADE model is L, a second-order TSE of Eq. 4-9 with $s \to 0$ yields:

$$\hat{C}_{\mathrm{ADE}}(x,s) = 1 - \frac{L}{u}s + \left(\frac{L^2}{2u^2} + \frac{DL}{u^3}\right)s^2 + \mathrm{HOT}, \qquad \text{(Eq. 4-10)}$$

where HOT represents the High-Order-Terms.

A second-order TSE of Eq. 4-7 with $s \to 0$ yields:

$$\hat{C}_{\mathrm{ADE}}(s) = 1 + (-\tau - AN)s + \left(\frac{A^2N(N+1)}{2} + \frac{\tau^2}{2} + AN\tau\right)s^2 + \mathrm{HOT}. \qquad \text{(Eq. 4-11)}$$

It is easy to check that the above two expressions are equivalent provided that:

$$u = \frac{L}{AN+\tau}, \qquad \text{(Eq. 4-12a)}$$

$$D = \frac{A^2NL^2}{2(AN+\tau)^3}. \qquad \text{(Eq. 4-12b)}$$

The above equivalence is valid provided that s is small so that HOT remains small compared to the first and the second-order terms. Small s in Laplace domain corresponds to large response time, t.

4.2.2.2 Equivalence with the ADE model with non-uniform parameters

A consistency analysis is carried out to study the equivalence between the TFA and a two-segment ADE model: the first segment corresponds to the delay effect in the TFA and the second segment corresponds to the reactor cascade of the TFA (Figure 4.2). A constant velocity, u, is assumed for the 2 segments. The dispersion in the first segment is defined as 0, while the second region dispersion is larger than 0. To make the delay effect, the length of the first segment is $L_1 = u\tau$.

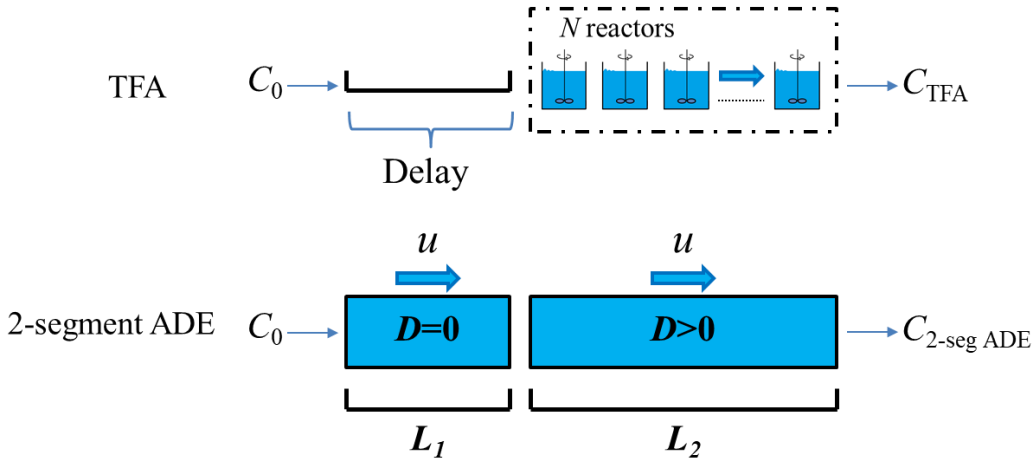

Figure 4.2. Equivalence between TFA and the two-segment ADE.

We analyze the transport process in the TFA using consistency analysis. The concentration in the k^{th} reactor is denoted as $C_{\mathrm{TFA}}(x_k,t) = C_k$. The length of one reactor is: $\Delta x = \frac{L_2}{N}$. To derive the governing equation of the concentration variation in the reactor series, we need to find another expression of $C_{k\text{-}1}$. In the limit of $\Delta x \to 0$, we apply TSE to $C_{k\text{-}1}$:

$$C_{\mathrm{TFA}}(x_{k-1},t) = C_{\mathrm{TFA}}(x_k - \Delta x, t) = C_{\mathrm{TFA}}(x_k,t) - \Delta x\frac{\partial C_{\mathrm{TFA}}(x_k,t)}{\partial x} + \frac{\Delta x^2}{2}\frac{C_{\mathrm{TFA}}(x_k,t)}{\partial x^2} + \mathrm{HOT}. \qquad \text{(Eq. 4-13)}$$

Substituting Eq. 4-13 into Eq. 4-2, yields:

$$\frac{\mathrm{d}C_{\mathrm{TFA}}(x_k,t)}{\mathrm{d}t}+\frac{1}{A}\Delta x\frac{\partial C_{\mathrm{TFA}}(x_k,t)}{\partial x}-\frac{\Delta x^2}{2A}\frac{\partial^2 C_{\mathrm{TFA}}(x_k,t)}{\partial x}=\mathrm{HOT}. \quad \text{(Eq. 4-14)}$$

Assuming that the TFA is equivalent to this two-segment ADE model, we compare Eq. 4-14 to Eq. 4-8. The two expressions are equivalent provided that:

$$u=\frac{L_2}{AN}, \quad \text{(Eq. 4-15a)}$$

$$D=\frac{{L_2}^2}{2AN^2}. \quad \text{(Eq. 4-15b)}$$

The above equivalence is valid provided that N is big, which means Δx is small so that HOT remains small compared to the first and the second-order terms.

Since the ADE model with non-uniform parameters is rarely used by the researchers, Eq. 4-12 will be applied to correlate the TFA and the ADE parameters. Summarizing the above two analyses (Section 4.2.2.1 and 4.2.2.2), we conclude that under the conditions that N is large, t is large, and Eq. 4-12 are satisfied, the signal of the TFA would be approximate to the ADE. We provide two practical examples to illustrate this equivalence (Figure 4.3).

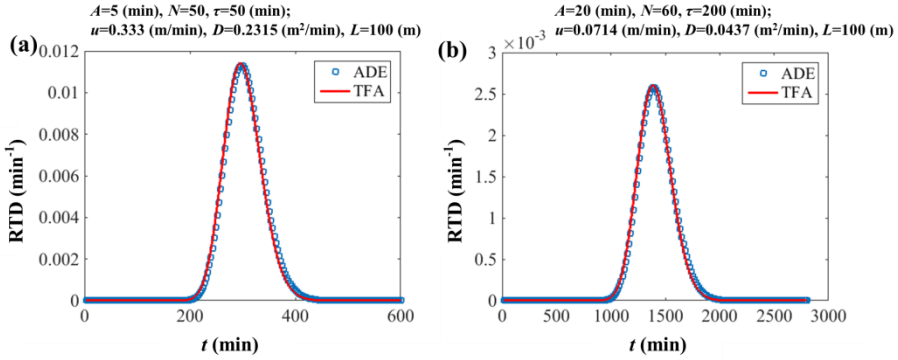

Figure 4.3. Two examples of equivalence between TFA and ADE.

Under the assumption of normal dispersion in porous media, the dispersivity $\alpha = D/u$. From Eq.12, one has:

$$\alpha=\frac{A^2NL}{2(AN+\tau)^2} \quad \text{(Eq. 4-16)}$$

4.2.3 Mobile ImMobile (MIM) model

In this study, we will compare the fitting performance of three numerical models: ADE, TFA, and MIM. The ADE and TFA have been given as Eq. 4-8 and Eq. 4-7. The one-dimensional MIM for a conservative solute transport during steady water flow is given by (van Genuchten and Wierenga, 1976). It (Figure 4.4) consists of a mobile region governed by the conventional ADE (Eq. 4-17a) and an immobile region; the two regions are coupled by an exchange term (Eq. 4-17b):

$$w_{\mathrm{m}}\frac{\partial C_{\mathrm{m}}}{\partial t}+w_{\mathrm{im}}\frac{\partial C_{\mathrm{im}}}{\partial t}=w_{\mathrm{m}}D_{\mathrm{m}}\frac{\partial^2 C_{\mathrm{m}}}{\partial x^2}-w_{\mathrm{m}}u_{\mathrm{m}}\frac{\partial C_{\mathrm{m}}}{\partial x} \quad \text{(Eq. 4-17a)}$$

$$w_{\mathrm{im}}\frac{\partial C_{\mathrm{im}}}{\partial t}=k(C_{\mathrm{m}}-C_{\mathrm{im}}) \quad \text{(Eq. 4-17b)}$$

$$w_{im} + w_m = 1 \quad \text{(Eq. 4-17c)}$$

where C_m (ML^{-3}) and C_{im} (ML^{-3}) are the solute transport concentrations in the mobile and immobile region, respectively, D_m is the dispersion coefficient (L^2T^{-1}) in the mobile region, k (T^{-1}) is the mass transfer coefficient, u_m (LT^{-1}) is the flow velocity in the mobile region, w_m (-) and w_{im} (-) are the volumetric fraction of the mobile region and the immobile region, respectively. Since the relationship between w_m and w_{im} is fixed (Eq. 4-17c), four independent parameters are calibrated to fit the experimental BTCs: u_m, D_m, k and w_m. The concentration at the outlet of the mobile region is determined as the output of the MIM model.

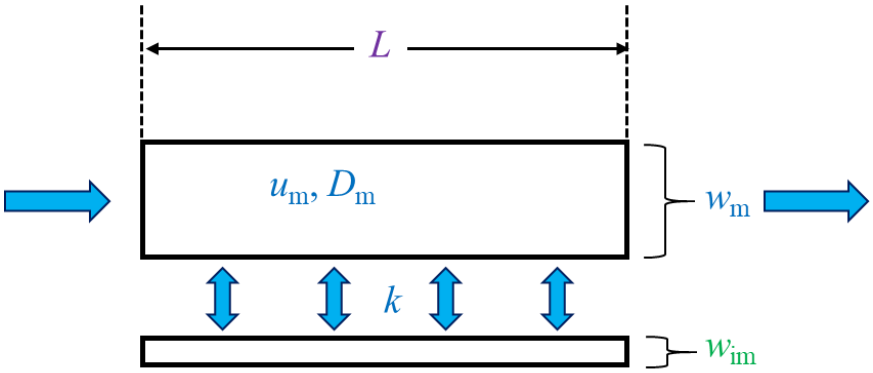

Figure 4.4. Diagram of MIM model.

4.2.4 Parameter calibration

The models' parameters are calibrated with the Markov Chain Monte Carlo (MCMC) method (Haario et al., 2006). The MCMC method is a Bayesian approach that evaluates the posterior distributions of parameters (Vrugt et al., 2006).

We first perform a manual fitting of the model's response to the experimental BTCs to find the initial parameter set. Then the Metropolis-Hastings (MH) algorithm successively draws samples from the posterior distribution by forming a Markov chain of the model parameter set. The Root-Mean-Square-Error (RMSE) objective function is applied to evaluate the deviation and the convergence of the MCMC chains:

$$\mathrm{RMSE} = \sqrt{\frac{\sum_{i=1}^{n}(C_i - Y_i)^2}{n}}, \quad \text{(Eq. 4-18)}$$

where C is the experimental data, Y is the calibrated data, n is the data quantity. Each MCMC chain includes 8000 iterations. The mean value of the last 100 sampled parameter sets is determined as the calibrated parameter value.

4.3 Computational examples

Two groups of BTCs are fitted by the three numerical models: ADE, TFA, MIM. And we compare the performance of the three models. For the convenience of modeling, all of the simulated BTCs in this study are transformed into Residence Time Distribution (RTD) with Eq. 4-19.

$$\mathrm{RTD}(t) = \frac{C(t)Q(t)}{\int_{t=0}^{t=\infty} C(t)Q(t)\mathrm{d}t}. \quad \text{(Eq. 4-19)}$$

4.3.1 Experimental BTCs

4.3.1.1 Origin of BTCs

The first group of BTCs is from our lab-scale experiments. Because the three models generate the BTCs with only one peak, we only take the single-peaked experimental BTCs: most BTCs in Chapter 2 are dual-peaked; we just take the single-peaked BTCs in Chapter 3. In total, 15 experimental BTCs (3 flow rates × 5 physical models) are used in this study (Figure 4.5).

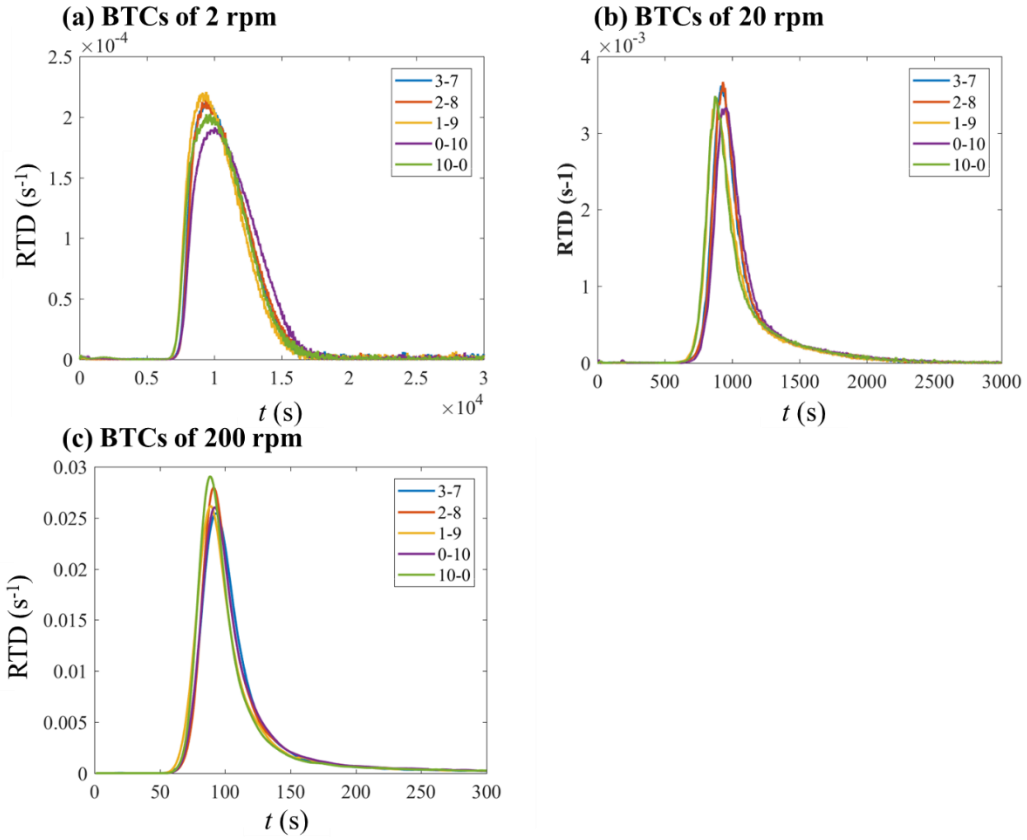

Figure 4.5. Experimental BTCs to be modeled.

4.3.1.2 Modeling the experimental BTCs

How the three models fit the 15 experimental BTCs can be found in Appendix C. We randomly choose two experimental BTCs and exhibit the fitting performance of the three models (Figure 4.6). For Experiment 3-7, 2 rpm, the ADE exhibits obvious deviation from the experimental BTC (Figure 4.6a). Both the TFA and the MIM present satisfying fitting performance (Figure 4.6b, c). For experiment 10-0, 200 rpm, again the ADE curve shows obvious deviation with the experimental BTC (Figure 4.6d). In this case, the TFA fails to well reproduce the experimental BTC (Figure 4.6e). The MIM exhibits better characterization to the experimental BTC (Figure 4.6f): the peak and the tailing are well captured by the MIM. The calibrated

parameters are shown in Table 4.1. As we have already studied how the calibrated parameters vary for these experiments in Chapter 3, we do not introduce the variation of the parameters.

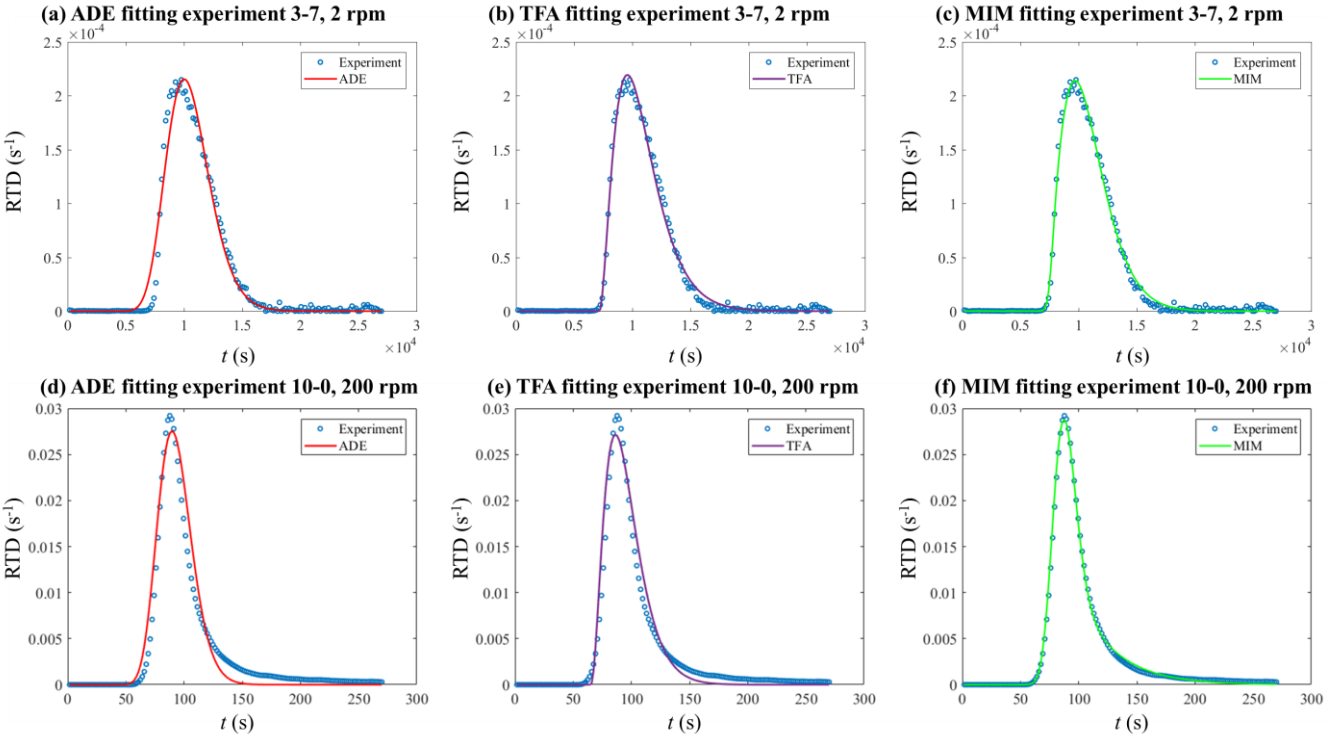

Figure 4.6. Three models fit experiments of 3-7, 2 rpm (a, b, c) and 10-0, 200 rpm (d, e, f).

Table 4.1. The calibrated model parameters to the experimental BTCs.

Q (rpm)	Experiments	Configurations	Data ADE			Data TFA				Data MIM				
			u (m/s)	D (m²/s)	RMSE	A (s)	N	τ (s)	RMSE	u_m (m/s)	D_m (m²/s)	k (1/s)	w_m (-)	RMSE
2	1	3-7	1.47×10^{-4}	3.68×10^{-6}	1.05×10^{-5}	1270.89	2.90	7053.21	6.71×10^{-6}	1.88×10^{-4}	3.04×10^{-7}	3.72×10^{-4}	0.74	4.81×10^{-6}
	2	2-8	1.47×10^{-4}	3.76×10^{-6}	1.13×10^{-5}	1396.07	2.60	7210.33	6.61×10^{-6}	1.80×10^{-4}	4.88×10^{-7}	2.99×10^{-4}	0.77	4.90×10^{-6}
	3	1-9	1.52×10^{-4}	3.94×10^{-6}	1.02×10^{-5}	1269.24	2.85	6813.38	6.40×10^{-6}	1.95×10^{-4}	4.51×10^{-7}	3.92×10^{-4}	0.74	4.68×10^{-6}
	4	0-10	1.42×10^{-4}	4.02×10^{-6}	8.76×10^{-6}	1269.04	3.42	6814.52	6.43×10^{-6}	1.87×10^{-4}	3.24×10^{-7}	3.85×10^{-4}	0.71	4.76×10^{-6}
	5	10-0	1.49×10^{-4}	4.18×10^{-6}	8.95×10^{-6}	1057.67	4.14	6198.92	6.72×10^{-6}	1.95×10^{-4}	5.85×10^{-7}	3.99×10^{-4}	0.72	5.86×10^{-6}
20	6	3-7	1.58×10^{-3}	1.81×10^{-5}	2.08×10^{-4}	83.21	2.86	742.41	2.11×10^{-4}	1.61×10^{-3}	8.32×10^{-6}	5.10×10^{-4}	0.87	3.20×10^{-5}
	7	2-8	1.57×10^{-3}	1.77×10^{-5}	2.09×10^{-4}	82.81	2.79	764.35	1.78×10^{-4}	1.60×10^{-3}	7.87×10^{-6}	5.30×10^{-4}	0.87	3.82×10^{-5}
	8	1-9	1.64×10^{-3}	2.31×10^{-5}	2.06×10^{-4}	97.45	2.49	724.32	1.68×10^{-4}	1.68×10^{-3}	9.84×10^{-6}	5.83×10^{-4}	0.86	4.14×10^{-5}
	9	0-10	1.54×10^{-3}	1.90×10^{-5}	1.95×10^{-4}	95.23	2.61	775.84	1.64×10^{-4}	1.57×10^{-3}	9.01×10^{-6}	4.98×10^{-4}	0.87	3.25×10^{-5}
	10	10-0	1.64×10^{-3}	2.36×10^{-5}	2.33×10^{-4}	103.03	2.34	725.17	1.87×10^{-4}	1.70×10^{-3}	9.06×10^{-6}	6.44×10^{-4}	0.85	2.96×10^{-5}
200	11	3-7	1.57×10^{-2}	3.40×10^{-4}	1.17×10^{-3}	10.44	3.30	65.51	1.29×10^{-3}	1.60×10^{-2}	2.01×10^{-4}	4.07×10^{-3}	0.88	2.23×10^{-4}
	12	2-8	1.59×10^{-2}	3.19×10^{-4}	1.54×10^{-3}	10.48	3.05	67.32	1.48×10^{-3}	1.65×10^{-2}	1.50×10^{-4}	5.46×10^{-3}	0.86	3.59×10^{-4}
	13	1-9	1.65×10^{-2}	3.89×10^{-4}	1.33×10^{-3}	10.08	3.45	61.11	1.34×10^{-3}	1.68×10^{-2}	2.13×10^{-4}	4.59×10^{-3}	0.86	2.84×10^{-4}
	14	0-10	1.58×10^{-2}	3.61×10^{-4}	1.38×10^{-3}	13.46	2.37	70.66	1.22×10^{-3}	1.63×10^{-2}	1.82×10^{-4}	4.83×10^{-3}	0.85	3.39×10^{-4}
	15	10-0	1.65×10^{-2}	3.17×10^{-4}	1.50×10^{-3}	9.49	3.24	64.62	1.47×10^{-3}	1.70×10^{-2}	1.62×10^{-4}	5.16×10^{-3}	0.87	3.44×10^{-4}

We compare the RMSE values of the three models fitting the experimental BTCs (Figure 4.7). First, Experiments 1-5 present the smallest RMSE values, Experiments 6-10 lie in between, and Experiments 11-15 present the largest RMSE values. Because Experiments 1-5 are under the lowest flow rate (2 rpm), the durations for these experiments are longer, then the RTD values of these experiments are lower (Figure 4.5). Thus, the calculated RMSE values are lower. For the experiments under larger flow rates (Experiments 6-

10: 20 rpm and Experiments 11-15: 200 rpm), the RTD values are larger, so the calculated RMSE values are higher.

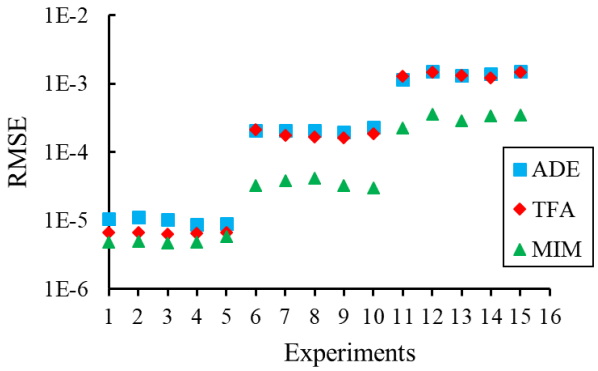

Figure 4.7. RMSE of the three models to the experimental BTCs.

For all of the experiments, the ADE exhibits the largest RMSE values, the MIM exhibits the smallest RMSE values, the RMSE values of the TFA lie in between. For Experiments 1~5 (Q = 2 rpm), the TFA can well reproduce these BTCs (for example, Figure 4.6b). So the TFA exhibits smaller RMSE values than the ADE. For Experiments 6~15 (Q = 20 and 200 rpm), the BTCs have a strong tailing effect (Figure 4.5b, c). The TFA cannot well reproduce these BTCs (for example, Figure 4.6e). Thus for Experiments 6-15, the TFA exhibits large RMSE values that are approximate to RMSE values of the ADE.

4.3.2 Numerical simulation BTCs

To make a more reliable evaluation for the three models, we apply the models to fit more BTCs. We numerically simulate the transport processes in some synthetic conduit networks and generate more transport BTCs in karst media.

4.3.1.1 Numerical simulation of transport process in karst networks

(i) Geometry of the synthetic conduit networks.

We simulate the solute transport process in synthetic conduit networks. The basic network pattern is located within a 210 m × 50 m rectangular domain (Figure 4.8). It is made of conduit segments arranged on a square lattice. Each conduit segment is 10 m long. We have intentionally located the inlet at a lower position and the outlet at a higher position. If we apply a line segment to connect the inlet and outlet, then this line segment is not vertical or parallel to any conduit. We arranged the inlet and outlet in this way because, in nature, the main flow direction cannot always be exactly vertical or parallel to the flow paths; after all, the natural conduit networks cannot always be exactly orthogonal.

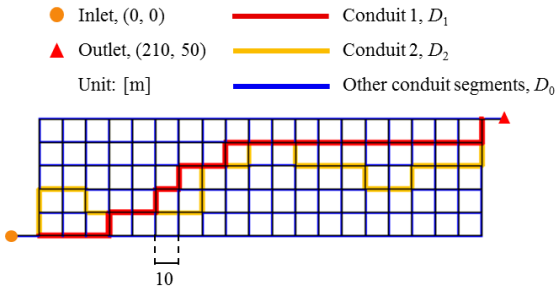

Figure 4.8. Schematic illustration of synthetic network.

Two groups of conduit segments (conduit 1 and conduit 2 in Figure 4.8) are assigned with larger diameters (D_1, D_2) to make the heterogeneity of this network. D_1 includes 24 conduit segments, D_2 includes 24 conduit segments, and D_0 includes 168 conduit segments. By adjusting the diameter setting of the conduit segments, we make eight different networks (Table 4.2). We calculate the standard deviation (S) and variance (S^2) of the diameters of the conduit segments to quantitatively evaluate the diameter contrast of the networks. The values of S and S^2 indicate that the diameter contrast increases from Network 1 to Network 8.

Table 4.2. Conduit diameters of synthetic networks.

Networks	D_1 (cm)	D_2 (cm)	D_0 (cm)	S (cm)	S^2 (cm^2)	Volume (cm^3)
Network 1	6	5.75	5	0.37	0.14	4.60
Network 2	7	6.5	5	0.74	0.55	5.02
Network 3	8	7.25	5	1.11	1.23	5.50
Network 4	9	8	5	1.48	2.18	6.03
Network 5	10	8.75	5	1.85	3.41	6.63
Network 6	11	9.5	5	2.22	4.91	7.28
Network 7	12	10.25	5	2.59	6.69	7.99
Network 8	13	11	5	2.95	8.73	8.77

(ii) Governing equations.

For simulation, we assume that the karst conduits are 1-D segments; fluid is single-phase and incompressible; conduits are fully saturated; the gravity effect is neglected. The steady-state flow is solved by the following continuity and momentum equations (Barnard et al., 1966):

$$\nabla \cdot (A\boldsymbol{u}) = 0, \qquad \text{(Eq. 4-20a)}$$

$$\rho \frac{\partial \boldsymbol{u}}{\partial t} + \rho \boldsymbol{u} \cdot \nabla \boldsymbol{u} = -\nabla p - f_{\mathrm{d}} \frac{\rho}{2d} \boldsymbol{u}|\boldsymbol{u}|, \qquad \text{(Eq. 4-20b)}$$

where A is the cross-sectional area of the conduit (L^2), d is the hydraulic diameter (L), f_{d} is Darcy's friction factor (unitless), p is the fluid pressure(M/LT^2), $\boldsymbol{u}$ is the flow velocity vector (L/T), ρ is the fluid density (M/L^3). The velocity field obtained by Eq. 4-20 is used in the ADE equation:

$$A \frac{\partial C}{\partial t} + A\boldsymbol{u} \cdot \nabla C = \nabla \cdot (A(D_{\mathrm{c}} + D_{\mathrm{d}}) \nabla C) + R, \qquad \text{(Eq. 4-21)}$$

where C is the concentration (M/L^3); D_{c} is the molecular diffusion coefficient (L^2/T); D_{d} is the

dispersion coefficient (L^2/T). The finite-element analysis is conducted with COMSOL Multiphysics.

(iii) Simulation setup.

Under steady-state flow conditions, we inject a pulse of solution (C = 1 mol/m^3, the duration of solute injection equals the time step, which is a relatively quick infusion compared to the simulation time) at the model inlet. Then the solute is transferred through the network, and the concentration variation at the model outlet is registered. Except for the flow inlet and outlet, there is no other flow exchange with outside. The model parameters are given in Table 4.3.

Table 4.3. Numerical model parameters.

	Parameters	Symbol	Value
Fluids	Density	ρ	1000 kg/m^3
	Viscosity	μ	0.89 mPa·s
Conduit parameters	Diffusion	D_c	1.25×10^{-9} m^2/s
	Dispersion	D_d	0.02 m^2/s
	Diameters	d	5 ~ 13 cm
	Friction factor	f_d	0.1
Boundary conditions	Inflow flow rate	Q	0.001 m^3/s
	Outflow pressure	p_{in}	101325 Pa
Initial conditions	Pressure	p_i	101325 Pa
	Concentration	C_i	0 mol/m^3
Simulation Settings	Simulation time	T	500 min
	Tracer pulse	T_{tracer}	0.1 min
	Time step	t_{step}	0.1 min

The density and viscosity of the incompressible fluid are determined according to the value of water at 25 °C. The diffusion coefficient is determined according to the diffusion coefficient of Cl^- in water at 25℃ (Cussler, 1997). In the experimental study of (Field and Leij, 2012), the dispersion of one conduit (diameter of 3.175 cm) is 7.4×10^{-3}m^2/s. In the experimental study of (Zhao et al., 2019), the dispersion of one conduit (diameter of 1.9 cm) ranges between 0.009 to 0.01 m^2/s. By comparison, the dispersion value applied in our simulations (0.02 m^2/s) is realistic. The numerical conduit diameters range from 0.05 to 0.13 m, which are realistic in natural karst aquifers.

Assuming a flow rate Q=0.001 m^3/s flowing through six conduits (corresponding to the six lines of conduits in the horizontal direction) with a diameter of 0.05 m, the mean velocity is 0.084 m/s. Then, the calculated Reynolds number is 4768, which corresponds to the turbulent flow regime generally observed in karst conduits (Quinlan and Ewers, 1985; Dreybrodt, 2012).

The line segment mesh size is 0.2 m. The simulation time should be long enough for most of the solute to be transported to the outlet (500 min). Each simulation compromises 5000 simulation time steps of 0.1 min.

(iv) The simulated BTCs.

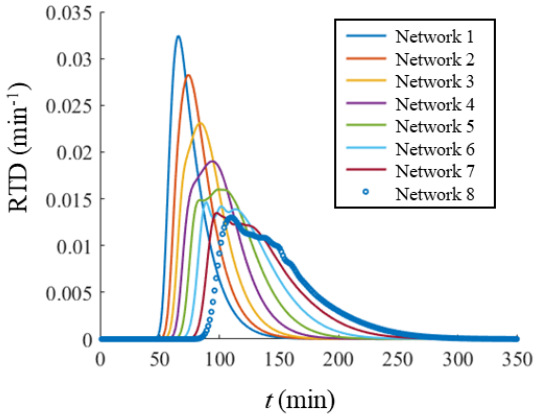

Figure 4.9. Simulated BTCs from synthetic networks.

As shown in Figure 4.9, from Network 1 to 8, the BTC gets increasingly delayed. This is because the volume of the network structure increases from Network 1 to 8 (Table 4.2). Under the same flow rate, it requires a longer time for the tracer to pass through the whole network. From Network 1 to 8, we also notice that the peak value of the curves (RTD_{peak}, min^{-1}) decreases and the curve becomes more widespread in time scale. For Networks 1~4, the BTCs have one peak and exhibit a smooth variation of the RTD value. While for Network 5, there is a bump on the RTD curve, which comes earlier than the peak of the BTC. For Networks 6~8, the concentration variations are not smooth, with multiple small peaks on the BTCs.

4.3.2.2 Modeling the simulated BTCs

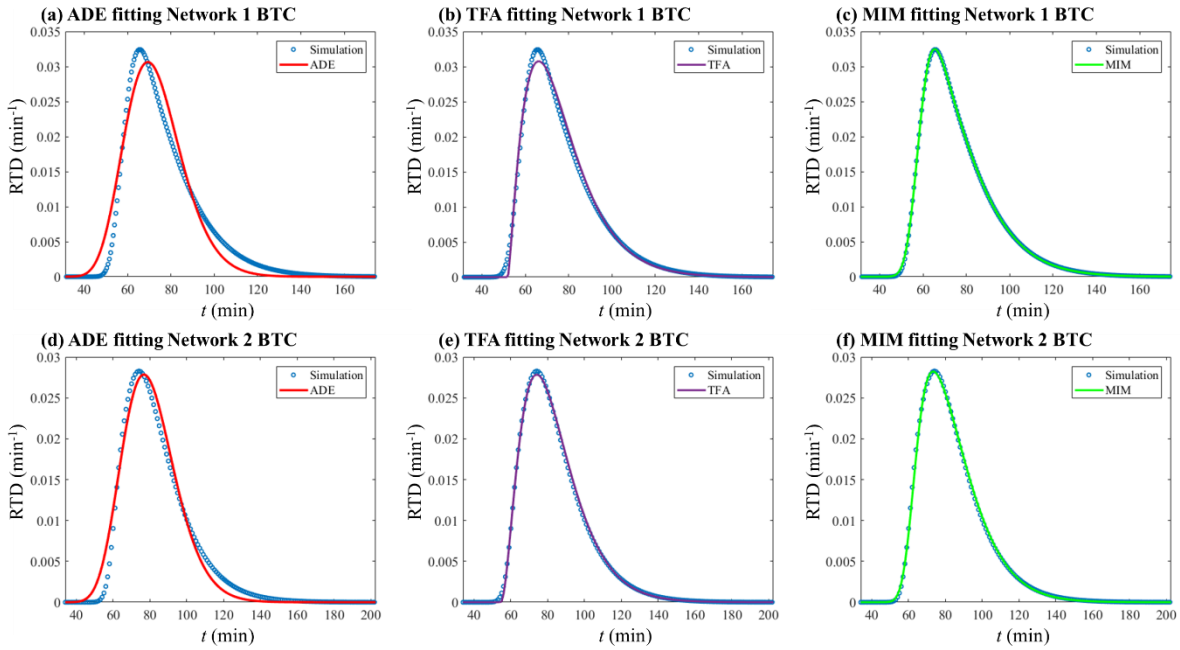

Figure 4.10. Three models fit simulated BTCs on Networks 1 and 2.

How the three models fit the eight simulated BTCs can be found in Appendix C. We randomly choose two simulated BTCs and exhibit the fitting performance of the three models (Figure 4.10). For both

networks, the ADE exhibits obvious deviation from the simulated BTCs (Figure 4.10a, d). The TFA presents better fitting performance (Figure 4.10b, e), despite a minor deviation is observed at the peak part in Figure 4.10b. The MIM presents satisfying fitting performance for both BTCs (Figure 4.10c, f).

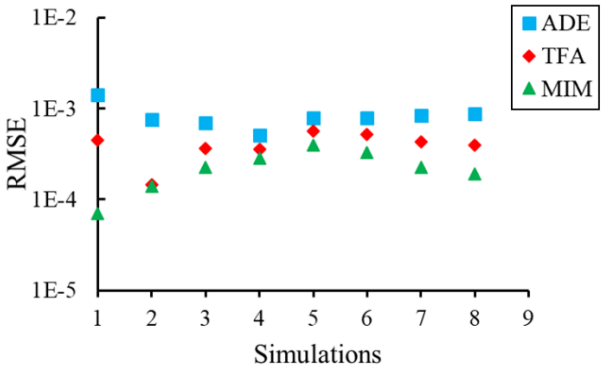

Figure 4.11. RMSE of the three models fitting simulated BTCs.

We quantitatively compare the fitting performance of the three models in Figure 4.11. The ADE presents the largest RMSE values, the MIM exhibits the smallest RMSE values, and the TFA lies between the other two models.

4.3.2.3 The calibrated parameters

Table 4.4. Calibrated model parameters to simulated BTCs.

Network	S (cm)	ADE				TFA				MIM					
		u (m/s)	D (m^2/s)	RMSE	α (m)	A (s)	N	τ (s)	RMSE	u_m (m/s)	D_m (m^2/s)	k (1/s)	w_m (-)	RMSE	α_m (m)
1	0.37	5.10×10^{-2}	1.89×10^{-1}	1.40×10^{-3}	3.71	627.97	2.36	3137.73	4.50×10^{-4}	5.84×10^{-2}	4.83×10^{-2}	3.77×10^{-4}	0.82	7.03×10^{-5}	0.83
2	0.74	4.61×10^{-2}	1.69×10^{-1}	7.62×10^{-4}	3.67	581.76	3.01	3273.15	1.46×10^{-4}	5.46×10^{-2}	4.22×10^{-2}	4.89×10^{-4}	0.80	1.40×10^{-4}	0.77
3	1.11	4.18×10^{-2}	1.78×10^{-1}	6.94×10^{-4}	4.25	603.78	3.69	3258.89	3.62×10^{-4}	5.61×10^{-2}	1.36×10^{-2}	7.97×10^{-4}	0.70	2.24×10^{-4}	0.24
4	1.48	3.81×10^{-2}	1.91×10^{-1}	5.12×10^{-4}	5.01	687.84	4.00	3337.70	3.58×10^{-4}	5.28×10^{-2}	1.08×10^{-2}	7.36×10^{-4}	0.67	2.83×10^{-4}	0.20
5	1.85	3.49×10^{-2}	2.00×10^{-1}	7.81×10^{-4}	5.71	920.45	3.21	3725.67	5.62×10^{-4}	4.79×10^{-2}	1.10×10^{-2}	5.68×10^{-4}	0.67	3.98×10^{-4}	0.23
6	2.22	3.21×10^{-2}	2.03×10^{-1}	7.96×10^{-4}	6.31	1283.14	2.37	4331.32	5.22×10^{-4}	4.31×10^{-2}	1.05×10^{-2}	4.34×10^{-4}	0.68	3.30×10^{-4}	0.24
7	2.59	2.95×10^{-2}	1.94×10^{-1}	8.36×10^{-4}	6.58	1550.44	2.09	4836.02	4.29×10^{-4}	3.89×10^{-2}	1.28×10^{-2}	3.51×10^{-4}	0.69	2.27×10^{-4}	0.33
8	2.95	2.72×10^{-2}	1.81×10^{-1}	8.72×10^{-4}	6.64	1788.37	1.96	5330.38	4.00×10^{-4}	3.52×10^{-2}	1.27×10^{-2}	3.00×10^{-4}	0.70	1.91×10^{-4}	0.36

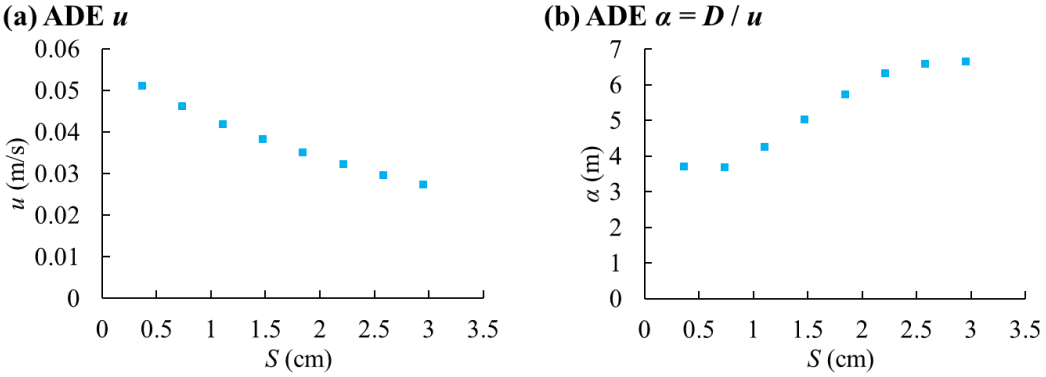

Figure 4.12. Calibrated ADE parameters for the simulations.

The calibrated parameters of the ADE model are presented in Table 4.4 and shown in Figure 4.12. As S value increases from 0.37 to 2.95 cm, u decreases from 5.10×10^{-2} to 2.72×10^{-2} m/s (Figure 4.12a).

Parameter D shows a discontinuous trend: it varies between 1.69×10^{-1} and 2.03×10^{-1} m^2/s. Since the transport velocities for these networks are different, we present the dispersivity values ($\alpha = D/u$) of the simulations in Figure 4.12b. As S value increases from 0.37 to 2.95 cm, α increases continuously from 3.71 to 6.64 m.

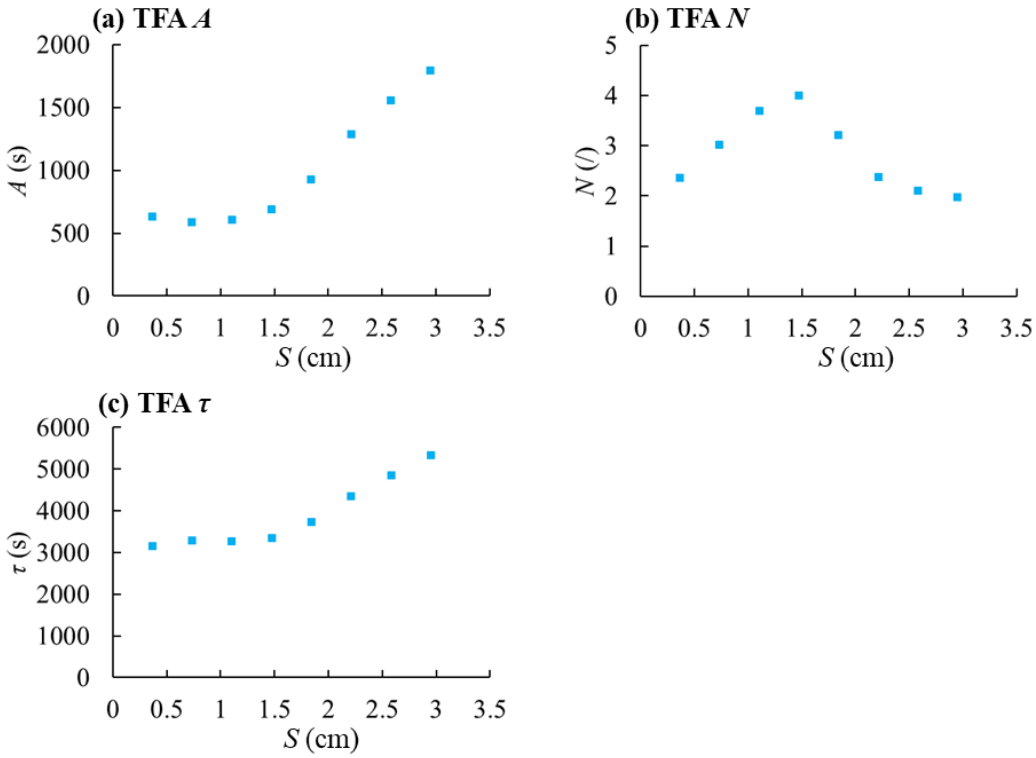

Figure 4.13. Calibrated TFA parameters for the simulations.

The calibrated parameters of the TFA model are presented in Table 4.4 and shown in Figure 4.13. As S value increases from 0.37 to 2.95 cm, A increases from 627.97 to 1788.37 s (Figure 4.13a). The variation of parameter N has two stages: as S increases from 0.37 to 1.48 cm (Network 1 to 4), N increases from 2.36 to 4.00 (Figure 4.13b); as S increases from 1.48 to 2.95 cm (Network 4 to 8), N decreases from 4.00 to 1.96. As S value increases from 0.37 to 2.95 cm, τ increases from 3137.73 to 5330.38 (Figure 4.13c). According to Figure A1b in Appendix A, parameter N represents the right-skewness of the BTCs, which may represent the heterogeneity of the karst system. We explain the variations of Figure 4.13b in Appendix D.

The limitation of the TFA becomes obvious here. The TFA parameters do not bring us information about the transport process. The physical meanings of TFA parameters are some properties of the cascade. We are unclear how to apply them to evaluate the transport processes. We overcome this limitation in Section 4.3.2.4.

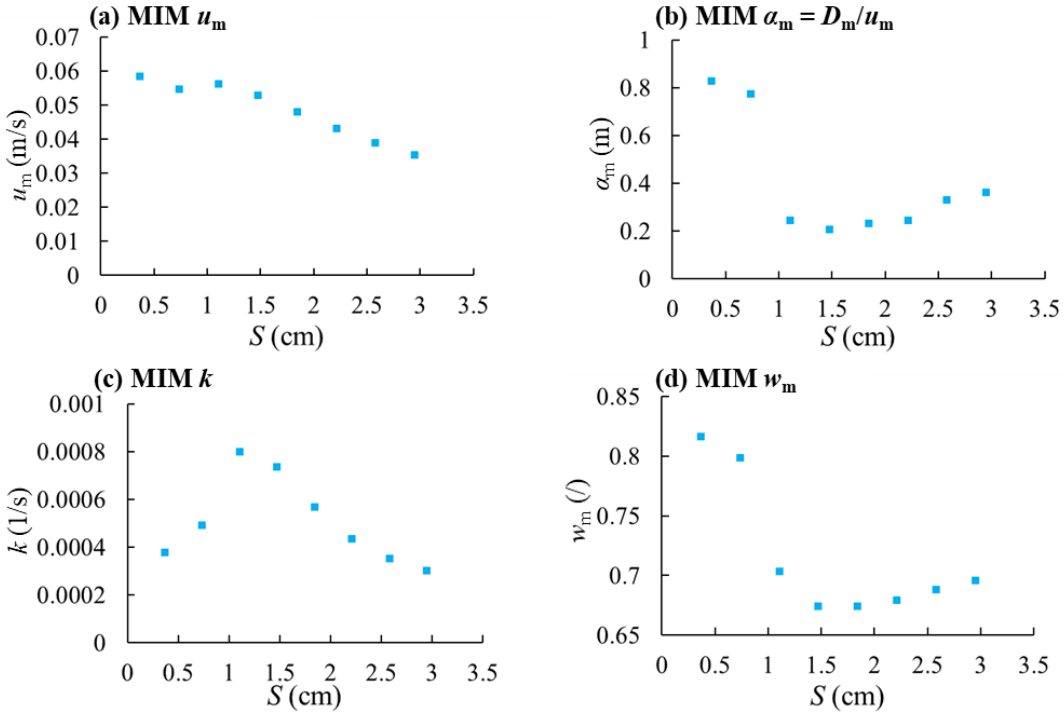

Figure 4.14. Calibrated MIM parameters for the simulations.

The calibrated parameters of the MIM model are presented in Table 4.4 and shown in Figure 4.14. As S value increases from 0.37 to 2.95 cm, the calibrated parameter u_m exhibits a decreasing trend on the whole (Figure 4.14a), it decreases from 5.84×10^{-2} to 3.52×10^{-2} m/s; despite u_m increases from 5.46×10^{-2} to 5.61×10^{-2} m/s from S = 0.74 to 1.11 cm (Network 2 to 3). For parameters α_m and w_m, these two parameters exhibit different variation trends for the networks with $S \leqslant 1.48$ cm and $S \geqslant 1.48$ cm. As S increases from 0.37 to 1.48 cm (Network 1 to 4), α_m decreases from 0.83 to 0.20 m (Figure 4.14b), and w_m decreases from 0.82 and 0.67 (Figure 4.14d). As S increases from 1.48 to 2.95 cm (Network 4 to 8), α_m increases from 0.20 to 0.36 m (Figure 4.14b), and w_m increases from 0.67 and 0.70 (Figure 4.14d). As S increases from 0.37 to 1.11 cm (Network 1 to 3), the exchange rate, k, increases from 3.77×10^{-4} to 7.97×10^{-4} 1/s (Figure 4.14c); and as S increases from 1.11 to 2.95 cm (Network 3 to 8), the exchange rate, k, decreases from 7.97×10^{-4} to 3.00×10^{-4} 1/s (Figure 4.14c). Between Network 2 and Network 3, the most significant variations of α_m and w_m values have happened.

Except for u_m, the other three parameters (α_m, k, and w_m) show discontinuous variation trends with S. The MIM parameter α_m fails to characterize the widespread degree of the simulated BTCs. As the diameter contrast increases (S increases), the simulated RTD curve becomes increasingly widespread (Figure 4.9). However, the MIM parameter α_m firstly decreases then increases with S (Figure 4.14b).

4.3.2.4 The transformation of the TFA parameters

The TFA parameters are unsuitable for characterizing a transport process because they don't bear the physical meanings related to transport. To over this limitation, we apply the derived two equations (Eq. 4-12) to transform the calibrated TFA parameters into equivalent ADE parameters.

In this study, the calibrated values of parameter N are between 2.36 and 4.0. We are clear that it requires a large N value to realize the rigid equivalence between the TFA and the ADE. Because under the condition that N is small ($N < 10$), TFA generates BTCs with right-skewness, this non-Gaussian shape cannot be well replicated by the ADE. We still transform the TFA parameters into equivalent ADE parameters (u_{TFA}, D_{TFA}, $\alpha_{TFA}=D_{TFA}/u_{TFA}$) and check whether the transformed parameters may still correspond to the actual values of the apparent flow velocity and dispersion effect under the condition of N is small.

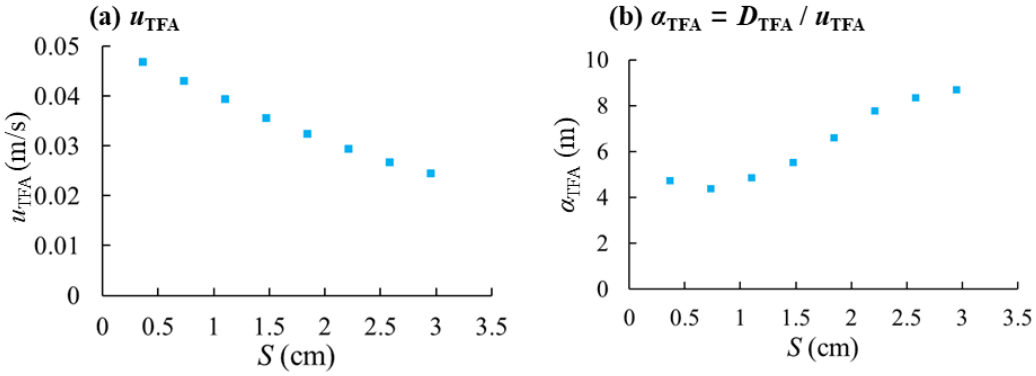

Figure 4.15. Transformed TFA parameters for the simulations.

Table 4.5. Transform TFA parameters into equivalent ADE parameters for the simulations.

Network	S (cm)	u_{TFA} (m/s)	D_{TFA} (m²/s)	α_{TFA} (m)
1	0.37	4.67×10^{-2}	2.20×10^{-1}	4.70
2	0.74	4.30×10^{-2}	1.87×10^{-1}	4.36
3	1.11	3.93×10^{-2}	1.90×10^{-1}	4.82
4	1.48	3.55×10^{-2}	1.95×10^{-1}	5.51
5	1.85	3.23×10^{-2}	2.13×10^{-1}	6.58
6	2.22	2.93×10^{-2}	2.27×10^{-1}	7.75
7	2.59	2.67×10^{-2}	2.22×10^{-1}	8.32
8	2.95	2.44×10^{-2}	2.12×10^{-1}	8.67

The transformed TFA parameters are presented in Table 4.5. Since the transport velocities for these networks are different, we only exhibit the values of u_{TFA} and α_{TFA} in Figure 4.15. As S value increases from 0.37 to 2.95 cm, the transformed parameter u_{TFA} decreases from 4.67×10^{-2} to 2.44×10^{-2} m/s (Figure 4.15a). As S increases, α_{TFA} increases from 4.70 to 8.67 m (Figure 4.15b).

The above results suggest that when the N value is small, the transformed TFA parameters still reflect the properties of the transport process. Firstly, u_{TFA} effectively reflects the advection velocity of the transport processes. From Network 1 to Network 8, the model volume has increased from 4.60 to 8.77 cm^3 (increased by 1.91 times), the average cross-section area has increased by 1.91 times. Under the same Q, the mean advection velocity may decrease by 1.91 times. The calibrated u_{TFA} has decreased exactly by 1.91

times (from 4.67×10^{-2} to 2.44×10^{-2} m/s). The above results illustrate that u_{TFA} is strictly correlated to the advection velocity in the network system.

Secondly, α_{TFA} reflects the dispersivity of the transport processes. The increasing trend of α_{TFA} reflects the variation trend for the curves in Figure 4.9: the BTCs become more widespread in time scale. As shown in Figure 4.15b, α_{TFA} effectively reflects the diameter contrast of the networks: α_{TFA} is found to be linearly correlated to the value of *S*. D_{TFA} didn't exhibit continuous and monotonous variation trends for these networks because D_{TFA} is influenced by the advection velocity. Thus, for transport processes of different transport velocities, it is better to apply α_{TFA} rather than D_{TFA} to evaluate them.

4.4 Discussion

4.4.1 Physical meaning of the TFA parameters

The TFA has one limitation: the TFA parameters are unsuitable for characterizing transport processes because they don't bear a direct physical meaning about transport. Many researchers used the cascade reactor models and the transfer function theory to interpret artificial tracer tests in karst systems (Becker and Bellin, 2013; Labat and Mangin, 2015; Sivelle and Labat, 2019; Sivelle et al., 2020). Their work proved the competence of this model in reproducing the BTCs, but their parameters did not have the physical meaning that is closely related to transport properties. We tried to overcome this limitation by studying the equivalence between the TFA and the ADE (Equation 12).

According to Section 4.2.2.2, a large value of N ($N \geq 50$) is required for the rigid equivalence between the ADE and the TFA. While Section 4.3.2.4 suggests that when N is small ($N \leq 4$), the transformed TFA parameters still effectively reflect the characteristics of the transport process: (i) u_{TFA} represents the advection velocity of the transport process; (ii) α_{TFA} represents the dispersivity of the transport process and is positively correlated to the diameter contrast (S) of synthetic networks. And the TFA parameter N characterizes skewness of the experiment curves (Figure 4.16 in Appendix A), which represents the heterogeneity of the transport process (Appendix D).

In summary, after fitting the BTCs with the TFA, we can transform the fitted parameters into corresponding ADE parameters with Equation 12. In total, we obtain three parameters to evaluate the transport process: u_{TFA}, D_{TFA} (or α_{TFA}), and N.

4.4.2 Comparison of the three models

We evaluate the fitting performance of the three transport models by applying them to 23 various BTCs (15 experimental BTCs and 8 numerical simulated BTCs). According to the modeling results, the ADE cannot well characterize all of the BTCs in this study. The TFA performs different performances for different BTCs: it can well reproduce some BTCs with right-skewness (such as Figure 4.6b, Figure 4.10b, e); while cannot well reproduce the BTCs with tailing effect (Figure 4.6e).

The MIM model exhibits the best fitting performance: its RMSE values are always smaller than the ADE and TFA. For the BTCs with a strong tailing effect, the MIM model is more valid than the TFA (Figure 4.6e, f). However, the MIM parameter α_m fails to characterize the widespread degree of the simulated BTCs (Figure 4.9, Figure 4.14b). Possibly, the widespread degree of the MIM BTCs is not only influenced by the dispersion effect of the mobile region (D_m) but also influenced by the immobile region parameters (w_{im} and k). The parameters D_m, w_m, and k should interact to characterize the widespread degree of the simulated curves. Thus parameters D_m and α_m cannot represent the widespread degree of the simulated BTCs.

In contrast, the transformed TFA parameter α_{TFA} (Figure 4.15b) effectively reflects the increasing

widespread degree of the BTCs (Figure 4.9). Thus, for the BTCs with the right skewness and without a strong tailing effect, it is better to apply the TFA than the MIM.

According to the above analysis, the three models are suitable for characterizing different BTCs. In Table 4.6, we summarize our suggestions on choosing the optimal transport model for different BTCs. (As the three numerical models can only generate single-peaked BTCs, we do not consider the multi-peaked BTCs in this study.)

Table 4.6. Suggested model for different BTCs.

BTCs shape.	Optimal model.	Follow-up
1. BTCs in Gaussian shape.	ADE	No.
2. BTCs in right skewness, and tailing effect is weak.	TFA	Transform TFA parameters into equivalent ADE parameters.
3. BTCs with strong tailing effect.	MIM	No.

4.5 Conclusions

In this paper, we applied a transfer function approach (TFA) for characterizing the karst solute transport process. In this study, we studied the similarities between the responses of the TFA and ADE models. Under the conditions that the derived equations are satisfied and the TFA parameter N value is large enough ($N \geq 50$), the TFA and ADE generate identical BTCs. If we apply the TFA to model transport BTCs, it is necessary to transform the TFA parameters (A, N, and τ) to equivalent ADE parameters (u and D). Because the TFA parameters did not have the physical meaning that is closely related to transport properties. Even when N is small (when the equivalence between ADE and TFA is not strictly realized), the transformed parameters (u_{TFA}, D_{TFA}) still reflect the characteristics of the transport process. Thus, after applying the TFA to fit some BTCs, we can do this transformation to make the fitted parameters more relevant to the transport process.

We apply three transport models to fit 23 various BTCs (15 experimental BTCs and 8 numerical simulated BTCs). According to the modeling results, the ADE fails well reproduce all of the BTCs in this study. TFA has better performance than the ADE, but it cannot well reproduce the BTCs with a strong tailing effect. MIM can well reproduce most of the BTCs, including BTCs with a strong tailing effect. The limitation of the MIM is that its parameter α_m (or D_m) fails to correctly represent the widespread degree of the simulated BTCs. The three models are suitable for different situations. We provide suggestions on choosing the optimal transport model for different BTCs.

The diameter contrast of the conduit network influences the transport process significantly. Increasing the diameter contrast makes the curve more widespread in time scale. When the diameter contrast is low, the BTCs have only one peak; as diameter increases, the BTCs may exhibit multiple peaks.

Reference

Bear, J., 1972. Dynamics of Fluids in Porous Media. American Elsevier Publishing, New York.

Bakalowicz, M., 2005. Karst groundwater: a challenge for new resources. Hydrogeology journal, 13(1), pp.148-160.

Becker, M. and Bellin, A., 2013. A reservoir model of tracer transport for karstic flow systems. Hydrogeology Journal, 21(5), pp.1011-1019.

Cussler, E. L., 1997. Diffusion: Mass Transfer in Fluid Systems (2nd ed.). New York: Cambridge University Press.

Dreybrodt, W., 2012. Processes in karst systems: physics, chemistry, and geology (Vol. 4). Springer Science & Business Media.

Edwardson, K.J., Bowden, W.B., Dahm, C. and Morrice, J., 2003. The hydraulic characteristics and geochemistry of hyporheic and parafluvial zones in Arctic tundra streams, north slope, Alaska. Advances in Water Resources, 26(9), pp.907-923.

Florea, L.J. and Wicks, C.M., 2001. Solute transport through laboratory-scale karstic aquifers. Geography/Geology Faculty Publications, p.11.

Field, M.S. and Leij, F.J., 2012. Solute transport in solution conduits exhibiting multi-peaked breakthrough curves. Journal of Hydrology, 440, pp.26-35.

Goldscheider, N., Meiman, J., Pronk, M. and Smart, C., 2008. Tracer tests in karst hydrogeology and speleology. International Journal of Speleology, 37(1), pp.27-40.

Ghodrati, M. and Jury, W.A., 1992. A field study of the effects of soil structure and irrigation method on preferential flow of pesticides in unsaturated soil. Journal of contaminant Hydrology, 11(1-2), pp.101-125.

Gooseff, M.N., Wondzell, S.M., Haggerty, R. and Anderson, J., 2003. Comparing transient storage modeling and residence time distribution (RTD) analysis in geomorphically varied reaches in the Lookout Creek basin, Oregon, USA. Advances in Water Resources, 26(9), pp.925-937.

Haario, H., Laine, M., Mira, A. and Saksman, E., 2006. DRAM: efficient adaptive MCMC. Statistics and Computing, 16(4), pp.339-354.

Hauns, M., Jeannin, P.Y. and Atteia, O., 2001. Dispersion, retardation and scale effect in tracer breakthrough curves in karst conduits. Journal of Hydrology, 241(3-4), pp.177-193.

Keefe, S.H., Barber, L.B., Runkel, R.L., Ryan, J.N., McKnight, D.M. and Wass, R.D., 2004. Conservative and reactive solute transport in constructed wetlands. Water Resources Research, 40(1).

Labat, D. and Mangin, A., 2015. Transfer function approach for artificial tracer test interpretation in karstic systems. Journal of Hydrology, 529, pp.866-871.

Levy, M. and Berkowitz, B., 2003. Measurement and analysis of non-Fickian dispersion in heterogeneous porous media. Journal of contaminant hydrology, 64(3-4), pp.203-226.

Majdalani, S., Chazarin, J.P., Delenne, C. and Guinot, V., 2015. Solute transport in periodical heterogeneous porous media: Importance of observation scale and experimental sampling. Journal of Hydrology, 520, pp.52-60.

Majdalani, S., Guinot, V., Delenne, C. and Gebran, H., 2018. Modeling solute dispersion in periodic heterogeneous porous media: Model benchmarking against experiment experiments. Journal of Hydrology, 561, pp.427-443.

Massei, N., Wang, H.Q., Field, M.S., Dupont, J.P., Bakalowicz, M. and Rodet, J., 2006. Interpreting tracer breakthrough tailing in a conduit-dominated karstic aquifer. Hydrogeology Journal, 14(6), pp.849-858.

Martinez, C.J. and Wise, W.R., 2003. Analysis of constructed treatment wetland hydraulics with the transient storage model OTIS. Ecological Engineering, 20(3), pp.211-222.

Mohammadi, Z., Gharaat, M.J. and Field, M., 2019. The Effect of Hydraulic Gradient and Pattern of Conduit Systems on Tracing Tests: Bench-Scale Modeling. Groundwater, 57(1), pp.110-125.

Moreno, L. and Tsang, C.F., 1991. Multiple‐peak response to tracer injection tests in single fractures: A numerical study. Water Resources Research, 27(8), pp.2143-2150.

Morales, T., Uriarte, J.A., Olazar, M., Antigüedad, I. and Angulo, B., 2010. Solute transport modelling in karst conduits with slow zones during different hydrologic conditions. Journal of Hydrology, 390(3-4), pp.182-189.

Nash, J.E., 1957. The form of the instantaneous unit hydrograph. IASH Publications, 45 (3-4), 114-121.

Perrin, J. and Luetscher, M., 2008. Inference of the structure of karst conduits using quantitative tracer tests and geological information: example of the Swiss Jura. Hydrogeology Journal, 16(5), pp.951-967.

Quinlan, J. F. and Ewers, R. O., 1985. Ground water flow in lime-stone Terranes: Strategy, rationale and procedure for reliable, efficient monitoring of ground water quality in Karst areas. Proceedings of the Fifth National Symposium and Exposition on Aquifer Restoration and Ground Water Monitoring, Columbus, Ohio. pp. 197-234.

Runkel, R.L., 1998. One-dimensional transport with inflow and storage (OTIS): A solute transport model for streams and rivers (Vol. 98, No. 4018). US Department of the Interior, US Geological Survey.

Roth, K. and Jury, W.A., 1993. Linear transport models for adsorbing solutes. Water resources research, 29(4), pp.1195-1203.

Silva, O., Carrera, J., Dentz, M., Kumar, S., Alcolea, A. and Willmann, M., 2009. A general real-time

formulation for multi-rate mass transfer problems. Hydrology and Earth System Sciences, 13(8), pp.1399-1411.

Skopp, J., Gardner, W.R. and Tyler, E.J., 1981. Solute movement in structured soils: Two-region model with small interaction. Soil Science Society of America Journal, 45(5), pp.837-842.

Sivelle, V., 2019. Couplage d'approches conceptuelles, systémiques et distribuées pour l'interprétation de traçages artificiels en domaine karstique: implications pour la détermination de la strucure interne des aquifères karstiques (Doctoral dissertation, Université Paul Sabatier-Toulouse III).

Sivelle, V. and Labat, D., 2019. Short-term variations in tracer-test responses in a highly karstified watershed. Hydrogeology Journal, 27(6), pp.2061-2075.

Sivelle, V., Labat, D., Duran, L., Fournier, M. and Massei, N., 2020. Artificial tracer tests interpretation using transfer function approach to study the Norville Karst system. In Eurokarst 2018, Besançon (pp. 193-198). Springer, Cham.

Tinet, A.J., Collon, P., Philippe, C., Dewaide, L. and Hallet, V., 2019. OM-MADE: An open-source program to simulate one-dimensional solute transport in multiple exchanging conduits and storage zones. Computers & Geosciences, 127, pp.23-35.

Van Genuchten, M.T. and Wierenga, P.J., 1976. Mass transfer studies in sorbing porous media I. Analytical solutions 1. Soil Science Society of America Journal, 40(4), pp.473-480.

Vrugt, J.A. et al. (2006) “Multi-objective calibration of forecast ensembles using Bayesian model averaging,” Geophysical Research Letters, 33(19).

Wang, C., Wang, X., Majdalani, S., Guinot, V. and Jourde, H., 2020. Influence of dual conduit structure on solute transport in karst tracer tests: An experimental laboratory study. Journal of Hydrology, 590, p.125255.

Zhao, X., Chang, Y., Wu, J. and Xue, X., 2019. Effects of flow rate variation on solute transport in a karst conduit with a pool. Environmental Earth Sciences, 78(7), pp.237.

Appendix

Appendix A. The sensitivity test of TFA

As many researchers are not familiar with the TFA, we show the sensitivity tests of the TFA parameters. Figure. A1 shows how the three TFA parameters influence the BTCs' shape. Higher *A* value makes BTCs more widespread and peak more delayed (Figure 4.16a). Figure 4.16b-c show seven BTCs related to the influence of the parameter *N*. If *N*=1, the concentration rises to the peak instantly then decreases exponentially, reflecting the idealized assumption of instantaneous injection and perfect mixing in the tanks. Such a shape is rarely observed, so the *N* value should be defined to be larger than 1 in practical application. Small *N* values produce curves with a right-skewness (Figure 4.16b), which indicates anomalous transport. As the *N* value increases, the skewness of the curves gradually reduced. When the *N* value becomes big enough ($N \geq 50$), the curves appear symmetrical (Figure 4.16c). Increasing *N* causes the peak time to be increasingly delayed. Increasing τ value causes the BTCs to be increasingly delayed (Figure 4.16d), while it does not influence the shape of the BTCs.

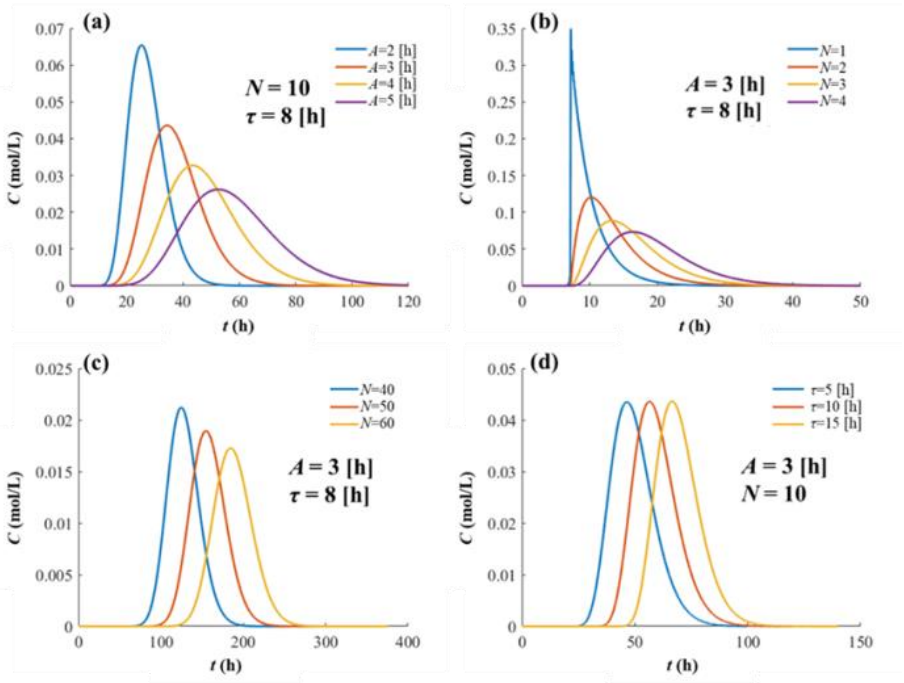

Figure 4.16. The sensitivity tests of the TFA parameters.

Appendix B. The solution of the ADE in the Laplace domain

Advection Dispersion Equation (ADE) is the classical model for characterizing the solute transport process. If we do not consider solute degradation or adsorption/desorption, the governing equation is:

$$\frac{\partial C_{ADE}(x,t)}{\partial t} + u\frac{\partial C_{ADE}(x,t)}{\partial x} - D\frac{\partial^2 C_{ADE}(x,t)}{\partial x^2} = 0, \qquad \text{(Eq. 4-22B1)}$$

where, $C_{ADE}(x, t)$ [M/L^3] is the concentration, u [L/T] is the flow velocity, and D [L^2/T] the dispersion coefficient, x [L] is the distance in the model. The concentration observation is at distance L [L].

Doing Laplace transform to (B1) yields:

$$s\hat{C}_{ADE}(x,s) + u\frac{\partial \hat{C}_{ADE}(x,s)}{\partial x} - D\frac{\partial^2 \hat{C}_{ADE}(x,s)}{\partial x^2} = 0. \quad \text{(Eq. 4-23B2)}$$

Solving the second-order differential equation yields:

$$\hat{C}_{ADE}(x,s) = k_1 \exp(\lambda_1 x) + k_2 \exp(\lambda_2 x), \quad \text{(Eq. 4-24B3a)}$$

$$\lambda_1 = \frac{1}{2}\left(\frac{u}{D} - \sqrt{\left(\frac{u}{D}\right)^2 + \frac{4s}{D}}\right), \quad \text{(Eq. 4 24B3b)}$$

$$\lambda_2 = \frac{1}{2}\left(\frac{u}{D} + \sqrt{\left(\frac{u}{D}\right)^2 + \frac{4s}{D}}\right). \quad \text{(Eq. 4 24B3c)}$$

Since λ_2 is larger than 0, we need to let k_2 =0, otherwise, the solution will be unbounded concerning x. The value of k_1 is determined by the boundary condition. As we also give a Dirac delta function as the solute injection at x = 0, we obtain:

$$k_1 = \hat{C}_{ADE}(0,s) = 1. \quad \text{(Eq. 4-25B4)}$$

So, (B3) becomes:

$$\hat{C}_{ADE}(x,s) = \exp\left(\frac{x}{2}\left(\frac{u}{D} - \sqrt{\left(\frac{u}{D}\right)^2 + \frac{4s}{D}}\right)\right). \quad \text{(Eq. 4-26B5)}$$

Appendix C. The fitting performance of the three models

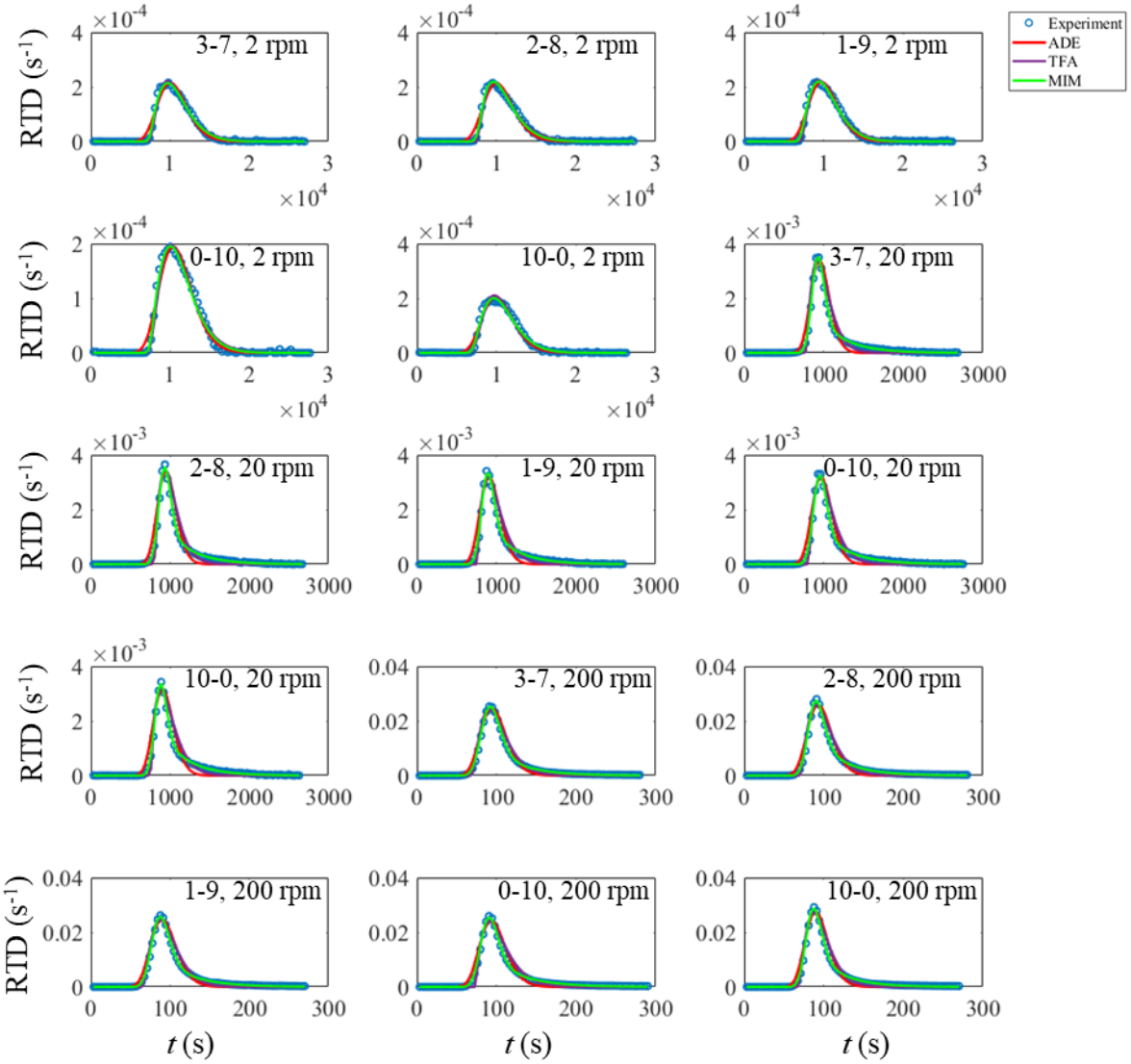

Figure 4.17. Three models fit experimental BTCs.

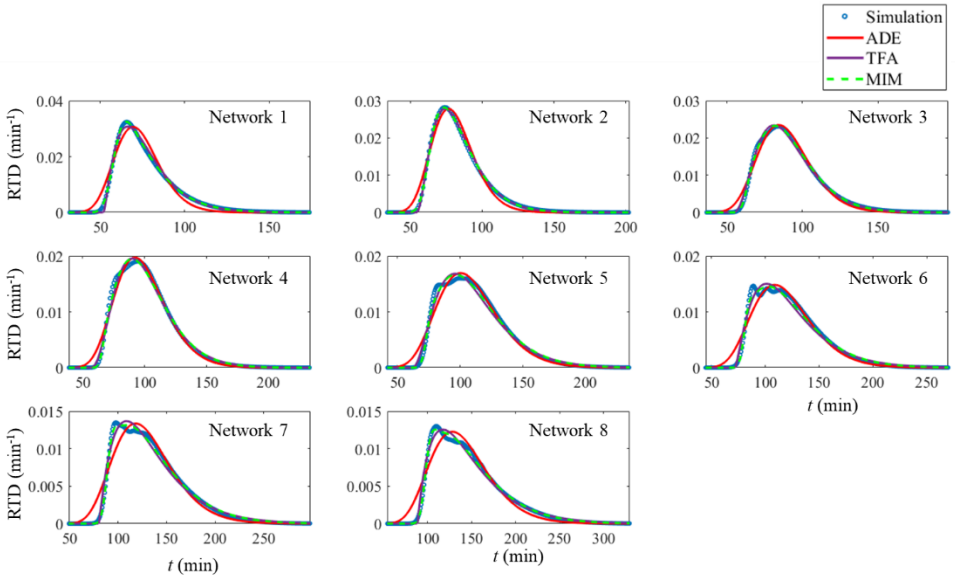

Figure 4.18. Three models fit simulated BTCs.

Appendix D. Explanation of calibrated parameter *N* for the synthetic networks.

Figure 4.16b shows that as *N* value decreases, the TFA generates BTCs with stronger right skewness, which should correspond to the stronger heterogeneity of a karst system.

In this study, we simulated the transport process in eight synthetic conduit networks and we applied the TFA to fit the simulated BTCs. We have expected that: as the network diameter contrast increases, the karst system exhibits stronger heterogeneity, then the simulated BTCs may become more right-skewed, a smaller *N* value should be obtained. However, this expected result (stronger diameter contrast induces smaller *N* value) is not true: in Figure 4.13b, we observed non-monotonic relationship between parameter *N* and conduit diameter contrast for the synthetic networks.

We manage to explain the variation of parameter *N* (Figure 4.13b) by further investigating the transport processes. Consider: 1. *N* is a transport model parameter; 2. the simulated transport process is influenced by the diameter distribution and simulated velocity distribution in the networks. Thus, we extract and check the flow rate (Q_{seg}) values on the 214 conduit segments of networks from the numerical simulations:

$$Q_{seg} = \frac{v_{seg} d_{seg}^2 \pi}{4}, \qquad \text{(Eq. 4-27D1)}$$

where d_{seg} is the diameter of each conduit segments, v_{seg} is the velocity of each conduit segments. To make it dimensionless, the Q_{seg} values are compared to the main flow rate Q.

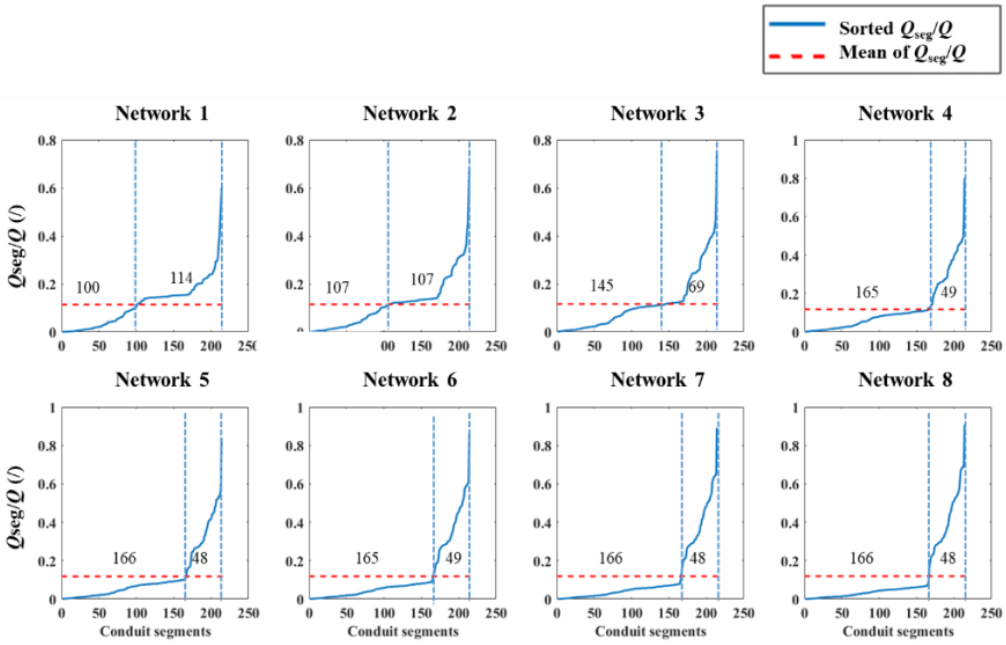

Figure 4.19. The sorted (Q_{seg}/Q) value of the transport simulations of the eight networks.

We check the (Q_{seg}/Q) values to explore how parameter *N* is actually influenced by the diameter contrast. As shown in Figure 4.19, we sort the values (Q_{seg}/Q) for each network, as denoted by blue solid line; the mean value of (Q_{seg}/Q) is denoted by the red dashed line. The red dashed line divides the curve

into two parts: first part (left side) represents the conduit segments whose flow rate is smaller than the mean flow rate; second part (right side) represents the conduit segments whose flow rate is larger than the mean flow rate. As shown in Figure 4.20a, from Network 1 to 4, the quantity of the smaller-flow-rate (SFR) conduit segments increases and the quantity of the larger-flow-rate (LFR) conduit segments decreases; from Network 4 to 8, the both parts remain the same. Network 4 is dividing line for the variation of the quantities of LFR and SFR; while it is also the dividing line for the variation of parameter *N* (Figure 4.13b). This suggests that the quantities of the LFR / SFR segments may play a role in the variation of parameter *N*.

In Figure 4.20b, we present the distribution of the LFR and SFR conduit segments. For Networks 1-3, the diameter contrast is not large enough to confine the main flow in the larger-diameter conduits. Thus, more conduits segments are ranked as the LFR segments and they are distributed all over the whole network. Networks 1-3 exhibit more complex LFR segment structures. More complex LFR structure may cause higher right-skewness of the BTCs, which induces smaller value of the TFA parameter *N*. For Networks 4-8, the LFR segments only gather around the larger-diameter segments (Figure 4.8), which means the diameter contrast is so significant that the larger-diameter segments bear most of the flow. With above analysis, we can explain the relationship between parameter *N* and diameter contrast (*S*) of the networks (Figure 4.13b). From Network 4 to 1, the LFR segments make up increasingly complex network structures. This more complex LFR segment structure causes the BTCs to be more right-skewed, thus the *N* value decreases from 4.0 to 2.36 from Network 4 to 1. And from Network 4 to 8, the LFR segments make up almost same structures. Under a constant LFR structure, the increasing diameter contrast causes stronger heterogeneity. This stronger heterogeneity should cause the simulated BTCs to be more right-skewed, so the calibrated *N* value decreases from 4.0 to 1.96 from Network 4 to Network 8.

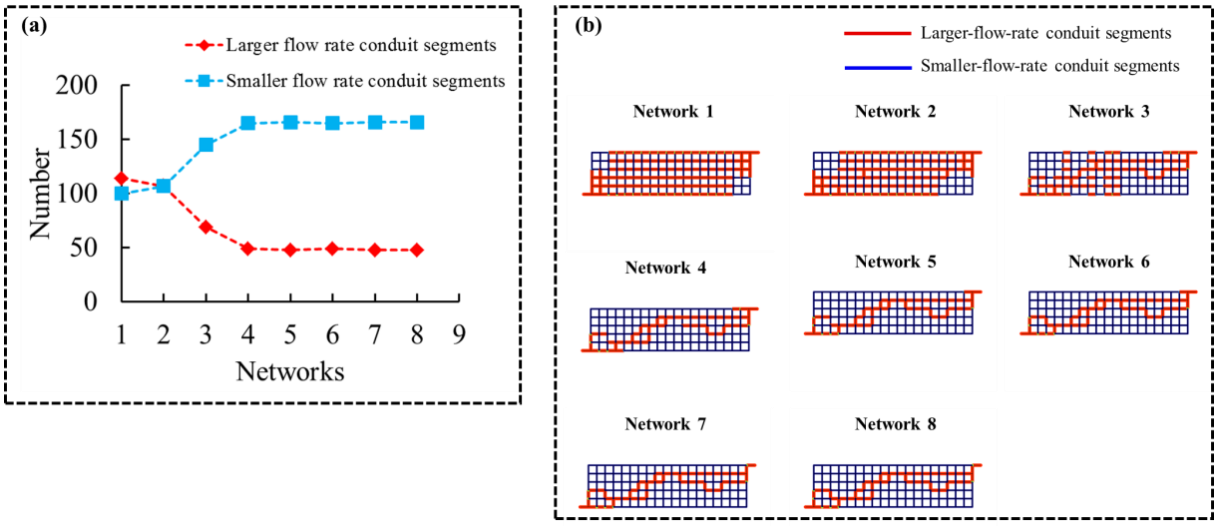

Figure 4.20. The distribution of the LFR and SFR conduit segments for the 8 networks of group 1.

In summary, for networks with relatively small diameter contrast (for example, Networks 1-3),

parameter *N* is mostly influenced by the complexity of the LFR network: more complex LFR network causes smaller *N*. For networks with relatively strong diameter contrast (for example, Networks 4-8), parameter *N* is mostly influenced by the diameter contrast: larger diameter contrast causes smaller *N*.

CHAPTER 5

Résumé :

Ce chapitre propose une nouvelle méthodologie pour caractériser un réseau de conduits karstiques à l'échelle d'un site expérimental comprenant une vingtaine de forages. Celle-ci repose sur une méthode de tomographie hydraulique qui considère un modèle de réseau de conduits discrets pour représenter explicitement le réseau de conduits souterrains, et intègre les réponses hydrodynamiques aux essais par pompage et des données de traçage de colorant pour contraindre la distribution de diamètre du réseau de conduits karstiques. Cette méthode est appliquée au site expérimental du Terrieu, où divers tests hydrauliques et différents essais par traçage ont été réalisés, afin de préciser les propriétés du réseau de conduits connu à l'échelle de ce site.

Chapter 5 Inversion characterization of karst conduit network of a karst aquifer

Abstract

Recently, different HT methods have been applied on the Terrieu well site, which corresponds to an experimental site of about 2500 m^2 with 22 boreholes, located on the Lez karst aquifer. Former studies considered equivalent porous media model to represent the main flow path network at the scale of the experimental site. In this chapter, we propose a new inverse approach, based on: 1) The use of discrete conduit network (DCN) model to explicitly represent the conduits; 2) the consideration of the spatial variation of the parameters of the DCN segments; 3) the joint inversion of steady-state pumping test data and transient tracing test data. We aim to realize a more precise characterization of the main flow paths of the experimental site, but also figure out the relative importance of pumping test data and tracing test data to the inversion results.

In our application, we considered segments of both small-diameter parts and large-diameter parts for each conduit in order to be more representative of a natural karst conduit network. For each flow path, theinfluence of the large-diameter part is adjusted by the diameter (dia) of the numerical conduits, while the influence of the small-diameter is constrained by the friction factor (fd). We show that the forward model can appropriately reproduces the two types of field data, only when the both parameters (dia, fd) are considered to adjust the field data.

With the proposed methodology, we better characterized the properties of the conduit network at the scale of the Terrieu field siteThe diameter distribution of each karst conduit is a more direct representation of the main flow paths properties than the transmissivity of the EPM models. The application of the new inversion method may provide insight for the researchers who are interested in characterizing fractured and karst aquifers with HT techniques when both pumping test data and tracing test data are available.

5.1 Introduction

Hydraulic tomography (HT) is a sequential cross-hole hydraulic test followed by inversion of all the data to map the spatial distribution of aquifer hydraulic properties, e.g. transmissivity (K) and storativity (S). After constructing a numerical geological model to imitate the real aquifer, researchers adjust the parameters of the model to reproduce the data of the real hydraulic tests. Then the calibrated parameter field can effectively characterize the heterogeneous distribution of the hydraulic properties of the real aquifer (Hao et al., 2008; Illman et al., 2007; Liu et al., 2007; Sharmeen et al., 2012).

Recently, HT has been applied to estimate the hydraulic properties of fractured and karst aquifers.

Some researchers have applied the equivalent porous medium (EPM) model to characterize groundwater flow in fractured/karstified rocks. For these applications, the fractures and karst conduits are represented by the grids of high *K* values and low *S* values; the matrix is represented by the grids of low *K* and high *S* values. It is relatively easier to apply the EPM model because its application doesn't require the presumption about the location and geometry of the underground fractures or karst conduits. Although the EPM models may seem to be oversimplified and less appropriate to conceptually represent fractured rocks, they can still capture the spatial variability of flow properties and the connectivity of preferential flow paths (Abusaada & Sauter, 2013; Larocque et al., 1999; Neuman, 2005). For example, Wang et al. (2016) have obtained the transmissivity field of the Terrieu well site, which is a fractured and karst formation. Their inverted transmissivity fields exhibited that highly conductive channels are embedded in a low transmissivity matrix region. And the spatial trend of the main flow channels is in good agreement with that of the main fracture sets mapped on outcrops in the vicinity of the Terrieu site, suggesting that the hydraulic anisotropy is consistent with the structural anisotropy. Some researchers have adjusted the classical HT technique to make it more adaptive to the discrete geometries of fractured and karst aquifers. For example, Lee and Kitanidis (2013) have induced restrictions on the total variation from the prior model. Some researchers (Hale, 2009; Lochbühler et al., 2015; Soueid Ahmed et al., 2015) introduced constraints of a priori knowledge to the inverse model. Fischer et al. (2017a) proposed the Cellular Automata-based Deterministic Inversion (CADI) method based on a bayesian formulation, adapted for the inversion of linear structures. It can be used to identify preferential flow paths in highly heterogeneous karst aquifer.

Despite these advances, the EPM model remains an oversimplification of natural flow paths and cannot properly represent most of the main flow paths properties of fractured and karst aquifers (Borghi et al., 2016; Wang et al., 2016). For these aquifers, the EPM may be feasible under some specific conditions: karstic aquifers at a kilometric scale (Abusaada and Sauter, 2013; Larocque et al., 1999b) and when fracture networks have a high density (Long et al., 1982; Sahimi, 2011). If the scale of investigation is not that large, the EPM becomes unreliable to represent the fractured and karst aquifers, which can be extremely heterogenous (Illman, 2014). Because the EPM cannot explicitly incorporate crucial structural information such as statistics on main fracture/ conduit orientations or locations. May 2000, a severe accident of 7 deaths has been caused by the application of EPM to estimate the hydraulic behavior in a karst aquifer (Goldscheider and Drew, 2014; Kresic and Stevanovic, 2009; Worthington et al., 2002). The severe accident always reminds the karst community to adopt the models that are more applicable to more accurately characterize the hydraulic properties of karst aquifers.

The discrete fracture network (DFN) or discrete conduit network (DCN) model is more appropriate to represent the main flow paths network of the fractured and karst aquifers at the scale of the Terrieu site (Wang et al., 2016). In these models, discrete fractures or karst conduits are simplified as 1-D line segments. The most appealing feature of these models is that the connectivity of the flow paths is explicitly expressed.

Such model has significantly improved the modeling performance for the fractured and karst aquifers (le Goc et al., 2010; Saller et al., 2013). However, the main challenge associated with this approach is that the field data describing the location, geometry, spatial distribution and hydraulic properties of each fracture and karst are often limited (Borghi et al., 2016; Wang et al., 2016).

Numerous researchers managed to estimate the fracture/ karst network geometry and their properties by inverting the data of hydraulic tests realized in the field. Two main strategies have been developed. Strategy 1 focuses on estimating the structure of the fracture/ karst network. It has three main steps: 1) randomly generate a large number of different structures; 2) take those structures into account to carry out forward simulations of the hydraulic tests; 3) evaluate the structures by comparing the simulated data of the structures to the observed data in the field. For example, Borghi et al. (2016) have generated 150 karst network structures and they identified the optimal karst network structure by inverting the hydraulic test data and tracing test data; Somogyvari et al. (2017) developed a reversible jump Markov Chain Monte Carlo method that updates the structure of the discrete network semi-randomly and they evaluate the structures by comparing the simulated tracing BTCs on these networks to the reference BTCs. However, the limitation of the first strategy is that the spatial distribution of the parameters of the discrete segments is not effectively characterized. Because they have assumed a constant diameter (or aperture) for the conduit (or fracture) segments.

Instead of generating numerous different structures, the second strategy refers to the serial studies realized by Klepikova et al. (2013, 2014, 2020). First, they presume several simplified structures to integrally represent the underground fracture network; second, characterize the spatial distribution of the hydraulic parameters of the fracture segments by the inversion field test data. Klepikova et al. (2013, 2014, 2020) have applied different types of field data for inversion, including inter-borehole flowmeter tests, heat transfer tests, and transient hydraulic pumping tests. Strategy 2 considers the spatial variation of discrete fracture properties, thus overcomes the limitation of Strategy 1. However, Strategy 2 also has one limitation: the presumed network structures are over-simplified and ideally orthogonal.

The above inversion studies have been realized with various types of field test data. The steady-state pressure data are especially common in these studies (Cardiff et al., 2009; Hao et al., 2008; Illman, 2014; Liu et al., 2002; Wang et al., 2016; Yeh and Liu, 2000). It is also common to apply the transient pressure variation data during the pumping tests, which allows for determining the storativity field of the aquifer (Bohling and Butler Jr, 2010; Cappa et al., 2008). Recently researchers have applied the data of harmonic pumping tests to identify the fracture networks in karst aquifers (Cardiff et al., 2013; Fischer et al., 2018b, 2018a; Lavenue and de Marsily, 2001; Soueid Ahmed et al., 2015; Zhou et al., 2016). In addition to the pressure data, transport data from tracing tests also have been applied for the inversion studies. The utilized tracers include solutes (Borghi et al., 2016; Somogyvári et al., 2017) and heat (Klepikova et al., 2014). However, no research has been carried out to study the difference between the contributions of pressure

and tracing data to the inversed results.

Considering the existing studies, we are motivated to realize a new inversion study. We chose the Terrieu field site as the target aquifer. It is a typical fractured and karst aquifer. Numerous hydraulic tests have been previously carried out to investigate this well site, including pumping tests, tracing tests, and well-borehole video logging (Dausse, 2015; Jazayeri, 2009; Jazayeri et al., 2011). The borehole video recordings allow us to verify the inversion result conveniently. This new inversion study has the following four advantageous implementations: 1) DFN/ DCN model is applied to explicitly represent the fractures/ conduits; 2) the spatial variation of the parameters of the DFN/DCN segments should be considered; 3) the DFN/ DCN network structures should be determined with reliable basis; 4) the joint inversion of two kinds of data: steady-state pumping tests data and solute transport data. Considering the previous inversion studies on the Terrieu well site, they did not apply the DCN model, and they only applied the pressure data for inversion. If we combine the four implements, possibly we can realize a better characterization of the target aquifer.

This study has two main objectives. First, we check whether we can realize better characterization of the target aquifer if include all of the four advantageous implements in one inversion study. Secondly, we investigate whether the two kinds of data (steady-state pumping tests data and solute transport data) can bring us different information about the target aquifer. In this study, first we introduce the basic information about the target well site. Then we introduce the previous inversion characterization studies on the well site. Then we carry out this new inversion study with four main steps: 1) we construct the DCN model as the forward model; 2) we determine the spatial distribution of the discrete conduit segments according to previous pumping tests; 3) we choose the data for inversion: steady-state pressure data, tracing data; 4) we calibrate the parameter field for the conduit network by inversion of the field data.

5.2 Summary of main properties of Lez aquifer and Terrieu field site

5.2.1 General conditions

The Lez aquifer is a fractured/ karstic carbonate reservoir that gives rise to the Lez spring, which served as the major water supply for the Montpellier urban area since the mid-19th century (Wang et al., 2016). The catchment of the Lez karst aquifer belongs to the fractured and karst aquifer system constituted of the Jurassic and Cretaceous limestone.

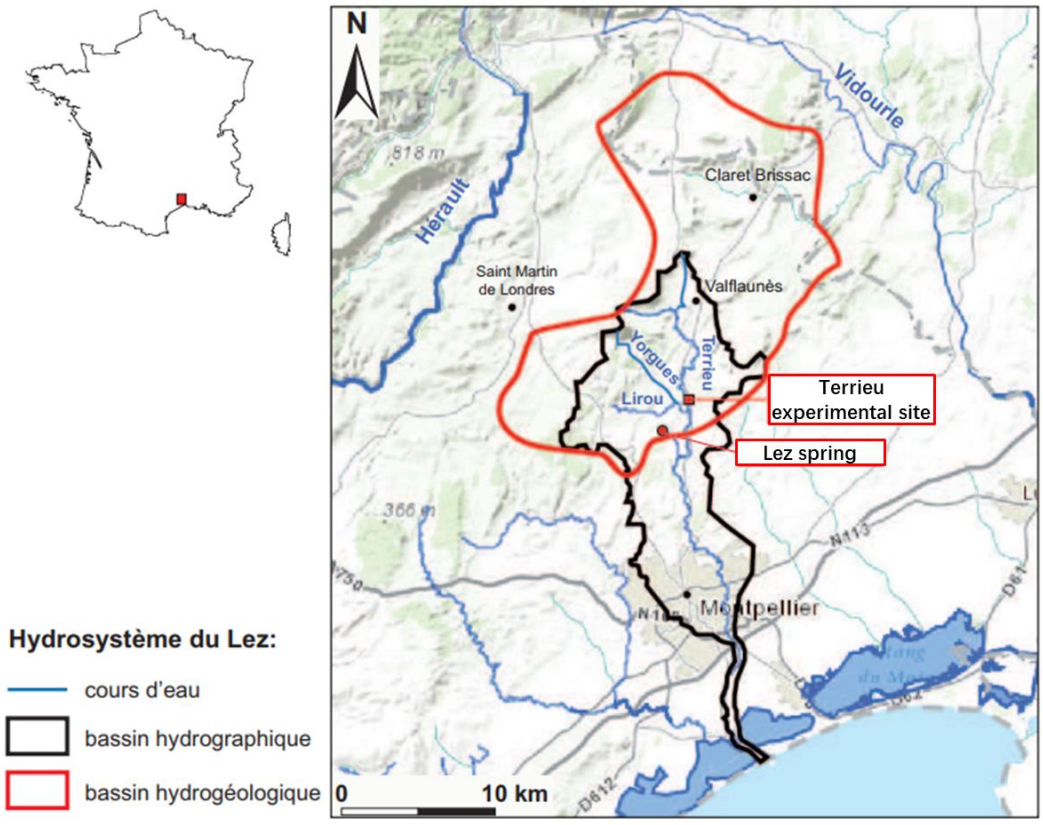

Figure 5.1. The Lez spring and its hydrogeological catchment area (Dausse, 2015).

Figure 5.2 gives information about the hydrological condition of Lez spring between the years 2005 and 2020: (1) the precipitation rainfall at Lez's aquifer, (2) the watertable level, (3) the observed discharge at Lez's spring. The water table level is given as the level above mean sea level (AMSL).

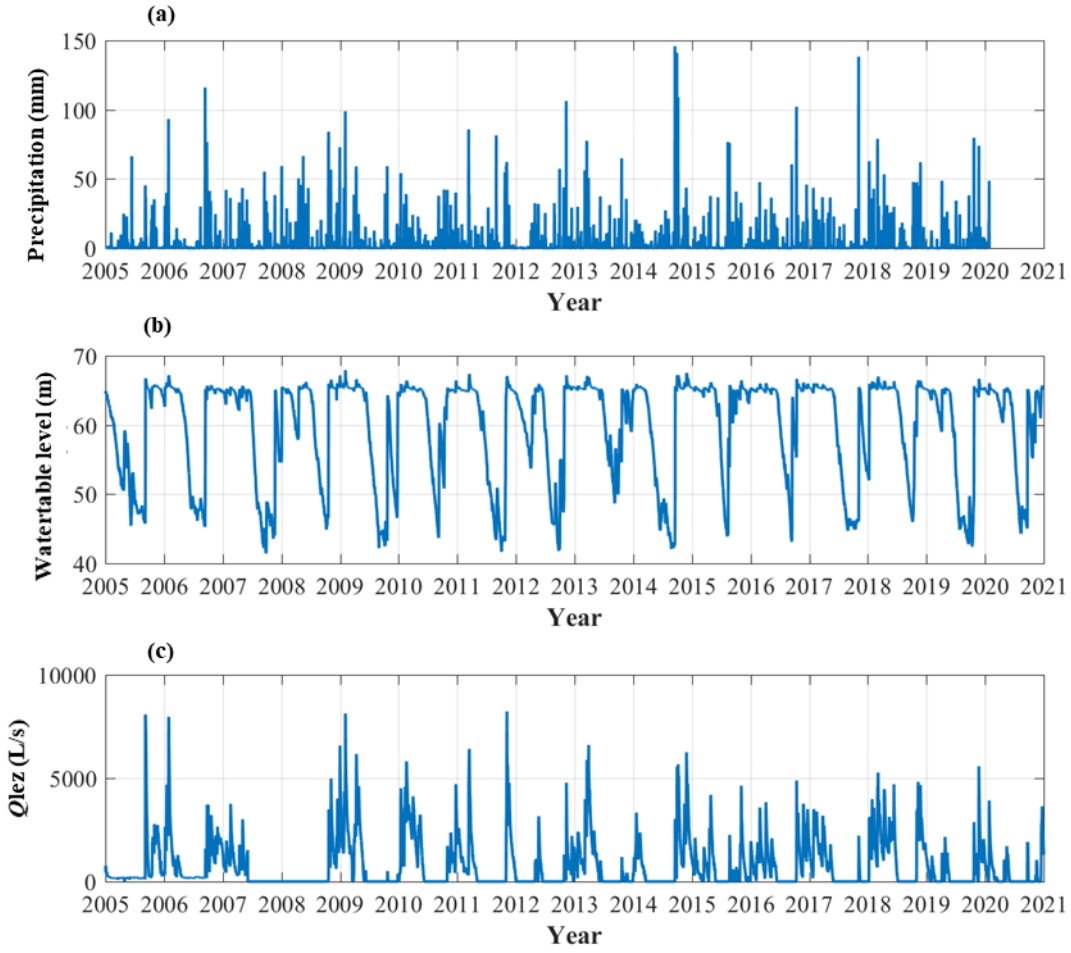

Figure 5.2. The hydraulic conditions of Lez between 2005 and 2021. (a) Rainfall; (b) Watertable level; (c) Discharge at Lez's spring.

The Terrieu experimental site is located 15 km north of the town of Montpellier, southern France. The site has been set up to investigate groundwater hydrodynamic behavior in the Lez aquifer. The site has been used as a field laboratory for testing new field hydraulic methods and tools developed for the characterization of karstic aquifers (Dausse, 2015; Fischer et al., 2018b, 2017b; Jazayeri, 2009; Jazayeri et al., 2011; Jourde et al., 2011, 2002; Wang et al., 2017, 2016). This experimental site is about 1500 m^2 (30 m × 50 m) in size, with 22 boreholes drilled into the aquifer. The drilled depth of the boreholes ranges between 50 ~ 60 m. These boreholes are spaced with an average spacing of about 5 m (Figure 5.3). This allows detailed investigation of groundwater flow on a fine scale. All of the boreholes are uncased; among these boreholes P0, P8, and P22 have a diameter of 0.33 m and all others have a diameter of 0.22 m.

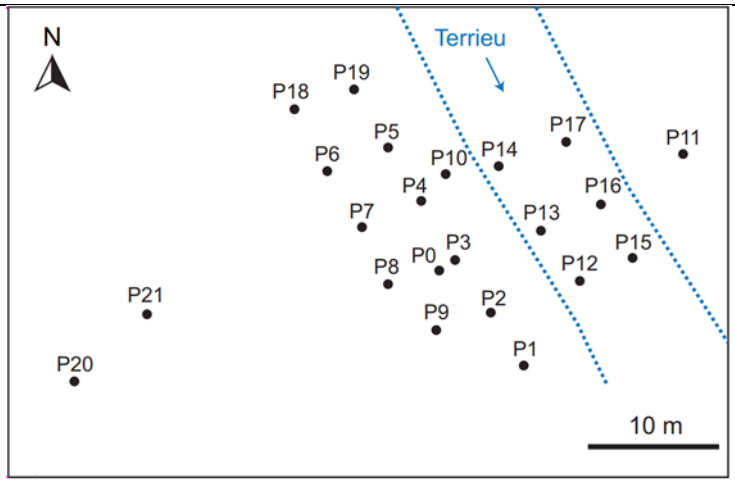

Figure 5.3. Investigation wells at Terrieu well site.

5.2.2 Field investigation tests on Terrieu site

During the last two decades, extensive hydraulic studies have been conducted at the Terrieu site using temperature, and electrical conductivity loggings (Jazayeri et al., 2011). Temperature and conductivity logs were recorded in all the boreholes, except for P0 because of permanent pump equipment. Log anomalies have been observed in the wells P2, P8, P11, P12, P15, and P20 (Figure 5.4). A peak in temperature and conductivity logs is observed in these wells at different depths. This has been interpreted as a high permeability flow path crossing these wells. Such temperature and conductivity anomalies are not observed in the other wells. Figure 5.4 shows that recorded anomalies in the temperature and conductivity logs descend gradually from 60 m (AMSL) in well P11 down to 40 m (AMSL) in well P20. This vertical difference of 20 m through a distance of 50 m corresponds to a gradient of about 15–20° for this highly permeable zone in an EW direction which dips towards the W.

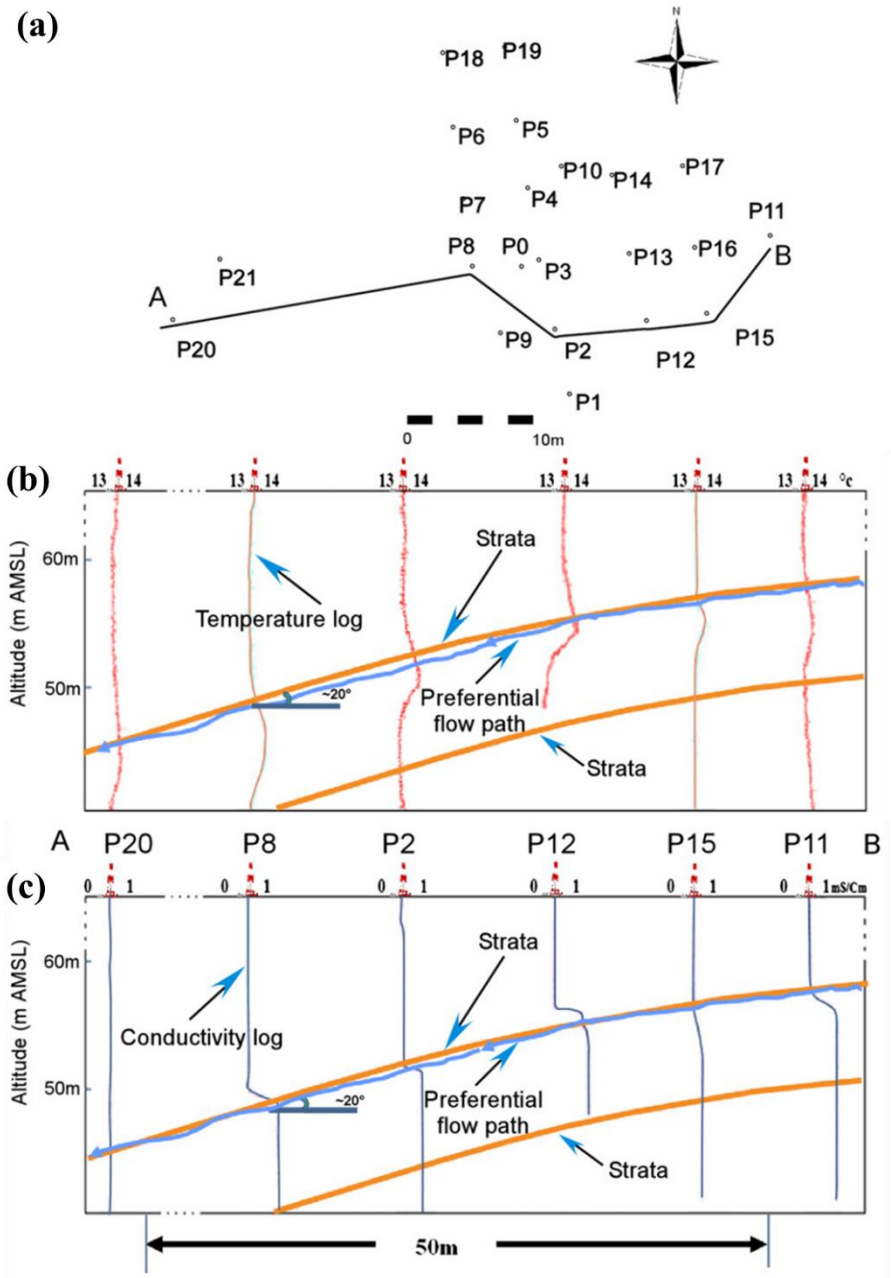

Figure 5.4. (a) Cross-section trace at Terrieu site, (b) well temperature logs along the AB cross-section, (c) well electrical conductivity logs along the AB cross-section. (Jazayeri et al., 2011)

Borehole videos were recorded in 10 boreholes. Downhole videos in the boreholes show that karstic conduits with aperture up to 50 cm are present (Jazayeri et al., 2011). A karst conduit (about 0.2 m diameter) is observed in wells P11, P15, P12, P2, P8, and P20 (Figure 5.5) at the depth where temperature and conductivity log anomalies were recorded (Figure 5.4) (Jazayeri et al., 2011). These karstic conduits are found to be present at a depth between 35 and 40 m (Jazayeri et al., 2011; Wang et al., 2016).

Vertical view of a conduit karst inside the P8 skin.

Presence of a very wide conduit in the W side of the borehole P11 with a diameter of 0.2m.

Illustration of a karst conduit with a diameter of 0.4m in P15.

Figure 5.5. Borehole image logging; a very wide karst conduit (0.2 m diameter) is observed in some wells (Jazayeri et al., 2011).

When borehole video data are used in conjunction with the temperature and conductivity logs, it is found that the preferential flow paths are strongly restricted within a limited member of karstified fractures and karst conduits developed along an important, gently tilted, bedding plane. Its depth varies between 25 and 40 m from the site surface in different boreholes (Jazayeri et al., 2011) (Figure 5.5). Packer tests were performed in 5 boreholes (Dausse, 2015). Those straddle packer tests further indicate that this open bedding plane (Figure 5.4) is the most conductive feature which intersects the boreholes over the entire penetrated interval and its transmissivity is found to be more than 3 orders of magnitude higher than that of the other tested intervals.

To obtain complete information on the permeability between wells at the local scale, a series of interference tests have been conducted in 16 wells out of the 22 present at the Terrieu experimental field site (Jazayeri, 2009; Jazayeri et al., 2011). According to Table 5.1, the pumping rate in P0 and P8 are much larger than the other wells: 53 m^3/h for P0 and 72 m^3/h for P8. It is a relatively large pumping rate of 12.2 m^3/h for P21. The pumping rate for the other wells varied between 0.2 and 3.6 m^3/h. The productivity index value (PI) indicates the ability of the reservoir to deliver fluid to the wellbore. The most significant values of PI are determined for boreholes P0, P8, and P20. Although all boreholes are situated over a very small area (1500m^2) with an average distance of 5m, there are high contrasts between PI values. This highlights the strong heterogeneity of the reservoir properties at the Terrieu experimental field site scale.

Table 5.1 Pumping rate, associated drawdown and productivity index.

Well name	Rate (m^3/h)	Drawdown (m)	PI (m^2/h)
P0	53	9.84	5.39
P2	2.4	8.26	0.29
P3	3.6	0	0.96
P4	0.2	12.5	0.02
P5	0.2	3.54	0.06
P8	72	0.8	90
P9	1	12	0.08
P10	0.2	4.89	0.04
P11	3.2	1.32	2.42
P12	3	0	–
P13	0.5	11	0.05
P15	3	0	–
P16	0.5	8.31	0.06

P17	0.2	3.43	0.06
P20	2.4	0.4	6
P21	12.2	25.05	0.49

Pumping individually in each well, we observed hydraulic drawdown in other wells. This provides evidence of connectivity and directional permeability at the scale of the Terrieu experimental field site, by considering the water table level at the end of each drawdown period (Figure 5.6). This figure shows the zone of influence related to the different pumping tests performed in the Terrieu experimental field site. For some of the pumping tests in Figure 5.6b, the pressure response is only observed at some observation wells that are close to the pumping well.

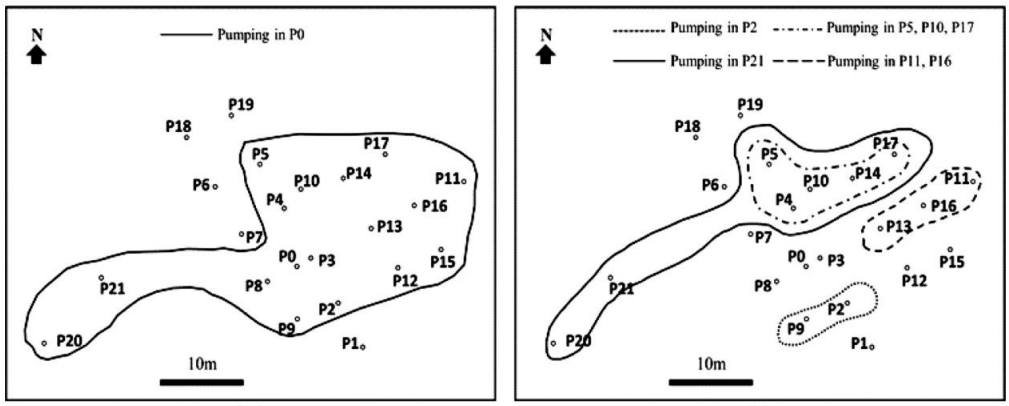

Figure 5.6. Water table affected zone at the end of drawdown for several different interference tests (Jazayeri et al., 2011; Wang et al., 2016).

5.2.3 Tracing tests

A series of tracing tests have been carried out at the Terrieu site to investigate the inter-borehole connectivity of the site and derive the effective transport parameters. These tracer tests allowed to highlight several hydraulic continuities across the Terrieu well site. In this subsection, first, we present the basic information about these tracing tests; second, we select some of the tracing tests as the inversion data to characterize the site.

The basic information of these tracing tests is summarized in Table 5.2. The water table level during the tracing tests is summarized in the table and further exhibited in Figure 5.7. These tracing tests were realized for 5 different trajectory pathways: P9- P0, P16-P0, P2-P0, P13-P0, and P13-P8. The pumping rate for the tracing tests ranges between 30 to 53 m^3/h. The utilized tracer includes NaCl, Sulforhodamine B, and Fluoresceine. The data of rainfall and spring flow rate are provided in Figure 5.8.

Table 5.2. Basic information of tracing tests.

Tests	Date	Water table level, h_w (m)	Point of injection	Points of pumping/ concentration monitoring	Pumping rate (m^3/h)	Tracer
1	2005-10-18	65.214	P9	P0	52	NaCl
2	2005-10-18	65.214	P16	P0	52	NaCl
3	2005-11-09	65.477	P2	P0	53	NaCl
4	2006-10-11	64.905	P9	P0	52.2	NaCl

5	2007-05-25	64.32	P9	P0	51	NaCl
6	2007-10-24	45.73	P9	P0	37.5	NaCl
7	2008-11-18	65.42	P2	P0	49.5	Sulforhodamine B
8	2008-11-18	65.42	P9	P0	49.5	NaCl
9	2008-11-18	65.42	P13	P0	49.5	Fluoresceine
10	2009-11-03	62.11	P2	P0	49.6	Sulforhodamine B
11	2009-11-03	62.11	P9	P0	49.6	NaCl
12	2009-11-03	62.11	P13	P0	49.6	Fluoresceine
13	2010-03-19	65.17	P13	P0	53	NaCl
14	2010-10-14	62.06	P13	P0	53	NaCl
15	2011-03-25	65.59	P13	P0	53	NaCl
16	2011-05-27	59.92	P13	P0	53	NaCl
17	**2013-07-11**	**59.46**	**P13**	**P0**	**50**	**Fluoresceine**
18	2013-10-03	55.15	P13	P8	46.3	NaCl
19	2014-10-02	66.54	P13	P0	53	NaCl
20	**2015-03-18**	**65.39**	**P2**	**P0**	**50**	**Fluoresceine**
21	2016-10-05	56.88	P2	P0	50	Fluoresceine
22	2017-10-05	45.31	P13	P8	35	NaCl
23	2017-10-05	45.31	P12	P8	35	Fluoresceine
24	2018-10-03	46.28	P2	P0	33	NaCl
25	2018-10-03	46.28	P13	P0	33	Fluoresceine

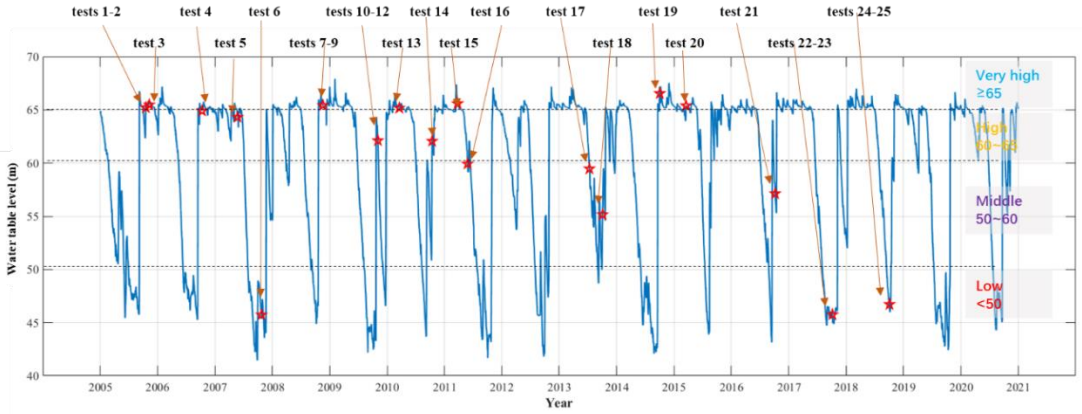

Figure 5.7. Watertable level information during tracing tests.

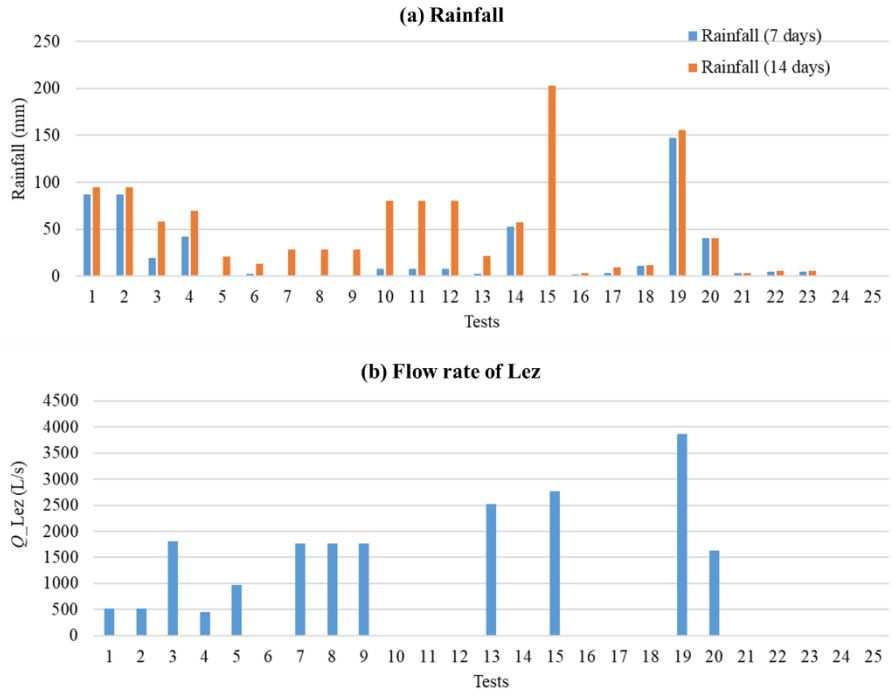

Figure 5.8. Hydraulic information during tracing tests. (a) Cumultated rainfall 7 days and 14 days before tracing tests; (b) Natural flowrate of Lez's spring during tracing tests.

From the above 25 tests, we choose several tracing tests as the data for inversion. The tests are selected according to three main criteria: (i) watertable level; (ii) repetition of tracer injection-monitoring pattern; (iii) does the BTC falling limb decreases to the concentration value of the formation water without tracer.

We briefly explain the above three criteria. (i) The watertable level exert strong influence on the properties of a natural karst system. Because some drainage structures can be activated/deactivated depending on the water level in the system. In this study, we will characterize the Terrieu well site by joint inversion of pumping test data and tracing tests. Thus we need to apply the tracing tests that are under similar watertable level (h_w) with the pumping tests to evaluate the HT results. The pumping tests of (Jazayeri et al., 2011) have been carried out at February of 2008. According to Figure 5.2b the h_w values of the tests are above 64 m. Thus, the tracing tests with h_w values under 60 m are excluded. Figure 5.7 gives a convenient exhibition on which tests can be used. (ii) Several tests have been carried out between same injection- monitoring borehole patterns. For each pattern, we only need one tracing test for inversion data. (iii) Not all of the tracing tests were terminated before the monitored concentration decreases to a sufficiently low value in the pumping borehole. The BTCs of these tests exhibit BTCs that are relatively less complete. We prefer the tracing test that were terminated after the monitored concentration decreased to a sufficiently low value. As a result, four tests are selected: test 1, 2, 17 and 20.

The breakthrough curves (BTCs) of the four tests are shown in Figure 5.9. For normalization, the concentration of the first three BTCs are transformed in Residual Time Distributions (RTD, $[T^{-1}]$) for exhibition:

$$\mathrm{RTD}(t) = \frac{C(t)}{\int_0^{+\infty} C(t)\mathrm{d}t}. \quad (5\text{-}1)$$

Tests 1 and 2 (Figure 5.9a-b) were realized on the same date, with NaCl as tracer. Test 17 (Figure 5.9c) was carried out to study the connectivity between P13 and P0 and the tracer is Fluoresceine. Test 20 (Figure 5.9d) reveals the connectivity between P2 and P0, and the tracer in this test is Fluoresceine. Test 20 has an incomplete falling limb. We still select this test because there are no other tracing tests between P2 and P0.

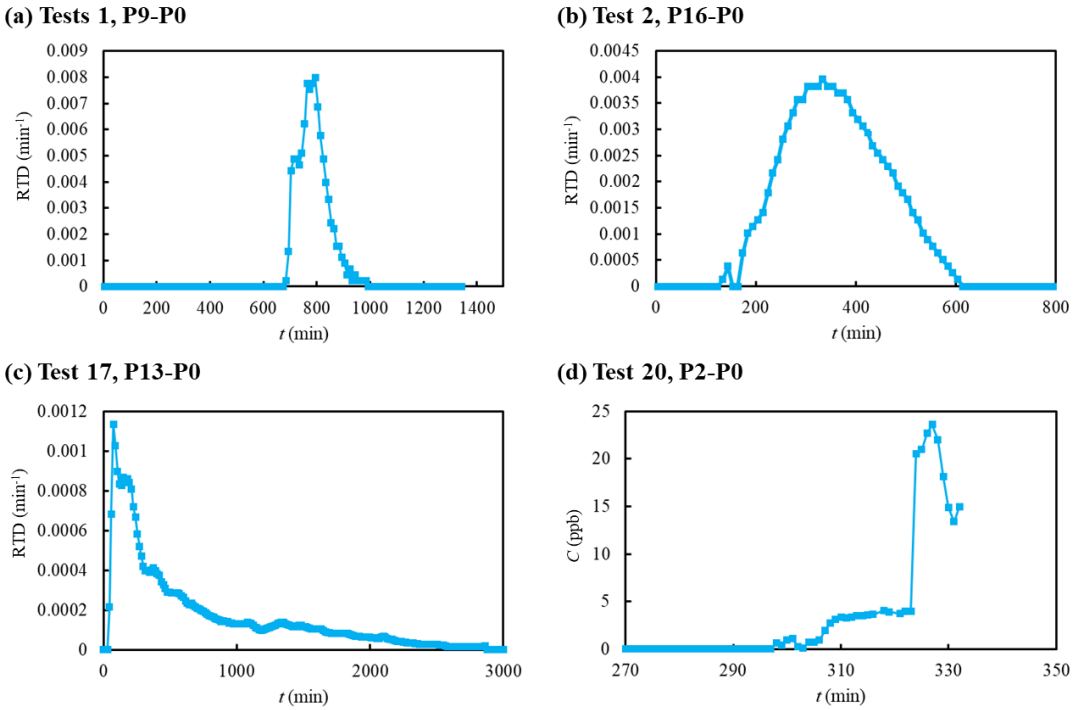

Figure 5.9. BTCs of four selected tracing tests.

5.3 Previous inversion studies (based on pumping test data only)

5.3.1 Characterized transmissivity of Terrieu well site

To realize a detailed characterization of the heterogeneity of the Terrieu well site, the technique of Hydraulic tomography (HT) has been applied to characterize the spatial distribution of aquifer hydraulic properties, e.g. transmissivity (K) and storativity (S). Wang et al. (2016) applied an EPM model to represent the Terrieu well site and simulated the sequential pumping tests that have been carried out on the site. The simulated hydraulic drawdowns (h_d) in each borehole are then compared to the true responses observed in the interference pumping tests. By iteratively adjusting the hydraulic transmissivity field of the EPM model, the difference between the simulations and true measurement is finally minimized. Two of the obtained transmissivity fields are shown in Figure 5.10 (Figure 5.10a was inverted with a grid size of 1 m × 1 m, Figure 5.10b was inverted with a grid size of 0.5 m × 0.5 m). The K fields exhibit the high heterogeneity of the well site. The watertable level, h_w, values of the interference pumping tests in (Wang et al., 2016) are above 64 m.

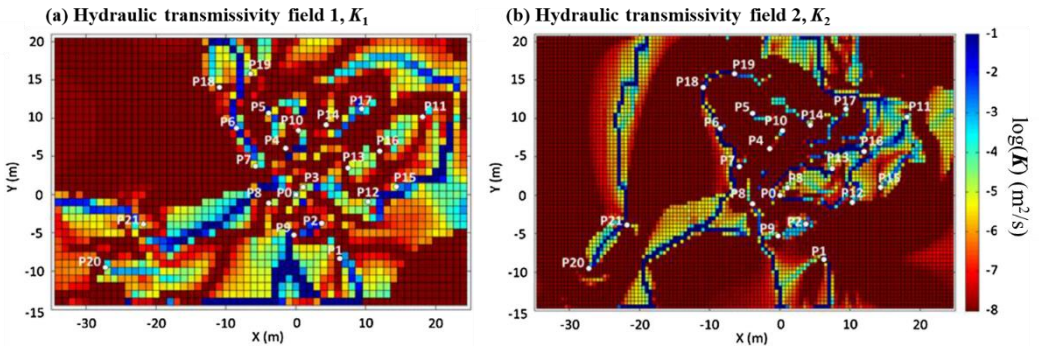

Figure 5.10. Characterized transmissivity field of Terrieu by (Wang et al., 2016).

Fischer et al. (2017a,b) applied the cellular automata-based deterministic inversion CADI method to image the spatial distribution of the hydraulic transmissivities in the Terrieu experimental site using steady-state hydraulic head data of cross-hole pumping tests. A synthetic study to investigate the harmonic pumping tests in karst aquifers was carried out (Fischer et al. 2018a) and results showed that harmonic pumping tests data allow to distinguish the type of connectivity between boreholes (conduit connectivity, matrix connectivity or dual connectivity). Harmonic pumping tests were performed in four boreholes at the Terrieu experimental site (The watertable level of the harmonic pumping tests is about 62.0 m); for each pumping borehole, two pumping tests with two different periods of pumping sinusoid signal, 2 min and 5 min, were conducted. Harmonic pumping tests data were used to reconstruct the transmissivity field of the Terrieu experimental site using CADI approach (Fischer et al. 2018b). Results are shown in (Figure 5.11). Figure 5.11a represents the inverted hydraulic transmissivity using sequentially the "2 min" period followed by the "5 min" period datasets. Figure 5.11b shows the inverted hydraulic transmissivity using sequentially the "5 min" period followed by the "2 min" period datasets.

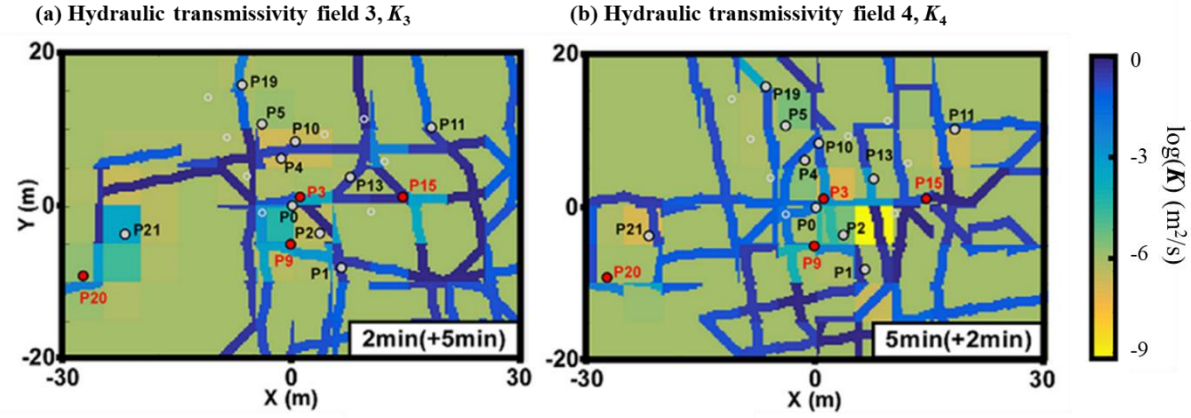

Figure 5.11. Characterized transmissivity field of Terrieu by (Fischer et al., 2018b).

In the above two studies, the thickness of the 2-D EPM models has been assumed as 1 m. The flow behavior is governed by Darcy's law (Figure 5.12a):

$$Q = -AK\nabla \cdot h = -\frac{LdK}{\rho g}\nabla \cdot h, \tag{5-2}$$

where, A is the cross-section area, m^2; d is the aquifer thickness as shown in Figure 5.12a, m; L is the width of the assumed aquifer in Figure 5.12a, m; g is gravitational acceleration, m/s^2; h is the hydraulic head, m;

K is hydraulic transmissivity, m/s; Q is the flow rate, m^3/s; ρ is the fluid density, kg/m^3.

However, in the Terrieu well site, the preferential flow paths are strongly restricted within the karstified fractures along the bedding plane. If we conceptualize the bedding plane as a huge fracture with the various aperture at different positions, then the flow behavior is then governed by the Cubic law (Figure 5.12b):

$$Q = A_{\text{aperture}} v = -\frac{Lb^3}{12}\frac{\Delta P}{\mu \Delta x}, \tag{5-3}$$

where, A_{aperture} is the cross-section area of the fracture, m^2; b is fracture aperture as shown in Figure 5.12b, m; μ is fluid viscosity, mPa·s. Assume the values of Q and $\Delta P/\Delta x$ remain constant for the above two equations, we have:

$$b = \left(\frac{12K\mu d}{\rho g}\right)^{\frac{1}{3}}. \tag{5-4}$$

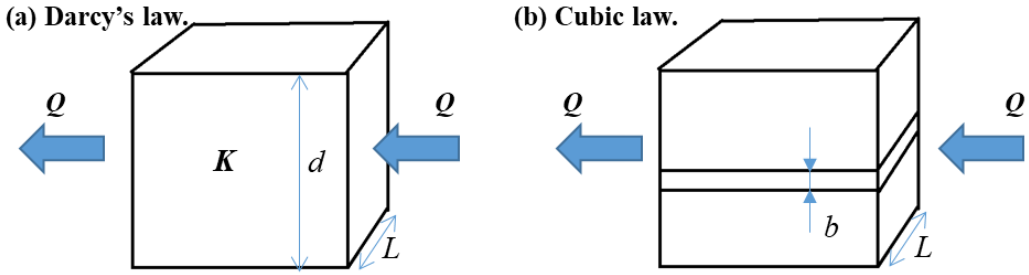

Figure 5.12. The comparison between Darcy's law and cubic law.

With Eq. 5-4, we can transform the inverted K fields (Figure 5.10 and Figure 5.11) into equivalent aperture distribution of the bedding plane of Terrieu (Figure 5.13). The aperture field is a more direct representation than the K field for the bedding plane. For b_1 and b_2, the maximum aperture is 5 mm; for b_3 and b_4, the maximum aperture is 10.7 mm. There is significant contrast among the four fields.

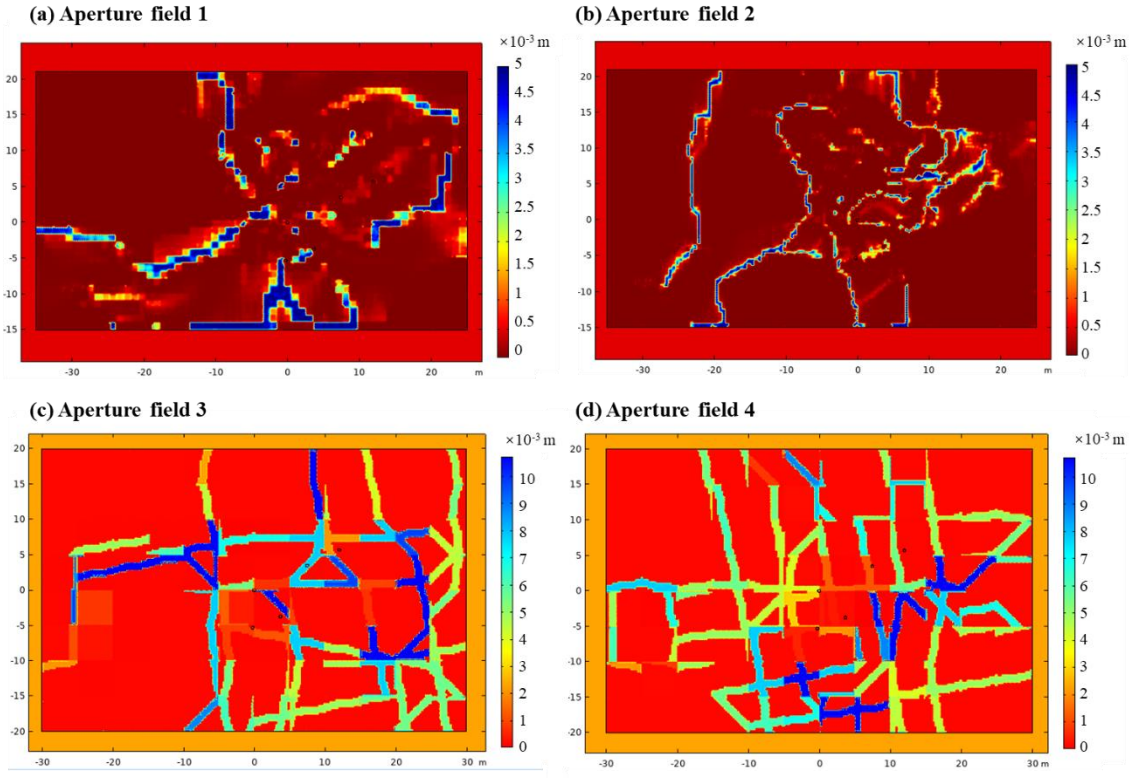

Figure 5.13. Aperture fields derived from previous transmissivity fields (b_1 and b_2 correspond to the K fields of Figure 5.10a-b, b_3 and b_4 correspond to Figure 5.11a-b).

5.3.2 Forward flow simulation at the scale of the Terrieu experimental Site

Different K fields should induce different hydraulic behaviors during the pumping tests. So we apply the four previously presented K fields to numerically simulate the groundwater flow during the pumping test in P0 of the Terrieu site. With the method provided in Section 5.4.1.2, we simulate the groundwater flow process at the steady-state of the pumping tests.

The numerical setup for the simulations is introduced as follows. The setup is mostly the same as the original studies (Fischer et al., 2018b; Wang et al., 2016). The two studies defined different areas for the Terrieu site. As shown in Figure 5.10, the site area for K_1 and K_2 is, x: -35~25m, y: -15~21m; as shown in Figure 5.11, the site area for K_3 and K_4 is, x: -30 ~ 30 m, y: -20 ~ 20 m. The local site is surrounded by a large buffer region to reduce the influence of the hydraulic flow boundaries. For K_1 and K_2, the buffer region area is x: -600 ~ 600 m, y: -600 ~ 600 m, and the buffer region is assumed to have a constant hydraulic transmissivity of 10^{-4} m/s; the buffer region of K_3 and K_4 is, x: -500 ~ 500 m, y: -500 ~ 500 m, and the buffer region has a constant hydraulic transmissivity of 10^{-2} m/s. The simulations are realized in 2-D. The aquifer thickness is assumed to be 1 m. The initial condition is set in the entire model by assuming a static water table level (60 m). The external boundaries of the buffer zone are built with imposed Dirichlet boundary conditions as presented, h_d = 60 m. We simulated the test of pumping in borehole P0, its coordinate is (0 m, 0 m). The pumping flow rate $Q_{pumping}$ is 53 m^3/h.

We exhibit the simulated Darcy's velocity (u) fields in Figure 5.14. The flow velocity field is an

effective display of hydraulic behavior. The four u fields are different from each other. According to u values, we calculate the flow rate, q, for each high-K region that can be conceptualized as a conduit. Then we also calculate the ratio of conduit flow rate to the total pumping flow rate, $q/Q_{pumping}$. If the conduit bears less than 10% of the pumping rate, it is indicated by a blue arrow; if the conduit bears more than 10% of the pumping rate, it is indicated by a red arrow and the actual value of the ratio is provided beside the red arrow.

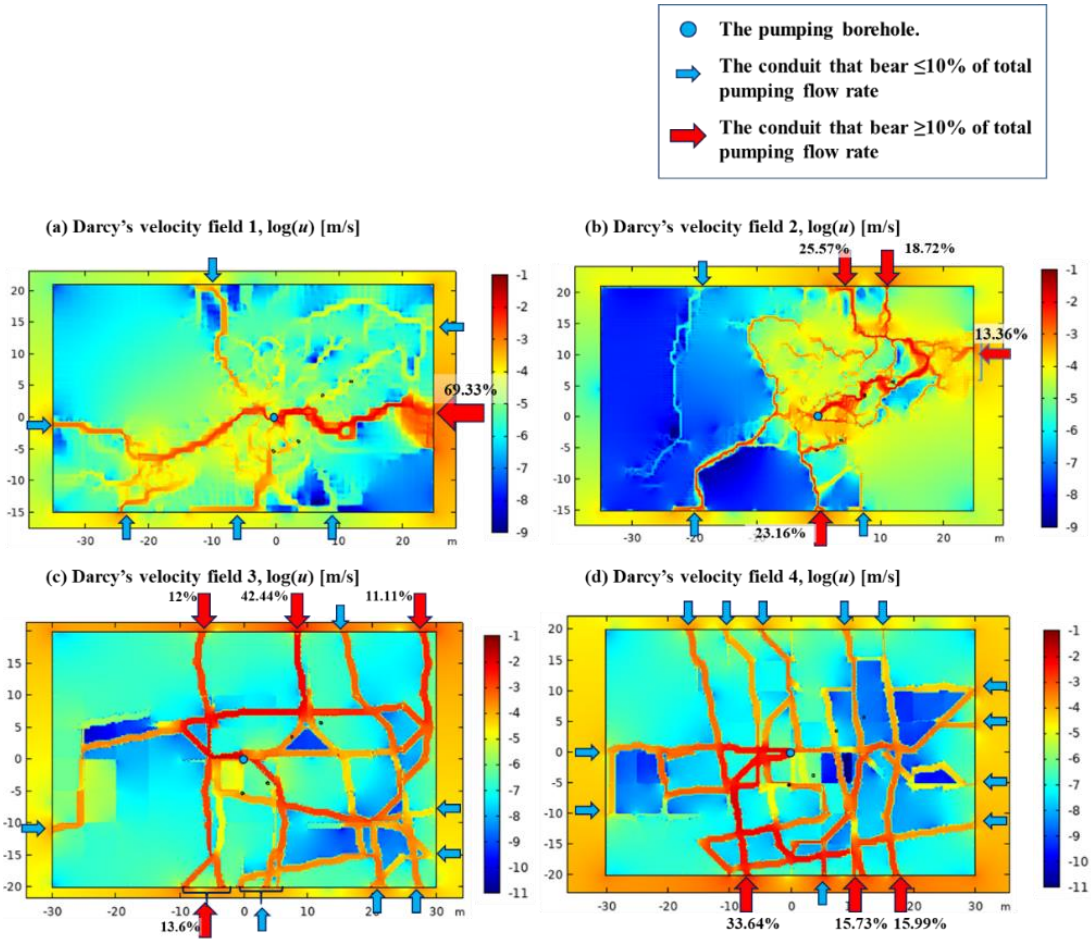

Figure 5.14. Simulated velocity fields from the four *K* fields.

On the whole, the strong heterogeneity of the K fields has caused the simulated $\boldsymbol{u}$ fields to also exhibit significant heterogeneity: the velocity within the same site can vary by multiple orders of magnitude. In Figure 5.14a, 69% of $Q_{pumping}$ comes from the east side. In Figure 5.14b, most of the flow rate comes from the north side, two conduits take up 26% and 19% of $Q_{pumping}$ respectively; one conduit on the east side and another on the south side also take up substantial proportions: 13% and 23% respectively. In Figure 5.14c, three conduits in the north provide the most proportion of $Q_{pumping}$: the percentages are 12%, 42%, and 11% respectively. In Figure 5.14d, three conduits in the south provide the most proportion of $Q_{pumping}$: the percentages are 34%, 16%, and 16% respectively.

In summary, the previous researchers have obtained very different K fields by inversion of the hydraulic data. This reflects the inherent limitation of the Hydraulic Tomography (HT) technique noted by (Bohling and Butler Jr, 2010): a high degree of non-uniqueness remains in the estimation of hydraulic

parameter fields. As an underdetermined problem, the inversion studies generate non-unique solutions. Until now, we cannot effectively evaluate which *K* field approximates the true condition to the largest extent. Figure 5.14 further indicates that if we apply those *K* fields to predict the flow behavior in the well site, the predictions are highly different.

However, Figure 5.14 provides us inspiration on evaluating the obtained *K* fields. If we can obtain the velocity data measured in Terrieu and this velocity data are compared to the simulated ***u*** fields in Figure 5.14, we will be able to determine which *K* field is optimal and realize a more reliable characterization of the well site.

5.3.3 Forward transport simulation at the scale of the Terrieu experimental Site

With the above EPM model, we numerically simulate the flow and transport process of some tracing tests, applying the method introduced in Section 5.4.1.1. Then we compare the simulated BTCs to the true BTCs monitored in-situ. According to Eq. 5-11, ***u*** influences the transport process significantly. For the forward simulations of flow and transport, different *K* fields result in different ***u*** fields and further result in different simulated BTCs. On the contrary, if one of the *K* fields allows the simulated BTCs to be similar to the real BTCs obtained on the site, this *K* field should be deemed as a good representation of the well site.

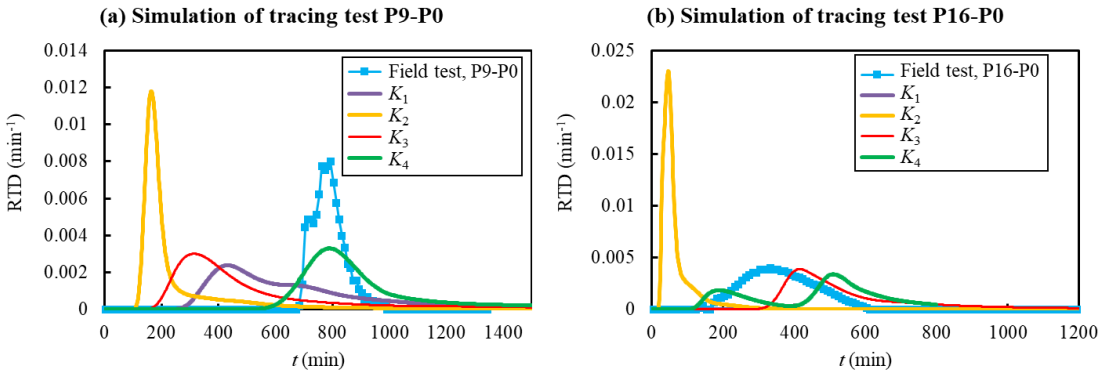

Figure 5.15. The comparison between the simulated BTCs and the true BTCs.

We simulated the tracing tests of test 1 and test 2: P9-P0 and P16-P0. In Figure 5.15, we compare the simulated BTCs with the true BTCs. In Figure 5.15a, we find that the simulated BTCs of the K_1, K_2, and K_3 have a very large contrast with the field test data. The transition times of the three BTCs are different from the field test, which means the simulated ***u*** field is different from the true flow behavior in Terrieu under the same pumping flow rate. The simulated BTC of P9-P0 by K_4 has a similar transition time to real BTC. However, in Figure 5.15b, the simulated BTC of K_4 exhibits large contrast with the field test. Thus, none of the *K* fields can reproduce the transport behavior of the true tracing tests realized in Terrieu.

The above results indicate that the constructed *K* fields are not satisfying. Thus we propose to use both pumping test data and tracing data to better assess conduit network properties at the scale of the Terrieu site. By realizing a joint inversion of the two types of data, we may well realize better characterization of the

well site. Another question arises: what is the difference between the inversions realized by pressure data and tracing data? We are also curious about the difference between the network properties obtained by the inversion of the pumping test data and the tracing data.

5.4 Method

5.4.1 Flow and transport simulations

5.4.1.1 Discrete conduit network (DCN) model

To simulate the solute transport process in the two-dimensional conduit networks, the karst conduits are conceptualized as 1-D segments. We focused on the transport process in karst conduits and ignored the matrix. We assumed single-phase, incompressible fluid. The steady-state flow is solved by the following continuity and momentum equations (Barnard et al., 1966):

$$\nabla \cdot (A\boldsymbol{u}) = 0, \tag{5-5}$$

$$\rho \frac{\partial \boldsymbol{u}}{\partial t} + \rho \boldsymbol{u} \cdot \nabla \boldsymbol{u} = -\nabla p - f_{\mathrm{d}} \frac{\rho}{2d} \boldsymbol{u}|\boldsymbol{u}|, \tag{5-6}$$

where A is the cross-sectional area of the conduit (L^2), $\boldsymbol{u}$ is the flow velocity vector (L/T), ρ is the fluid density (M/L^3), p is the fluid pressure (M/LT^2), f_{d} is Darcy's friction factor (unitless), d is the hydraulic diameter (L). The velocity field obtained by solving Equations 2~3 is used in the ADE equation:

$$A \frac{\partial C}{\partial t} + A\boldsymbol{u} \cdot \nabla C = \nabla \cdot (A(D_{\mathrm{c}} + D_{\mathrm{d}})\nabla C) + R, \tag{5-7}$$

where C is the concentration (M/L^3); D_{c} is the molecular diffusion coefficient (L^2/T); D_{d} is the dispersion coefficient (L^2/T). The finite-element analysis is conducted with COMSOL Multiphysics.

5.4.1.2 Flow and transport simulation in equivalent porous media

In comparison to the DCN model, we will also simulate the flow and solute transport process 2-D EPM model. The steady-state flow is solved by the following simple continuity and constitutive equations:

$$\nabla \cdot \boldsymbol{u} = Q_{\mathrm{s}}, \tag{5-8}$$

$$\boldsymbol{u} = -T\nabla h, \tag{5-9}$$

where A is the cross-sectional area of the conduit (L^2), $\boldsymbol{u}$ is the flow velocity vector (L/T), ρ is the fluid density (M/L^3), p is the fluid pressure(M/LT^2), f_{d} is Darcy's friction factor (unitless), d is the hydraulic diameter (L).

$$h = h_{\mathrm{D}} \text{ on } \Gamma_{\mathrm{D}}, \tag{5-10}$$

The velocity field obtained by solving Equations 2~3 is used in the ADE equation:

$$\frac{\partial \varepsilon C}{\partial t} + \boldsymbol{u} \cdot \nabla C = \nabla \cdot \left((D_{\mathrm{c}} + D_{\mathrm{d}})\nabla C\right) + R, \tag{5-11}$$

where C is the concentration (M/L^3); D_{c} is the molecular diffusion coefficient (L^2/T); D_{d} is the dispersion coefficient (L^2/T); ε is porosity, (-); R represents the source term, (M/L^3T). Also, the finite-element

analysis is conducted with COMSOL Multiphysics.

5.4.2 Optimization

5.4.2.1 Optimization algorithms

We applied two optimization algorithms to minimize the objective functions. The first inversion algorithm is the Sparse Nonlinear Optimizer (SNOPT) (Gill et al., 2006, 2005). It uses a gradient-based optimization technique to find the optimal solutions. The SNOPT algorithm has been proved effective in solving the HT problems in both porous media (Ahmed et al., 2015; Cardiff and Kitanidis, 2008) and the karst aquifers (Fischer et al., 2017b; Wang et al., 2016). The second inversion algorithm is the Globally Convergent version of the Method of Moving Asymptotes (Svanberg, 2007, 2002). GCMMA is essentially a linear method. We adopted two methods to improve the feasibility of the inversion study: if one optimization algorithm does not effectively converge, we will apply another algorithm.

5.4.2.2 Objective function

The coefficient of determination, denoted as R^2, is applied to evaluate how well the field data are replicated by the forward simulations:

$$R^2 = 1 - \frac{\sum_{i=1}^{n}(Y_i - f_i)^2}{\sum_{i=1}^{n}(Y_i - \bar{Y})^2}. \quad (5\text{-}12)$$

where Y is the experimental data, f is the calibrated data, and n is the data quantity.

5.4.3 Characterization of the conduit network by inversion of field test data

5.4.3.1 Implementation 1

A new inversion study is carried out to characterize the underground conduit network of the Terrieu well site. The new implementation of the study has the following five features: i). DFN/ DCN model is applied to explicitly represent the fractures/ conduits and the matrix effect is ignored; ii). the DFN/ DCN network structures should be determined on a reliable basis; iii) the spatial variation of the parameters of the DFN/DCN segments should be considered; iv). Inversion of both hydraulic drawdown (h_d) and tracing data. v). Instead of direct inversion of the transport BTCs and h_d data, the inversion study is carried out in two steps.

(i) For the Terrieu site, the karst features form the dominant media for the hydraulic behaviors of the aquifer (introduced in Section 5.3). So we apply the discrete conduit network (DCN) model to simulate the hydraulic behaviors of this site. The governing equations have been introduced in Section 5.4.1.1. The parameters to be calibrated are the diameter, dia, and dispersion coefficient, D_d.

(ii) We estimate the geometric structure of the karst conduit network of Terrieu, according to the interference pumping tests. The concept is: if pumping in one borehole caused the hydraulic drawdown in another borehole, we deem that there exists a conduit that connects these two boreholes.

First, pumping in P0 has caused drawdown in many other wells (Figure 5.6). P0 is deemed to be

located at a junction of the whole conduit network.

For P2 and P9. Pumping in P2, only P9 has a drawdown response, and no clear hydrodynamic response is measured at other observation boreholes. Pumping in P3 causes drawdown responses in P0 and P9. Thus we deem that P2 and P9 are connected to the main conduit network. So we add two conduits to make the connectivity of P2-P0 and P9-P0.

For P4, P5, P10, P14, and P17. Three pumping tests have been carried out in P5, P10, and P17, and hydrodynamic responses have been identified at the five wells P4, P5, P10, P14, and P17. So we consider the five wells are connected. Pumping in P0, we found that $h_{\text{d-P4}}$ (0.62m) is larger than $h_{\text{d-P5}}$ (0.36m), $h_{\text{d-P10}}$ (0.5m), and $h_{\text{d-P14}}$ (0.32m), and $h_{\text{d-P17}}$ (0.3m). Thus we deem that P4 lies between P0 and the other wells of P5, P14, and P17 on the conduit network. So we connect P4 and P0 with a conduit. Pumping in P10, we found that $h_{\text{d-P4}}$ (3.83m) is much larger than $h_{\text{d-P5}}$ (0.52m). Thus, P4 should lie between P5 and P10. So we add two conduits to connect P4-P5, P4-P10. For the three pumping tests, we always observe that $h_{\text{d-P10}} > h_{\text{d-P14}} > h_{\text{d-P17}}$. Thus, we add the conduits of P10-P14 and P14-P17.

For P3, P11, P13, P16. Pumping in P16 (drawdown of 7.93m) generates drawdown at P11 and P13. Pumping in P11 generates drawdown at P3, P13, and P16. No clear hydrodynamic response is measured at other observation boreholes. Pumping in P0, all of the above wells (P3, P11, P13, P16) exhibited drawdown response. Thus the boreholes of P0, P3, P11, P13, and P16 are deemed to be connected by conduits.

For P7, P8, and P20. Pumping in P0, hydraulic responses have been observed in P7, P8, and P20. So these three boreholes are deemed to be connected to the main structure. We connect these boreholes to the main structure by three conduits.

P12 and P15. Pumping in P0, hydraulic responses have been observed in P12 and P15. According to Figure 5.4, P12 and P15 exhibited continuous hydraulic responses with the other wells in the well logging tests. We deem that P12 and P15 are also connected to this network.

According to the above analysis, we obtain the underground karst geometry of the Terrieu well site (Figure 5.16a). This structure is rather simplified and all of the conduit segments exist between the boreholes. This structure may be different from the true underground network for some parts. While we estimated this structure according to the observations of the interference pumping tests, this structure is still an effective characterization of the inter-borehole connectivity of the site.

Since the inter-borehole connectivity is addressed, we consider the connectivity between this site and the aquifer. Eight boreholes are located at the outermost positions of the structure: P20, P7, P5, P17, P11, P15, P2, and P9. Eight long conduits of 50 m length are added to these wells and function as the buffer region of the well site (Figure 5.16b). We assume a rather long length and low flow resistance for these boundary conduits, to reduce the influence of the hydraulic boundaries on the local simulations.

With this structure, we carry out forward simulations of flow and transport process of the field tests.

For the flow simulation, we assumed a constant hydraulic head boundary condition of 60 m for the boundary nodes (green dots). We impose a constant outflow rate boundary condition for the pumping well position, and the flow rate is the same with the field pumping tests. We assume a constant hydraulic head of 60 m as the initial condition. It is hard for us to evaluate the roughness for the underground conduits, so we assume a constant friction factor of 1 for the conduit network. The simulated hydraulic drawdown in different well positions will be compared to the measurements of the real pumping tests.

For the transport simulation, we realize the tracer injection by imposing a pulse concentration at the injection well position and the duration of the tracer pulse equals a time step. At the pumping borehole, we assume a tracer outflow boundary condition, which allows the tracer leave the model at the pumping borehole. The concentration at the pumping borehole is monitored to be the simulated BTCs. The simulated BTCs will be compared to the BTCs of the real tracing tests. The 1-D line segment mesh has the size of 0.1 m. For the transient transport simulations, the time step is assumed to be 0.02 min.

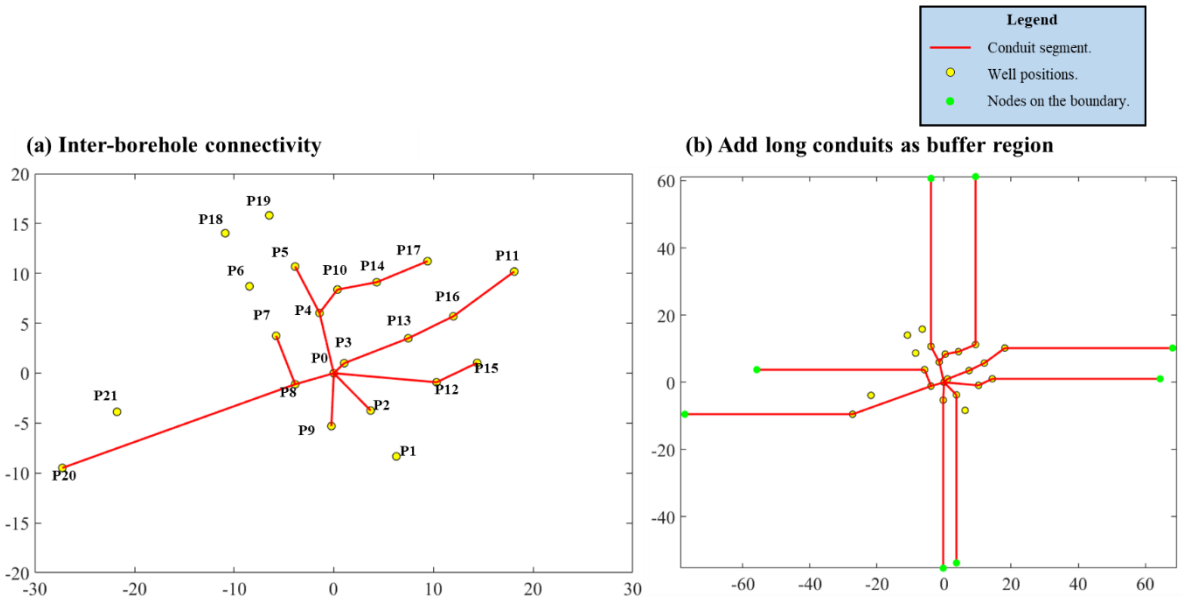

Figure 5.16. The karst conduit network is estimated according to the pumping tests.

(iii) Since the structures are determined and the forward model is constructed, we presume the initial parameter sets for the conduit segments: the diameter, dia_0, and dispersion coefficient, D_{d0}. The initial diameter distribution is assumed to be constant for all of the conduits. We first perform a manual fitting of the model response to the field data to find the values of dia_0 and D_{d0}. And we carry out numerical simulations of the pumping tests and tracing tests realized in Terrieu. By gradually adjusting the parameters of the conduit segments (dia, D_d), we make the simulated results of the DCN model to be approximate to the field test data. In this process, the different conduits can have different parameters values. Thus, we can characterize the spatial variation of the parameters of the discrete conduit segments. Note that we do not impose bound for the conduit parameters, because by determining the structure of the conduit network, we have already imposed enough priori information for the inverse model as the restriction.

(iv) We will carry out three inversion tests: test 1 inverts the steady-state h_d data of the pumping test

in P0; test 2 inverts the transient transport data: the four tracing BTCs (Figure 5.9); test 3 integrates both h_d and transport data. By comparing the results of test 1 and test 2, we may figure out the difference in how the two types of data may contribute to the characterization of conduit networks. By carrying joint inversion with both data, we may realize a better characterization of the conduit network, and reveal more information about the underground network in Terrieu.

(v) One innovative feature of this inversion study is that: instead of realizing direct inversion of the measured transport BTCs and h_d data, we divide the inversion study into two steps. First, we calibrate the conduit diameter distribution (dia) to fit the measured h_d and the transport velocity ($v_{trasnport}$, which is determined according to the transport BTCs) data; Second, we calibrate the dispersion coefficient (D_d) to fit the measured BTCs. The forward simulation of Step 1 is the steady-state simulation of water flow, and Step 2 is the transient simulation of solute transport.

We make this adjustment with two reasons. First, the inversion of the transient responses is much more computationally demanding than the steady-state responses (Cardiff et al., 2013; Fischer et al., 2018b). According to Section 5.5.1, it takes about 10 min to realize one transient simulation of the solute transport process on a simple conduit structure (Mesh size: 0.002 m; time step: 0.2 s. Length 10 m, the duration of the simulated process 1200 s). It would require much more than 10 min to simulate the transport process on a complex conduit network like Figure 5.16. And according to our experience of carrying out the inversion studies, the inversion characterization of the dia field requires more than thousands of iterations to converge, we roughly make it 2000 iterations. Thus, in our most conservative estimation, it requires more than 2000×10 min $\approx$13.9 days to realize one inversion study. We cannot afford such a huge cost of time. This large time cost is the main motivation for us to adjust the inversion method. If we can change the forward model from the transient simulation of solute transport to the steady-state simulation, the simulation efficiency can be greatly improved.

The second reason: the results in Section 5.5.1 support that the new inversion application with two steps is feasible. We found in Section 5.5.1 that the following equation holds constantly true in the transport simulations of the forward model:

$$t_{\text{transport,M}} = \sum_i^n \frac{L_i}{v_i}. \tag{5-13}$$

where, L_i is the length of the i^{th} continuous conduit segment, v_i is the advection velocity of the i^{th} continuous conduit segment, $t_{\text{transport,M}}$ is the mean residence time for the simulated transport BTC, 'M' means modeled.

From the measured BTCs of the field tracing tests, we can determine the mean transport time of the transport process ('F' means field):

$$t_{\text{transport,F}} = \frac{\sum_i^n c_i t_i}{\sum_i^n c_i}. \tag{5-14}$$

To make the forward model reproduce the measured transport BTCs, it is necessary to make the

simulated transport time $t_{\text{transport,M}}$ be equal to the value of $t_{\text{transport,F}}$. Or to make the modeled mean transport velocity on the transport route, $v_{\text{transport,M}}$, to be equal to the measured mean transport velocity in field tracing tests, $v_{\text{transport,F}}$:

$$v_{\text{transport,F}} = \frac{\sum_i^n L_i}{t_{\text{transport,F}}}. \tag{5-15}$$

$$v_{\text{transport,M}} = \frac{\sum_i^n L_i}{t_{\text{transport,M}}} = \frac{\sum_i^n L_i}{\sum_i^n \frac{L_i}{v_i}}. \tag{5-16}$$

Now, we are clear that one mission of the inversion study is the inversion of $v_{\text{transport,F}}$. The simulation of $v_{\text{transport,m}}$ only requires the steady-state simulation to be the forward model. So in Step 1, we calibrate the dia field to invert the measured h_{d} and $v_{\text{transport,F}}$ data. In Step 2, we only calibrate the D_{d} value to fit the transport BTCs. If the two steps are completed, the successful inversion of the two types of data is completed. We calculate the transport distance of the tracing tests on the route of Figure 5.16 (Table 5.3). Then we calculate the values of $v_{\text{transport,F}}$.

Table 5.3. Advection velocity was determined from the tracing tests.

	Route Distance (m)	$t_{\text{transport,F}}$ (min)	$v_{\text{transport,F}}$ (m/s)
P2P0	5.27	327.03	2.68×10^{-4}
P9P0	5.30	786.9	1.12×10^{-4}
P13P0	8.36	170.1	8.19×10^{-4}
P16P0	13.39	360.31	6.19×10^{-4}

5.4.3.2 Implementation 2

Implementation 2 is mostly the same as Implementation 1. Except that for each conduit segment, we consider one more parameter, the friction factor, fd. The inversion test still has two steps. In Step 1, we calibrate the dia and fd fields to invert the measured h_{d} and $v_{\text{transport,F}}$ data. In Step 2, we calibrate the D_{d} value to fit the transport BTCs.

Implementation 2 is proposed because Implementation 1 fails to reproduce the two types of field test data at the same time (Section 5.5.2.3, inversion test 3). We will discuss the reason for this failure in Section 5.6.3. In Section 5.6.3, we will also explain why this implementation 2 can improve the flexibility of the DCN model and realize better characterization of the conduit network.

5.5 New inversion study of Terrieu well site

5.5.1 A test with the forward model for solute transport

We carry out a series of forward simulations of flow and transport processes on some simple conduit structures, to reveal the characteristics of the forward transport model, and also to investigate whether the bending angle of a conduit influences the transport process. The forward simulations are realized with the governing equations introduced in 5.5.1.1. In this section, we first introduce the conduit structures, second

introduce the numerical model setup, and third introduce the simulation results.

We make 19 simple conduit structures and the structures have two conduit segments (Figure 5.17). The 19 conduit structures have the same diameter setting: constant diameter of 0.1 m; same starting point (-4, 0), and same endpoint (4, 0). The structures have the same total length, L_{total} = 10 m, while the turning point of these structures has different positions, thus the turning points are distributed on an ellipse structure (the dotted line in Figure 5.17b). The lateral coordinates of the 19 turning points are x = [-4.5: 0.5: 4.5]. The vertical coordinate can be calculated by the ellipse formula given in Figure 5.17.

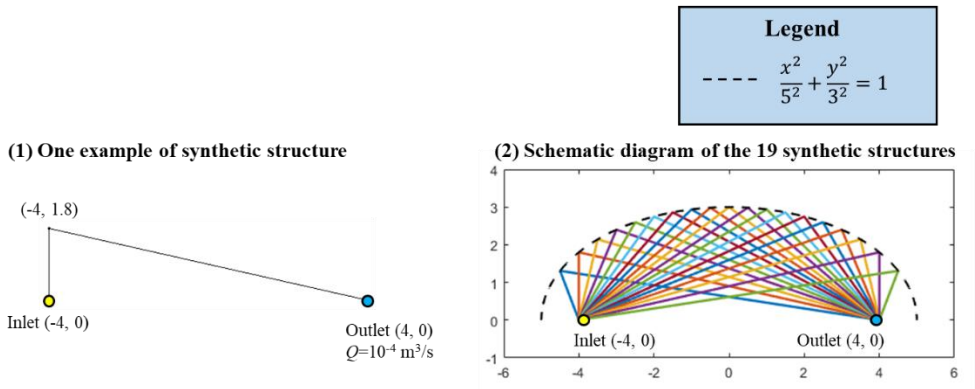

Figure 5.17. 19 two-segment conduit structures.

We assume a constant pressure boundary condition for the inlet; assume a constant flow rate for the outlet, $Q = 10^{-4}$ m^3/s. Fluid is pure water. At the inlet, a pulse of tracer is injected, and the duration of the injection lasts for one time-step. Diffusion $D_c = 1\times10^{-9}$ m^2/s, and dispersion $D_d = 3\times10^{-4}$ m^2/s. Mesh size: 0.002 m. Time step: 0.2 s.

The simulated BTCs are shown in Figure 5.18. It seems only one BTC is exhibited, while it is actually 19 BTCs overlaping each other. The results indicate that the bending angles of the conduit structure cannot influence the simulated BTCs.

Since we know the Q and d of the conduit, the flow velocity of the conduit can be calculated

$$v = \frac{Q}{0.25\pi d^2} = 0.0127 \ \ (\mathrm{m/s}) \tag{5-17}$$

And the advection velocity can be calculated with the length of the conduit and the mean transport time:

$$v_{\mathrm{transport,M}} = \frac{L_{\mathrm{total}}}{T_{\mathrm{transport}}} = 0.0126 \ \ (\mathrm{m/s}) \approx v \tag{5-18}$$

The results of Eq. 5-17 and 5-18 indicate that the mean transport time of the simulated BTC can be applied to estimate the flow velocity on the conduit network corresponding to the routes of the tracing tests.

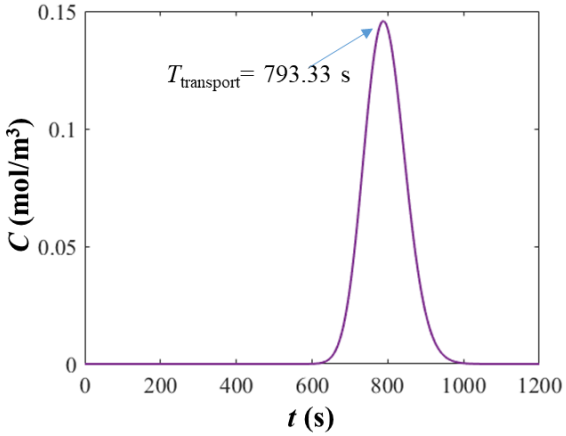

Figure 5.18. The simulated BTCs from the 19 structures.

5.5.2 The first implementation of inversion

5.5.2.1 Inversion test 1

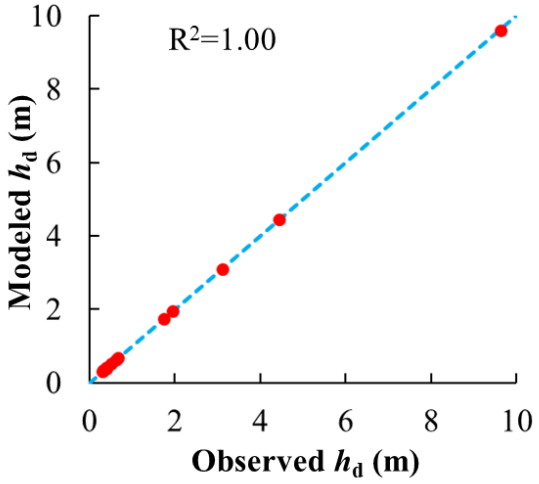

Figure 5.19. Scatter plots of modeled hydraulic heads versus observed hydraulic heads.

The data for inversion test 1 are the h_d data of the pumping test in P0 (pumping rate 52 m^3/h). The initial diameter field for the inversion study is dia_0 = 0.05 m. The inversion study converged and good fitness of the inverted and measured hydraulic data was obtained (Figure 5.19). The modeled diameter of the numerical conduit network ranges from 0.04 to 0.13 m (Figure 5.20a). Inside the central region (denoted by the black dotted line), the dia values are smaller than the outside. Inside, the dia values are smaller than 0.067 m. The largest dia values are exhibited by the eight conduits that are intersecting the boundary of this region: the dia values of these conduits are larger than 0.09 m. The modeled conduit network has much smaller diameter values than the field observations, which can be up to 0.50 m.

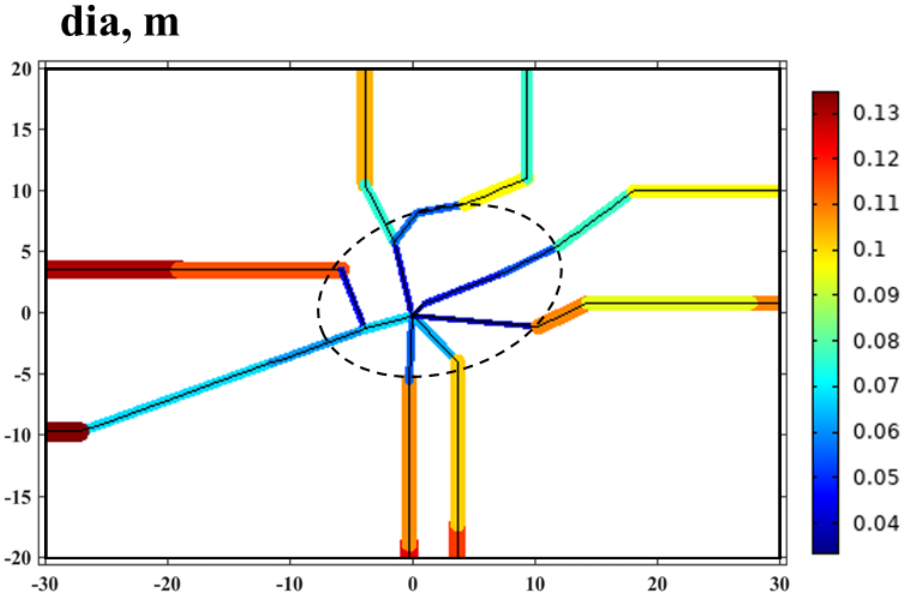

Figure 5.20. Diameter distribution modeled by inversion of h_d data.

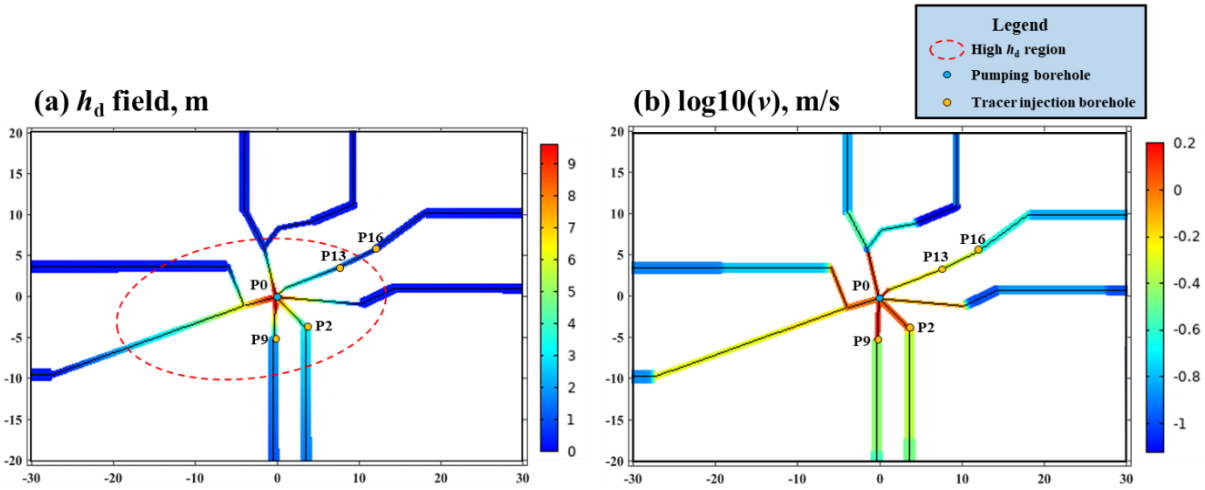

Figure 5.21. (a) Hydraulic drawdown field modeled by inversion of h_d data. (b) Velocity field modeled by inversion of h_d data.

We simulate the pumping tests in P0 finally. The modeled hydraulic drawdown (h_d) is exhibited in Figure 5.21a. Inside the oval area (enclosed by red dotted line), the modeled h_d value ranges from 2 to 9.62 m; outside of the oval area, the modeled h_d value ranges from 0 to 2 m. This reveals that the hydraulic drawdown is most significant in a relatively small area. The modeled velocity distribution (v) is also presented in Figure 5.21b. It is presented in the form of a log scale because there is large contrast among the velocities of the different conduits. The conduits in the central region exhibit larger velocity than the outside. The modeled velocity values range between 0.08 and 1.35 m/s. According to Table 5.4, the modeled $v_{transport}$ values are too large to be realistic, the values can be 4 degrees of magnitude larger than the velocity information determined from the tracing tests.

Table 5.4. Modeled v from h_d data versus mean $v_{transport}$.

Trajectory	$v_{transport,F}$ (m/s)	$v_{transport,M}$ (m/s)

P2P0	2.68×10^{-4}	1.11
P9P0	1.12×10^{-4}	1.35
P13P0	8.19×10^{-4}	1.41
P16P0	6.19×10^{-4}	1.41

5.5.2.2 Inversion test 2

Table 5.5. Modeled v by inversion of v_{BTC} data versus measured $v_{transport}$.

Trajectory	$v_{transport,F}$ (m/s)	$v_{transport,M}$ (m/s)	Calibrated D_d (m^2/s)
P2P0	2.68×10^{-4}	2.68×10^{-4}	7.55×10^{-8}
P9P0	1.12×10^{-4}	1.12×10^{-4}	1.31×10^{-6}
P13P0	8.19×10^{-4}	8.19×10^{-4}	7.10×10^{-4}
P16P0	6.19×10^{-4}	6.19×10^{-4}	3.55×10^{-4}

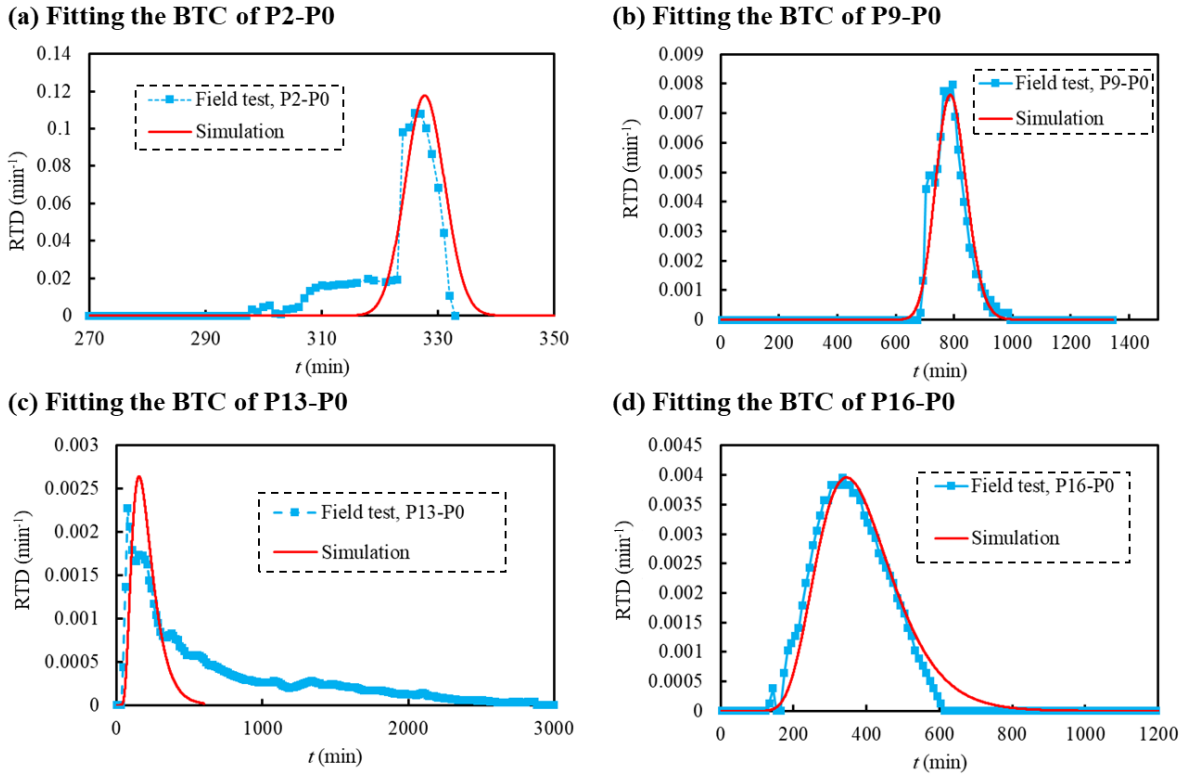

Figure 5.22. Comparing simulated BTCs to real BTCs.

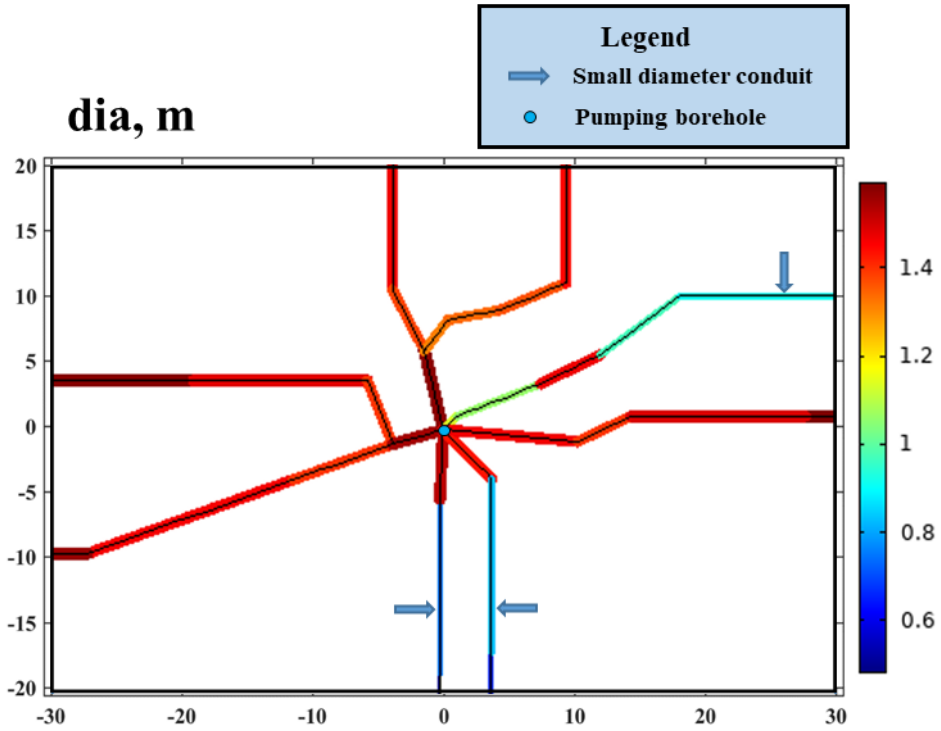

Figure 5.23. Diameter distribution modeled by inversion of v_{BTC} data.

The data for inversion test 2 are the four tracing BTCs, the pumping during the tracing tests was in P0 and the flow rates range from 50 to 52 m^3/h. The initial diameter field for the inversion study is dia_0 = 1.2 m. The inversion study converged and good fitness was obtained (Table 5.5, Figure 5.22). The modeled diameter of the conduit network ranges from 0.48 m to 1.60 m (Figure 5.23a). Three conduits exhibit relatively smaller dia values among the whole region, the values are smaller than 0.87 m. The other conduits exhibit large diameters, which are mostly larger than 1.2 m. The modeled conduit network has larger diameter values than the field observations (maximum to 0.50 m).

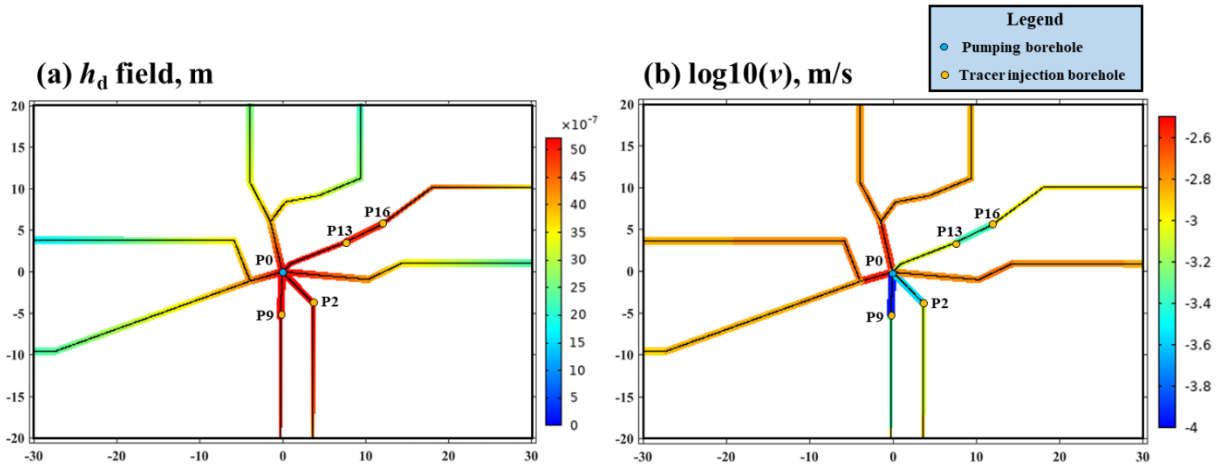

Figure 5.24. (a) Spacial distribution of modeled hydraulic head by inversion of v_{BTC} data. (b) Velocity field modeled by inversion of v_{BTC} data.

We also simulate the pumping tests in P0. The modeled hydraulic drawdown (h_d) is exhibited in Figure 5.24a, the value ranging from 0 to 5×10^{-6} m. These h_d values are too small to be realistic. These values can be 6 degrees of magnitude smaller than the h_d values observed in the pumping tests. The modeled velocity

(v) exhibits strong heterogeneity (Figure 5.24b): the velocity in some conduits can be 20 times larger than the other conduits. We have applied four tracing tests as the inversion data. For the conduits that bear the tracer injection boreholes, the v values are smaller than the other conduits. According to Table 5.5, v ranges between 1×10^{-4} to 8×10^{-4} m/s for these conduits. While the other conduits exhibit v values ranging from 1.3×10^{-3} to 2.7×10^{-3} m/s.

Comparing Test 2 to Test 1, the inversions of h_d and v_{BTC} data lead to very different results in three aspects. i) The modeled diameter fields are different. The diameter derived from the inversion of h_d data (Figure 5.20) is significantly smaller than the diameter derived from v_{BTC} data (Figure 5.23). ii) The modeled hydraulic drawdowns of the pumping test are different. If the inversion is carried out with h_d data, the simulated h_d can well fit the measured data in the field (Figure 5.19). If the inversion is carried out with v_{BTC} data, the simulated h_d field (0 to 5×10^{-6} m) can be several orders of magnitude smaller than the measured values (0 ~ 9.6 m). iii) The modeled velocity fields are different. If the inversion is carried out with h_d data, the simulated v can be three orders of magnitude larger than the velocity data determined by the field tracing test data (Table 5.4). If the inversion is carried out with v_{BTC} data, the simulated v values are identical to the measured data (Table 5.5).

5.5.2.3 Inversion test 3

Table 5.6. Modeled v by inversion of v_{BTC} data versus measured $v_{transport}$.

Trajectory	$v_{transport}$ (m/s)	Modeled $v_{transport}$ (m/s)
P2P0	2.68×10^{-4}	4.66×10^{-3}
P9P0	1.12×10^{-4}	4.58×10^{-3}
P13P0	8.19×10^{-4}	3.66×10^{-3}
P16P0	6.19×10^{-4}	3.87×10^{-3}

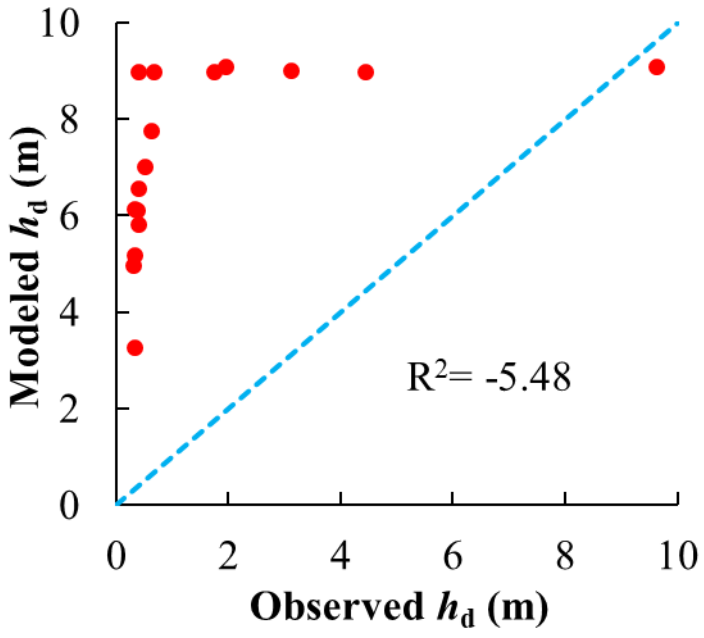

Figure 5.25. Modeled hydraulic heads by inversion of h_d data.. (a) Scatter plots of modeled hydraulic heads versus observed hydraulic heads. (b) Spacial distribution of modeled hydraulic head.

For test 3, we realize the joint inversion of the h_d data (pumping test in P0) and the four tracing BTCs. The initial diameter field for the inversion study is dia_0 = 0.072 m. The inversion study does not converge; two types of field data have not been well reproduced. As shown in Figure 5.25, the modeled h_d is highly different from the observed h_d values. The fitting performance of h_d is poor, with R^2= -5.48. The $v_{transport}$ data are also poorly fitted (Table 5.6). The modeled $v_{transport}$ values are much larger than the observed $v_{transport}$ determined by field tracing tests. To the best of our attempt, this forward model still cannot well reproduce the two kinds of data at the same time.

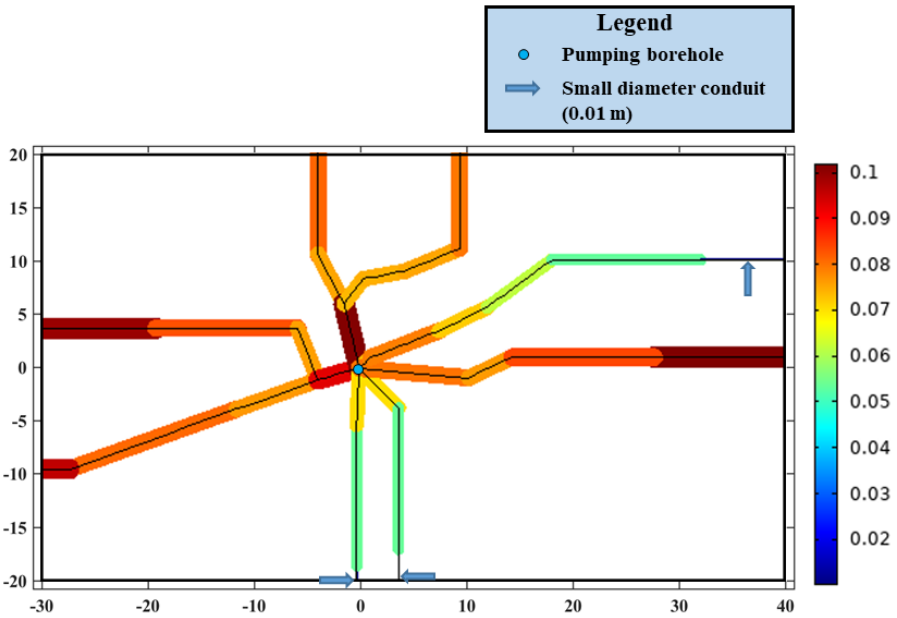

Figure 5.26. Diameter distribution modeled by joint inversion of h_d and v_{BTC} data.

The modeled diameter of the numerical conduit network ranges from 0.01 cm to 0.10 m (Figure 5.26). Three segments exhibit the smallest diameter (denoted by the blue arrows) of 0.01 m. The other conduits exhibit relatively larger dia values, the dia values range between 0.07 and 0.1 m. According to Table 5.6, the modeled $v_{transport,F}$ on these routes are much larger than $v_{transport,F}$. The inversion model adjusted the diameter in this way to fit the $v_{transport,F}$ data. Because such dia distribution increases the resistance on the route of the tracing tests and decreases the flow resistance of the other conduits; further it can decrease the flow velocity on the routes (Figure 5.27b). However, this diameter distribution still fails to reproduce the $v_{transport,F}$ data.

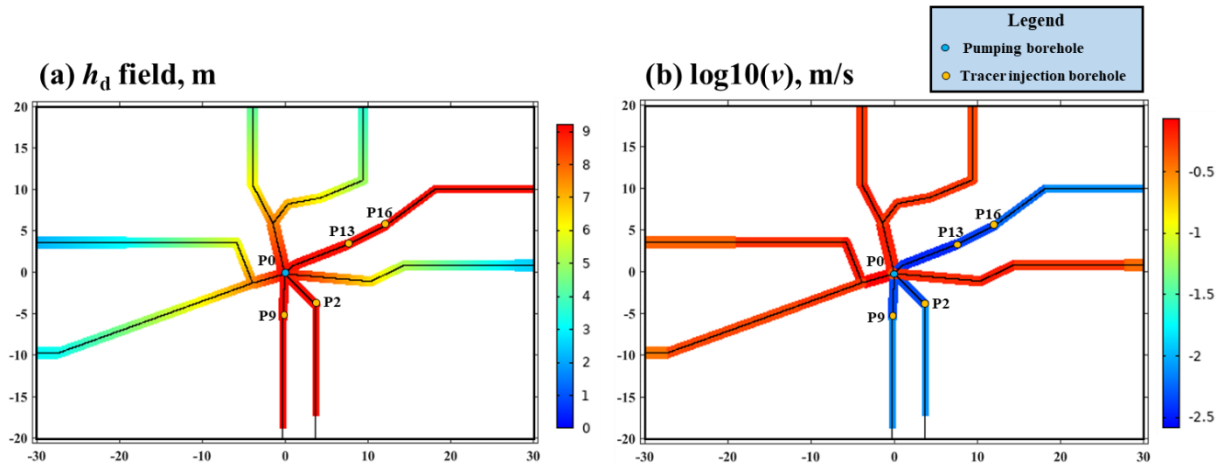

Figure 5.27. Velocity field modeled by joint inversion of h_d and v_{BTC} data.

5.5.3 The second implementation of inversion

In this section, we first discuss the possible reason why the pipe model failed to reproduce the two types of field test data at the same time, second, we propose the possible solution to save this failure and further realize better characterization of the Terrieu site by joint inversion of the two types of field data.

To figure out the reason for the failure of inversion test 3, we summarize the key points from the previous three inversion studies: i). In inversion test 1, the modeled diameter is less than 0.12 m (Figure 5.20); and the modeled velocity on the routes can be larger than 0.1 m/s (Figure 5.21), which is significantly larger than the observations. ii). In inversion test 2, the modeled diameter range between 0.5 ~ 2.6 m (Figure 5.23); and the modeled h_d are about 4 magnitudes smaller than the observations (Figure 5.24). iii) In comparison, the dia values of test 1 is significantly smaller than test 2. iv). This forward model cannot reproduce the two kinds of data at the same time (Figure 5.25, Table 5.6).

After reviewing the above points, the low h_d value modeled by the inversion test 2 (Figure 5.24) caught our attention. If we can improve the flow resistance for each conduit segment while keeping the diameter values, the modeled h_d value is possible to be modified to the same degree as the field observations.

To increase the flow resistance for the conduit segments, one possible method is to add a small diameter conduit segment on each conduit segments, as Figure 5.28. According to Eq. 5-9, the pressure loss for a single conduit segment can be express as:

$$\nabla p = -f_d \frac{\rho}{2d}\boldsymbol{u}|\boldsymbol{u}| = -f_d \frac{\rho}{2d}\frac{\boldsymbol{Q}|\boldsymbol{Q}|}{\pi^2 r^4} = -f_d \frac{8\rho}{d}\frac{\boldsymbol{Q}|\boldsymbol{Q}|}{\pi^2 d^4} = -f_d \frac{8\rho}{\pi^2 d^5}\boldsymbol{Q}|\boldsymbol{Q}|, \quad (5\text{-}19)$$

which means the flow resistance for each conduit is highly sensitive to the diameter. Thus the small diameter segment will significantly increase the flow resistance of the conduit. Then this implementation is possible to allow the conduit network model to reproduce the tracing data and h_d data at the same time. For each conduit, the small diameter segment bears most of the pressure drop. The large diameter part makes the large cross-section area of the conduit; under a same flow rate, then the flow velocity in this part can be

much lower. So the large-diameter part takes up most of time of tracer transport.

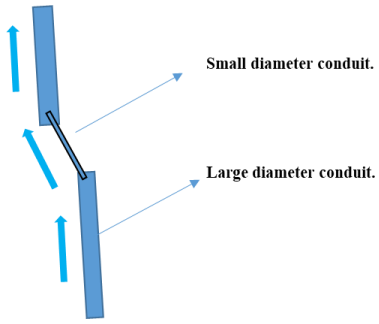

Figure 5.28. Conceptual diagram of singular headloss effect caused by diameter variation.

And this implementation of small-diameter part (Figure 5.28) can be more realistic than assuming constant diameter for each conduit segments. In nature, the karst conduits rarely exhibit a constant diameter. The continuous variation of the diameter (or the aperture) has been recorded for karst conduits (Morales et al., 2010; Cardenas et al., 2007). Two typical karst structures mapped by (Palmer, 1991) from are shown in Figure 5.29. And the conduit diameters exhibit continuous variations.

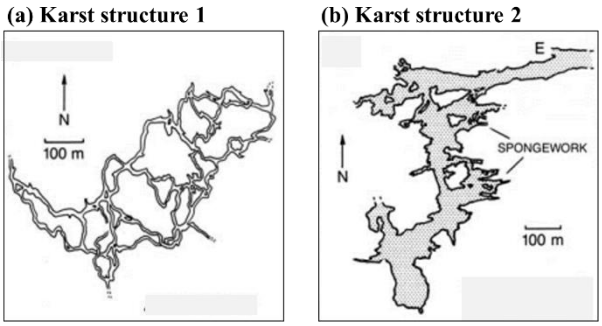

Figure 5.29. Two conduit structures mapped by Palmer, 1991.

However, if we add a small-diameter segment for the conduit segments, we will need to include two extra parameters for each conduit segment: the length and the diameter for this smaller-diameter part. The two extra parameters may interact to characterize the flow resistance of this conduit. For a single conduit, if the smaller-diameter segment has different lengths, the modeled results for the inversion studies should also be different. The available field data cannot help us to determine a realistic length for this small-diameter conduit.

There is another method to characterize the small diameter effect: to adopt the friction factor (fd) as a conduit parameter. According to Eq. 5-19, under the same flow rate and same diameter, increasing fd causes the flow resistance of a conduit to increase, which means the smaller-diameter part of this conduit is functioning to cause more significant pressure loss. By adopting fd as a conduit parameter to model the effect of small-diameter part, we only include one extra parameter.

The second method is more feasible than the first one in this study. Because it does not require us to split the conduit segment into some parts with different diameters and specific lengths. The second method realizes an integral characterization of the flow resistance of a conduit. According to Eq. 5-19, the pressure resistance for a single conduit segment can be express as:

$$R = f_{\mathrm{d}} \frac{8\rho}{\pi^2 d^5} \quad . \tag{5-20}$$

Thus, we construct a new forward model on the conduit network. For this new forward model, each conduit segment has two parameters: dia and fd. dia represents the diameter of the conduit, and the two parameters together can be used to characterize the flow resistance of a conduit according to Eq. 5-20. We carry out the following new inversion studies with the new forward model. We check whether we can realize the joint inversion of the two types of data at the same time.

5.5.3.1 Inversion test 4

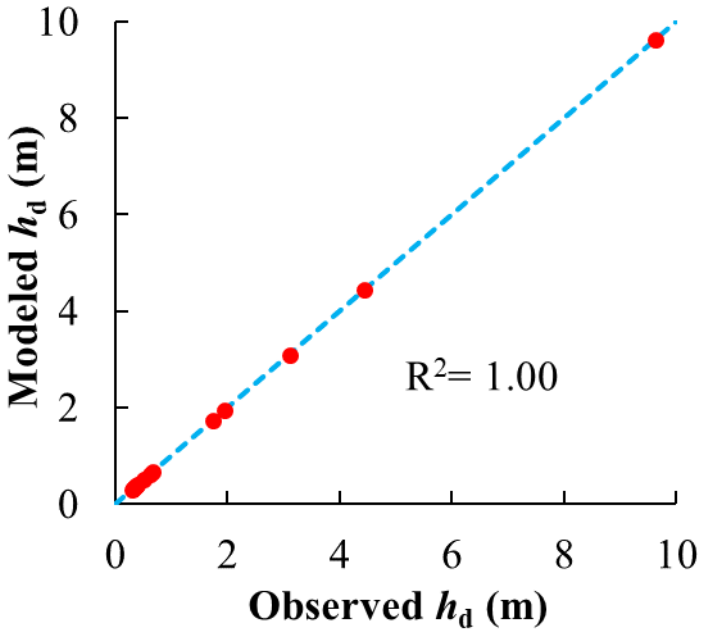

Figure 5.30. Modeled hydraulic heads by joint inversion of h_d and $v_{transport}$ data. (a) Scatter plots of modeled hydraulic heads versus observed hydraulic heads. (b) Spacial distribution of modeled hydraulic head.

Table 5.7. Modeled v by joint inversion of h_d and $v_{transport}$ data versus measured $v_{transport}$.

Trajectory	$v_{transport}$ (m/s)	Modeled $v_{transport}$ (m/s)
P2P0	2.68×10^{-4}	2.68×10^{-4}
P9P0	1.12×10^{-4}	1.12×10^{-4}
P13P0	8.19×10^{-4}	8.19×10^{-4}
P16P0	6.19×10^{-4}	6.19×10^{-4}

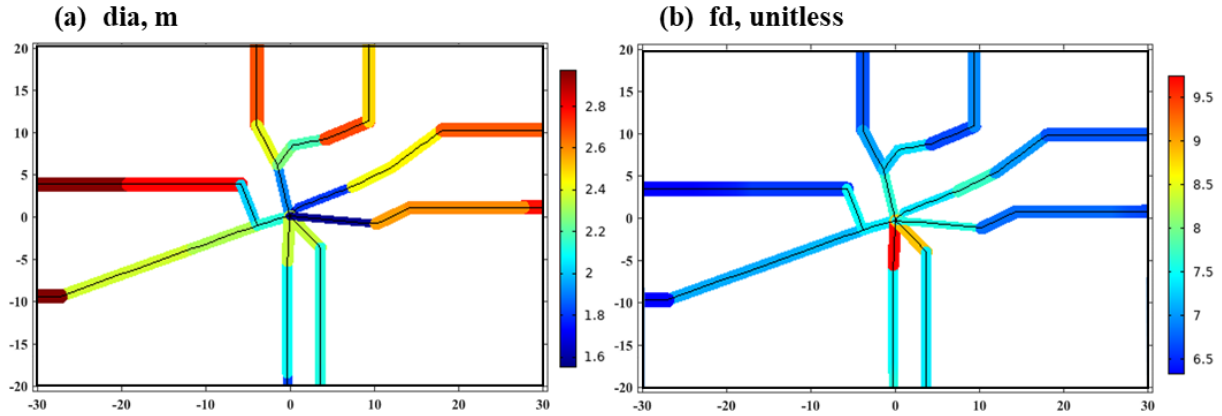

Figure 5.31. Conduit parameters modeled by joint inversion of h_d and v_{BTC} data.

For test 4, we realize the joint inversion of the h_d data (pumping test in P0) and the four tracing BTCs. The initial diameter field for the inversion study is dia_0 = 2.2 m; the initial friction factor field for the inversion study is $\log(fd_0) = 7.3$. The inversion study converged and good fitness of both data was realized. Not only the measured h_d data are well reproduced (Figure 5.30), the $v_{transport}$ data derived from the tracing tests are also well reproduced (Table 5.7). The modeled BTCs are the same with Figure 5.22. When compared to inversion test 3, inversion test 4 has one more parameter: friction factor (fd) of the conduit segments. With one more parameter, the model flexibility has been effectively improved. Thus it could well reproduce the both kinds of data.

The modeled dia field is shown in Figure 5.31a. The dia values range between 1.54 and 2.97 m. The modeled conduit network has larger diameter values than the field observations (maximum to 0.50 m). The modeled fd field is shown in Figure 5.31b. The conduit of P9-P0 has the largest fd among the whole region, about 5.5×10^9. The conduit of P2-P0 has the second largest fd, about 7.3×10^8.

The new implementation has allowed the forward model to well reproduce the h_d data of the pumping tests. From the pumping borehole to the outside, the modeled h_d value gradually decreases from 9.6 to 0 m (Figure 5.32a). Since the conduit diameters are large, the modeled v are reduced to realistic range (Figure 5.32b), 1.1×10^{-4} to 1.6×10^{-3} m/s.

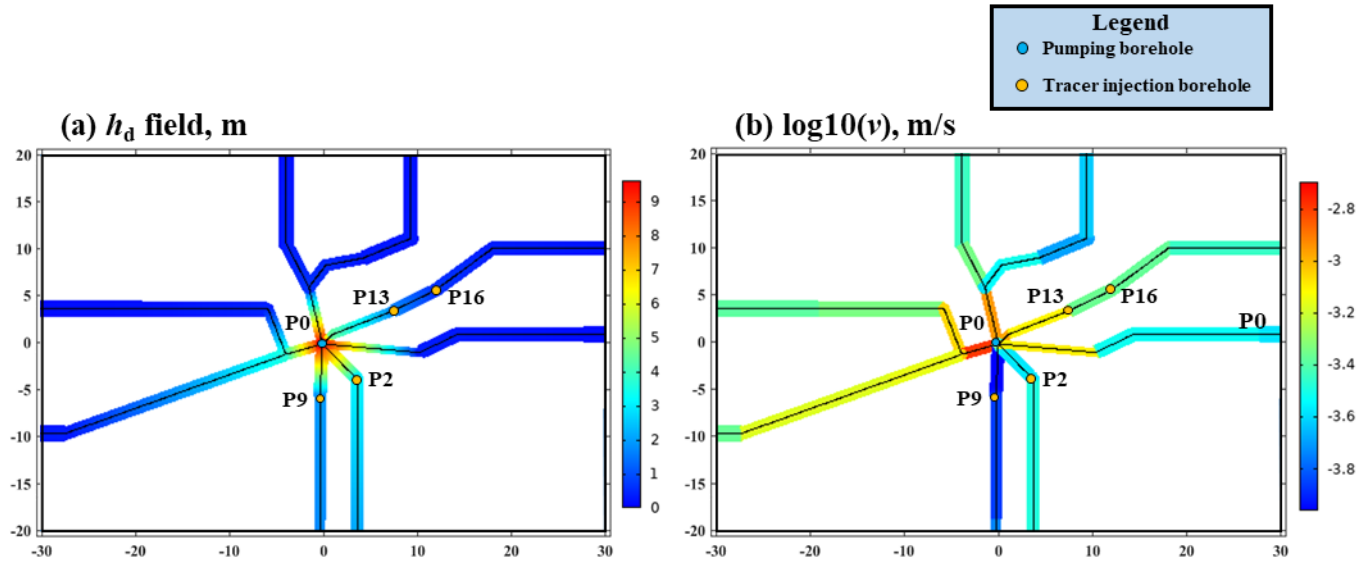

Figure 5.32. Modeled velocity fields by joint inversion of h_d and $v_{transport}$ data. (a) Scatter plots of modeled hydraulic heads versus observed hydraulic heads. (b) Spacial distribution of modeled hydraulic head.

5.5.3.2 Inversion test 5

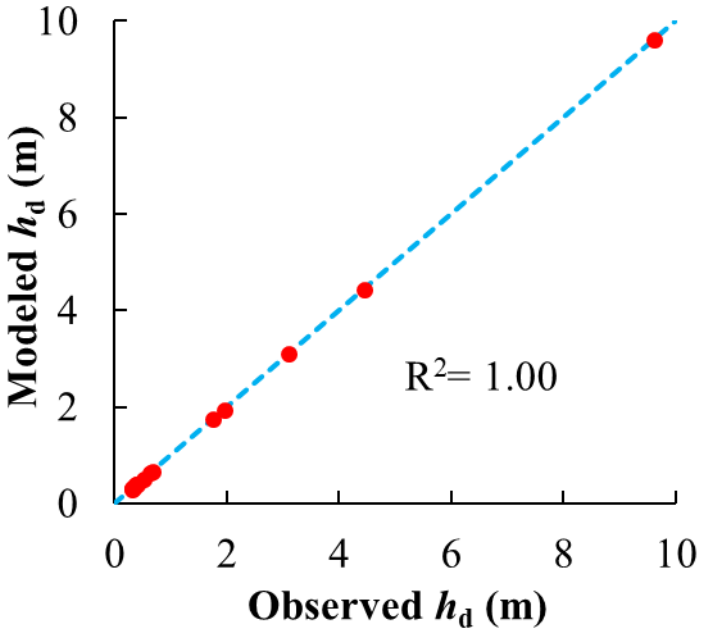

Figure 5.33. Modeled hydraulic heads by joint inversion of h_d and $v_{transport}$ data. (a) Scatter plots of modeled hydraulic heads versus observed hydraulic heads. (b) Spacial distribution of modeled hydraulic head.

The previous inversion test has generated unrealistically high diameters. In this test, we impose an upper bound of 0.5 m for the diameter value. The initial diameter field for the inversion study is $dia_0 = 0.40$ m; the initial friction factor field for the inversion study is $\log(fd_0) = 4$. While the other settings remain the same with Test 4. The inversion study converged and good fitness of both data was realized again. Not only

the measured h_d data are well reproduced (Figure 5.33), the $v_{transport}$ data derived from the tracing tests are also well reproduced (Table 5.8). Test 5 realized good fitting to the measured data.

Table 5.8. Modeled v by joint inversion of h_d and $v_{transport}$ data versus measured $v_{transport}$.

Trajectory	$v_{transport}$ (m/s)	Modeled $v_{transport}$ (m/s)
P2P0	2.68×10^{-4}	2.68×10^{-4}
P9P0	1.12×10^{-4}	1.12×10^{-4}
P13P0	8.19×10^{-4}	8.19×10^{-4}
P16P0	6.19×10^{-4}	6.19×10^{-4}

The modeled dia field is shown in Figure 5.34a. The dia values range between 0.30 and 0.46 m. The obtained diameter values are realistic. The modeled fd field is shown in Figure 5.34b. The conduit of P9-P0 has the largest fd among the whole region, about 3.5×10^8. The conduit of P2-P0 has the second largest fd, about 7.3×10^8. The three conduits that bear the tracing tests (marked by the yellow points) exhibit relatively larger fd value than the other conduits. The log(fd) value of these three conduits range from 5 to 8.5, while the log(fd) value of the other conduits are smaller than 5.

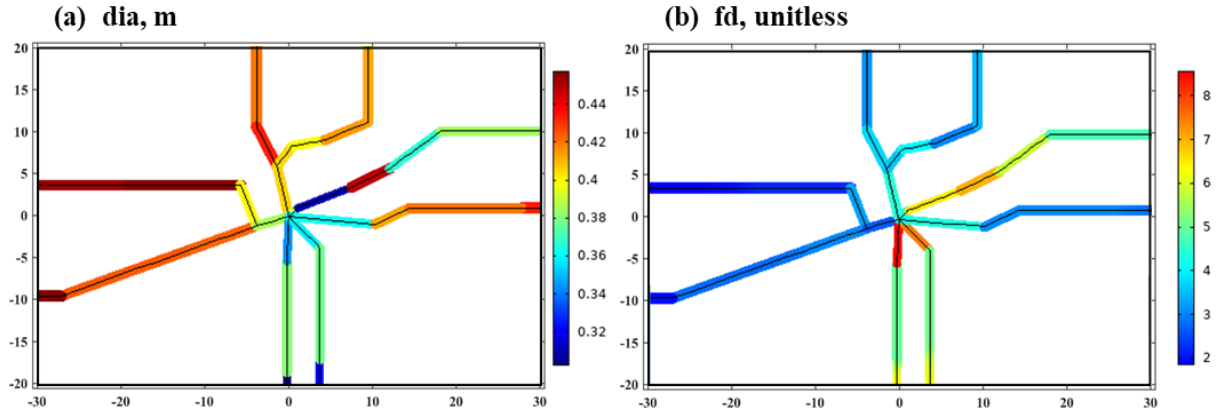

Figure 5.34. Conduit parameters modeled by joint inversion of h_d and v_{BTC} data.

Figure 5.35a shows that the model has generated realistic h_d values. Figure 5.35b shows the modeled log(v) values range from -4 to -1. The conduits on the tracing routes exhibit relatively smaller v values, log(v) values range between -4 and -3. The two west conduits exhibit the largest v values among the whole region. Which suggests that most of the flow rate is supported by the west direction.

Combining Figure 5.34 and Figure 5.35, we know that the conduits of P9-P0 and P2-P0 have especially high flow resistance and low flow rate. The conduits in the west directions have much smaller flow resistance and high flow rate. These information is in agreement with the regional investigation in the well site realized by Fischer et al., 2022. Thus the results of Figure 5.34 can be deemed as a reliable characterization of the Terrieu well site.

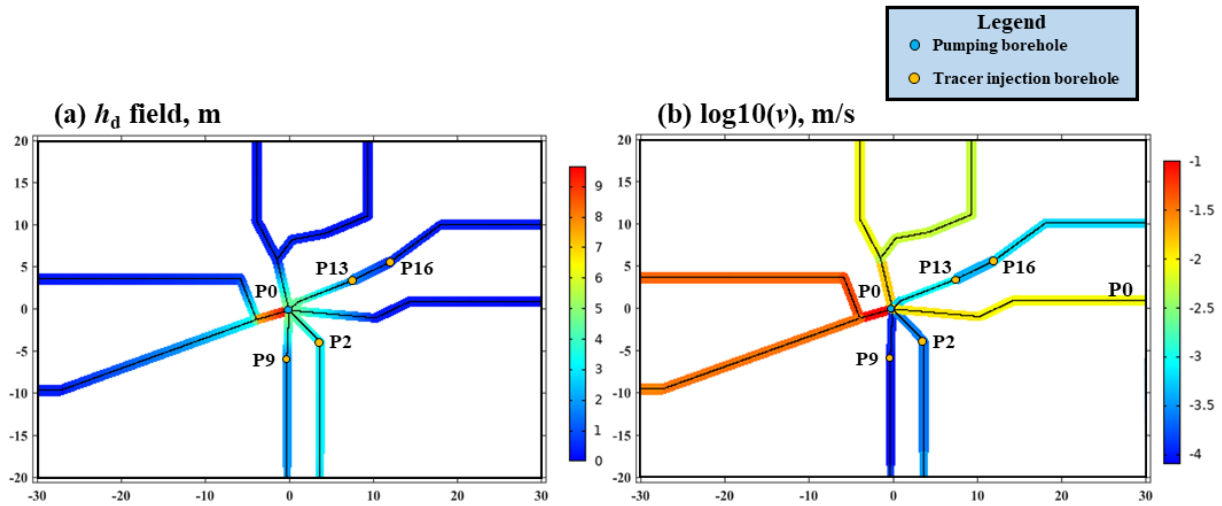

Figure 5.35. Modeled velocity fields by joint inversion of h_d and $v_{transport}$ data. (a) Scatter plots of modeled hydraulic heads versus observed hydraulic heads. (b) Spacial distribution of modeled hydraulic head.

5.6 Discussion

5.6.1 The innovative implementations

This study an advancement to the previous studies that have applied EPM method to conceptualize the well site (Fischer et al., 2017b, 2018b; Wang et al., 2016, 2017). Because in this study, we have applied a discrete conduit model to conceptualize one part of the karstified Lez aquifer. Numerous studies claimed that the DCN/ DFN model is more appropriate for characterizing the karstified and fractured media; the EPM often fail to model the high flow in the karstified and fractured media. We also notice another advantage of the DCN model over EPM, namely the inverted diameter field of a conduit structure is a more direct characterization of the natural karstified features. The new inversion results bring us direct information about the diameter of the underground conduits. The inverted K field of the EPM cannot directly illustrate this property.

Two innovative implementations played vital roles in the inversion study. The first innovative implementation is to assume two parameters for each conduit segment: diameter and friction factor. With these two factors, we can separately characterize the two parts of each conduit segment: a large-diameter part and a small-diameter part. For the numerical model, dia value characterizes the flow volume of the conduit segment; while for a natural karst conduit, the large diameter part makes the main volume for flow. Thus dia represents the large-diameter part of the conduit segment. Again, numerically the combination of (Eq. 5-20) characterizes the flow resistance of the conduit segment; while in nature, the small diameter part dominantly determine the flow resistance. Thus, (Eq. 5-20 represents the small-diameter part of the conduit segment. This implementation is so necessary for two reasons: first, if we don't conside the two parts for each conduit segment, then the forward model cannot well reproduce the two types of the field test data at the same time (see inversion Test 3). Second, this implementation make the numerical DPN model more

approximate to the true condition of a natural karstified network (according to the discussions in Section 5.5.3).

The second innovative implementation is to divide the inversion investigation into two steps. In Step 1, we calibrate the dia and fd fields to invert the measured h_d and $v_{transport,F}$ data. In Step 2, we calibrate the D_d value to fit the transport BTCs. Previously the inversion study needs to fit the BTCs directly. This innovative implementation is effective and necessary for two reasons. First, this implementation has made the inversion tests much more efficient. Because it allows us to change the forward model from the transient simulation of solute transport (relatively longer simulation time) to the steady-state simulation (relatively shorter simulation time) of water flow. According to Section 5.5.1, in our most conservative estimate, it requires 10×2000 min ≈13.9 days to realize one inversion study with the transient simulation of solute transport as the forward model. It would be huge cost of time. In comparison, steady-state simulation of fluid flow takes about 6 s. After the values of $v_{transport,F}$ are fitted by the forward model, it requires very few iterations (about 100) for the forward model to reproduce the transport BTCs by adjusting the dispersion coefficient. Thus this implementation reduced the time cost for the inversion tests to an acceptable extent. Second, this implementation can help the inversion study to converge. During the inversion tests, we found that it is easier for the inversion model to converge if we fit the $v_{transport}$ values than we fit the BTCs.

In summary, the two implementations are effective and necessary in this inversion study. Without implementation 1, it would be hard to realize the successful joint inversion of the two types of field tests data. Without implementation 2, the inversion study may take huge time cost and may not effectively converge. These two implementations have made this inversion study successful.

5.6.2 The difference of inversions with h_d data and $v_{transport}$ data

In this study, two types of data are applied for the characterization (diameter field) of the underground karst conduit network of Terrieu well site: the steady-state h_d data of interference pumping tests and the BTCs of the tracing tests. We further analyze what different information that the two types of data can bring us about the underground karst network.

h_d data bring us information about the small-diameter part of each conduit segments. We make this judgment on two grounds. First, under the same flow rate, decreasing the diameter should cause the flow resistance to increase significantly (according to Eq. 5-20). Then the small-diameter part dominantly determines the flow resistance of a conduit. And the flow resistance dominantly determines the spatial distribution of h_d from the pumping tests. Thus the measured h_d data is closed related to the small-diameter part of the conduit segments. Second, in practice when we characterize the karst conduit network by inverting the h_d data, the modeled dia is much smaller than the field observations. Thus, by inverting the h_d data we can obtain information about the small-diameter part of each conduit segments.

The $v_{transport,F}$ data, which is derived from the tracing BTCs, alone cannot bring us information about

the conduit network. Because $v_{\text{transport,F}}$ is determined by two factors:

$$v_{\text{transport,F}} = \frac{Q_{\text{route}}}{A_{\text{route}}} \ , \tag{5-21}$$

where Q_{route} means the flow rate on this route, m^3/s, and A_{route} is the mean cross-section area on this route, m^2. Under a constant total pumping flow rate, Q_{route} is actually determined by the spatial distribution of flow resistance, thus the property of the small-diameter part of all of the conduit segments. The value of A_{route} is determined by large-diameter part of all of the conduit segments. Thus the transport data alone cannot effectively characterize the diameter distribution of conduit network.

With the joint inversion of both the h_d data and $v_{\text{transport}}$ data, we can characterize the conduit network comprehensively: both the small-diameter part and large-diameter part. The inversion of the h_d data characterizes the small-diameter part, in the meantime, it also determines the spatial distribution of Q_{route}. With Q_{route} and $v_{\text{transport}}$ data, the inversion model will be able to characterize the large-diameter part.

Previously, numerous researchers have applied the h_d data and the transport data to characterize the karst and fractured media. But rarely did they consider the different effects of the two types of data. So it was unclear what different information the two types of data can bring us. The result and discussion in this study provide important implications to the researcher who is interested in applying these two types of data in investigating the highly heterogeneous aquifers.

5.7 Conclusions

In this study, we propose a new inverse approach to characterize the spatial property of a karst conduit network. In total, 5 tests have been carried out to inverse the field data. These 5 tests have been realized by applying different inversion data and imposing different numerical setups for the model.

Test 1 is realized by the inversion of pumping test data, Test 2 is realized by the inversion of tracing test data, Tests 3-5 are realized by joint inversion of pumping tests data (h_d data) and tracing test data. By comparing the results of these tests, we understand that the two types of data bring us different information about the underground karst network. h_d data characterizes the small-diameter part of each conduit segments; tracing test data bring us information about the advection velocity and dispersion coefficient on the transport route during the tests. With the joint inversion of both the h_d data and $v_{\text{transport}}$ data, we can characterize the conduit network comprehensively: both the small-diameter part and large-diameter part.

The failure of Test 3 and the success of Test 4 highlight that it is necessary to consider the small-diameter part and the large-diameter part of each conduit segment if we need to characterize a natural karst conduit network. The two parts have different influences on hydraulic behaviors. The small diameter dominantly influences flow resistance for each flow connectivity. The large-diameter influences the large flow space, which dominantly influences the flow velocity.

The information obtained from the borehole videos has effectively improved the characterization. In

Test 4, despite both types of data have been well reproduced, the constructed conduit diameters are too large to be realistic. According to the maximum conduit diameter observed in borehole videos, we imposed the upper bound for the conduit diameter for Test 5. Then the constructed dia field has become realistic. And the characterization is further improved because the constructed heterogeneity is found to be consistent with a regional investigation of the well site.

References

Abusaada, M., Sauter, M., 2013. Studying the flow dynamics of a karst aquifer system with an equivalent porous medium model. Groundwater 51, 641–650.

Ahmed, A.S., Zhou, J., Jardani, A., Revil, A., Dupont, J.-P., 2015. Image-guided inversion in steady-state hydraulic tomography. Advances in Water Resources 82, 83–97.

Bohling, G.C., Butler Jr, J.J., 2010. Inherent limitations of hydraulic tomography. Groundwater 48, 809–824.

Borghi, A., Renard, P., Cornaton, F., 2016. Can one identify karst conduit networks geometry and properties from hydraulic and tracer test data? Advances in Water Resources 90, 99–115.

Botton, R., 1984. Etude de certaines modalités du fonctionnement de l'aquifère karstique (zone d'infiltration et zone saturée) sur deux champs de forages Nord-Montpellierains. Université des Sciences et Techniques du Languedoc.

Cappa, F., Guglielmi, Y., Rutqvist, J., Tsang, C.-F., Thoraval, A., 2008. Estimation of fracture flow parameters through numerical analysis of hydromechanical pressure pulses. Water Resour Res 44.

Cardenas, M.B., Slottke, D.T., Ketcham, R.A., Sharp Jr, J.M., 2007. Navier-Stokes flow and transport simulations using real fractures shows heavy tailing due to eddies. Geophysical Research Letters 34.

Cardiff, M., Bakhos, T., Kitanidis, P.K., Barrash, W., 2013. Aquifer heterogeneity characterization with oscillatory pumping: Sensitivity analysis and imaging potential. Water Resources Research 49, 5395–5410.

Cardiff, M., Barrash, W., Kitanidis, P.K., Malama, B., Revil, A., Straface, S., Rizzo, E., 2009. A potential-based inversion of unconfined steady-state hydraulic tomography. Groundwater 47, 259–270.

Cardiff, M., Kitanidis, P.K., 2008. Efficient solution of nonlinear, underdetermined inverse problems with a generalized PDE model. Computers & Geosciences 34, 1480–1491.

Cussler, E.L., 1997. Diffusion: mass transfer in fluid systems (2nd ed.). Cambridge university press.

Dausse, A., 2015. Facteurs d'échelle dans la hiérarchisation des écoulements au sein d'un aquifère karstique: Analyse multi-échelles des propriétés hydrodynamiques et de transport de l'aquifère du Lez. Université Montpellier.

Day-Lewis, F.D., Hsieh, P.A., Gorelick, S.M., 2000. Identifying fracture-zone geometry using simulated annealing and hydraulic-connection data. Water Resources Research 36, 1707–1721.

Fischer, P., Jardani, A., Cardiff, M., Lecoq, N., Jourde, H., 2018a. Hydraulic analysis of harmonic pumping tests in frequency and time domains for identifying the conduits networks in a karstic aquifer. Journal of Hydrology 559, 1039–1053.

Fischer, P., Jardani, A., Jourde, H., Cardiff, M., Wang, X., Chedeville, S., Lecoq, N., 2018b. Harmonic pumping tomography applied to image the hydraulic properties and interpret the connectivity of a karstic and fractured aquifer (Lez aquifer, France). Advances in Water Resources 119, 227–244.

Fischer, P., Jardani, A., Lecoq, N., 2017a. A cellular automata-based deterministic inversion algorithm for the characterization of linear structural heterogeneities. Water Resources Research 53, 2016–2034.

Fischer, P., Jardani, A., Wang, X., Jourde, H., Lecoq, N., 2017b. Identifying flow networks in a karstified aquifer by application of the cellular automata-based deterministic inversion method (Lez aquifer, France). Water Resources Research 53, 10508–10522.

Gill, P.E., Murray, W., Saunders, M.A., 2005. SNOPT: An SQP algorithm for large-scale constrained optimization. SIAM review 47, 99–131.

Gill, P.E., Murray, W., Saunders, M.A., 2006. User's guide for SNOPT version 7: Software for large-scale nonlinear programming.

Goldscheider, N., Drew, D., 2014. Methods in Karst Hydrogeology: IAH: International Contributions to Hydrogeology, 26. Crc Press.

Hale, D., 2009. Structure-oriented smoothing and semblance. CWP report 635.

Hao, Y., Yeh, T.-C.J., Xiang, J., Illman, W.A., Ando, K., Hsu, K.-C., Lee, C.-H., 2008. Hydraulic tomography for detecting fracture zone connectivity. Groundwater 46, 183–192.

Illman, W.A., 2014. Hydraulic tomography offers improved imaging of heterogeneity in fractured rocks. Groundwater 52, 659–684.

Illman, W.A., Liu, X., Craig, A., 2007. Steady-state hydraulic tomography in a laboratory aquifer with deterministic heterogeneity: Multi-method and multiscale validation of hydraulic conductivity tomograms. Journal of Hydrology 341, 222–234.

Jazayeri, N.M.R., 2009. Characterisation of relationship between fracture network and flow-path network in fractured and karstic reservoirs. Numérical modelling and field investigation (Lez aquifer, Southern France).

Jazayeri, N.M.R., Jourde, H., Massonnat, G., 2011. Influence of the observation scale on permeability estimation at local and regional scales through well tests in a fractured and karstic aquifer (Lez aquifer, Southern France). Journal of Hydrology 403, 321–336.

Jourde, H., Batiot-Guilhe, C., Bailly-Comte, V., Bicalho, C., Blanc, M., Borrell, V., Bouvier, C., Boyer, J.-F., Brunet, P., Cousteau, M., others, 2011. The MEDYCYSS observatory, a multi scale observatory of flood dynamics and hydrodynamics in karst (Mediterranean border Southern France). In: Advances in the Research of Aquatic Environment. Springer, pp. 551–560.

Jourde, H., Cornaton, F., Pistre, S., Bidaux, P., 2002. Flow behavior in a dual fracture network. J Hydrol (Amst) 266, 99–119.

Klepikova, M., Brixel, B., Jalali, M., 2020. Transient hydraulic tomography approach to characterize main flowpaths and their connectivity in fractured media. Advances in Water Resources 136, 103500.

Klepikova, M. v, le Borgne, T., Bour, O., de Dreuzy, J.-R., 2013. Inverse modeling of flow tomography experiments in fractured media. Water Resources Research 49, 7255–7265.

Klepikova, M. v, le Borgne, T., Bour, O., Gallagher, K., Hochreutener, R., Lavenant, N., 2014. Passive temperature tomography experiments to characterize transmissivity and connectivity of preferential flow paths in fractured media. Journal of Hydrology 512, 549–562.

Kresic, N., Stevanovic, Z., 2009. Groundwater hydrology of springs: engineering, theory, management and sustainability. Butterworth-heinemann.

Larocque, M., Banton, O., Ackerer, P., Razack, M., 1999a. Determining karst transmissivities with inverse modeling and an equivalent porous media. Groundwater 37, 897–903.

Larocque, M., Banton, O., Ackerer, P., Razack, M., 1999b. Determining karst transmissivities with inverse modeling and an equivalent porous media. Groundwater 37, 897–903.

Lavenue, M., de Marsily, G., 2001. Three-dimensional interference test interpretation in a fractured aquifer using the pilot point inverse method. Water Resources Research 37, 2659–2675.

le Goc, R., de Dreuzy, J.-R., Davy, P., 2010. An inverse problem methodology to identify flow channels in fractured media using synthetic steady-state head and geometrical data. Adv Water Resour 33, 782–800.

Lee, J., Kitanidis, P.K., 2013. Bayesian inversion with total variation prior for discrete geologic structure identification. Water Resources Research 49, 7658–7669.

Liu, S., Yeh, T.-C.J., Gardiner, R., 2002. Effectiveness of hydraulic tomography: Sandbox experiments. Water Resources Research 38, 1–5.

Liu, X., Illman, W.A., Craig, A.J., Zhu, J., Yeh, T.-C., 2007. Laboratory sandbox validation of transient hydraulic tomography. Water Resources Research 43.

Lochbühler, T., Vrugt, J.A., Sadegh, M., Linde, N., 2015. Summary statistics from training images as prior information in probabilistic inversion. Geophysical Journal International 201, 157–171.

Long, J.C.S., Remer, J.S., Wilson, C.R., Witherspoon, P.A., 1982. Porous media equivalents for networks of discontinuous fractures. Water Resour Res 18, 645–658.

Morales, T., Uriarte, J.A., Olazar, M., Antigüedad, I., Angulo, B., 2010. Solute transport modelling in karst conduits with slow zones during different hydrologic conditions. Journal of Hydrology 390, 182–189.

Neuman, S.P., 2005. Trends, prospects and challenges in quantifying flow and transport through fractured rocks. Hydrogeology Journal 13, 124–147.

Palmer, A.N., 1991. Origin and morphology of limestone caves. Geological Society of America Bulletin 103, 1–21.

Sahimi, M., 2011. Flow and transport in porous media and fractured rock: from classical methods to modern approaches. John Wiley & Sons.

Saller, S.P., Ronayne, M.J., Long, A.J., 2013. Comparison of a karst groundwater model with and without discrete conduit flow. Hydrogeol J 21, 1555–1566.

Sharmeen, R., Illman, W.A., Berg, S.J., Yeh, T.-C.J., Park, Y.-J., Sudicky, E.A., Ando, K., 2012. Transient hydraulic tomography in a fractured dolostone: Laboratory rock block experiments. Water

Resources Research 48.

Somogyvári, M., Jalali, M., Jimenez Parras, S., Bayer, P., 2017. Synthetic fracture network characterization with transdimensional inversion. Water Resources Research 53, 5104–5123.

Soueid Ahmed, A., Jardani, A., Revil, A., Dupont, J.P., 2015. HT2DINV: A 2D forward and inverse code for steady-state and transient hydraulic tomography problems. Computers & Geosciences 85, 36–44.

Svanberg, K., 2002. A class of globally convergent optimization methods based on conservative convex separable approximations. SIAM journal on optimization 12, 555–573.

Svanberg, K., 2007. MMA and GCMMA-two methods for nonlinear optimization. vol 1, 1–15.

Wang, X., Jardani, A., Jourde, H., 2017. A hybrid inverse method for hydraulic tomography in fractured and karstic media. Journal of Hydrology 551, 29–46.

Wang, X., Jardani, A., Jourde, H., Lonergan, L., Cosgrove, J., Gosselin, O., Massonnat, G., 2016. Characterisation of the transmissivity field of a fractured and karstic aquifer, Southern France. Advances in Water Resources 87, 106–121.

Worthington, S.R.H., Smart, C.C., Ruland, W.W., 2002. Assessment of groundwater velocities to the municipal wells at Walkerton. Ground and Water: Theory to Practice 1081–1086.

Yeh, T.-C.J., Liu, S., 2000. Hydraulic tomography: Development of a new aquifer test method. Water Resources Research 36, 2095–2105.

Zhou, Y., Lim, D., Cupola, F., Cardiff, M., 2016. Aquifer imaging with pressure waves—Evaluation of low-impact characterization through sandbox experiments. Water Resources Research 52, 2141–2156.

Chapter 6 Conclusions

In this paper, we carried out several groups of lab-scale transport experiments to study the solute transport process in dual conduit structures. The results confirmed that the dual conduit structure triggers the double-peaked BTCs. We figured out how different factors can influence the transport process: 1) As the length ratio increases, on the c-t plot, the two peaks get more separated, the concentration value of the first peak (C_{peak1}) increases and the second peak (C_{peak2}) decreases; 2) As the total length increases, the two peaks become increasingly separated and the concentration value of both peaks decreases, while C_{peak2} decreases much more than C_{peak1}; 3) As the (θ_1-θ_2) value of the dual-conduit connection increases, the size of the first peak (A_1), and thus the mass transported through the shorter conduit, gets smaller and the size of the second peak (A_2), and thus the mass transported through the longer conduit, gets bigger. 4) When the shorter conduit has a larger aperture than the longer conduit, the dual-conduit structure presents dual-peaked breakthrough curves (BTC) or single-peaked BTCs with a bump on the falling limb; when the shorter conduit has a smaller aperture than the longer conduit, the dual-conduit structures lead to either single-peaked BTCs or dual-peaked BTCs whose early peak is lower than the late peak. 5) As the flow rate increases, the dual-conduit structures are more likely to present dual-peaked BTCs. Based on these results, a method has been proposed for estimating underground karstic conduit lengths from experimental dual peaked BTCs.

Different numerical models have been applied to fit the experimental BTCs. The dual-peaked BTCs have been fitted by three models: DRAD, DRMIM, and WSADE. DRAD achieved a good fitting with stronger parameter identifiability except that the exchange coefficient is insensitive during fitting; the DRMIM model has better fitting performance than the WSADE model. The single-peaked BTCs have been fitted by four models: ADE, TFA, MIM, and DRAD. The ADE fails well reproduce most of the BTCs in this study. TFA has better performance than the ADE, but it cannot well reproduce the BTCs with a strong tailing effect. MIM can well characterize the BTCs with a strong tailing effect. The three models are suitable for different situations. We provide suggestions on choosing the optimal transport model for different BTCs. The DRAD can be inappropriate for some single-peaked BTCs due to strong interaction between model parameters, although the data fitting appears acceptable.

We applied a transfer function approach (TFA) for characterizing the karst solute transport process. It is shown that the TFA allows a better fitting than the ADE model and has advantage over the MIM model under certain conditions. In this study, we studied the similarities between the responses of the TFA and ADE models, so that we can relate the TFA parameters to physical variables and parameters (velocity and dispersion) considered in the ADE. Under the conditions that the derived equations are satisfied and the TFA parameter N value is large enough ($N \geqslant 50$), the TFA and ADE generate identical BTCs. If we apply the TFA to model transport BTCs, it is necessary to transform the TFA parameters (A, N, and τ) to equivalent

ADE parameters (u_{TFA} and D_{TFA}). Because the TFA parameters did not have the physical meaning that is closely related to transport properties. Even when N is small (when the equivalence between ADE and TFA is not strictly realized), the transformed parameters (u_{TFA}, D_{TFA}) still reflect the characteristics of the transport process. Thus, after applying the TFA to fit some BTCs, we can do this transformation to make the fitted parameters more relevant to the transport process.

In this study, we propose a new inverse approach to characterize the spatial property of a karst conduit network. The new inverse approach integrates four advantageous implementations: 1) Discrete conduit network (DCN) model is applied to explicitly represent the conduits; 2) the spatial variation of the parameters of the DCN segments should be considered; 3) the DCN network structures should be determined with reliable basis; 4) the joint inversion of two kinds of data: steady-state pumping test data and transient tracing test data. With the above implementations, we have characterized the diameter properties of the conduit network of the Terrieu well site. The result provides us with important implications about the heterogeneous properties of the target aquifer.

As a summary of this thesis, the experimental results have helped people to better understand the transport processes in karst aquifers. The modeling results may guide hydrogeologists to select the most suitable model for interpreting their dye tracing experiment. These results should further help hydrogeologists to better interpret the results of the tracing tests realized in real karst aquifers. Applying the proposed numerical tools, hydrogeologists may realize a better characterization about the properties of the karst aquifer.